On the Origin of Magnetoresistance in Organic Spin Valves

Dissertation

zur Erlangung des Doktorgrades der Naturwissenschaften
(Dr. rer. nat.)

der
Naturwissenschaftlichen Fakultät II
Chemie, Physik und Mathematik

der
Martin-Luther-Universität Halle-Wittenberg

vorgelegt von

Herrn **Matthias Grünewald**
geb. am 31. Oktober 1980 in Erlenbach am Main

Gutachter:

1. Prof. Dr. Georg Schmidt
Martin-Luther-Universität Halle-Wittenberg

2. Prof. Dr. Kathrin Dörr
Martin-Luther-Universität Halle-Wittenberg

3. Prof. Dr. Bert Koopmans
TU Eindhoven

Eröffnung des Promotionsverfahrens: 17. Dezember 2014
Tag der öffentlichen Verteidigung: 3. Juni 2015

Contents

List of Figures

List of Abbreviations and Symbols

Acronyms

AFM . . . . . . Atomic Force Microscopy

BLC . . . . . . Bilayer Contact

BRS . . . . . . Base Resistance State

CMR . . . . . . Colossal Magnetoresistance

CSA . . . . . . Channel-Spark Ablation

DOS . . . . . . Density Of States

EBL . . . . . . Electron Beam Lithography

EM . . . . ElectroMagnet

ESEM . . . . . Environmental Scanning Electron Microscopy

FM . . . . FerroMagnet

GMR . . . . . Giant MagnetoResistance

HFMR . . . . High-Field MagnetoResistance

HIS . . . . Hybridisation-Induced State (often also Hybridised Interface State)

HOMO . . . . Highest Occupied Molecular Orbital

HRS . . . . . . High Resistance State

HV . . . . High Vacuum

IRS . . . . Intermediate Resistance State

LRS . . . . . . Low Resistance State

LUMO . . . . . Lowest Unoccupied Molecular Orbital

MIM . . . . . . Metal-Insulator-Metal

MOKE . . . . Magneto-Optical Kerr Effect

MR . . . . MagnetoResistance

MTJ . . . . . . Magnetic Tunnel Junction

MTR . . . . . . Multiple Trapping and Release

NM . . . . Non-Magnetic material

OFET . . . . . Organic Field Effect Transistor

OMAR . . . . Organic MAgnetoResistance

OMBD . . . . Organic Molecular Beam Deposition

OSC . . . . . . Organic Semiconductor

OSV . . . . . . Organic Spin Valve

PLD . . . . . . Pulsed Laser Deposition

RS . . . . Resistive Switching

SCM . . . . . . SuperConducting Magnet

SLC . . . . . . Single Layer Contact

SNR . . . . . . Signal-to-Noise-Ratio

SQUID . . . . Superconducting QUantum Interference Device

TAMR . . . . . Tunneling Anisotropic MagnetoResistance

TEM . . . . . . Transmission Electron Microscopy

TMR . . . . . . Tunneling MagnetoResistance

TOF . . . . . . Time-Of-Flight

UHV . . . . . . Ultra-High Vacuum

VRH . . . . . . Variable Range Hopping

Materials

Al . . . . aluminium

AlOx . . . . . . alumina (aluminium oxide)

AlQ$_3$ . . . . . . Tris(8-hydroxyquinolinato)aluminium

Au . . . . gold

Co . . . . cobalt

CoFe . . . . . . cobalt iron alloy ($Co_{30}Fe_{70}$)

Cu . . . . copper

H$_2$Pc . . . . . . metal-free Phthalocyanine

LSMO . . . . . lanthanum strontium manganite ($La_{0.7}Sr_{0.3}MnO_3$)

NGO . . . . . . neodymium gallate ($NdGaO_3$)

Ni . . . . nickel

NDI . . . . . . core-chlorinated Naphthalene Tetracarboxylic Diimide

PDI . . . . . . N,N'-bis(Heptafluorobutyl)-3,4:9,10-Perylene Diimide

***p*-Si** . . . . *p*-doped silicon

SiO$_2$ . . . . . . silicon dioxide

STO . . . . . . strontium titanate ($SrTiO_3$)

Ti . . . . titanium

Symbols

A . . . . device area

$B, \boldsymbol{B}$ . . . . . . magnetic field, magnetic flux density

c . . . . concentration

D . . . . diffusion constant

DOS . . . . . . density of states

$d_{\mathbf{barrier}}$ . . . . . thickness of a tunnel barrier

$d_{\mathbf{material}}$ . . . . thickness of a material layer

Δx . . . . difference of the measure x

E . . . . energy

$\mathcal{E}, \boldsymbol{\mathcal{E}}$ . . . . electric field

e . . . . elementary charge

$F, \boldsymbol{F}$ . . . . force

G . . . . conductance

g . . . . electron spin g-factor

$H, \boldsymbol{H}$ . . . . . . magnetic field

$H_{\mathbf{c}}$ . . . . coercive field of a ferromagnetic layer

$\hbar$ . . . . reduced Planck constant

I . . . . current

$j, \boldsymbol{j}$ . . . . current density

$l_{\mathbf{channel}}$ . . . . . channel length

$l_{\mathbf{sf}}$ . . . . spin-diffusion length

$M, \boldsymbol{M}$ . . . . . . magnetisation

MR . . . . amplitude of any MR effect

$m_{\mathbf{e}}$ . . . . electron rest mass

$\mu_{\mathbf{material}}$ . . . . charge carrier mobility in a material

$N_{\mathbf{pinholes}}$ . . . . number of pinholes in a device

n . . . . charge carrier density

$\omega_{\mathbf{L}}$ . . . . Larmor frequency

P . . . . spin polarisation

Φ_0 . . . . energetic height of a barrier

φ . . . .   angle in the sample plane or single spinfs phase

R . . . .   device resistance

ρ . . . .   resistivity

$s, \boldsymbol{s}$ . . . .   spin

T . . . .   temperature

$\mathcal{T}$ . . . .   tunnel matrix element

$TAMR$ . . . . .   amplitude of the TAMR effect

TMR . . . . . .   amplitude of the TMR effect

t . . . .   time

$\theta_{\mathbf{evap}}$ . . . . . .   tilt of sample with respect to material source during evaporation

U . . . .   voltage

$\mathbf{V_O}$ . . . .   oxygen vacancy

W . . . .   work function of a material

$w_{\mathbf{channel}}$ . . . .   channel width

$\uparrow / \downarrow$ . . . . . .   spin up/down

Other Abbreviations

HAL . . . . . .   Martin-Luther-Universität Halle-Wittenberg

WÜ . . . . . .   Julius-Maximilians-Universität Würzburg

Chapter 1

Introduction

Organic spintronics is a research area working at the intersection of spintronics and organic electronics. The main objective of organic spintronics is the best possible combination of promising advances that so far have been separately achieved in both fields and of the clear advantages over established technologies.

Spintronics can be regarded as entirety of all kinds of research activities and technological applications exploiting the charge carriers' spins and spin-polarised currents for the purpose of information processing and storage. In the last decade the first spintronics-operated information technology devices have been developed to market maturity leading to a, generally speaking, remarkably increased efficiency. The most prominent examples in this context presumably are data storage and memory applications making use of magnetoresistance (MR) effects, e.g. hard disk read-and-write heads and the magnetic random access memory.
The implementation of organic semiconductors (OSCs) into spintronics devices holds the prospect of adding several additional and enriching advantages to them. Compared to inorganic semiconductors, organic compounds which likewise already are successfully implemented in some everyday objects, e.g. organic light emitting diodes, usually are cheaper (considering purchase costs and the required processing equipment) and offer a high flexibility and tunability of their physical and chemical properties. Furthermore, at the advent of organic spintronics it has frequently been argued that OSCs may be the ideal candidates for pushing forward semiconductor spintronics because of the low spin orbit coupling resulting in a good spin-transport performance in these light molecular-weight materials. This reasoning, however, has been rendered questionable in the past years.

The observation of spin-dependent phenomena in lateral and vertical transport structures by Dediu *et al.* and Xiong *et al.* in 2002 and 2004 [Dediu02, Xiong04], respectively, can be considered as the starting point of organic spintronics initiating a lot of subsequent research activities. These comprise, on one side, investigations in actual transport devices, mostly with respect to either MR in vertical organic spin valves (OSVs) with two ferromagnetic electrodes, i.e. spin-valve functionality [Wang05, Majumdar06b, Xu07, Santos07, Dediu08, Schoonus09, Lin10, Nguyen10], or intrinsic effects related to the OSC material in vertical devices with non-magnetic electrodes like, for instance, organic magnetoresistance [Francis04, Desai07, Bloom07, Bergeson08]. On the other side, fundamental studies of

the properties and spin dynamics at inorganic-organic interfaces have been successfully undertaken such as the demonstration of spin-injection into an OSC [deJong03, Zhan08, Drew09, Cinchetti09, Boehme09].

However, despite the extensive investigation of a variety of materials and material combinations, in a specific experiment usually the question concerning the physics behind an observed spin-valve effect remains more or less open: on the one hand, the origin of a spin-valve signal in an OSV can be actual spin injection into the OSC, subsequent diffusive spin transport and electrical spin detection (giant magnetoresistance) [Dediu02, Xiong04, Nguyen10, Nguyen12]. On the other hand, also effects based on a spin-polarised current tunneling through the OSC layer, e.g. tunneling magnetoresistance [Santos07, Xu07], can play a role. Whereas both scenarios are separately sustained but not unambiguously proved by a large amount of results, they are only seldom investigated in explicit comparative studies [Yoo09, Lin10]. It is noteworthy that this rather unsatisfying situation similarly has been present in the field of inorganic spintronics as well, where several experimental results have been misinterpreted as a proof of spin injection, diffusive spin transport and electrical spin detection in semiconductor-based devices, e.g. in [Monzon99].

Therefore, one main objective of the present work is to establish a characterisation protocol that allows for a complete understanding of the physics behind the MR effect that is observed in vertical OSVs. Most structures under investigation comprise an n-type OSC that, so far, has not been investigated with respect to spintronics applications, namely N,N'-bis(Heptafluorobutyl)-3,4:9,10-Perylene Diimide (PDI). This material exhibits rather outstanding characteristics concerning its stability in ambient conditions and charge carrier mobility, thus giving prospect to well-performing devices. Another open issue in the field of organic spintronics which should be addressed by this work is the quite common lack of results obtained in lateral transport structures, which is presumably due to the fact that the fabrication of such devices is considerably more challenging than this of standard vertical OSVs. Hence, in this context, first technological requirements have to be met before emphasis can be put on device characterisation and the results' interpretation.

This thesis is organised as follows. Chapter 2 comprises all fundamentals necessary for an understanding of this work, which includes the theoretical background of, for instance, spin-valve functionality (MR effects) and charge transport mechanisms in OSCs, as well as an introduction to the materials under investigation. All relevant results obtained in vertical transport structures are summarised in chapter 3 that itself consists of four parts. First, extensive investigations undertaken for conventional OSVs based on PDI are presented (chapters 3.2 and 3.3). As the results thereof are indicative of a dominating role of tunneling processes for both charge transfer and MR, the relevance of tunneling is probed in another type of structures, so-called single-sided spin valves with only one ferromagnetic electrode. Similarly as in analogous experiments in inorganic devices, these experiments result in the observation of the tunneling anisotropic magnetoresistance (TAMR, chapter 3.4). So far, this effect virtually never has been taken into account when interpreting data obtained in OSVs, thus motivating its investigation in structures employing one of the standard OSCs in organic spintronics, Tris(8-hydroxyquinolinato)aluminium (AlQ$_3$), as well. Examined in their

entirety, all results for PDI-based devices yield a conclusive picture of the charge transport and the spin-valve signal's origin which can be described by the model presented in chapter 3.5.

Next, in chapter 3.7 another effect with a high potential of being exploited in multifunctional devices, often referred to as resistive switching (RS) effect, is demonstrated in AlQ$_3$-based TAMR structures. Here, RS is carefully analysed by, amongst other techniques, applying TAMR as a tool for the investigation of the functional interface between one of the electrodes and the organic interlayer. Equally as for the MR in conventional spin valves, also for this effect a governing role of tunneling processes is experimentally proved.

In chapter 4 all relevant information concerning lateral OSVs can be found. After a detailed description of the fabrication process, results of preliminary studies and magnetotransport investigations are presented. Again, a model explaining the observed MR effect and its peculiarities is provided. The key conclusion that has to be drawn from the experiments with this device geometry is similar to the one for the vertical OVSs, namely that tunneling effects are presumably dominating the charge transfer and MR.

Finally, a summary of the work is given in chapter 5 with a special focus on the novel findings and their potential further exploitation.

Chapter 2

Fundamentals and Theory

2.1 Spintronics and Magnetoresistance Effects in Spin-Valve Structures

As already mentioned in the introduction to this work, research in spintronics is related to the investigation of spin-dependent (transport) phenomena. In this context, an electrical current's spin polarisation P_I can be considered a key figure. Assuming two possible orientations of the charge-carriers' spin, namely up and down ($\uparrow$ and $\downarrow$), P is defined as:

$$P = \frac{I_\uparrow - I_\downarrow}{I_\uparrow + I_\downarrow} \tag{2.1}$$

The detection of tunneling magnetoresistance (TMR) by Jullière in 1975 [Jullière75] and the observation of spin injection from a ferromagnetic into a non-magnetic metal by Johnson and Silsbee in 1985 [Johnson85] can be quoted as founding results of spintronics. The latter finally resulted in the realisation of devices exploiting the giant magnetoresistance (GMR) effect, which was achieved a few years later only by Baibich *et al.* and Binasch *et al.* [Baibich88, Binasch89].

Magnetoresistance (MR) effects are usually observed and investigated in a so-called spin valve which can be considered the canonical spintronics device. Its structure can be reduced to three functional components, two ferromagnetic electrodes (FM) and a non-magnetic spacer layer (NM) in between which are arranged in an either lateral or vertical configuration. The working principle of a spin valve is based on the fact that its resistance depends on the relative magnetisation of the ferromagnetic electrodes (also named spin-valve state in the following) which can be either parallel or anti-parallel. It is worth noting that there are two possible realisations of the spin-valve structure. In the first one, the actual spin valve, one electrode's magnetisation is fixed, e.g. by coupling to an antiferromagnetic layer, and the second electrode's magnetisation is free, i.e. it can be changed by an external magnetic field, whilst in a so-called pseudo-spin-valve the magnetisation of both electrodes' is free. All spintronics-related fundamentals will be outlined on the basis of the latter as this type of device is mostly investigated in the field of organic spintronics. Thus, for the sake of simplicity, pseudo-spin-valves will be referred to as spin valves hereafter.
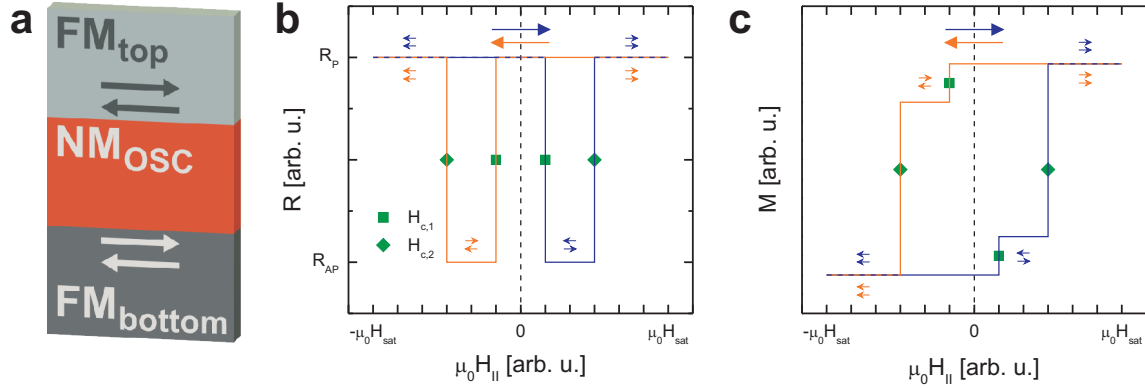
Figure 2.1: **a**: Schematic structure of a vertical (pseudo-)spin-valve device consisting of two ferromagnetic electrodes (FM) with different coercive fields and a non-magnetic spacer layer (NM) sandwiched in between. The NM is an organic semiconductor in the case of an OSV. **b**: MR trace of an OSV exhibiting a negative spin-valve effect. **c**: Ideal magnetisation behaviour of an OSV device comprising two electrodes with different coercive fields. The large arrows in the top of the panels indicate the sweep direction for $H_{||}$, and the small ones near the plots represent the current magnetisation-state of the device's electrodes.

The schematic structure of a vertical organic spin valve (OSV) in which the non-magnetic spacer layer consists of an organic semiconductor (OSC) is depicted in Fig. 2.1**a**. As the two ferromagnetic electrodes usually are made of different materials, they exhibit different coercive fields $H_{c,i}$ allowing for the preparation of a parallel and anti-parallel magnetisation alignment. As aforementioned, the resistance R of a spin-valve device is correlated to this alignment and therefore can be modified by an external magnetic field applied in the sample plane ($\boldsymbol{H}_{||}$). The blue curves in Figs. 2.1**b** and **c** show the behaviour of R and the complete structure's magnetisation M for a $\boldsymbol{H}_{||}$ sweep from negative to positive saturation. The relative magnetisation of the electrodes' is represented by the small arrows. Starting in the parallel alignment at negative fields with the device resistance R_{P}, the magnetisation of the magnetically softer electrode is reversed at low positive $H_{||}$ ($H_{c,1}$) yielding the anti-parallel spin-valve state (R_{AP}). In the case of OSVs mostly $R_{\mathrm{AP}} < R_{\mathrm{P}}$ is observed which usually is referred to as a negative or inverted spin-valve effect. When the coercive field $H_{c,2}$ is reached, the device is set back to the highly resistive parallel state again. Mostly, the signal is symmetric with respect to $\mu_0 H_{||} = 0\,mT$, i.e. for the opposite sweep direction (orange curves in Figs. 2.1**b** and **c**) an analogous behaviour is obtained. The amplitude MR of the effect is calculated as follows:

$$MR = \frac{R_{\mathrm{AP}} - R_{\mathrm{P}}}{R_{\mathrm{AP}}} \tag{2.2}$$

In a very simplified picture, the electrodes can be considered as spin polariser/injector and analyser/detector and the spacer layer as the layer which is transporting a spin-polarised current. In order to obtain spin-valve functionality, in this scenario therefore the thickness d_{spacer} of the spacer layer (assuming a vertical device structure) must not surpass the spin-

diffusion length l_{sf} of the material under investigation (see next chapter).

In the following chapters three types of MR effects that can cause spin-valve behaviour are briefly presented. It should be noted here that the models which will be introduced together with these effects usually are consulted to explain a positive spin-valve signal, whereas in OSVs commonly a negative one is observed. However, the fundamental principles of these models are necessary for the understanding of the existing approaches to an explanation of this alleged deviation, which will be addressed later (chapter 2.2.2).

2.1.1 Giant Magnetoresistance - GMR

In general, the giant magnetoresistance (GMR) effect can be observed in two different geometries. In structures for the investigation of the so-called current in-plane GMR (cip-GMR) the spin-polarised current is driven parallel to the functional layer stack . Most of the founding research has been done in fully metallic cip-GMR devices [Baibich88, Binasch89], whilst GMR in the alternative geometry, the current perpendicular-to-plane GMR (cpp-GMR), has been experimentally realised a few years later only [Pratt91]. As the focus of organic spintronics is definitely on vertical OSVs like the one shown in Fig. 2.1a, the origin of GMR will be discussed considering this geometry and on the basis of a rather simplified and phenomenological approach in the following.
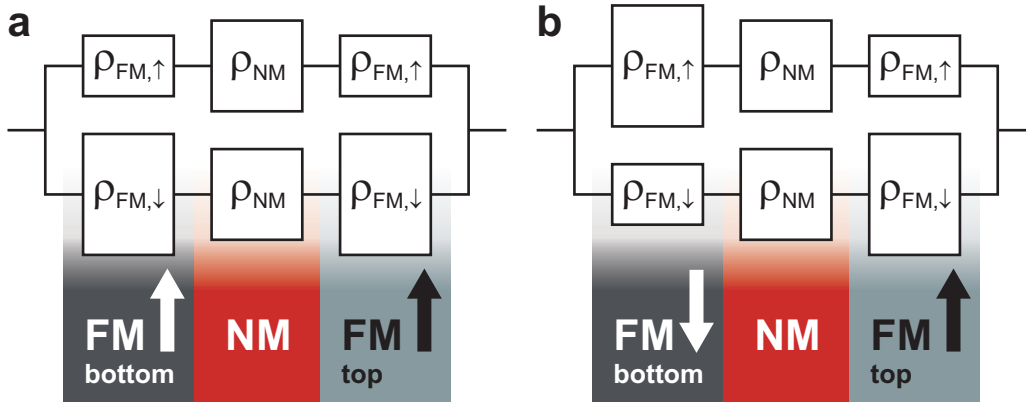
Figure 2.2: Two channel representation of a vertical spin valve (consisting of a ferromagnetic bottom and top electrode and a non-magnetic spacer in between) according to the Mott model which is based on separate channels for charge carriers with spin ↑ and ↓. The total device resistance depends on the relative magnetisation of the electrodes indicated by the large arrows in the electrodes (parallel state in **a**, anti-parallel state in **b**).

In this approach, often referred to as Mott model, a spin valve is described as a two channel device with separate conduction channels for charge carriers (electrons hereafter) with spin momentum ↑ and ↓, respectively, as indicated in the equivalent circuit diagrams in Fig. 2.2. The two channels, each of which is a serial connection of three resistors corresponding to the spin-valve components depicted 2.1a, are connected in parallel. Evidently, in this picture, the resistivity ρ_{NM} of the non-magnetic spacer can be considered identical for both spin channels. $\rho_{\mathrm{FM},\uparrow/\downarrow}$ of a ferromagnetic electrode, on the contrary, depends on the orientation of the electrons' spins with respect to the electrode's magnetisation as indicated

by the differently sized resistors in Fig. 2.2. Already in 1936, Mott and Wills [Mott36] found a clear theoretical description of this phenomenon which is caused by a low (high) scattering probability for electrons with a spin momentum aligned parallel (anti-parallel) to a ferromagnetic layer's magnetisation. The different scattering probabilities usually are expressed by the spin-dependent scattering rates $\tau_{\mathrm{FM},\uparrow/\downarrow}$, which can be stemming from intrinsic properties and processes as they have been considered by Mott and Wills, e.g. the band structure in transition metals, and from extrinsic sources like impurities [Fert68]. From the diagrams in Fig. 2.2 it becomes obvious that the differences in $\rho_{\mathrm{FM},\uparrow/\downarrow}$ of the single electrodes result in different total device resistances for the parallel (Fig. 2.2**a**) and anti-parallel (Fig. 2.2**b**) spin-valve state when a spin-polarised current is driven through the whole structure. Normally, GMR yields a positive spin-valve signal, i.e. $R_{AP} > R_P$.

As aforementioned, the electrodes can be regarded as spin injector and detector and the spacer layer as carrying a diffusive spin-polarised current in this model, in which a potential loss of spin polarisation in the non-magnetic material is not taken into account. In reality, however, the spin lifetime in any material has to be regarded as finite. Hence, in order to be able to detect a spin-polarised current at the detector electrode of a GMR structure the spin information must not be lost in the non-magnetic layer. This requisite thus is determining an upper limit of the spacer layer thickness d_{spacer}. For a more detailed analysis and theoretical description of GMR the reader is referred to the work of Valet and Fert [Valet93].

It is worth mentioning here that the application of semiconductors in GMR devices is not feasible in a straightforward manner. Due to the so-called conductance mismatch an efficient injection of a sufficiently highly spin-polarised current from a ferromagnetic metal contact into a semiconductor layer is not possible in the regime of diffusive transport [Schmidt00] in which GMR usually is occurring [Valet93]. However, on the one hand, in the case of inorganic semiconductors this problem can be surmounted by the introduction of a spin-dependent interface resistance [Rashba00, Fert01]. On the other hand, it is questionable whether the concept of conductance mismatch can be transferred one-to-one to organic spintronics devices, i.e. metal-OSC contacts. This is mainly because of the significantly different physics behind charge injection into and charge transport in these materials which will be extensively discussed in chapters 2.2.1 and 2.2.2. Consequently, it is very likely that also spin injection into OSCs is based on other mechanisms than those playing a role for this process in their inorganic counterparts.

2.1.2 Tunneling Magnetoresistance - TMR

TMR has been initially observed in 1975 by Jullière at low temperatures in a magnetic tunnel junction (MTJ) consisting of two ferromagnetic electrodes and a germanium-based tunnel barrier in between [Jullière75]. It has regained substantial research interest at the beginning of the 1990s due to its room temperature existence in structures comprising other barrier materials [Miyazaki91]. As the resistance of an MTJ depends on the relative magnetisation of the electrodes as well, MTJs are another realisation of a spin valve. Thus, the origin of a spin-valve signal caused by TMR can be explained in a similar way as in the case of GMR being the underlying mechanism.
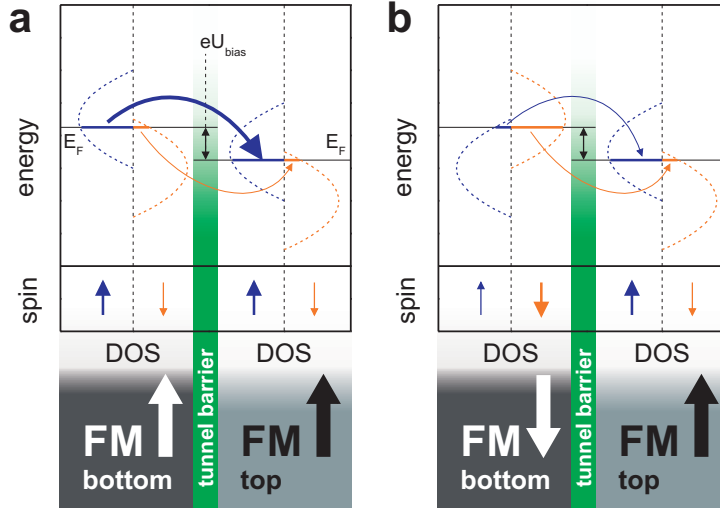
Figure 2.3: Illustration of TMR causing a spin-valve signal in an MTJ on the basis of the electrodes' *DOS*. Assuming spin conservation during tunneling the total current can be treated as sum of separate currents for both spin momenta ($\uparrow$ / $\downarrow$, blue/orange). **a**: In the parallel spin-valve state electrons with spin $\uparrow$ are majority charge carriers (large arrows in the spin panels) in both electrodes. Consequently the tunneling current is high and the device resistance low. **b**: The spins of the majority and minority charge carriers are oppositely oriented for both electrodes in the anti-parallel configuration yielding a lower tunneling current and thus a higher device resistance than for the parallel alignment.

The model introduced by Jullière [Jullière75] and summarised in Fig. 2.3 is based on spin-conserving tunneling between the two ferromagnetic electrodes. Similarly as in the two-spin-channel model for GMR, the spin-polarised tunneling current between the two electrodes of an MTJ can be treated separately for the two spin directions $\uparrow$ and $\downarrow$ (blue and orange curves/arrows). In this scenario, the current flowing through an MTJ is mainly determined by the ferromagnetic electrodes' density of states near the fermi energy (DOS_{E_F}, see also Equ. 2.4). The charge carriers in a specific electrode can be classified as majority or minority as depicted by differently sized arrows in the bottom panels of Fig. 2.3. This classification is based on the spin-dependent DOS_{E_F} (top panels of Fig. 2.3) which is high (low) when the charge carriers' spins are aligned parallel (anti-parallel) with respect to the electrode's magnetisation. This phenomenon is originating from ferromagnetic exchange coupling in the d-bands of ferromagnetic transition metals, which usually are used as electrode materials in actual devices.

Fig. 2.3**a** shows the situation for the parallel spin-valve state. In both electrodes electrons with spin $\uparrow$ are the majority charge carriers, i.e. on both sides of the tunnel barrier $DOS_{E_\mathrm{F},\uparrow}$ is equally high. In consequence the spin-$\uparrow$ contribution to the total current, $I_{\uparrow,P}$, is rather large. Electrons with the opposite spin momentum, on the contrary, can only provide a small current contribution $I_{\downarrow,\mathrm{P}}$ as they are minority charge carriers in both electrodes. Thus, the rather high total tunneling current and the consequently low device resistance R_P in the parallel spin-valve state can be regarded dominated by $I_{\uparrow,\mathrm{P}}$. In the case of an anti-parallel magnetisation alignment (Fig. 2.3**b**) the spin orientation of majority and minority charge

carriers is different in the two electrodes, respectively. As a result, $I_{\uparrow,\text{AP}}$, $I_{\downarrow,\text{AP}}$ and the total tunneling current are smaller and hereby the device resistance R_{AP} higher than in the parallel configuration.

In the Jullière model the maximum magnitude TMR of the spin-valve effect can be described using the charge carriers' spin polarisations P_i in the ferromagnetic electrodes [Jullière75]:

$$TMR = \frac{2P_1P_2}{1 - P_1P_2} \tag{2.3}$$

Equ. 2.3 only describes the influence of P_1 and P_2 on TMR. Obviously, there are several additional factors which can cause a reduction of the effect size, amongst them the height and thickness of the tunneling barrier which both are decisive for the tunneling resistance and consequently for TMR [Moodera99]. Impurities in the barrier [Tsymbal99] and magnon excitations [Tsui71] at the interface between the electrode and the barrier can diminish the effect as well. The latter likewise mostly are taken into account when the dependence of the TMR ratio on the applied bias voltage U_{bias} is discussed, which usually exhibits a sharp maximum at low U_{bias} and strongly drops with increasing U_{bias} [Jullière75].

Spin-valve signals originating from TMR can be either positive ($R_{\text{AP}} > R_{\text{P}}$) or negative ($R_{\text{AP}} < R_{\text{P}}$). As discussed above, a positive signal can be derived from the Jullière model in a straightforward manner. For a negative MR, by contrast, further ingredients are necessary which, for instance, can be bonding effects at the interface between the electrode and the barrier [DeTeresa99] modifying the electrodes' DOS or phenomena occurring inside the barrier [Tsymbal03] influencing the charge carriers' spin polarisation during the tunneling.

As will be discussed in chapters 2.2.1 and 2.2.2 tunneling processes may provide substantial contributions to the charge transfer in organic transport structures. Hence, TMR is of particular interest for the interpretation of magnetotransport results in vertical OSV devices.

2.1.3   Tunneling Anisotropic Magnetoresistance - TAMR

As pointed out above, both TMR and GMR require devices with two ferromagnetic electrodes for spin-valve functionality. Another effect named tunneling anisotropic magnetoresistance (TAMR), on the contrary, can mimic spin-valve behaviour in structures with only one ferromagnetic electrode and a non-magnetic counterelectrode (so-called single-sided spin valves). The effect has first been observed in (Ga,Mn)As-AlOx-Au tunnel junctions [Gould04, Rüster05a]. The necessary prerequisites for TAMR and the physics of the spin-valve effect in single-sided spin valves will be outlined in this chapter on the basis of the findings and the theoretical approach of Gould *et al.*

Generally speaking, there are two ingredients which together are causing a spin-valve-like signal in TAMR devices and both have to be ascribed to the ferromagnetic material under investigation. First, the tunneling current (described by the tunneling conductance G_{tunnel}) extracted from the ferromagnetic electrode is anisotropic, i.e. it depends on the relative ori-

entation of the electrode's magnetisation M_{rel} with respect to its crystalline axis. Second, the magnetisation dynamics of this electrode in an external in-plane magnetic field $\boldsymbol{H}_{||}$ has to comprise so-called two-step magnetisation reversal processes [Cowburn95].

The anisotropy of G_{tunnel} can be explained on the basis of an anisotropic $DOS_{E_{\text{F}}}^{\text{FM}}$ in materials exhibiting magnetocrystalline anisotropy and a sufficiently large spin-orbit coupling. Due to spin-orbit coupling the $DOS_{E_{\text{F}}}^{\text{FM}}$ in k-space is correlated to M_{rel} and therefore changes with M_{rel}. As a result, G_{tunnel} depends on M_{rel}:

$$G_{\text{tunnel}} \propto DOS_{E_{\text{F}}}^{\text{FM}}(M_{\text{rel}}) \cdot \mathcal{T} \cdot \left(1 - DOS_{E_{\text{F}}}^{\text{NM}}\right) \tag{2.4}$$

The tunnel matrix element $\mathcal{T}$ as well as $DOS_{E_{\text{F}}}^{\text{NM}}$, which is the DOS in the non-magnetic electrode, can be considered constant. The relation expressed in Equ. 2.4 can provide a good qualitative understanding of the conductance anisotropy. However, for a good quantitative agreement of theory and experiment it usually is necessary to assume a partial conservation of the in-plane momentum during the tunneling process [Gould04]. This can be the case for epitaxial barriers and rather clean interfaces, for which the tunneling probability of charge carriers with a momentum parallel to the barrier-normal direction (k_z) is higher than for those with a large in-plane momentum. Consequently, instead of the total $DOS_{E_{\text{F}}}^{\text{FM}}$ only a fraction thereof, namely this comprising states with large k_z, is relevant for G_{tunnel} in Equ. 2.4. With this approach differences of G_{tunnel} in the range of several % up to hundred's of %, depending on the barrier's quality (e.g. interface cleanliness), can be explained for devices with an electrode made of the diluted magnetic semiconductor (Ga,Mn)As.

(Ga,Mn)As, as well as LSMO grown on STO(001), a material frequently used as electrode in vertical OSVs, exhibits a biaxial magnetocrystalline anisotropy (see chapter 2.4.4). The physics behind the DOS anisotropy itself is not completely unraveled, however, a phenomenological theoretical description and analysis is feasible by the introduction of an additional, rather weak, uniaxial magnetic anisotropy along one of the strong easy axes. Such a symmetry breaking can be originating from the films' morphology which may be substantially influenced by so-called step-flow growth when substrates exhibiting a miscut are used. This explanation is given for (Ga,Mn)As in [Rüster05a] and likewise may hold true for LSMO on STO(001) [Mathews05].

As aforementioned, also the ferromagnetic electrode's magnetisation dynamics in an external in-plane magnetic field $\boldsymbol{H}_{||}$ is relevant for the occurrence of a spin-valve-like signal in a TAMR device. This dynamics is exemplarily sketched in Fig. 2.4a for a crystalline ferromagnetic layer with a biaxial magnetoctrystalline anisotropy and a $\boldsymbol{H}_{||}$ sweep (blue arrow) from negative to positive fields in a direction off the easy axes (orange lines).

The magnetisation $\boldsymbol{M}$ of materials with a magnetocrystalline anisotropy is always oriented such that the energy of single domains is minimal according to the theory of magnetisation rotation introduced by Stoner and Wolfarth [Stoner48]. Therefore, at the beginning of the sweep $\boldsymbol{M}$ is rotating towards one of the easy axes (step 1 and easy axis $easy_1$ in Fig. 2.4a). However, at small positive fields a deviation from the Stoner-Wolfarth-behaviour can be observed for a material with a combined uniaxial-biaxial anisotropy. This deviation can be
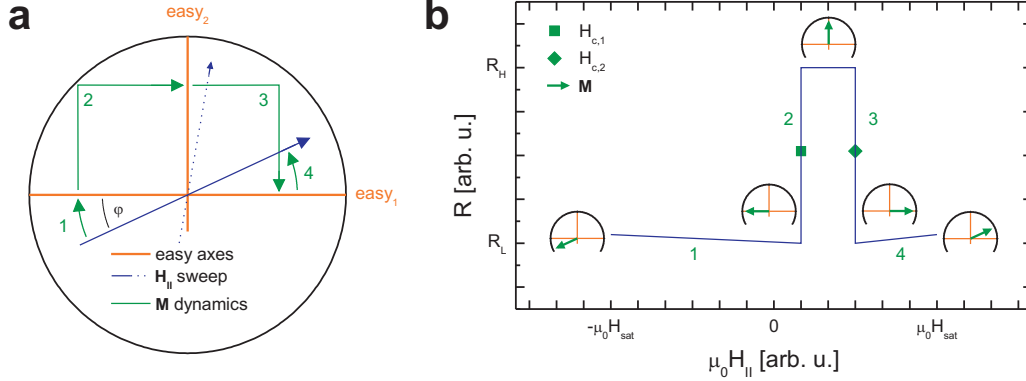
Figure 2.4: Two-step magnetisation reversal and origin of the spin-valve-like signal in a TAMR device. **a**: If an in-plane magnetic field $\boldsymbol{H}_{||}$ is swept along a direction off the easy axes of a material with a biaxial anisotropy, the magnetisation may be reversed in two 90° steps instead of one 180° step. **b**: In combination with an anisotropic tunneling conductance the two-step magnetisation reversal can lead to a spin-valve-like signal in magnetotransport studies.

explained by the model of Cowburn *et al.* [Cowburn95] which suggests that a magnetisation reversal via two 90° steps (steps 2 and 3 in Fig. 2.4**a**) instead of one 180° step takes place if energetically favourable. Hence, within a certain interval of $H_{||}$, limited by the fields $H_{c,1}$ and $H_{c,2}$, respectively, at which the 90° switchings occur, $\boldsymbol{M}$ is oriented along $easy_2$. Finally, at a sufficiently high positive magnetic field $\boldsymbol{M}$ is rotated from $easy_1$ towards the direction of $\boldsymbol{H}_{||}$ again (step 4 in Fig. 2.4**a**).

It is obvious that a combination of these two phenomena in one material which is part of a tunnel junction can evoke a spin-valve-like behaviour. This interplay is schematically depicted in Fig. 2.4**b**, where the magnetisation dynamics is referred to by the step numbers used above and the insets show the direction of $\boldsymbol{M}$ with respect to the easy axes for distinguished points on the MR trace. Assuming that the device resistance is low (high) when $\boldsymbol{M}$ is oriented along the axis $easy_1$ ($easy_2$) due to the anisotropic G_{tunnel}, a positive spin-valve signal with the two distinct resistive states R_{L} and R_{H} can be expected. The amplitude of TAMR usually is calculated as:

$$TAMR = \frac{R_{\text{H}} - R_{\text{L}}}{R_{\text{L}}} \tag{2.5}$$

Two characteristics features of a spin-valve-like signal originating from TAMR can be extracted from the representations in Fig. 2.4 in a straightforward manner. First, the width of the R_{H} interval in Fig. 2.4**b** is decreased (increased) when the orientation of $H_{||}$ is shifted towards (away from) $easy_1$, i.e. the positions of the $H_{c,i}$ strongly depend on the orientation of $\boldsymbol{H}_{||}$ denoted by the angle φ. Second, if the field is oriented near the other easy axis ($easy_2$) as indicated by the dotted arrow in Fig. 2.4**a**, the sign of the effect is inverted. Besides other experiments (see chapter 3.4), the observation of these features in magnetotransport measurements can be regarded as indication for TAMR.

Finally, it should be noted that TAMR must not only be considered as a further effect causing spin-valve-like MR behaviour but also can be exploited as a probing tool. Since TAMR is a tunneling based effect, its observation in a specific experiment thus is an unambiguous proof of the charge transfer being dominated by tunneling processes. In this context, it is also worth keeping in mind that a positive TAMR result must not be interpreted with respect to the tunneling current's spin polarisation. This is because for TAMR, in contrast to TMR or GMR, the spin polarisation does not need to be (partially) conserved during the charge carriers transition between the electrodes.

2.1.4 The Hanle Effect

Despite the facts that a lot of effort has been put into the investigation of OSVs and that the observed MR effect is very often ascribed to GMR, a decisive and robust proof rarely is provided in a specific experiment. One possibility to identify GMR as underlying mechanism of a spin-valve signal is the investigation of a phenomenon originating from spin precession which usually is referred to as the Hanle effect.
Before the physics behind this effect is outlined, it should be explicitly stated that the origin of any MR effect caused by GMR consists of three components: electrical spin injection from the first electrode, diffusive spin transport through the spacer layer, and electrical spin detection in the second electrode. Although several techniques have been established which can be used to gain evidence for the first two components in organic devices as well [Cinchetti09, Drew09, Nguyen12], the entirety of the aforementioned three processes can only be regarded as more or less strongly indicated by a few experiments, e.g. by the investigation of two materials in an OSV which only differ concerning the incorporated hydrogen isotopes [Nguyen10]. Therefore, so-called Hanle experiments in OSVs are very promising as they are targeting the proof of electrical spin detection.

The Hanle effect [Johnson85, Johnson88] itself is originating from the very basic phenomenon of the precession of the charge carriers' (electrons for this consideration) spins in a magnetic field $\boldsymbol{H}_\perp$ that is applied perpendicular to the spins' orientation (perpendicular geometry). The precession can be described as Larmor precession with the frequency ω_L which depends on $H_\perp$, the electron rest mass m_e and the electron spin g-factor:

$$\omega_\mathrm{L} = \frac{eg\mu_0 H_\perp}{2m_\mathrm{e}} \tag{2.6}$$

Thus, the spin $\boldsymbol{s}$ (phase φ_0 at time $t = 0$) becomes time-dependent and can be described by:

$$\boldsymbol{s} = \frac{1}{2}\hbar \begin{pmatrix} \cos\left(\varphi_0 + \omega_\mathrm{L} \cdot t\right) \\ \sin\left(\varphi_0 + \omega_\mathrm{L} \cdot t\right) \end{pmatrix} \tag{2.7}$$

Hereafter, a vertical OSV in a distinct magnetisation and consequently resistance state is assumed. This remanent spin-valve state is prepared by sweeping the in-plane magnetic field $\boldsymbol{H}_{||}$ in a suitable manner, whilst the current flow is perpendicular to the sample plane. For the Hanle experiments $\boldsymbol{H}_{||}$ is turned off after the preparation sweep. When GMR is causing the spin-valve signal of this device, the current has to be spin polarised as illustrated in Fig.

2.5**a**, which shows the device in the anti-parallel spin-valve state and at zero (in-plane and perpendicular) magnetic field. If no processes reducing the spin polarisation occur, a single electron's spin is conserved during the time t_{trans} which is needed for the travel through the organic spacer layer.

As already stated above, a non-zero $H_\perp$ causes a precession of the electrons' spins as illustrated in Fig. 2.5**b**. For the electron on the left hand side of Fig. 2.5**b** this precession results in a spin rotation by $\Delta\varphi \approx 180°$ and hereby changes the spin's orientation with respect to the electrodes' magnetisation. Obviously, this is equivalent to the transition from the anti-parallel to the parallel spin-valve state as the electron's spin is now aligned parallel to the top electrode's magnetisation. According to the basic picture of GMR outlined in chapter 2.1.1, thus any spin rotation due to the precession in a non-zero $H_\perp$ is reflected in the MR traces that are obtained by measurements in the perpendicular geometry.
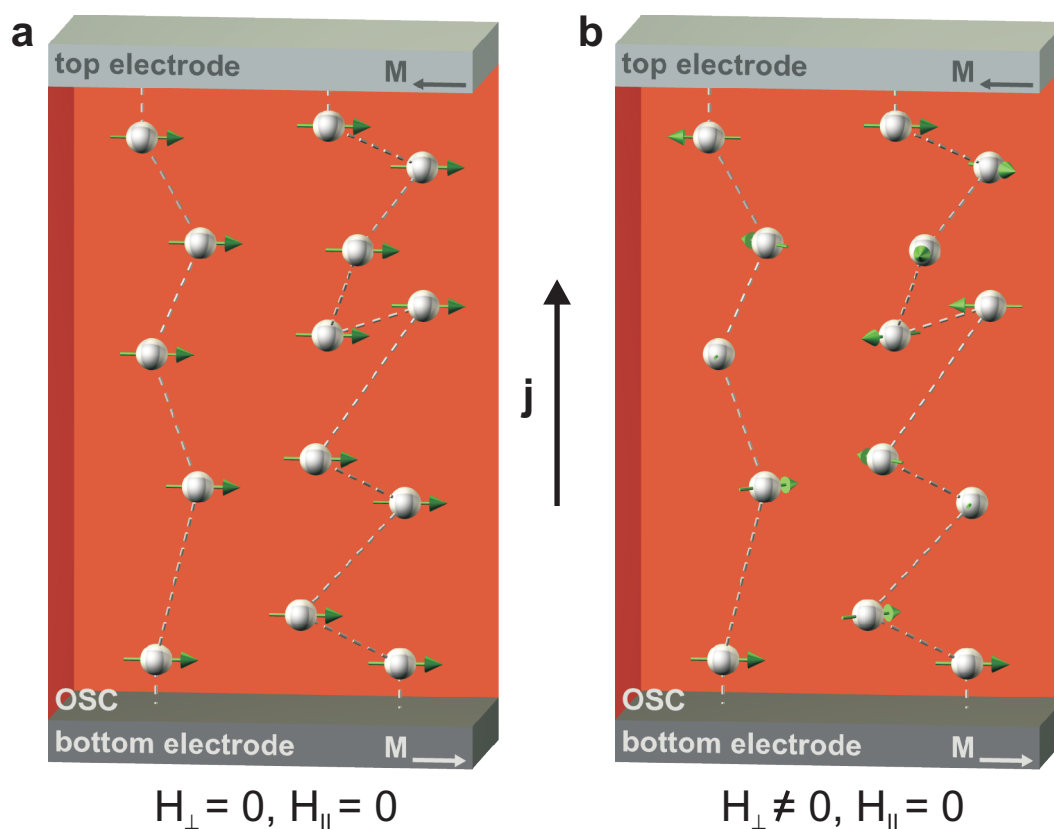
Figure 2.5: Spin precession in a vertical OSV device induced by the application of a perpendicular magnetic field $\boldsymbol{H}_\perp$. The charge carriers are injected into the OSC layer from the bottom electrode.

Obviously, $\Delta\varphi$ depends on t_{trans} and the magnitude of $H_\perp$. Whereas the latter can be regarded as a global parameter, t_{trans} may be significantly different for single electrons. This is indicated in Fig. 2.5 by the juxtaposition of two electrons on two alternative paths for which t_{trans} differs by a factor of ~ 2 (it is assumed that t_{trans} is proportional to the number of steps in this picture). Actually, such significant variations in t_{trans}, also referred to as incoherent charge transport, are very likely in organic devices as will be discussed in chapter 2.2.1. As

a consequence thereof, the spin polarisation is strongly diminished or even completely lost when the electrons reach the second electrode due to the averaging of the $\Delta\varphi$ of all electrons' spins. This behaviour is known as spin dephasing and is reflected in MR measurements in the perpendicular geometry as quench of the spin-valve signal, i.e. as disappearance of the resistance difference between the anti-parallel and parallel configuration [Lou07, Tombros07]. As illustrated in Fig. 2.6a for a negative MR effect ($R_{AP} < R_P$), already at small $H_\perp$ spin dephasing causes a modification of R towards an intermediate state R_{int}.

If, on the contrary, the charge and spin transfer is rather coherent, the variations in t_{trans} are small. Thus, the variations in the single electrons' $\Delta\varphi$ are equally small and the spins' precession can be regarded as coherent as well. Consequently, so-called Hanle oscillations as shown in Fig. 2.6b, periodic changes between the anti-parallel and parallel spin-valve state, can be observed at small $H_\perp$ [Huang07]. This periodic signal is superimposed by the quench of the spin-valve effect due to the spin dephasing. A total loss of spin polarisation is only observed at sufficiently high $H_\perp$ equivalent to several full precessions in this case.
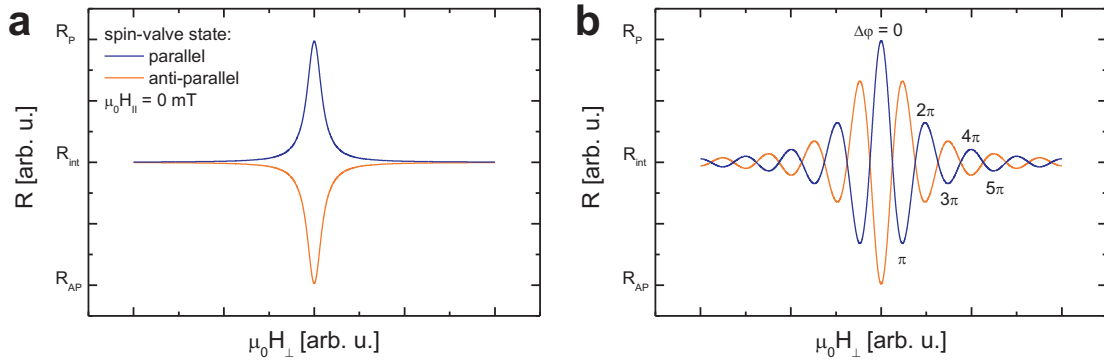
Figure 2.6: Modification of a negative spin-valve signal ($R_{AP} < R_P$) due to the spins' precession in a perpendicular magnetic field $\boldsymbol{H}_\perp$. Measurements in the perpendicular geometry usually are performed after the preparation of the either parallel (blue curves) or anti-parallel (orange curves) remanent spin-valve state. **a**: In the case of incoherent charge transport only spin dephasing is reflected in the MR trace. **b**: Hanle oscillations, periodic changes between the anti-parallel and parallel spin-valve state, are observed when coherent charge transport is dominating. These oscillations are superimposed by the spin-dephasing signal which is broader in this case.

It should be borne in mind that the effects caused by a perpendicular magnetic field only occur for the aforementioned sequence of spin injection, transport and detection in a spin valve. If one of these ingredients for GMR, e.g. the electrical detection in one of the ferromagnetic electrodes, is missing, as a logical consequence the spins' precession cannot be reflected in the corresponding magnetotransport measurements. Experiments in the perpendicular geometry have been successfully applied in the field of inorganic spintronics to prove spin injection, diffusive spin transport and electrical spin detection [Lou07, Tombros07, Huang07]. Likewise, they can be employed as a powerful tool to gain strong and unambiguous experimental for the presence or absence of GMR in OSV devices as demonstrated by Riminucci *et al.* [Riminucci13] and the author of the present work (chapter 3.3, [Grünewald13b]).

2.2   Organic Semiconductors - OSCs

Organic semiconductors (OSCs) are a class of organic materials which exhibit semiconducting properties. Compared to their inorganic counterparts they have to be treated differently in many aspects, amongst them also concerning the description and modeling of the charge transport. Existing models and peculiarities will be introduced in chapter 2.2.1. With respect to the use of OSCs in spintronics applications intrinsic MR effects that can be originating from the OSC layer in an actual device, e.g. the so-called organic magnetoresistance (OMAR, chapter 2.2.3), have to be considered as well. Finally, in chapters 2.4.2 and 2.4.3 the materials under investigation will be briefly presented.

2.2.1   Charge Transport in OSCs

A first difference between inorganic and organic semiconductors exists concerning their classification as either n- or p-type. Whereas for the former this distinction is undertaken on the basis of the respective material's doping with donors or acceptors, OSCs are labeled n-type (p-type) when electrons (holes) can be injected more easily into the material under consideration than the respective other charge carrier species [Klauk06].
Another, more important, difference has to be stated with respect to the theoretical approaches describing the charge transport. In inorganic semiconductors the charge transport normally is explained by theories based on the band structure, which is formed by delocalised electronic states in the respective material [Sze06]. As in OSCs, on the contrary, the energetic landscape is mostly influenced by the molecular orbitals and polaronic states, this approach cannot be directly transferred to organic materials.

The molecular orbitals can be determined, for instance, by the linear combination of atomic orbitals (LCAO) theory. Analogies to the band structure in inorganic materials can be drawn with respect to the highest occupied molecular orbital (HOMO, equivalent to the valence band) and the lowest unoccupied molecular orbital (LUMO, equivalent to the conduction band). These orbitals are mainly formed by delocalised π-orbitals. The LUMOs of neighbouring molecules usually are overlapping and can provide free energetic states for the charge transport. It is obvious that this overlap decisively depends on the molecules' ordering, i.e. the crystalline quality of the OSC layer under investigation.
Thus, in highly homogeneous monocrystals the charge transport indeed can be considered band-like. The decisive energy bands are narrower than those in inorganic materials due to the relatively weak intermolecular interaction (van-der-Waals interaction). As aforementioned, they are constituted by the HOMO and the LUMO which usually are described by a Gaussian (see Fig. 2.7a). However, this scenario represents an exceptional case as OSC layers in actual devices mostly are amorphous or polycrystalline. As a result, alternative theories for the description of charge transport in such OSC layers are necessary.

In amorphous or polycrystalline layers, energy levels originating from polaronic states equally have to be taken into account in addition to those constituted by the molecular orbitals. Polarons are quasi-particles consisting of a charge carrier and a polarisation or deformation, respectively, of the molecule where the charge carrier is localised. These particles

usually are formed when charge carriers are travelling through an OSC layer [Horowitz98] and therefore have to be regarded as another species contributing to the charge transfer. Generally speaking, it can be stated that the occurrence of polaron formation leads to a decrease of the charge carrier mobility in a specific material as a polaron needs to overcome its binding energy in order to move from one localised state, i.e. from one molecule, to another. Thus, polaronic states can be considered to be trap states. Moreover, polaronic states cause a broadening of the LUMO and HOMO and provide additional states in the gap between these orbitals. The role of the latter two phenomena with respect to charge injection into and charge transfer through OSC layers in actual devices will be outlined in more detail in chapter 2.2.2.
Additionally, statistically distributed trap states stemming from defects, grain boundaries and impurities in OSC layers with a rather low crystalline quality can appear in the energetic landscape. They are commonly classified as energetically deep or shallow traps. Depending on the distribution and the nature of these additional trap states in an OSC layer different models are available for the description of the charge transport.

In the case of a polycrystalline morphology and predominantly shallow traps the theory of multiple trapping and release (MTR), a model initially proposed for amorphous silicon [Le Comber70], can be used for OSC materials as well [Horowitz98]. In this model, the charge transporting layer is assumed to be composed of crystalline regions in which band-like transport occurs. At the boundaries between these crystallites or grains shallow traps are formed from which trapped charge carriers can be released by thermal activation.
If, on the contrary, in a device the OSC layer is rather amorphous than polycrystalline, an energetically broad distribution of additional trap states is influencing the energy levels formed by the molecular and polaronic states. Charge carriers crossing such a layer are constantly trapped in shallow or deep traps between which they are transferred via thermally activated tunneling processes. Depending on the depth of the starting trap of such a tunneling step, the thermal energy allows for a short- or a long-range hop. Therefore, this mechanism also is referred to as variable range hopping (VRH) [Mott69, Brown94].

Both, MTR and VRH, suggest that the charge transfer in OSC materials is taking place rather incoherently, i.e. the time single carriers need to travel a given distance through an OSC layer may vary significantly, which, for instance, is important regarding experiments in the perpendicular geometry as discussed in the previous chapter. Furthermore, both approaches and any modifications of them, e.g. the model proposed in [Horowitz00], suggest a decrease of the charge carrier mobility μ at low temperatures. So far, mostly they have been successfully applied to describe the charge transfer in organic field effect transistors (OFETs), i.e. lateral transport devices which are very often optimised in order to obtain the highest μ possible, e.g. by a suitable substrate treatment prior to OSC deposition improving the growth of the OSC layer (see, for instance, [Oh07]). However, in vertical devices like organic light emitting diodes and OSVs such optimisations are only seldom feasible and, in consequence, the OSC layers in these structures should be considered amorphous in the aforementioned sense. Additionally, the role of charge injection and contact resistance, respectively, is more eminent in vertical devices due to the increased ratio of contact area and charge transfer

distance, which is rather small in OFETs with a channel length in the μm-scale. For these reasons the charge transport in vertical devices usually is classified differently and described by other, though partially similar models which will be presented hereafter.

Basically, vertical devices can be regarded as a serial connection of three resistors, one for each charge injection interface electrode-OSC and one for the OSC layer itself. If the latter dominates the total device resistance, the charge transport is considered bulk or space-charge limited, whilst in the opposite case the device is operated in the so-called injection limited regime. Bulk limited charge transfer can be described as an injection process followed by a mechanism well comparable to VRH [Bässler93]. In a specific device this transport mechanisms very often shows up in the room-temperature I/V curves as a diode-like characteristic with very low currents at small bias and a sharp increase when a threshold voltage, often in the $\gg 1\,\mathrm{V}$ regime, is surpassed (see, for instance, [Francis04, Lin10]). As suggested by the underlying VRH model and the dominance of the OSC layer's resistance contribution to the total device resistance, the latter is expected to increase dramatically in such devices when the temperature is decreased.

For the contrary scenario, injection limited charge transfer, the temperature dependence of the device resistance is dominated by the injection mechanism at the Schottky-like contacts between the OSC and the electrodes. The most common injection mechanisms are thermionic emission and tunneling processes. Which mechanism is prevailing depends on the several parameters, amongst others the temperature and the injection barrier height Φ_{inj}. In a simplified picture, Φ_{inj} can be regarded as the difference of the energy levels, i.e. this of the LUMO (HOMO) for electrons (holes) on the OSC side and the work function W on the electrode side (see Fig. 2.7**a**). Thermionic emission is mostly observed at room temperature and relatively low Φ_{inj} [Sze06], whereas tunneling processes primarily take place at high injection barriers and/or at low temperatures [Parker94]. Davids *et al.* [Davids97] propose a device model for organic light-emitting diodes according to which the transition from injection by thermionic emission to tunneling injection occurs at $\Phi_{\mathrm{inj}} \approx 0.3 - 0.4\,\mathrm{eV}$. Similarly as bulk limited also injection limited transport and charge transfer dominated by tunneling is reflected in a given device's I/V curve, which in this case exhibits a higher current at low bias voltage resulting in a rather parabolic trace for the device resistance [Stratton62, Parker94, Baldo01].

Obviously, Φ_{inj} can be tuned by choosing suitable combinations of electrode and OSC material [Mermer05b, Golmar12], which, however, is not feasible for all kinds of structures, e.g. when the choice of materials is limited by other prerequisites. Such a prerequisite is, for instance, the necessity of ferromagnetic electrodes in spin valves. It is very likely that in the devices of the present work the charge injection is dominated by tunneling processes. On the one hand, this is evident from the fact that most experiments are conducted at low temperatures. On the other hand, rather large Φ_{inj} (see Tab. 2.1) for electrons and holes in the electrode-OSC combinations under investigation can be expected on the basis of the energy levels listed in Tab. 2.2.

It is also worth mentioning here that the classification of OSCs as n- and p-type material shortly addressed at the beginning of this chapter also depends, to a certain extent, on the electrode-OSC combination in an actual device and thus has to be considered less rigorous

than in the case of inorganic materials.

	OSC	electrode material			
		LSMO	Co	Al	Cu
Φ_{inj,e^-} [eV]	AlQ$_3$	1.8-2.0	n.i.	n.i.	1.6
	PDI	0.8-1.05	1.35	0.65	n.i.
Φ_{inj,h^+} [eV]	AlQ$_3$	0.8-1.0	n.i.	n.i.	1.2
	PDI	1.6-1.8	1.3	2.0	n.i.

Table 2.1: Injection barrier heights Φ_{inj,e^-} and Φ_{inj,h^+} for electrons and holes of all material combinations that are actually investigated during this work (n.i. denotes 'not investigated'). The Φ_{inj} are calculated from the values listed in Tab. 2.2.

material	W [eV]	E_{LUMO} [eV]	E_{HOMO} [eV]	source
LSMO	$4.7 - 4.9$	-	-	[deJong03]
AlQ$_3$	-	2.9	5.7	[Lee98]
PDI	-	3.85	6.5	[Oh07], [Scholz09]
Co	5.2	-	-	[Springer05]
Al	4.5	-	-	[Springer05]
Cu	4.5	-	-	[Springer05]

Table 2.2: Work functions W of all electrode materials and energy levels corresponding to the molecular orbitals of all OSCs under investigation in vertical structures. The values are given with respect to the vacuum energy.

2.2.2   The Role of Organic-Inorganic Interfaces

In recent years, a lot of experimental and theoretical analysis dealing with organic-inorganic interfaces and injection of charge and spins into OSCs, partially with special respect to spintronics applications [Barraud10, Sanvito10, Zhan12], has been undertaken. Obviously, such analysis is also motivated by rather puzzling results, e.g. the observation of MR effects at bias voltages at which according to the energy levels and the alleged resulting Φ_{inj} not even a current should be measurable [Xiong04, Majumdar06a, Wang07, Dediu08]. Since similar findings will be presented in the course of this work as well, some of the effects that can occur at organic-inorganic interfaces will be outlined in this chapter.

One of the basic phenomena observed at these interfaces is the formation of dipoles. Already in 2001 Baldo and Forrest [Baldo01] have emphasised their importance for the charge injection process. According to Baldo and Forrest, the dipole moments may cause a shift and broadening of the molecular orbitals (HOMO/LUMO), eventually further reducing Φ_{inj} (see Fig. 2.7b). This phenomenon can be ascribed to an increased disorder in dipole layer, i.e. in the first few monolayers of the OSC. Another obvious effect of interfacial dipoles is a shift, either a decrease or an increase, of Φ_{inj} due to a modification of the electrode's
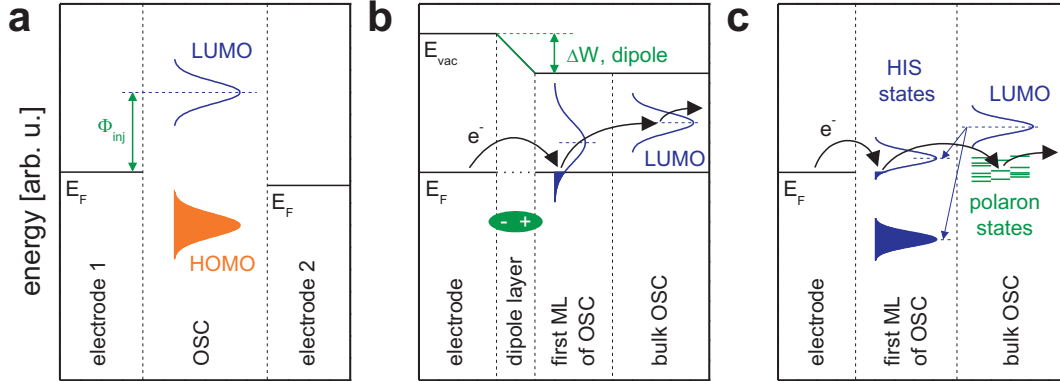
Figure 2.7: Energy levels in a vertical device and influence of interfacial effects. Possible conduction paths for an electron are represented by black arrows. **a**: Energy levels of a device without any voltage applied and any effects occurring at the interfaces. The energy levels in amorphous OSC layer usually are broadened due to trap and polaron states near the LUMO and HOMO, which can be described by a Gaussian. For the sake of clarity, only the potential paths of an electron injected into the LUMO is illustrated in **b** and **c**. **b**: According to Baldo and Forrest [Baldo01], an interfacial dipole can cause a shift and a broadening of the LUMO in the first monolayer of the OSC, which is significantly lowering Φ_{inj}. **c**: Energy levels according to an approach proposed by Zhan and Fahlman [Zhan12] based on the formation of hybridisation-induced states (HISs) at the interface between the electrode and the OSC layer. A splitting and lowering of the LUMO can reduce Φ_{inj}. Conduction through the bulk OSC layer via polaron states between the HOMO and LUMO are equally suggested by Zhan and Fahlman.

work function by ΔW. For instance, in one of the archetypical OSV material combinations, LSMO-AlQ$_3$-Co, a reduction of Φ_{inj} by $\sim 0.9\,eV$ ($\sim 1.4\,eV$) at the LSMO-AlQ$_3$ (Co-AlQ$_3$) interface has been proved by Zhan *et al.* [Zhan07,Zhan08]. It is suggested that this interfacial dipole, which similarly is found in other metal/oxide-OSC systems as well [Zhan12], is very likely originating from an intrinsic dipole moment of the AlQ$_3$ molecules.

As likewise stated by Zhan and Fahlman in their review [Zhan12], hybridisation-induced states (HISs) may additionally influence the energy landscape near the interface. The investigation and characterisation of these states requires rather sophisticated measurement techniques like near edge x-ray absorption fine structure or ultraviolet photoelectron spectroscopy and therefore cannot be provided in the framework of this work. HISs usually are caused by chemical interaction between the electrode material and the organic molecules and thus mainly have to be taken into account when the two materials are not separated by any kind of physical barrier like, for instance, a tunnel barrier [Dediu08].
Zhan and Fahlman are quoting two types of interaction. On one side, a reconstruction of molecules may occur in the first monolayer of the OSC due to chemisorption processes via covalent bonding between the electrode surface and the respective molecule or single atoms thereof. On the other side, in some materials systems a strong interaction between the π-orbitals in the OSC layer and the d-bands in an adjacent ferromagnetic electrode equally can cause the formation of HISs. Irrespective of their origin, HISs generally are located in the first few monolayers of the OSC layer and near the fermi level of the (metal) electrode. This may result in a quasi-ohmic contact at this interface, i.e. a substantially reduced injection

barrier (see Fig. 2.7c).

Moreover, Fig. 2.7c comprises energy levels in the bulk OSC layer which are originating from polaronic states. As already stated before, these states do not only cause a broadening of the LUMO and the HOMO but also can be situated in between these rather distinguished levels. According to Zhan and Fahlman, a reduced Φ_{inj} due to HISs in combination with this scenario can be used to explain why injection limited devices can be operated at bias voltages which are well below the nominal Φ_{inj} that can be estimated from the energy levels of the electrode and OSC materials (see Tab. 2.2).

Another feature of HISs which has been identified in various experiments is a possible modification of the spin polarisation P_{cc} of charge carriers passing the HISs. Due to the interaction of molecular orbitals with the spin-polarised d-bands of a ferromagnetic material the former can obtain a spin polarisation as well (spin-polarised HISs, [Lach12]). Consequently, P_{cc} of a current injected from these states into the bulk OSC may be substantially modified. Recently, also spin-dependent trapping has been proved as mechanisms influencing P_{cc} at the AlQ_3-Co interface [Steil13]. Such modifications obviously cannot only be an increase or decrease of P_{cc} but also a sign inversion as shown by Schulz et al. [Schulz11], who have modified HISs by adding a LiF barrier to the interface in an AlQ_3-based OSV and hereby obtained a sign change of the spin-valve signal. Thus, the fact that usually a negative MR effect is observed in OSV structures despite the materials under investigation suggest a positive signal may be ascribed to the presence of HISs at, at least one of, the interfaces.

An alternative model providing an explanation for a negative MR effect has been proposed by Barraud et al. [Barraud10] and equally underlines the role of organic-inorganic interfaces. Similarly as the concept of spin-polarised HISs, it takes into account probable modifications of the energy levels at the interface by effective spin polarisations P^*. According to Barraud et al., the P^* mainly depend on the ratio of Φ_{inj} and the broadening of the energy levels in the interfacial layers which is originating from the coupling of the OSC's molecules to the electrodes. By adding the P^* to the Jullière model [Jullière75] the apparent discrepancy concerning the sign of the spin-valve signal can be explained by this approach, which even allows for a positive and negative MR effect observed in structures of identical composition depending on their size. Whereas nm-scaled devices as those investigated by Barraud et al. normally probe the local energetic landscape, most of the reports in the literature employ results for large area junctions. In such devices the statistical average of P^* is reflected in MR measurements which therefore may yield different results.

Another important issue that has to be addressed in the context of interfaces in vertical transport structures is the one of so-called ill-defined interfaces. This keyword is often brought up with respect to the modification of a OSC layer's morphology by depositing a metal on top of it. The diffusion of metal atoms into the OSC layer and/or the formation of metal clusters inside this layer may result in a dramatic decrease of the effective layer thickness [Dürr03, Xiong04]. This reduction may occur to such an extent that direct tunneling [Santos07, Barraud10] or charge transfer via a small number of subsequent tunneling steps (multiple step tunneling, MST, [Schoonus09]) becomes probable even if initially the OSC layer's thickness

has been so large that, in the first instance, charge transport dominated by tunneling cannot be considered a realistic scenario. This issue is often circumvented by the insertion of a thin ($\ll$ 3 nm) oxide barrier between the OSC layer and the top electrode. Such an interlayer does not only act as a mechanical barrier but also, as already stated above, can result in interface modifications [Schulz11] and/or prevent chemical interactions between the OSC and the electrode [Dediu08].

2.2.3   OMAR - An intrinsic Magnetoresistance Effect

In 2004 Francis *et al.* [Francis04] have discovered a large MR effect at room temperature in vertical organic devices with non-magnetic electrodes, the so-called organic magnetoresistance (OMAR). Although the underlying effect can often be likewise measured as a modulation of the electroluminescence, photocurrent or fluorescence [Wagemans11], the following presentation of typical results and the effect's main characteristics will be limited to the MR.

Most of the results put forth since the first demonstration of the effect suggest that, in contrast to the spin-valve effect, OMAR does not depend on the orientation of the applied magnetic field $\boldsymbol{H}_{\mathrm{ext}}$ with respect to the sample plane. Typically, OMAR exhibits a weak temperature dependence only and has a magnitude of several % at room temperature. MR traces recorded in OMAR structures with non-magnetic electrodes (as outlined below the situation may be different in structures with a ferromagnetic component) always are symmetric with respect to $\mu_0 H_{ext} = 0$ mT (see, for instance, [Francis04]). Starting from zero magnetic field the traces comprise a monotonic increase/decrease of R; a deviation from this monotonic behaviour has only been found in a few exceptional cases, e.g. in [Nguyen10]. The MR signal can be described by either a Lorentzian

$$MR \propto \frac{(\mu_0 H_{\mathrm{ext}})^2}{(\mu_0 H_{\mathrm{ext}})^2 + B_0^2} \tag{2.8}$$

or a non-Lorentzian function

$$MR \propto \frac{(\mu_0 H_{\mathrm{ext}})^2}{(|\mu_0 H_{\mathrm{ext}}| + B_0)^2} \tag{2.9}$$

depending on the OSC under investigation. B_0 denotes a material parameter and can be interpreted as half width at half/quarter maximum in Equ. 2.8/2.9 [Mermer05a]. The effect's sign, which can be both positive (increase of R with increasing H_{ext}) and negative (decrease of R), is determined by the OSC material and certain measurement conditions, e.g. the applied bias voltage U_{bias} and/or the temperature [Mermer05a].

As already stated, dedicated OMAR devices usually do not comprise ferromagnetic electrodes. If, however, a ferromagnetic layer is present in an OMAR device, the fringe fields $\boldsymbol{B}_{\mathrm{fringe}}$ potentially originating from this layer may also affect the MR. In this case the charge carriers' spins are influenced by a superposition of the intrinsic, random local hyperfine field $\boldsymbol{B}_{\mathrm{hf}}$, $\boldsymbol{B}_{\mathrm{fringe}}$ and $\boldsymbol{H}_{\mathrm{ext}}$. As demonstrated by Wang *et al.* [Wang12], this can lead to a spin-valve-like, i.e. hysteretic, contribution to the MR traces in devices in which the ferromagnetic

layer is not even in direct contact to any of the electrodes or the OSC layer itself. It is impor-
tant to note here, that this behaviour is observed, similarly as pure OMAR, at elevated U_{bias}
only. Especially when a relatively high U_{bias} is applied during magnetotransport measure-
ments, OMAR therefore has to be borne in mind not only as possible origin of a background
signal in an OSV's MR trace but also as a side effect that can mimic spin-valve functionality.

Most of the experimental results and theoretical approaches addressing the effect's ori-
gin suggest that OMAR is strongly related to the charge transport in the bulk OSC layer.
Thus, OMAR usually is observed at high bias voltages ($|U_{\mathrm{bias}}| \gg 1\,\mathrm{V}$) in structures em-
ploying thick OSC layers where the charge transfer is dominated by hopping mechanisms
like VRH [Francis04, Desai07, Bergeson08, Wang12, Cox13]. In the past years several mod-
els have been brought up concerning the microscopic mechanisms behind OMAR, none of
which has been finally and unambiguously proved by experimental results up to now. For
a more detailed description of these theories, which is not necessary for the understand-
ing of the present work, the reader is referred to the literature here, e.g. to the review of
Wagemans and Koopmans [Wagemans11], the publications cited above and others as [Bob-
bert07, Schoonus09, Harmon2012, Alexandrov2012].

2.3   Resistive Switching Effects

Resistive switching (RS) is usually employed as an umbrella term for any kind of phenomenon comprising a remanent change of a device's resistance R, which is mostly induced by the application of a voltage or current pulse. RS has been first observed by Hickmott in 1962 [Hickmott62] in metal-insulator-metal (MIM) structures. Being a good candidate for novel memory applications, RS has been more intensively investigated since the late 1990s. RS has been demonstrated in devices comprising a huge variety of materials and material systems with a relatively strong focus on oxides, reaching from binary compounds to all kinds of perovskite oxides. Thus, likewise the understanding of the physics behind the RS effect has been substantially enhanced [Bruchhaus10], even though the available (phenomenological) models are often rather tightly related to a specific material or material system.

A short introduction to RS will be given in chapter 2.3.1, particularly with respect to terminology and classification. One fundamental approach explaining RS in (perovskite) oxides likewise will be presented there. An overview of RS effects in structures containing OSC layers, e.g. vertical OSVs, will be given in chapter 2.3.2.

2.3.1   General Overview

As aforementioned, RS describes a remanent change of R. Hereafter, a change between two distinct states, the high resistance (HRS, R_{HRS}) and low resistance (LRS, R_{LRS}) state, which is induced by a voltage pulse (U_{pulse}) will be considered. A figure of merit which is frequently used to quantify a RS effect is the so-called ON/OFF ratio R_{HRS}/R_{LRS}.

A first distinction of RS effects can be done on the basis of the polarities of U_{pulse} required for the transitions HRS→LRS and LRS→HRS. Mostly, so-called bipolar behaviour is observed, i.e. a positive U_{pulse} has to be applied for LRS→HRS and a negative U_{pulse} for the reset operation HRS→LRS or vice versa. If, on the contrary, only the magnitude of U_{pulse} is decisive and the polarity is the same for both transitions, the switching is regarded as unipolar or non-polar [Bruchhaus10].
A second criterion that can be employed for the classification of an RS effect is its origin. Just considering the localisation of the microscopic mechanisms causing the change of R, this allows, in the first instance, for a rough distinction between localised and distributed effects. An example for the former is RS evoked by the formation and rupture of highly conductive filaments in the insulating layer, whilst all kinds of effects occurring at the whole interface between the insulator and one of the electrodes are summarised in the class of distributed RS.

A more detailed analysis, as done in the review by Bruchhaus and Waser [Bruchhaus10], can be achieved on the basis of the actual microscopic processes involved yielding a variety of theoretical approaches nearly as large as the variety of materials and material systems under investigation. A lot of these approaches elucidate the relevance of the insulating layer's stoichiometry with respect to its oxygen content for the observed RS effect in the case of oxide-based devices. The oxygen content of an oxide can be controlled during the growth of the respective layer [Rajeswari98, Dho03, deJong05] and/or modified during the actual RS

experiment, e.g. by electrochemical processes. Such processes, for instance, can be redox reactions removing oxygen ions from the lattice and hereby leading to the formation of oxygen vacancies V_Os [Baikalov03, Sawa04, Waser07, Yang09]. However, despite the frequently good agreement between experimental results and the theoretical explanations, only seldom a clear and consistent experimental proof for the microscopic mechanisms and reactions proposed within the framework of a specific model is provided. One of the exceptional cases in this context is the clear experimental evidence for the generation of V_Os in vanadium dioxide by the application of an electric field recently reported by Jeong *et al.* [Jeong13].
It is worth noting that the oxygen removed from the lattice during such reactions can either remain in the material and equally contribute to or support the switching effect [Dong07, Hasan08] or escape the system as oxygen gas. For the former case, in which the RS usually is reversible without any external oxygen supply, the structure must comprise some sort of oxygen reservoir or allow for oxygen atom/ions at interstitial sites as demonstrated, for instance, in $La_{0.7}Ca_{0.3}MnO_3$- and MnO_2-based devices [Dong07, Yang09].

Many models proposing a governing role of V_Os are not only based on the assumption that the V_O concentration in the material under investigation is modified but also often involve a motion of these defects in an applied electric field. Such scenarios are sustained by the facts that V_Os are positively charged with respect to oxygen ions on lattice sites and that their mobility can be regarded as a relatively high compared to this of other defects [Waser90]. Thus, a motion of V_Os, for instance, can promote the formation or rupture of conducting paths in an insulating matrix [Yang09]. Likewise, they also may be attracted to or repelled from the interface between the insulating layer and one of the electrodes and hereby change this interface. One example for such a modification is the enhancement and reduction, respectively, of the injection barrier at the metal-insulator contact in $Ti/Pr_{0.7}Ca_{0.3}MnO_3$ structures [Sawa04].

Finally, it should be noted that the interpretation of results obtained for a specific device and (electrode and insulator) material combination has to be conducted carefully and should be sustained by suitable control experiments. The necessity of such a thorough analysis and procedure already gets evident from the above basic introduction to only a small selection of the proposed theoretical approaches explaining RS.

2.3.2 Resistive Switching in OSC-based Structures

In the field of organic electronics the phenomenon of RS has equally gained increased scientific interest in the past decade again motivated by the potential application in memory devices [Cho11]. A lot of OSC materials have been investigated in metal-OSC-metal structures (also referred to as MIM structures hereafter for the sake of simplicity), where one of the metal electrodes is often made of Al. As aforementioned, a complete understanding of any RS effect in inorganic MIM structures is hard to achieve resulting in a lack of robust experimental proof for many promising theoretical approaches. A similar general reasoning applies for organic RS devices, for which quite frequently an even more careful and sceptical procedure is mandatory. This becomes evident, for instance, considering the fact that in many cases the RS very likely is originating from the Al-OSC interface where either an Al-O compound [Mahapatro04, Lee08] or even a thin Al_2O_3 layer [Waser07] may be formed.

Eventually, as stated in the review by Waser and Aono [Waser07], there is only scarce experimental evidence for RS that can be unambiguously and exclusively attributed to the respective organic material under investigation.

Amongst the OSC materials for which RS has been reported so far also one of the materials used for the present work, namely AlQ_3, can be found. The respective experiments can be classified on the basis of the devices under investigation. On one side, bipolar RS has been demonstrated in organic MIM structures where the effect is assumed to originate either from the Al-OSC interface mentioned above [Mahapatro04, Lee08] or from a modification of the AlQ_3-layer by adding MoO_3 nanoarticles/-clusters during fabrication [Chang10]. On the other side, likewise bipolar RS has been observed in OSV devices with ferromagnetic electrodes [Hueso07, Prezioso11, Prezioso12].

The integration of RS effects in OSVs is of particular interest as it is deemed a very promising approach towards the realisation of multifunctional devices and their implementation into logic gates [Prezioso12]. As shown by Prezioso *et al.* [Prezioso11, Prezioso12], the amplitude of the MR effect in their devices, which is ascribed to GMR in these specific experiments, is strongly correlated with the device resistance. The latter can be modified by the application of a bias voltage in the $-1.5 - +3.0\,V$ regime within the range of a few tens of $k\Omega$ ($MR > 10\,\%$) up to a few $M\Omega$ (no measurable MR) [Prezioso12]. Prezioso *et al.* cite two possible scenarios explaining the apparent interplay of GMR and RS.
On the one hand, the formation of trapping domains in the AlQ_3 layer due to the applied bias voltage as proposed by Rozenberg et al. [Rozenberg04] may significantly elongate the distance a charge carrier and spin has to travel between the electrodes. As a result, the device resistance is increased and the spin polarisation at the spin-detecting electrode is decreased [Prezioso11]. This explanation is resembling the so-called Coulomb blockade, which also is quite often referred to in the context of organic RS devices [Simmons67, Bozano04], though substantially different from it. In the case of Coulomb blockade space-charge-induced strong local electric fields hamper further charge injection. The formation and charging of trapping domains, on the contrary, mainly influences the amount and length of the paths through the OSC layer which are available for the injected charge carriers, which eventually results in an increase of the resistance.
On the other hand, according to Prezioso *et al.*, the transport in the OSV devices may mainly occur through highly conductive filaments that are vertically penetrating the complete AlQ_3 layer and are connected in parallel. In this picture the RS behaviour can be caused by a voltage induced opening (closing) of single filaments [Prezioso12]. Although both scenarios provide a good phenomenological description of the observed effects, GMR and RS, they are, like most of the models proposed for inorganic MIM structures, not decisively sustained by further experimental evidence.

Hence, similarly as for inorganic MIM structures also for organic RS devices a variety of theoretical approaches is available. Therefore it is worth emphasizing once more that control experiments and a careful analysis of experimental results are mandatory for a complete understanding of any RS effect.

2.4   Materials under Investigation

In chapters 2.4.1-2.4.3 the OSC materials which are employed in any devices investigated in this work are briefly presented. Fundamental characteristics of one of the electrode materials, namely the half-metallic oxide LSMO, are outlined in chapter 2.4.4 as they are equally essential for the interpretation of many of the observed effects.

2.4.1   Tris(8-hydroxyquinolinato)aluminium - AlQ_3

AlQ_3 is a small molecular-weight n-type OSC which has gained technological relevance especially due to its application in organic light emitting diodes. Furthermore, it is also one of the most frequently investigated material in the field of organic spintronics. Usually it is employed either as thick spacer layer in spin valves where the MR effect is ascribed to GMR [Xiong04, Majumdar06b, Hueso07] or as thin tunnel barrier in TMR devices [Santos07]. Moreover, studies in OSVs with thick spacer layers have revealed the seemingly inconsistent result of a spin-valve effect that is originating from tunneling processes although the AlQ_3-films' thickness is in the range of $\sim 100\,\mathrm{nm}$ and more [Vinzelberg08, Riminucci13, Grünewald13b].

As shown by, for instance, time-of-flight (TOF, [Spear57]) measurements AlQ_3 exhibits, like most of the n-type OSCs, a rather low electron mobility of $\mu_{AlQ_3} \approx 1 \cdot 10^{-6}\,\mathrm{cm^2/Vs}$ (value for room temperature) which strongly depends on the temperature and the applied electric field [Kepler95]. Another drawback of many n-type materials, which also applies to AlQ_3, is a rather high sensitivity to ambient conditions, especially moisture. This obviously can be circumvented in industrial applications, however, often hampers the investigation of these materials if this issue is not addressed in an appropriate manner [Grünewald07].

It has been outlined in chapter 2.2.1 that the injection barrier for electrons Φ_{inj,e^-} can be roughly estimated from the work function of the electrode material and the LUMO of the OSC material under investigation. The latter is located at $\sim 2.9\,\mathrm{eV}$ with respect to the vacuum energy [Lee98] in the case of AlQ_3 suggesting a rather high Φ_{inj,e^-} ($> 1.6\,\mathrm{eV}$, see Tab. 2.1) which, however, is probably not a realistic value as likewise discussed previously (chapter 2.2.2). Experiments with this material are undertaken motivated by the facts that it is, as already stated, one of the standard materials in organic spintronics research and that particular issues, e.g. the occurrence of TAMR in devices comprising AlQ_3 layers, so far virtually not have been addressed yet.

AlQ_3, a commercially available material that is used as-received without any further processing or purification (purity 99.995 % according to the supplier Sigma-Aldrich), is deposited by thermal evaporation (organic molecular beam deposition, OMBD, see appendix A) under high or ultra-high vacuum (HV/UHV) conditions. If the substrate is kept at room temperature during this procedure, the resulting AlQ_3 layers are amorphous and rather flat exhibiting a *rms* roughness in the range of only a few nm [Tang87, Dediu08]. At elevated substrate temperatures T_{sub}, however, the latter is increased and the layer's morphology becomes rather granular [Bergenti07]. Preliminary studies [Grünewald07] have shown that working, i.e. non-

shorted, vertical devices can only hardly be achieved when the AlQ_3 films are too rough. Therefore, the samples investigated in this work, as most of those in the literature, comprise AlQ_3 layers which are deposited with the substrate at room temperature.

2.4.2 N,N'-bis(Heptafluorobutyl)-3,4:9,10-Perylene Diimide - PDI

N,N'-bis(Heptafluorobutyl)-3,4:9,10-Perylene Diimide, often referred to as PTCDI-C4F7 in the literature and named PDI hereafter, is a rather new n-type material which has been provided by the group of Prof. Frank Würthner (Institut für Organische Chemie, Universität Würzburg). It is part of a series of molecules based on a perylene diimide core with different bay and imide substituents which has been synthesised and investigated by the groups of Prof. Frank Würthner and Prof. Zhenan Bao (Stanford University) [Schmidt09]. With respect to spintronics applications, the investigations concerning the charge carrier mobility and the stability of the material under ambient conditions are of particular interest. These studies have shown that PDI is a promising material which may overcome the aforementioned commonly known drawbacks of n-type OSC compounds. The electron mobility in this material is very high ($\mu_{PDI} \approx 0.1 - 0.6 \, cm^2/Vs$ at room temperature) and is only hardly diminished when a device is stored in air for a long period of time [Steinbacher07, Oh07]. However, it should be emphasised that the value of μ_{PDI} reported by Oh *et al.* is determined by OFET characterisation and therefore cannot be directly compared to the value given for AlQ_3 in the previous chapter. This will be discussed more extensively in chapter 3.3.1.
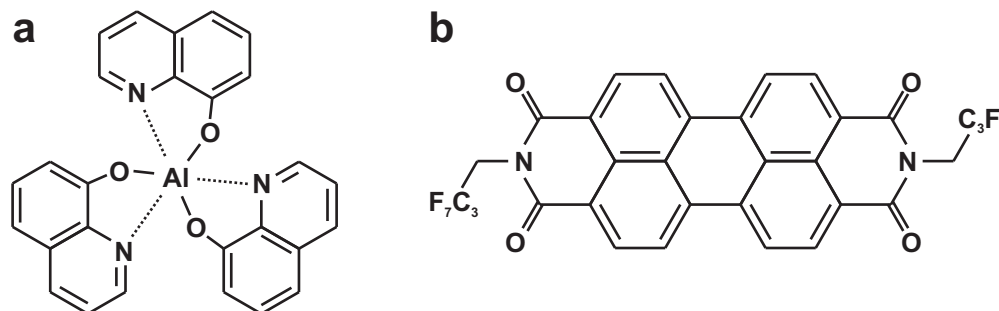
Figure 2.8:   Molecular structure of the organic compounds under investigation.   **a**: Tris(8-hydroxyquinolinato)aluminium - AlQ_3. **b**: N,N'-bis(Heptafluorobutyl)-3,4:9,10-Perylene Diimide - PDI.

As PDI does not comprise any bay substituents, the single molecules are flat and can be consequently arranged in close distance to each other in thin films. Actually, x-ray diffraction experiments reveal a very regular molecular arrangement in thin layers in which the molecules are tilted by $\sim 45°$ with respect to the substrate [Oh07]. This and additional effects caused by the heptafluorobutyl (C_3F_7) chains acting as imide substituent can explain both eminent features of PDI, its high charge carrier mobility and stability. On one side, the close and parallel packing provides a large overlap of the π-orbitals of neighbouring molecules which usually promotes the charge transport in OSC materials as already mentioned in chapter 2.2.1. On the other side, the C_3F_7 groups at the end of the molecules form a kinetic barrier on top of the PDI layer which hampers the diffusion of any deteriorating substance like air,

oxygen or moisture to the core of the layer where the charge transport is actually taking place [Oh07]. Additionally, also the rather low LUMO level of $\sim 3.9\,eV$ relative to the vacuum energy can be ascribed to the influence of the imide substituent. As a consequence of a low LUMO level, not only Φ_{inj} for electrons may be expected to be relatively low compared to AlQ$_3$ ($\lesssim 1.4\,eV$, see Tab. 2.1) but also oxidation to be suppressed [Jones04].

Furthermore, the investigations of Oh *et al.* comprise studies of the influence of T_{sub} on the deposited layer's morphology and its charge transport performance. The aforementioned tendency to a dense stacking of the molecules leads to the formation of polycrystalline films which is even enhanced at elevated T_{sub}. At $T_{\mathrm{sub}} = 125\,°$, for which the maximum μ_{PDI} is obtained, the PDI layer consists of single crystallites with lateral dimensions in the range of a few hundred nm [Oh07].
Similar results have also been obtained for films deposited with the equipment used for this work [Grünewald07, Wahler09]. The PDI films (thickness 100 nm) investigated by atomic force microscopy (AFM) exhibit a relatively low *rms* roughness of maximum $\sim 5\,$nm suggesting closed layers. With respect to their implementation in vertical devices, however, also the so-called peak-to-peak roughness has to be considered since this measure also takes into account local morphology features. Such features can occur at the boundary between two crystallites, where the layer thickness is substantially decreased. AFM studies reveal, that typically the peak-to-peak roughness of a 100 nm thick PDI film is in the range of $\sim 25\,$nm [Grünewald07]. As already mentioned in chapter 2.2.2, such a reduction of the OSC layer's thickness may have significant influence on the charge transfer in vertical structures. Hence, this issue will be addressed again and more precisely in the experimental section of this work.

2.4.3   Other Organic Materials

In lateral spin-valve devices (see chapter 4) two further OSC compounds are used as charge transporting material. The first one, which will be referred to as NDI in this work, again is a rather new n-type material of the family of core-chlorinated Naphthalene Tetracarboxylic Diimides and is well comparable to PDI with respect to its electrical performance and stability in ambient conditions [Oh10]. The second material is the well known metal-free Phthalocyanine (H$_2$Pc), a small discotic molecule the semiconducting properties of which have already been investigated in the 1950s [Eley53].

2.4.4   La$_{1-x}$Sr$_x$MnO$_3$ - LSMO

La$_{1-x}$Sr$_x$MnO$_3$ (LSMO), an oxide with a perovskite crystal structure (Fig. 2.9a), has gained significant interest in the research field of multiferroic oxides in the past years. Furthermore, it is frequently employed as electrode material in organic spintronics devices. Its electronic and magnetic properties strongly depend on the Sr concentration x [Fujishiro98]. For $x = 0.3$, as it applies to all LSMO layers used in the present work, the material is metallic and ferromagnetic at room temperature. The transition from paramagnetic to ferromagnetic behaviour is observed at a Curie temperature T_{C} of typically $\sim 350\,$K [Park98a]. Thin LSMO layers with high crystalline quality usually are grown on suitable substrates from stoichiometric targets by methods like Channel-Spark ablation (CSA) [Dediu95, Bergenti04]

or pulsed laser deposition (PLD).
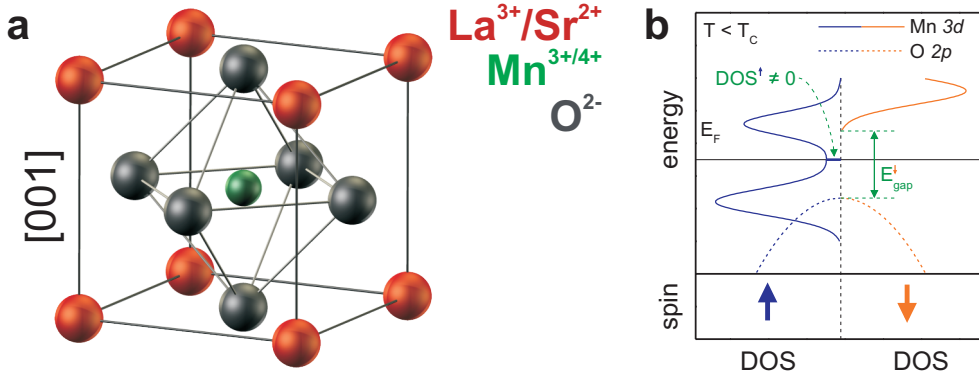
Figure 2.9: **a**: Perosvskite crystal structure of LSMO. **b**: The spin-dependent DOS of the half-metallic LSMO for $T < T_{\rm C}$ is adapted from [Park98a]. For spin $\uparrow$ the material exhibits metallic behaviour, whilst for the opposite spin orientation the DOS comprises a gap, i.e. the material is semiconducting.

Already in 1950 a clear correlation between the electronic and magnetic properties of LSMO, e.g. between a decreasing resistance and an increasing magnetisation at low temperatures, has been proved [Jonker50, VanSanten50]. Later theoretical and experimental investigations have shown that both, the metallic character and the ferromagnetism, and the correlation in between can be explained qualitatively in a straightforward manner on the basis of the double exchange model proposed by Zener [Zener51]. Nevertheless, other effects like small polaron effects and Jahn-Teller distortion equally have to be considered for a good quantitative description [Millis95, Park98a].

In a simplified picture the $3d$ energy levels of a Mn ion in the MnO_6 octahedrals (see Fig. 2.9**a**) can be regarded as split into three lower t_{2g} levels (core levels) and two higher e_g levels. The valence of Mn can be either 3+ or 4+ depending on the surrounding rare earth ions. It is assumed that the electrons occupying the e_g levels of Mn^{3+} are mainly contributing to the charge transport and can easily be transferred from a Mn^{3+} to a Mn^{4+} ion via hopping steps. The ferromagnetic behaviour, i.e. the parallel alignment of all spins in the system, is originating from the interaction of the e_g electrons' spins with the t_g electrons' spins and a strong Hund coupling in this scenario [Dagotto01].

Moreover, the Hund coupling also has an influence on the DOS which becomes spin dependent for $T < T_{\rm C}$ as depicted in Fig. 2.9**b** and experimentally proved by Park *et al.* [Park98a]. This is because a parallel alignment of all spins is energetically favourable. Thus, for one spin direction metallic behaviour is present ($DOS \neq 0$ for $E = E_{\rm F}$), whereas for the opposite spin orientation the DOS exhibits a gap at the Fermi edge, i.e. the material is semiconducting for charge carriers with this spin orientation. Consequently, only electrons with one spin direction can contribute to the charge transport, a behaviour which is usually known as half-metallic character. Similarly as for other half-metals, also for LSMO a high spin polarisation, namely $P = 100\%$, is predicted theoretically. Actually, experimental investigations in MTJs yield $P \approx 95\%$ [Bowen03] which is close to the theoretical value and justifies the use of LSMO as

spin injecting electrode in spin-valve devices.

For this work, LSMO grown on two different insulating substrates, namely $SrTiO_3(001)$ (STO) and $NdGaO_3(001)$ (NGO), is used. Obviously, the magnetic properties of a specific LSMO layer strongly depend on the substrate on which the layer is deposited. These properties comprise, for instance, the saturation magnetisation and the magnetic anisotropy. As the latter is very important for the interpretation of magnetotransport results, the different characteristics of the LSMO films under investigation should be briefly outlined. On one side, LSMO on STO(001) exhibits a biaxial anisotropy of magnetocrystalline origin [Steenbeck99, Berndt00] often superimposed by a strain-induced uniaxial easy anisotropy that very likely is stemming from step-flow growth [Mathews05]. Whereas the former is governing the magnetic properties at low temperatures, the uniaxial component is dominating at room temperature. On the other side, in the case of LSMO grown on NGO(001) only a uniaxial anisotropy is present due to the compressive in-plane lattice strain caused by the large mismatch between substrate and LSMO [Boschker09].
In addition to the substrate, also the crystalline quality has a substantial influence on the electrical and magnetic properties. In this context especially the material's stoichiometry with respect to the oxygen content has to be addressed. Various studies can be found in the literature demonstrating the deteriorating influence of oxygen deficiency on a LSMO layer's resistance [Goyal97] and magnetisation [Rajeswari98]. Also the electronic structure at the surface of LSMO films can depend on the stoichiometry and be modified by suitable treatments like, for instance, annealing [deJong05].

With respect to the application of thin LSMO layers as electrodes in OSV devices, finally two MR effects that are intrinsic to this material should be presented. The first one is the so-called colossal magnetoresistance effect (CMR) [Jin94], which also was the main motivation behind the investigation of LSMO in the field of material research for a long period of time. CMR, the origin of which is not completely understood up to now, can be identified as a decrease of an LSMO film's in-plane resistance with increasing external magnetic field $H_{||}$.
The second effect is phenomenologically similar to CMR and usually referred to as high-field magnetoresistance effect (HFMR). It is observed at the LSMO-OSC interface and can be ascribed, according to Wu *et al.* [Wu05], to a field-induced shift of the Fermi level at the surface of the LSMO layer which eventually enhances or hampers charge injection. Both, CMR and HFMR, may also occur in OSV devices comprising an LSMO electrode and cause a background signal in magnetotransport studies.

Chapter 3

Vertical Transport Structures

This chapter addresses all experiments that are performed in vertical OSVs and similar transport structures based on the OSC materials PDI and AlQ$_3$. After the description of the sample fabrication in chapter 3.1, results obtained in studies of PDI-based devices, also including investigations of the Hanle effect, are presented in chapters 3.2 and 3.3, respectively. In combination with those of TAMR experiments (chapter 3.4), which are undertaken for devices comprising both OSC materials, these results suggest a protruding role of tunneling processes for the charge transfer as well as for the observed spin-valve behaviour. A corresponding device model taking into account all experimental findings is presented in chapter 3.5.

In addition to MR effects a second effect, often referred to as resistive switching, is investigated in TAMR structures based on AlQ$_3$. The results of these investigations and a theoretical approach explaining the present devices' resistive switching behaviour can be found in chapter 3.7.

3.1   Sample Fabrication

In the course of this work several fabrication processes for vertical OSV structures are developed, which are summarised in the present chapter. The main focus during a process' design always is on clean and reproducible interfaces between the electrodes and the OSC layer, which are crucial in order to obtain the most reliable and reproducible device functionality. Differences between the fabrication processes are mainly due to different technological preconditions concerning existing equipment.

For the first fabrication processes the following equipment and fabrication technologies are available (location WÜ):

- optical lithography,

- UHV metal deposition chamber with a multi-source electron beam evaporator,

- UHV chamber equipped with thermal effusion cells for the deposition of OSC materials and two single source electron beam evaporators (OMBD chamber),

- dry etching (Ar ion milling).

The centrepiece of this process is the UHV chamber in which the OSC is deposited by OMBD (see appendix A). As this chamber is also equipped with two electron beam evaporators, the OSC and metallic electrode layers can be deposited in-situ, i.e. without breaking the UHV. This procedure represents the most reliable way to obtain clean and reproducible interfaces. The sample holder of this chamber is equipped with a heater unit capable to reach substrate temperatures of up to $500\,^{\circ}$C. Furthermore, it can be tilted with respect to the evaporation sources which has been widely exploited for fabrication of vertical as well as of lateral OSV devices (see chapter 4.2). All vertical structures based on the OSC PDI are fabricated in this chamber. Most of them are conventional OSVs (layer sequence LSMO-PDI-CoFe). However, PDI is also investigated in TAMR devices (layer sequence LSMO-PDI-Al) and reference structures with only metallic electrodes (layer sequence Al-PDI-Al). Thus, two fabrication processes have to be considered in the following, one for the samples with a bottom contact made of LSMO (flow chart of the process in Fig. 3.1) and a second one for samples with a bottom contact made of a metal (flow chart in Fig. 3.2).

The basis of conventional OSVs comprising a PDI layer are thin LSMO layers ($10-20\,\text{nm}$) deposited by Channel-Spark ablation on suitable insulating substrates [STO(001) or NGO(001)] [Bergenti04]. The LSMO films are provided by the group of Alek Dediu at ISMN Bologna. Before the deposition of the OSV layer-stack, i.e. of the OSC layer and the top contact layer, the samples are prepared as follows.
First, optical lithography, metal deposition and lift-off is used to pattern Ti/Au contact pads for the single devices (left hand side of Fig. 3.1**a**) and for the common LSMO bottom contact (large contact in Fig. 3.1**a**). These contact pads also serve as marks facilitating the alignment of solid shadow masks ($100\,\mu$m stainless steel) which are used later in the process. Subsequently, the LSMO layer is removed from one half of the sample by Ar ion milling
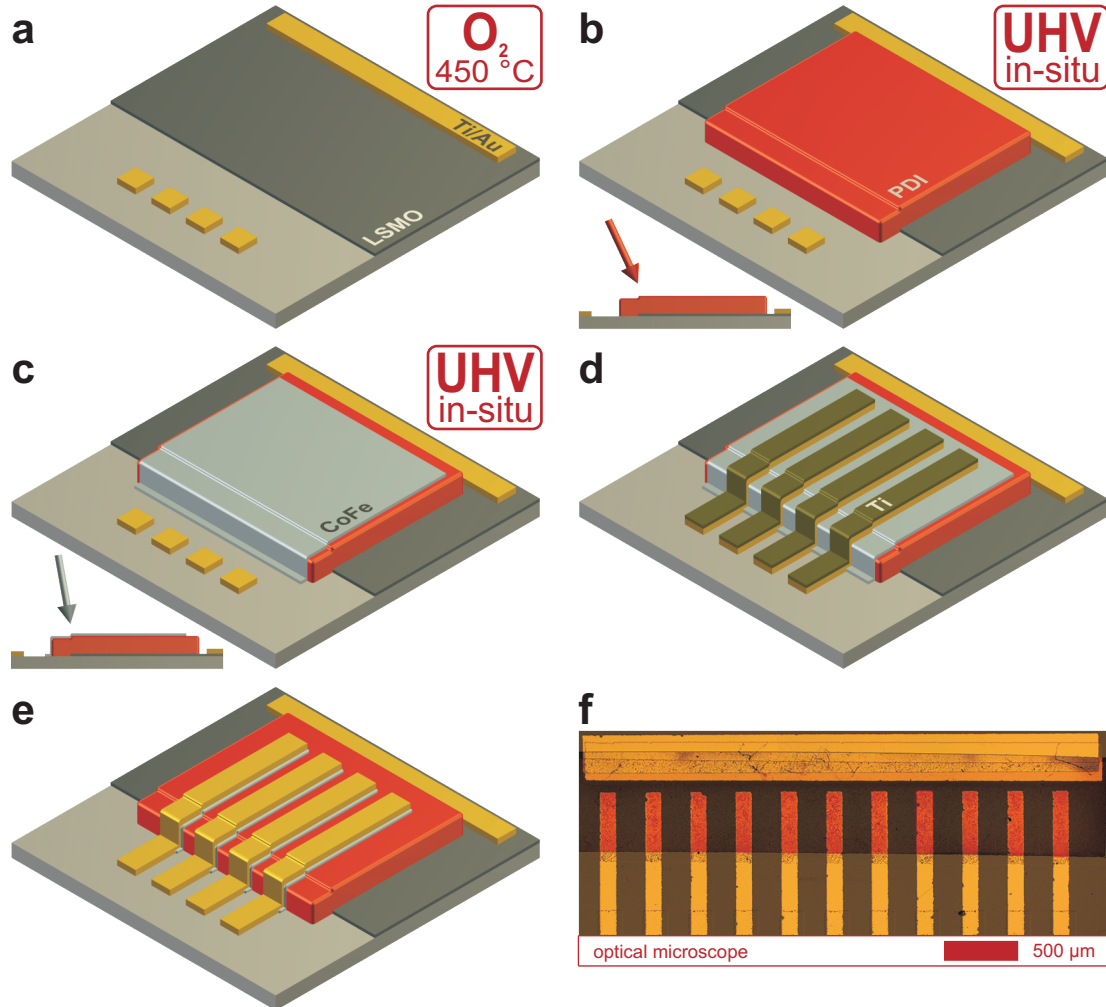
Figure 3.1: Flow chart of the fabrication process based on Ar ion milling for vertical OSV structures.
a: The LSMO bottom contact is patterned by optical lithography and dry etching. Ti/Au contacts
serve as alignment marks for the solid shadow masks. **b**: After annealing in the UHV chamber under
oxygen atmosphere, the OSC layer (PDI) is deposited with the sample slightly tilted as indicated. A
shadow mask with a large window is used. **c**: The top contact layer (CoFe) is deposited through the
same shadow mask under a different angle of incidence. **d**: A shadow mask with small rectangular
openings is used for the deposition of Ti/Au/Ti stripes connecting the top electrode layer and the
contact pads. **e**: Using the Ti/Au/Ti stripes as etching mask, the excess top contact material between
the stripes is removed by Ar ion milling resulting in several separate devices. The removal of parts
of the OSC layer as well as of the LSMO film during this step is not sketched here for the sake of
clarity. **f**: Optical micrograph of a sample with eleven devices. The active area of each device is
$150 \times 400\,\mu m^2$ in this case (highlighted in red).

uncovering the insulating substrate around the devices' contact pads. The required etching mask is patterned by optical lithography. Then the sample is covered with a solid shadow mask with a large rectangular window and inserted into the OMBD chamber.

Prior to the further processing the sample undergoes an annealing step. A bakeout at $450\,°C$ in oxygen atmosphere (pressure $1 \cdot 10^{-5}\,$mbar) is performed in order to remove any contaminations and solvent residuals. By exposing the sample to oxygen during this step underoxygenation due to the annealing, which very likely leads to changes of the material's properties, is prevented [deJong05]. Moreover, hereby the LSMO layer's surface stoichiometry that may have been altered during the preceding processing steps is recovered, at least with respect to the oxygen content.

In the subsequent steps the PDI (thickness $d_{PDI} = 50 - 600\,$nm) and the top electrode layer ($Co_{30}Fe_{70}$, thickness $15 - 30\,$nm) are deposited (Figs. 3.1**b** and **c**). During the OSC deposition the substrate temperature is set to $T_{sub} = 125\,°C$ in order to obtain optimum layer growth with respect to its charge transport performance [Oh07]. As indicated in Figs. 3.1**b** and **c**, different angles of incidence are used for the OSC and top contact layer leading to different overlaps between the respective layer and the LSMO bottom contact. Short circuits between the top and the bottom electrode layer are hereby prevented.

For the following step the shadow mask is replaced by another mask with seven or eleven small rectangular openings. Through this shadow mask Ti/Au/Ti stripes are deposited as shown in Fig. 3.1**d**. They provide an electrical connection between the contact pads and the top electrode layer and serve as etching mask for the last step. This is the removal of the excess top contact material between the stripes by Ar ion milling. During this step the terminating Ti layer of the stripes is also removed leaving Ti/Au contacts on the sample (Fig. 3.1**e**). The finished sample (optical micrograph in Fig. 3.1**f**) now can be mounted into a chip carrier and bonded via ultrasonic bonding. The active area, highlighted in red in Fig. 3.1**f**, of devices fabricated by this process is $150 \times 400 - 1500\,\mu m^2$ (width $\times$ length).

Obviously, TAMR devices can also be fabricated with this process when Al instead of CoFe is deposited as top contact layer. For the fabrication of reference structures with only metallic non-magnetic electrodes, on the contrary, further modifications are necessary. For devices with an LSMO bottom contact an ex-situ patterning of the bottom electrode is not crucial since oxidation obviously cannot influence the electrode's surface such that potential modifications could not be compensated by suitable in-situ cleaning treatments as described above. A metallic bottom electrode, however, should preferably be patterned in-situ, i.e. in the case of the reference samples three different layers have to be deposited in the OMBD chamber. This demand can be met by suitable changes in the fabrication process.

The basis for the reference samples are p-Si substrates with a $1\,\mu m$ thick thermal SiO_2 layer (Fig. 3.2**a**). The same contact pads as for the conventional OSVs are patterned by optical lithography and lift-off before the sample is inserted into the OMBD chamber, again covered by the shadow mask with one large window. The whole device layer-stack is deposited without breaking the UHV. First a $10\,$nm thick Al layer is evaporated with the substrate tilted rather strongly (Fig. 3.2**b**). Subsequently, the PDI layer (Fig. 3.2**c**) and top contact layer ($30\,$nm Al, Fig. 3.2**d**) are deposited at stepwise decreased angles of incidence, similarly as for the conventional OSV devices. Again, insulation between the top and the bottom electrode
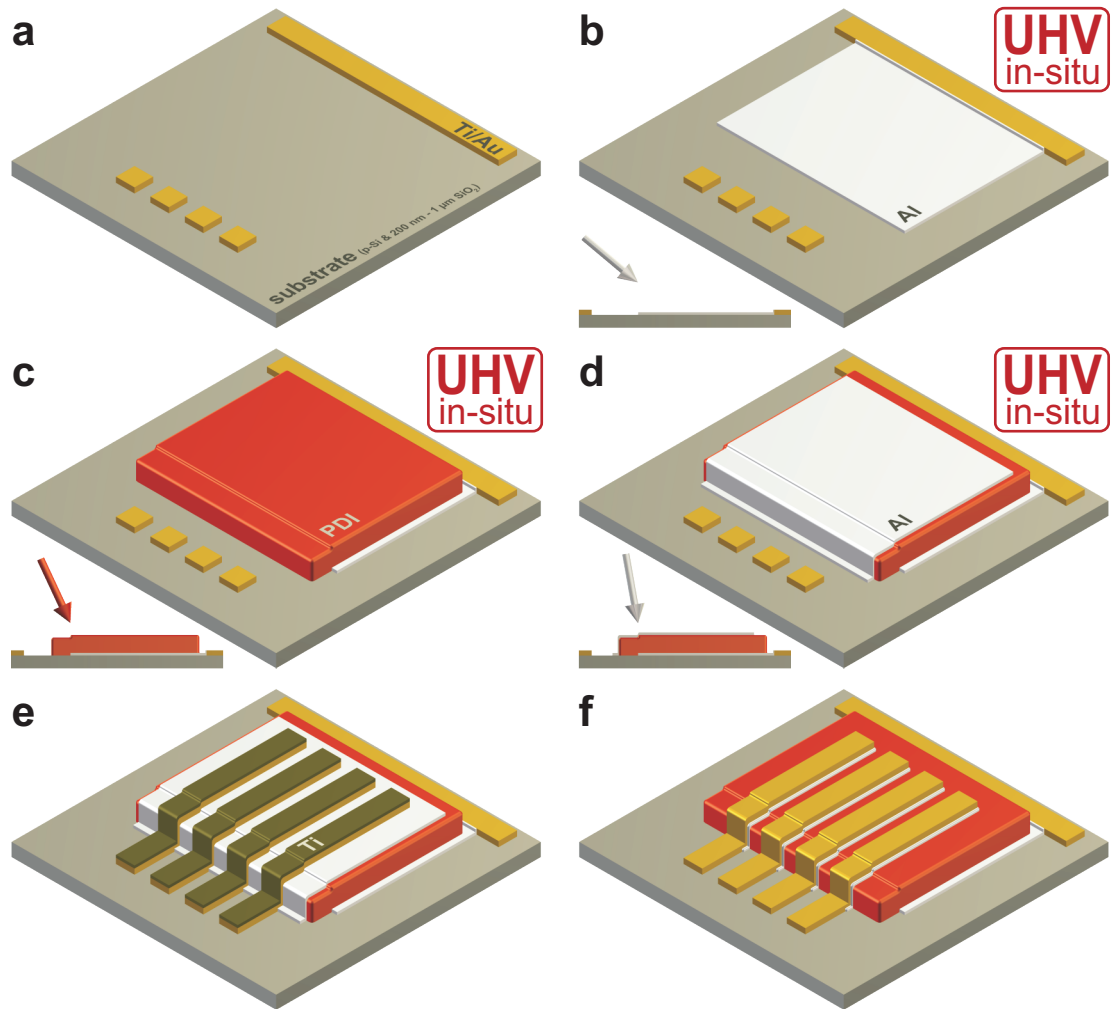
Figure 3.2: Flow chart of fabrication process for reference devices (Al bottom and top electrode).
a: Ti/Au contact pads are patterned by optical lithography and lift-off on a p-Si substrate covered with
a layer of insulating SiO_2. **b**: After insertion of the sample into the UHV chamber, the bottom contact
layer (Al) is evaporated by electron beam evaporation through the large-window shadow mask with
the sample strongly tilted. **c**: The OSC layer (PDI) is deposited under a smaller angle of incidence. **d**:
The top contact layer (Al) is evaporated after decreasing the sample tilt again. **e f**: Identically to the
previously presented fabrication process, Ti/Au/Ti stripes connecting the top contact layer and the
contact pads and serving as etching mask are deposited through another shadow mask. Finally, the
excess top contact material between the stripes is removed by Ar ion milling. The removal of parts of
the OSC layer as well as of the bottom Al electrode during this step is not sketched here again.

layer is provided by the different overlaps originating from the different angles of incidence used for the three deposition steps. Concerning the patterning of the top electrode layer (Figs. 3.2**e** and **f**) this fabrication process is identical to the one for samples with an LSMO bottom contact (Ti/Au/Ti etching mask and Ar ion milling).

Given the availability of new equipment (location HAL), a cluster of several UHV chambers connected with each other by a distribution chamber allowing for in-situ transfer between them, a new fabrication process for vertical devices (chapter 2.4.1) is developed. As a consequence of the in-situ fabrication, and similarly to the previously presented methods this process also provides clean and reproducible interfaces. However, due to the new equipment, the in-situ fabrication is feasible in a less complex, faster and more straightforward manner. Furthermore, no preliminary patterning, e.g. optical lithography, of the substrate and/or processing after the deposition of the devices' layer stack is necessary. The following deposition and fabrication techniques are used:

- PLD,

- metal deposition by electron beam evaporation,

- metal deposition by direct current sputtering,

- deposition of insulators by electron beam evaporation,

- OMBD (including substrate tilting and heating),

- in-situ exchange of solid shadow masks (positioning precision $\sim 100\,\mu$m).

The basis of the samples relevant for the present work (TAMR devices based on the OSC AlQ$_3$) are STO(001) substrates on which first a 20 nm thick film of LSMO is deposited by PLD. After cutting the sample to a size that fits the chip carrier ($3 \times 5\,\text{mm}^2$), it is prepared for the shadow mask exchange system and all following steps are performed in-situ. First the LSMO layer is patterned indirectly by the deposition of two layers of alumina (AlOx, electron beam evaporation) leaving uncovered a stripe of $200\,\mu$m $\times$ 5 mm (Fig. 3.3**a**). This stripe serves as common bottom contact for all devices. The first AlOx layer defines the width of this stripe and is rather thin (thickness $10 - 30$ nm) in order to avoid shadows during the following deposition steps probably leading to short circuits. The second AlOx layer is the basis for the contact pads of the counterelectrodes, i.e. it should provide good electrical insulation at high voltages and mechanical stability for the later ultrasonic bonding. The thickness of this layer, which obviously must not cover the first one completely as shown in Fig. 3.3**a**, therefore is chosen sufficiently large ($100 - 150$ nm). Due to the possibility of exchanging shadow masks in-situ, any preliminary patterning by methods involving solvents, e.g. optical lithography, are dispensable. Hence, likewise an in-situ cleaning by heating/annealing is not mandatory and consequently omitted. In the next step, an AlQ$_3$ layer of variable thickness is deposited by OMBD through a shadow mask with a large rectangular window and with the substrate kept at room temperature (Fig. 3.3**b**). Subsequently, direct current sputtering is applied to deposit the top electrode consisting of 20 nm Cu contact layer and a 10 nm Ru capping layer through a shadow mask with eight stripe-shaped openings (width $150\,\mu$m)
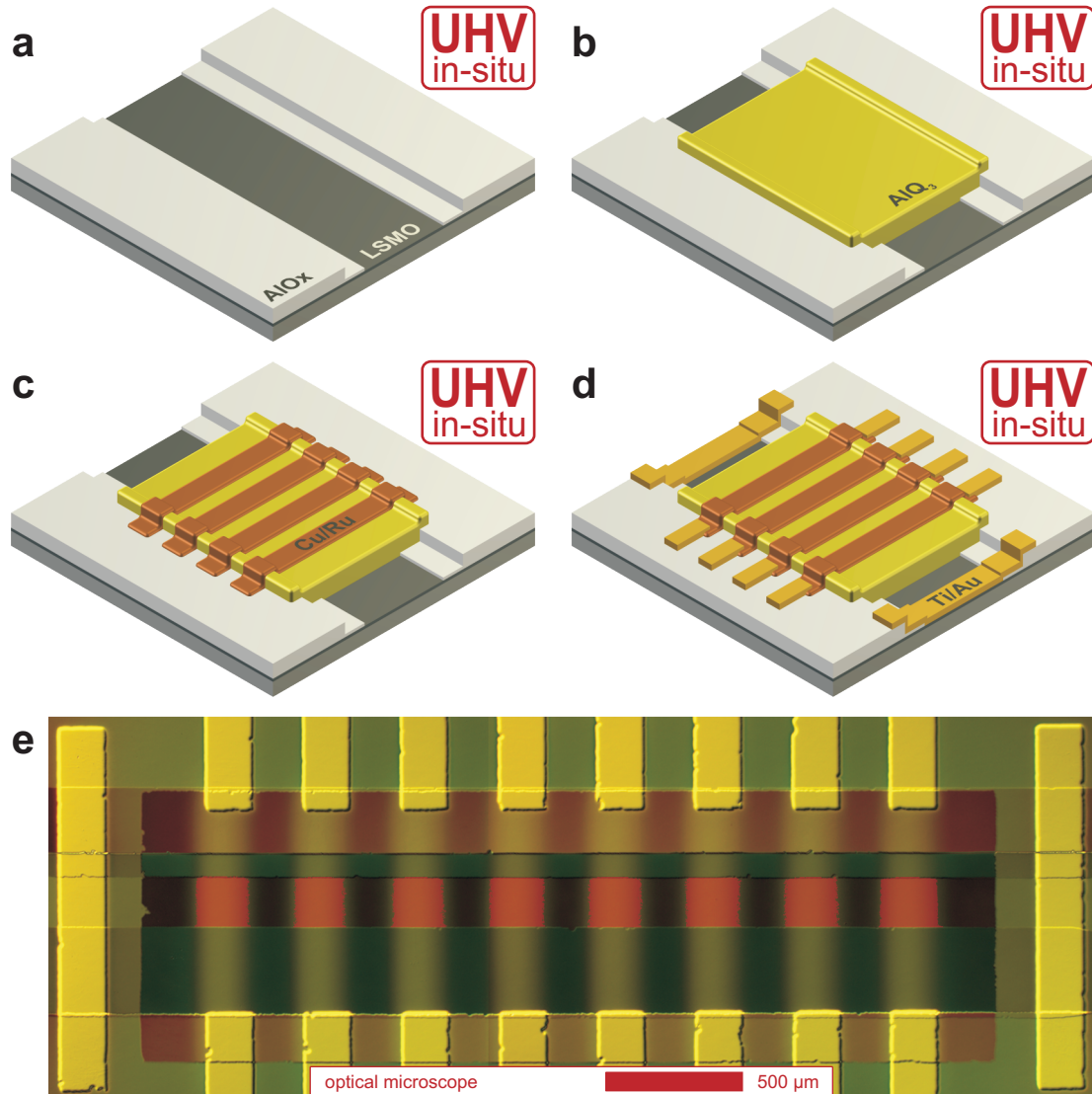
Figure 3.3: Flow chart of fabrication process for vertical TAMR devices using in-situ exchangeable shadow masks. **a**: The LSMO bottom contact is patterned indirectly by evaporating a thin insulating alumina (AlOx) layer. The following thick AlOx layer serves as basis for the Ti/Au contact pads of the counterelectrodes. **b**: During OMBD of the AlQ$_3$ layer the sample is covered by a shadow mask with a large rectangular window. **c**: The top contact stripes (Cu as electrode material and Ru as capping layer) are deposited by direct current sputtering. **d**: The devices' active area is shielded by the shadow mask during the deposition of the Ti/Au contact pads. **e**: Optical micrograph of a sample with eight devices; the active area is highlighted in red.

yielding separate devices (Fig. 3.3c). The last step is the evaporation of Ti/Au contact pads, two per device and two for the LSMO layer, by electron beam evaporation.

As can be seen in Fig. 3.3d, the counterelectrodes of the devices are not completely covered by the final Ti/Au contact layer which is in contrast to the former sample layouts in Figs. 3.1e and 3.2f . Instead, the top contact stripes are equipped with contact pads at both ends. As a result, the active area of the devices ($\sim 200 \times 200\,\mu m^2$, highlighted in red in the optical micrograph in Fig. 3.3e) is covered by the solid shadow mask during Ti/Au deposition by electron beam evaporation and therefore shielded from any X-radiation (Bremsstrahlung) probably emitted by the evaporator. X-radiation can dramatically influence the transport properties of an OSC layer exposed to it, very likely due to the formation of trap states [Rybicki12].

3.2   Results PDI-based Spin Valves

As already mentioned in chapter 2.4.2, PDI is a rather new material giving prospect to stable and high-performance devices. So far, PDI has only been investigated in terms of field effect mobility in OFET structures [Oh07]. Hence, one of the present work's objectives is the investigation of this material's suitability for the use in spintronics devices, which is done in collaboration with the group of Prof. Frank Würthner. Apart from this rather general motivation, additionally more insight into the underlying mechanisms of any potential spin-valve effect should be gained. For this purpose a series of conventional OSVs with an LSMO bottom and a CoFe top electrode is fabricated and investigated with respect to several parameters. The results of these experiments can be found in chapters 3.2.1-3.2.5. Furthermore, sustaining and additional results are obtained in dedicated TAMR devices (chapter 3.4.2) and reference structures with non-magnetic electrodes.

3.2.1   Transport Characteristics and the Spin-Valve Effect

After fabrication all samples pass a standard preliminary characterisation procedure, which is performed at setup #1 (^{4}He flow cryostat, see appendix B) and includes I/V characterisation and magnetotransport measurements at room temperature. This characterisation is employed as a test for obviously shorted devices and also brings forth a reasonably reliable indication whether a spin-valve effect can be measured at low temperatures or not. Subsequently, the OSVs are studied more extensively at $T = 4.2\,\mathrm{K}$ either in setup #1 as well or in setup #2 (^{4}He bath cryostat). Temperature dependent measurements, i.e. experiments at various temperatures between $4.2\,\mathrm{K}$ and $200\,\mathrm{K}$, are conducted for a subset of samples in setup #2.

Most of the experimental data presented hereafter are obtained from a device which can be regarded as representative for the entirety of all PDI-based OSVs that exhibit a distinct spin-valve effect. It is part of a sample which has an OSC layer thickness of $150\,\mathrm{nm}$. All data which have been recorded for this device are labeled 'PDI OSV' in the corresponding figures. If results of other devices are displayed, this will be explicitly indicated giving the relevant sample parameters.

Fig. 3.4 comprises typical results of the aforementioned preliminary characterisation. At room temperature non-linear and slightly asymmetric I/V curves (Fig. 3.4a) with a resistance R in the range of several $k\Omega$ to a few hundreds of $k\Omega$ are obtained for intact structures (U_{bias} is applied to the top CoFe electrode, the LSMO bottom contact represents electrical ground). This non-linearity may not always be very pronounced, however, becomes more evident regarding the corresponding differential resistance trace (dU_{bias}/dI, Fig. 3.4b), which obviously comprises a parabolic component and therefore suggests tunneling contributions to the charge transport [Stratton62].

The asymmetry of the I/V response is similar to many other results in the literature [Xiong04, Hueso07, Santos07, Wang07, Barraud10]. It is often interpreted as stemming from the devices' asymmetry, i.e. the different electrode materials and the resulting different injection barriers at the electrode/OSC interfaces (Schottky-like contacts, see chapter 2.2.1). OSV structures that do not show the described non-linear behaviour and a rather low resistance are omitted

for further measurements, whilst in the next step the magnetotransport behaviour of apparently intact ones is investigated. During these measurements usually a linear decrease of R with increasing magnetic field is observed (Fig. 3.4c). It is very likely that this MR effect occurs either in the LSMO electrode itself (CMR) or at the interface between the LSMO and the OSC (HFMR, see chapter 2.4.4).
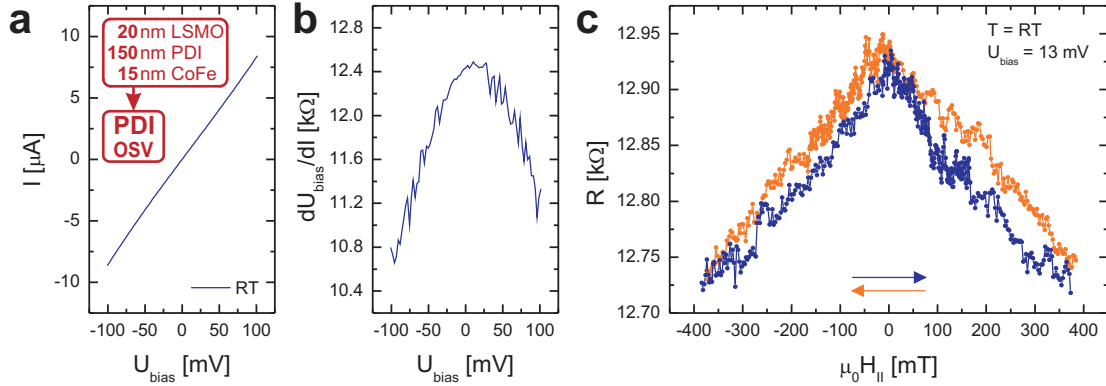
Figure 3.4: Basic transport properties of a PDI-based OSV device recorded at room temperature. **a,b**: Non-linear I/V curve and corresponding differential resistance trace indicating tunneling contributions to the charge transfer. **c**: MR trace exhibiting a linear effect, decreasing resistance with increasing magnetic field.

Subsequently, a similar procedure, I/V and MR characterisation, is performed at low temperatures ($T = 4.2$ K). The results of these measurements are summarised in Figs. 3.5a-c in comparison with the room temperature data of the same device. The non-linearity of the device's I/V response is significantly more pronounced at low temperatures and becomes evident from the I/V curve alone (Fig. 3.5a). As can be seen from the differential resistance traces in Fig. 3.5b, for this device R is increased compared to the room temperature value at low bias voltage ($|U_{\mathrm{bias}}| \leq 50$ mV) and decreased for higher U_{bias}. The change of R, however, be it a decrease or an increase, is less than one order of magnitude.

This weak temperature dependence of R constitutes a stronger indication for the dominating role of tunneling with respect to the charge transfer than the I/V curves' non-linearity alone. This is mainly because the latter easily may be misinterpreted in this context [J-Åkerman00, Lin10].

As already stated in the fundamentals section of this work (chapter 2.2.1), a significant contribution of tunneling processes to a vertical device's total resistance can be caused either during charge injection or when direct tunneling between the two electrodes is possible due to a reduced OSC layer thickness at pinhole sites.

If, by contrast, the charge transport occurs through a thick OSC layer by the VRH-like mechanism introduced in chapter 2.2.1, a strong increase of R is to be expected during cooldown of the sample. This is indeed also observed in some of the PDI-based OSVs as can be seen in Figs. 3.5d-f which show the results of the preliminary investigations at room temperature and 4.2 K for a device with $d_{\mathrm{PDI}} = 600$ nm. This structure can be considered exemplary

for a second class of non-shorted PDI-based OSVs, namely those which do not exhibit any MR effect at low temperatures. Just regarding the I/V and differential resistance characteristics at room temperature (blue curves in Figs. 3.5d and e), the transport behaviour of this device (non-linear I/V response, $R \approx 20\,\mathrm{k\Omega}$) can be declared similar to the one discussed above. However, when the sample is cooled to $4.2\,\mathrm{K}$, an elementary difference between the two structures under discussion is emerging. Whereas the change of R is relatively small in the aforementioned results, here R undergoes an increase by more than four orders of magnitude at small U_{bias}. Thus, the physics behind the charge transfer is apparently substantially different for this device.
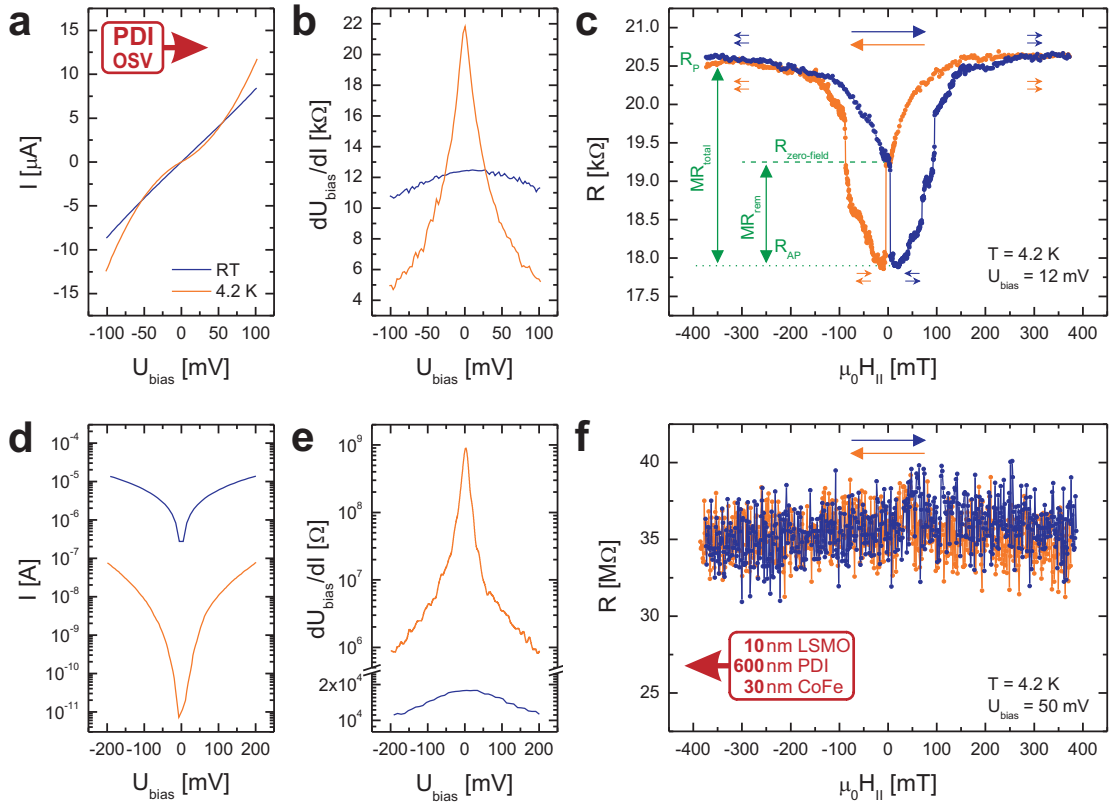
Figure 3.5: Basic transport properties of two types of PDI-based OSV devices recorded at $T = 4.2\,\mathrm{K}$ compared with the room temperature data. **a,b**: I/V curves and differential resistance traces showing the weak temperature dependence of this device's resistance. **c**: MR trace consisting of a non-linear background signal and the spin-valve effect (hysteretic switching). **d,e**: I/V curves and differential resistance traces of a device where the resistance is increased by several orders of magnitude during cool down from room temperature to $4.2\,\mathrm{K}$. **f**: No MR effect can be observed in this device.

This assumption is supported by MR experiments conducted at low temperatures, the results of which are presented in Figs. 3.5c and f for both devices. Obviously, the structure exhibiting the high increase of R upon cooling does not show any MR (Fig. 3.5f), neither any kind of symmetric effect as, for instance, is found at room temperature (Fig. 3.4c) nor any hysteretic behaviour. If, on the contrary, the temperature dependence of R is weak and

therefore reminiscent of tunneling processes dominating the charge transport, as it is the case for the first-mentioned class of devices, a clear spin-valve signal can be observed (Fig. 3.5c). Before going into the details of the MR trace in Fig. 3.5c it is worth mentioning that the described correlation between the temperature dependence of R and the magnetotransport properties agrees well with the findings of Yoo *et al.* and Lin *et al.* [Yoo09, Lin10]. In these studies, which comprise similar investigations in OSV structures based on the OSC material Rubrene, this link has been explicitly constituted for the first time.

As stated at the beginning of this chapter, the MR signal shown in Fig. 3.5c can be regarded as representative. It basically consists of two components, a non-linear and symmetric background effect, on the one hand, and a distinct switching between two resistive states, the spin-valve effect itself, on the other hand. The background signal is a constant increase of the device resistance with increasing magnetic field and is present in a more or less pronounced manner in all PDI-based OSVs and equally observed in other OSV experiments in the literature [Vinzelberg08, Xu07, Majumdar06a, Wang07]. Although the focus of the present work is not on this contribution to the MR, reference structures with two non-magnetic metallic electrodes made of Al are investigated at room temperature and 4.2 K. A complete characterisation sequence is summarised in Fig. 3.6 containing I/V curves, differential resistance traces and magnetotransport data.
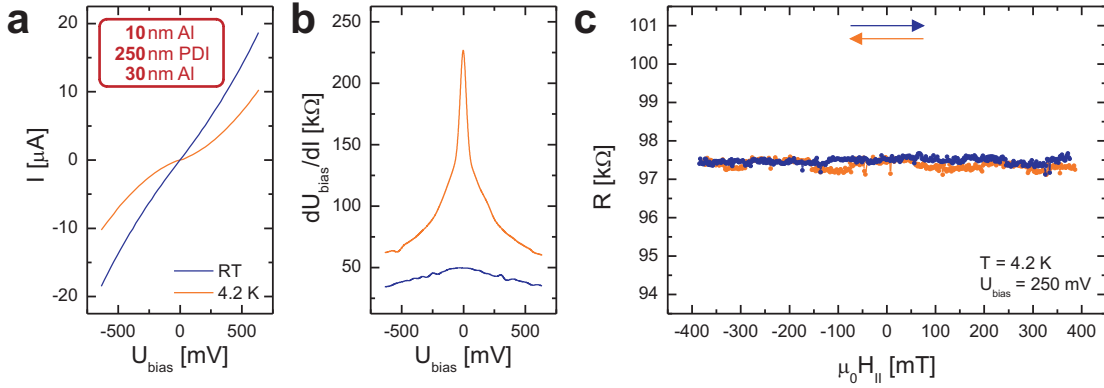
Figure 3.6: Basic transport properties of a PDI-based reference structure with non-magnetic electrodes at room temperature and 4.2 K. **a,b**: A weak temperature dependence of R can be identified in the I/V curves and differential resistance traces again. **c**: No MR effect is observed in these devices for $|U_{bias}| \leq 250\,mV$.

It can be seen that the temperature dependence of R (Fig. 3.6b) is similarly weak as in the conventional OSVs exhibiting spin-valve functionality. Likewise resemblances with respect to the I/V responses' non-linearity become evident from a comparison of the respective data in Fig. 3.6a with the I/V curves in Fig. 3.5a. Furthermore, it should be noted that the reference devices' I/V characteristics are nearly symmetric at room temperature and 4.2 K which is very likely due to the symmetric electrode configuration. These structures do not show any kind of MR effect for $|U_{bias}| \leq 250\,mV$ at any temperature between 4.2 K and room temperature. As Fig. 3.6c (data collected at low temperatures) shows, the resistance of the

structures is constant, apart from small variations of $\sim 0.05\,\%$, when the in-plane magnetic field is swept between $\mu_0 H_{\parallel} \approx -400\,\text{mT}$ and $\mu_0 H_{\parallel} \approx +400\,\text{mT}$ and back again. Thus, this experimental proof for the absence of any intrinsic MR suggests that in the bias range under investigation intrinsic effects in the PDI layer like, for instance, OMAR (see chapter 2.2.3), can be very likely excluded as origin of the background effect that is observed in nearly all PDI-based OSVs at low U_{bias}.

Neither does the background signal stem from any effect changing the in-plane resistance $R_{\text{ip,LSMO}}$ of the LSMO layer, which is contributing to the total device resistance as well. This has been experimentally verified by magnetotransport investigations undertaken for devices where the PDI layer has been omitted (CoFe and Ti/Au contacts on LSMO, [Wahler09]). These experiments yield $R_{\text{ip,LSMO}} \approx 180\,\Omega$ at $T = 4.2\,\text{K}$ and an MR magnitude in the range of $\sim 0.05\,\%$. When comparing these figures to the total device resistance and the MR ratio presented in Figs. 3.5a-c, it becomes clear that the background signal cannot be originating from any MR intrinsic to the LSMO layer. Instead, possible mechanisms causing this signal may be effects related to the LSMO electrode's interface to the OSC layer (e.g. HFMR, see chapter 2.4.4) or the magnetic saturation of the ferromagnetic electrode(s).

The second component of the MR trace in Fig. 3.5c can be attributed to actual spin-valve operation, i.e. to the change of the relative orientation of the electrodes' magnetisation (indicated by the small arrows in Fig. 3.5c). It is explained in the following by reference to the sweep from high negative fields to high positive fields (blue trace in Fig. 3.5c). The measurement is started in the parallel magnetisation state at $\mu_0 H_{\parallel} \approx -400\,\text{mT}$ with the corresponding device resistance $R_{\text{P}} \approx 20.6\,\text{k}\Omega$. When $H_{\parallel}$ is decreased to zero, the device resistance is lowered to $R_{\text{zero-field}} \approx 19.3\,\text{k}\Omega$ before at small positive $H_{\parallel}$ the first switching event occurs and the device is set to the anti-parallel state with $R_{\text{AP}} \approx 17.9\,\text{k}\Omega$. The transition from the parallel to the anti-parallel state is caused by the reversal of the LSMO electrode's magnetisation at $\mu_0 H_{\parallel} \approx 4.5\,\text{mT}$, a value which is in good agreement with the coercive field of LSMO determined by superconducting quantum interference device (SQUID) measurements (see below, Figs. 3.7a and b). When $H_{\parallel}$ is further increased, also the magnetisation of the CoFe counterelectrode is reversed, often in multiple steps as in the present data, restoring the parallel spin-valve state with $R_{\text{P}} \approx 20.6\,\text{k}\Omega$. As indicated by the green lines and arrows in Fig. 3.5c, two dimensions, MR_{total} and MR_{rem}, will be used to characterise the size of the observed effect hereafter. They are calculated as follows:

$$MR_{\text{total}} = \frac{R_{\text{AP}} - R_{\text{P}}}{R_{\text{AP}}} \tag{3.1}$$

$$MR_{\text{rem}} = \frac{R_{\text{AP}} - R_{\text{zero-field}}}{R_{\text{AP}}} \tag{3.2}$$

For the evaluation of MR_{total} the maximum resistance difference observed in an MR measurement is taken into account, whilst MR_{rem} uses the resistance values which are measured when $H_{\parallel}$ is set to zero field after preparing either the parallel or the anti-parallel magnetisation state. Equ. 3.2 can be easily derived from Equ. 3.1. For this purpose, R_{P} is replaced by $R_{\text{zero-field}}$, and R_{AP} is assumed to be remanent when the field is turned off once having reversed the LSMO electrode's magnetisation (experimental evidence for this remanence will

be provided in chapter 3.3.2). Hence, MR_{rem} is a measure for the size of the effect in the so-called remanent spin-valves state. The data plotted in Fig. 3.5c yield $MR_{\text{total}} \approx -15.1\%$ and $MR_{\text{rem}} \approx -10.1\%$. Absolute values in the range of several % to 50% at $T = 4.2\,\text{K}$ and low bias voltage ($\sim 10\,\text{mV}$) are typical for the PDI-based OSVs.

Evidently, the MR effect in the present devices is negative, i.e. $R_{\text{AP}} < R_{\text{P}}$, which likewise is reported for most of the OSV structures featuring an LSMO electrode and thick layers of various OSC materials [Xiong04, Xu07, Wang05, Dediu08]. Furthermore, in the first instance, this constitutes a deviation from spin-valve theory and the common behaviour of inorganic GMR and TMR devices (see chapters 2.1.1 and 2.1.2). Up to now, there are several approaches to explain the inverted sign of the effect observed in OSVs [Xiong04, Dediu08, Barraud10], reaching from a rather straightforward quoting of a negative spin polarisation in the counterelectrode [Xiong04] to a more complex elucidation of the interfaces' role for the spin and charge transport [Barraud10]. The latter scenario, which apparently has to be preferred as explanation as recently demonstrated by extensive research activities, has already been discussed more precisely in chapter 2.2.2.
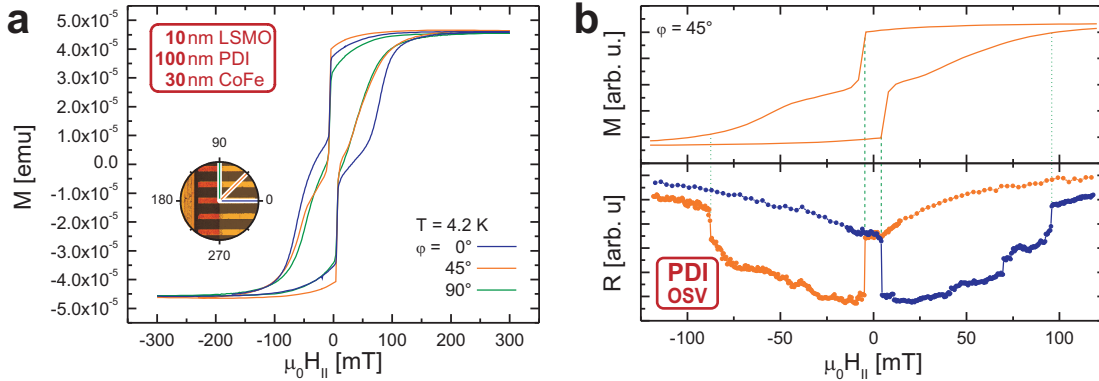
Figure 3.7: Comparison of SQUID and transport data for PDI-based OSVs. **a**: Magnetic hysteresis loops for three orientations of the magnetic field measured by SQUID showing a distinct switching of the LSMO electrode's and rotation-like behaviour of the CoFe layer's magnetisation. **b**: Direct juxtaposition of SQUID and magnetotransport results for $\varphi = 45\,^\circ$.

The switching fields that can be extracted from the MR traces are compared to the coercive fields H_{c} of the respective electrode materials in Fig. 3.7b. For this purpose the magnetic hysteresis of a fully processed OSV sample is measured by SQUID magnetometry at $4.2\,\text{K}$ with the magnetic field applied along different in-plane directions φ (Fig. 3.7a, $\varphi = 0°$ corresponds to the magnetic field applied parallel to the CoFe stripes). SQUID measurements are feasible for devices on STO substrates only as NGO would cause an enormous background signal due to its paramagnetic nature. Transport data, on the contrary, are collected from devices on STO and NGO substrates. Thus, the following analysis will focus on the behaviour of the CoFe top electrode's magnetisation, whereas this of the LSMO layer will not be discussed in detail.

As the SQUID data shows, the LSMO electrode's magnetisation performs a sharp reversal at

$\mu_0 H_{\rm c,LSMO} \approx \pm\, 4 - 6\,$mT. In the CoFe counterelectrode, by contrast, the magnetisation is apparently reversed in multiple steps or slowly rotated, respectively. Additionally, the behaviour of the CoFe stripes' magnetisation significantly depends on the orientation of the magnetic field, e.g. the rotation sets in at rather high magnetic fields only for $\varphi = 0\,^\circ$. This results in a plateau-like shape of the hysteresis loop between $\mu_0 H_{\rm c,LSMO}$ and $\mu_0 H_{||} \approx 50 - 60\,$mT (see blue line in Fig. 3.7**a**) as expected for an OSV device with two ferromagnetic electrodes. However, when the magnetic field is applied in the $45\,^\circ$- and $90\,^\circ$-direction a plateau can hardly be discerned in the SQUID data which can be explained in a straightforward manner by taking the shape anisotropy of the rectangular top electrodes into account [Aharoni98].

As aforementioned, the switching from the parallel to the anti-parallel spin-valve state can be ascribed to the reversal of the LSMO electrode's magnetisation. This can be seen from the comparison of magnetometry and magnetotransport data for $\varphi = 45\,^\circ$ in Fig. 3.7**b**, where these switching events are marked by dashed green lines. Another observation unveiled by the juxtaposition of these data is more remarkable and seems less sensible at first glance. Whilst the hysteresis measured by SQUID suggests that the CoFe's magnetisation undergoes a slow reversal by rotation, the spin-valve traces exhibit sharp switching events for the transition back to the parallel state (marked by dotted green lines).
This apparent inconsistency can be understood when having a closer look at the interface which is formed between the PDI layer and the CoFe electrode. The morphology of the polycrystalline PDI layer, which must not be regarded as completely flat as stated in chapter 2.4.2, can be transferred to the subsequent CoFe layer [Bergenti07]. The latter may also comprise small inclusions near the PDI-CoFe interface which can be formed due to material diffusion during the deposition of the top electrode by electron beam evaporation [Dürr03, Vinzelberg08]. In consequence, an ill-defined interface is evolved consisting of randomly shaped and sized metal clusters inside the PDI layer and a rather rough, closed bulk layer on top of it.
If part of an OSV device, this interface substantially may influence the magnetotransport behaviour, i.e. the actual counterelectrode is constituted rather by the CoFe inclusions than by the bulk layer. SQUID magnetometry, on the contrary, is a mass sensitive measurement technique. Therefore, the data acquired by SQUID very likely reveals the magnetisation dynamics of the latter, whereas the contribution of the often nano- or micron-sized inclusions cannot be sensed. Thus, their magnetic properties which very likely are different from those of bulk CoFe [Vinzelberg08] cannot be reflected in the magnetisation hysteresis loops in Figs. 3.7**a** and **b** but decisively influence the shape of the spin-valve signal shown in the bottom panel of Fig. 3.7**b**.

Although the magnetisation behaviour of the top electrode's bulk part very likely only plays a minor role with respect to the shape of the observed MR traces, it should be shortly compared to this of a flat CoFe layer. Thus, for instance, the 'coercive field' of a CoFe-layer on top of a PDI layer, which is $\sim 50 - 60\,$mT according to the $0\,^\circ$ trace in Fig. 3.7**a**, is $\sim 2 - 3$ times higher than that of a comparable smooth layer ($\mu_0 H_{\rm c,CoFe} \approx 15 - 25\,$mT when deposited on a bare silicon substrate, see Fig. 4.3). Such an increase of $H_{\rm c}$ may be originating from either the increased roughness of the electrode itself [Saragi09] or chemical interactions

at the OSC/ferromagnetic metal interface [Morley14].

As a preliminary summary it can be noted that a distinct spin-valve effect comparable to other results in the literature is observed in PDI-based OSVs. The results of transport experiments are in good agreement with the magnetometry data. Thus, the rather new material PDI is obviously well suited for spintronics applications. The weak temperature dependence of R suggests a tunneling-based MR effect like TMR as underlying mechanism. This scenario will be sustained by a more extensive discussion and characterisation of the spin-valve signal which will be set forth in the following chapters.

3.2.2 Angle Dependence of the Spin-Valve Effect

The results of SQUID measurements recorded with the magnetic field applied in different in-plane directions unambiguously reveal the influence of shape anisotropy on the magnetic properties of the top electrode's bulk part. This anisotropy may also affect the magnetisation behaviour of the CoFe layer's interfacial component that is presumably decisive for the charge and spin transfer and consequently reflected in the transport measurements. Fig. 3.8**a** comprises MR sweeps from negative to positive saturation recorded with $\boldsymbol{H}_{||}$ oriented along the three directions φ for which the magnetic hysteresis loops are displayed in Fig. 3.7**a**. As expected, the shape of the spin-valve signal apparently changes with φ.

When $\boldsymbol{H}_{||}$ is applied perpendicular to the CoFe stripes ($\varphi = 90\,°$, green curve in Fig. 3.8**a**), the MR trace does not exhibit any sharp transitions between distinct resistive states. However, this is not equivalent to a total loss of spin-valve functionality in the common sense as there is still a hysteretic contribution to the MR. When consulting the SQUID data for $\varphi = 90\,°$, the observed shape of the MR can be interpreted as meaning that for this direction the magnetic properties of the CoFe layer do not allow for the preparation of a fully anti-parallel magnetisation of the electrodes. This behaviour very likely is strengthened by the uniaxial anisotropy of the LSMO electrode, which is grown on an NGO substrate for this sample [Boschker09] (hard axis along the $90\,°$ direction, see also chapter 2.4.4). The MR trace recorded for $\varphi = 0\,°$, on the contrary, is very similar to the one extensively discussed in the previous chapter ($\varphi = 45\,°$) and exhibits a sharply pronounced spin-valve component.

Differences between the $0\,°$- and the $45\,°$-signal exist with respect to the switching fields. These differences are very subtle, however discernable, for the first switching event from the parallel to anti-parallel configuration (reversal of the LSMO electrode's magnetisation) and more striking for the second one. Despite a similar trend for the respective φ can be discerned in the magnetic hysteresis measured by SQUID (Fig. 3.7**a**) as well, full consistency cannot be stated as already mentioned above. Another comparative analysis of SQUID and magnetotransport data highlights these discrepancies. Whereas the SQUID results for $\varphi = 45\,°$ and $\varphi = 90\,°$ are nearly congruent, the corresponding MR traces are obviously substantially different from each other. The opposite can be stated for the $0\,°$- and $45\,°$-measurements. These observations can again be resolved by recalling the characteristics of a probably ill-defined interface between the PDI and the counterelectrodes. Hence, the eminent role of interfaces in OSV devices is underlined by these results, even though in the very tangible sense
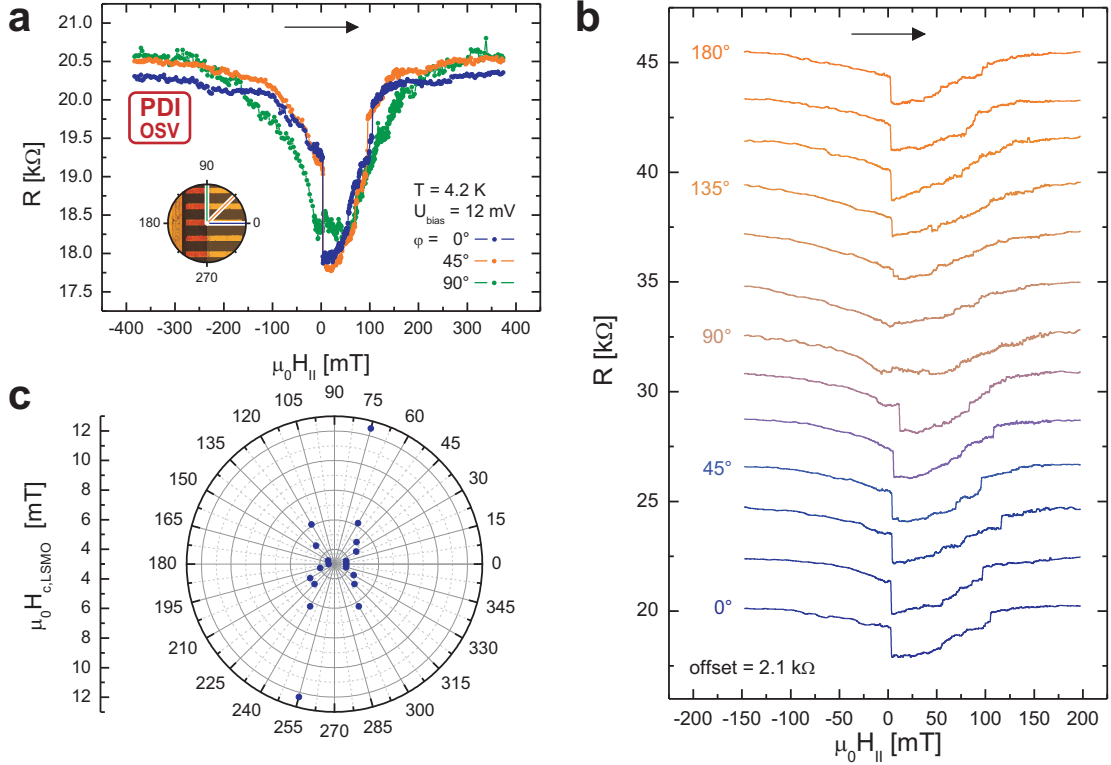
Figure 3.8: Angular dependence of spin-valve behaviour of a PDI-based OSV recorded at $T = 4.2\,\mathrm{K}$ and $U_{\mathrm{bias}} = 12\,\mathrm{mV}$. **a**: The MR traces for three orientations of the magnetic field are displayed without offset. **b**: Magnetotransport data of a full $0-180\,°$-series revealing the anisotropic behaviour of the spin-valve signal. **c**: The switching field $H_{\mathrm{c,LSMO}}(\varphi)$ extracted from the data in **b** reflects the uniaxial anisotropy of the LSMO electrode.

of the actual, physical interface and its morphology only. Another feature unambiguously discernable in the MR signals in Fig. 3.8**a** is that R in the saturation regime $(|\mu_0 H_{\|}| \geq 200\,\mathrm{mT})$ is different for different φ. This observation will be addressed in chapter 3.4.2 in the context of TAMR results.

The standard characterisation of the angular dependence of the spin-valve effect in any OSV device is a sequence of measurements in which φ is varied from $0\,°$ to $180\,°$ in $15\,°$ steps. The results of such a series are summarised in Fig. 3.8**b**, a so-called waterfall plot in which the traces of single measurements are offset by $2.1\,\mathrm{k\Omega}$. From this data more detailed information concerning the angular dependence of the spin-valve signal with respect to the magnetisation reversal of the LSMO layer, on one side, and to the switching of the CoFe counterelectrode, on the other side, can be gained.

For the former, a systematic dependence on φ is found as shown in Fig. 3.8**c**, a polar plot of the coercive field $H_{\mathrm{c,LSMO}}$ extracted from the MR traces. Starting from $\mu_0 H_{\mathrm{c,LSMO}} \approx 3.5\,\mathrm{mT}$ for $\varphi = 0\,°$, $H_{\mathrm{c,LSMO}}$ is increased when the orientation of $\boldsymbol{H}_{\|}$ is changed. For the $90\,°/270\,°$- and the $105\,°/285\,°$-direction, respectively, it is not possible to read any value for $H_{\mathrm{c,LSMO}}$ from the measurements in Fig. 3.8**b**. This observation can be attributed to the aforemen-

tioned uniaxial anisotropy in the LSMO electrode with the easy axis along $\varphi = 0\,°/180\,°$ and the hard axis along $\varphi = 90\,°/270\,°$.

As mentioned above, the magnetisation reversal of the CoFe counterelectrode also depends on φ. In addition to the previously discussed observations that can be identified when comparing SQUID and magnetotransport results, further angle-dependent features get evident from the waterfall plot in Fig. 3.8**b**. For instance, the position of the second switching event is changing with φ within the interval between $\varphi = 0\,°$ and $\varphi = 75\,°$, however, seemingly rather unsystematically. Such an apparently statistical behaviour as well as the presence of multiple step switching for certain φ is rendering questionable an evaluation of the MR signals with respect to $H_{\mathrm{c,CoFe}}$ similar to the one shown for $H_{\mathrm{c,LSMO}}$ in Fig. 3.8**c**.

Thus, from the angular dependence it becomes evident that the magnetic properties of both electrodes are influencing the shape of the spin-valve signal, which can be expected for an MR effect originating from a change of the electrodes' relative magnetisation. More insight into the underlying charge transfer mechanisms in the present OSVs is given in the following chapters.

3.2.3   Bias Dependence of the Spin-Valve Effect

The investigation of the MR effect's dependence on the applied bias voltage is part of the standard characterisation procedure at low temperatures as well. For this purpose a series of magnetotransport measurements with different U_{bias} is conducted.

The top panel of Fig. 3.9**a** shows the bias dependence of MR_{total} and MR_{rem} of the representative spin-valve structure recorded at $T = 4.2\,\mathrm{K}$ and $\varphi = 0\,°$. The data reveals a maximum effect around and is asymmetric with respect to $U_{\mathrm{bias}} = 0\,\mathrm{V}$. With increasing U_{bias} both measures decrease and are almost completely quenched at the maximum applied voltage of $\sim \pm 1\,\mathrm{V}$, whereby the decrease is slower for positive voltages. Such a behaviour can be expected for an MR effect based on tunneling processes in an asymmetric structure [Jullière75, Santos07, Zhan08, Barraud10]. Hence, the assumption that the spin-valve signal is originating from a tunneling-based mechanism can be regarded as sustained and strengthened by the observed voltage dependence.

A more detailed analysis of the bias dependence is depicted in the $MR_{\mathrm{rem}}/MR_{\mathrm{total}}$ plot in the bottom panel of Fig. 3.9**a**. Similarly to MR_{rem} and MR_{total} also this ratio, starting from its maximum value of $\sim 60\,\%$ at $0\,\mathrm{V}$, is significantly diminished when U_{bias} is increased, meaning that at low bias the actual spin-valve effect is dominating the MR. However, for $|U_{\mathrm{bias}}| \gtrsim 400\,\mathrm{mV}$ $MR_{\mathrm{rem}}/MR_{\mathrm{total}}$ apparently remains constant at the value of $\sim 25\,(35)\,\%$ for high negative (positive) U_{bias}.

The direct juxtaposition of two MR traces, one for each bias regime under discussion, in Fig. 3.9**b** reveals two rather striking differences. On the one hand, the shape of the background signal has changed from a constant increase of R with increasing $H_{\parallel}$ at low bias to an increase and subsequent decrease at elevated bias. On the other hand, the value of $H_{\parallel}$ where the minimum absolute resistance is observed for the anti-parallel spin-valve state is shifted to higher values in the MR signal recorded at high U_{bias} as indicated by the green lines and
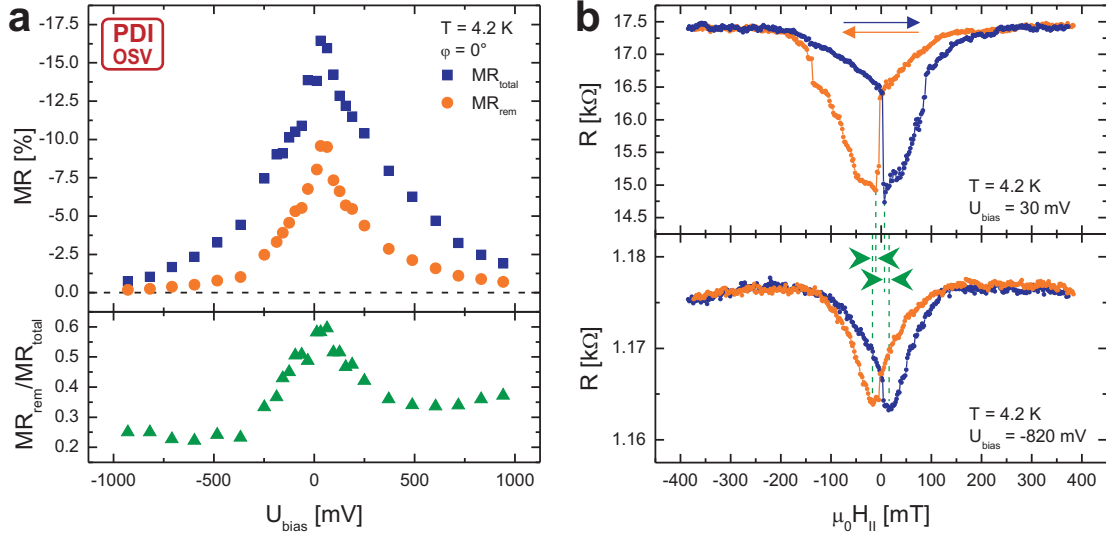
Figure 3.9: Bias dependence of spin-valve behaviour of the standard PDI-based OSV recorded at $T = 4.2\,\mathrm{K}$. **a**: Voltage dependence of MR_{total} and MR_{rem} (top panel) and the ratio $MR_{\mathrm{rem}}/MR_{\mathrm{total}}$ (bottom panel). The latter is indicating a transition concerning the underlying mechanisms at $U_{\mathrm{bias}} \approx \pm 400\,\mathrm{mV}$. **b**: Single MR traces recorded at low (top panel) and high (bottom panel) U_{bias} illustrate obvious differences in the shape of the spin-valve signal and the background effect.

arrows in Fig. 3.9**b**.

In a broader sense, this change of the MR signal can be interpreted as a transition similar to that from the injection limited to the space charge limited regime (see chapter 2.2.1). As stated in chapter 2.2.3, it has been shown by Wang *et al.* [Wang12] that OMAR can cause a hysteretic contribution to an MR effect, i.e. mimic spin-valve behaviour, when remanent, perpendicular fringe fields of a ferromagnetic electrode are present. In other words, the spin-valve behaviour that is observed for $|U_{\mathrm{bias}}| \gtrsim 400\,\mathrm{mV}$ (bottom panel of Fig. 3.9**b**) may also be partially caused by this mechanism, which likewise explains why the shape of the corresponding MR trace is less pronounced than a true rectangular spin-valve signal with sharp switching events. Thus, in this sense both effects, the background as well as the spin-valve signal, very likely are not exclusively caused by TMR or GMR but rather equally originate from processes inside the PDI layer, especially in the regime of rather high $|U_{\mathrm{bias}}|$.

It is important to note that this assumption is seemingly incompatible with the proof for the absence of OMAR in PDI-based devices for $|U_{\mathrm{bias}}| \lesssim 250\,\mathrm{mV}$ pointed out in chapter 3.2.1. However, the fact that OMAR is usually only observed at elevated bias [Francis04, Wang12] resolves this presumable contradiction.

The bias dependence of the MR and the ratio $MR_{\mathrm{rem}}/MR_{\mathrm{total}}$ discussed above can be regarded as typical for nearly all PDI-based OSVs. The results strengthen the assumption that, at least for small U_{bias}, a tunneling-based effect is dominating the magnetotransport response in these structures.

3.2.4   Temperature Dependence of the Spin-Valve Effect

The temperature dependence of the spin-valve signal in PDI-based OSV devices is investigated in setup #2 employing single magnetotransport measurements at various temperatures. The applied bias voltage is deliberately chosen to obtain the largest MR amplitude possible and I/V characterisation is performed in order to gain more information about the charge transfer mechanisms. On the basis of typical results that are summarised in Fig. 3.10**a** the evolution of the MR ratio with increasing temperature is discussed in the following.
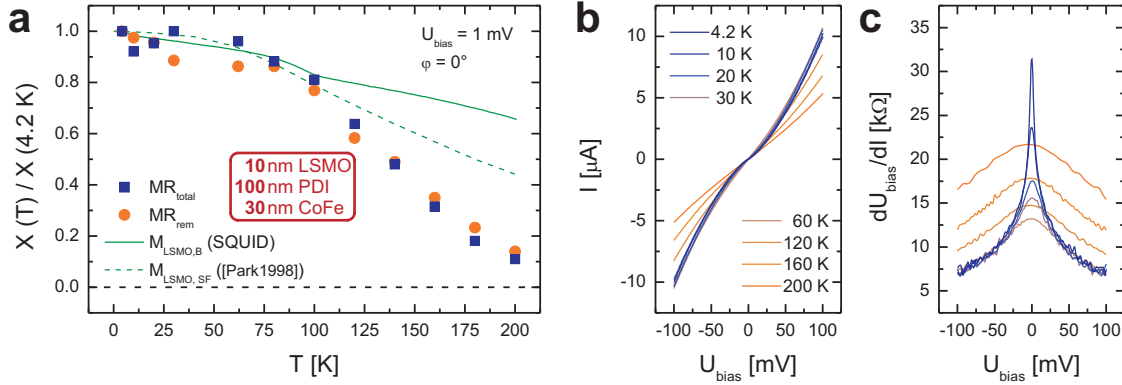
Figure 3.10: Temperature dependence of the spin-valve behaviour for a OSV. **a**: A constant decrease of the normalised MR ratios with increasing temperature is observed. For $\lesssim 100\,\mathrm{K}$ the results of transport measurements and the LSMO layer's magnetisation are in good quantitative agreement. **b,c**: I/V characteristics and differential resistance traces recorded at different temperatures indicate a decrease of the tunneling contribution to the charge transfer with increasing temperature.

Both MR ratios, MR_{total} and MR_{rem} are plotted as normalised values in Fig. 3.10**a** and show a similar behaviour apart from deviations of $\lesssim 10\,\%$ at low and $\lesssim 5\,\%$ at elevated temperatures. They are continuously dropping when the temperature increases starting from the respective maximum value at $T = 4.2\,\mathrm{K}$, whereby the decrease is enhanced for $T \gtrsim 80\,\mathrm{K}$, until at $T = 200\,\mathrm{K}$, the highest temperature achievable in this setup without detrimental fluctuations, the MR signal is reduced to $\sim 10\,\%$ of its original value.

The observed decrease of the MR effect is comparable to the behaviour that is usually obtained in OSV structures [Xiong04, Wang07, Dediu09]. It has been shown by Dediu *et al.* [Dediu08] that there may be a correlation between the temperature dependence of the spin-valve signal in an OSV device comprising an LSMO electrode and the latter's surface magnetisation $M_{\mathrm{LSMO,SF}}$. In the proposed scenario, a change of $M_{\mathrm{LSMO,SF}}$ with increasing temperature is equivalent to a change of the injected charge carriers' spin polarisation and is consequently reflected in the amplitude of the observed spin-valve signal. Evidently, this only applies if the MR effect is dominated by charge and spin injection from the LSMO electrode, as it is also the case for an MR originating from tunneling processes.
$M_{\mathrm{LSMO,SF}}$ is often significantly different from the bulk magnetisation $M_{\mathrm{LSMO,B}}$ as can be seen from the respective data included in Fig. 3.10**a**. $M_{\mathrm{LSMO,SF}}$, for example, can be measured by spin-resolved photoemission spectroscopy (dashed green line, taken from [Park98b]) and

$M_{\mathrm{LSMO,B}}$ is measured by SQUID for an LSMO layer as it used for the fabrication of the devices under investigation (solid green line). A good quantitative agreement between $MR_{\mathrm{total/rem}}(T)$ and $M_{\mathrm{LSMO,SF/B}}(T)$ can be clearly identified for $T \lesssim 100\,\mathrm{K}$. At higher temperatures, however, the size of the MR effect is dropping faster than the LSMO layer's magnetisation which indicates that additional temperature-dependent mechanisms are very likely quenching the spin-valve signal.

Obvious mechanism causing such a behaviour are spin scattering and relaxation, i.e. the reduction of the charge carriers' spin polarisation and the spin lifetime inside the OSC layer, which may be enhanced at elevated temperatures. A theoretical, comparative description and summary of spin relaxation mechanisms in OSCs can be found in the work of Harmon and Flatté [Harmon2013].
Although any decisive role of spin relaxation has been excluded for a number of OSC materials employed in OSVs (not including PDI) on the basis of experimental results [Dediu09], it must not be neglected here completely. Moreover, a reduced spin lifetime at elevated temperatures may also influence a spin-valve signal originating from tunneling processes when charge transfer via mechanisms like multiple step tunneling instead of direct tunneling between the electrodes is taken into account (see chapter 2.2.1). In this case the transition time t_{trans} of the charge carriers is short but finite thus allowing for relaxation mechanisms to take effect. Unfortunately, such a scenario can hardly be decisively proved in magnetotransport experiments but requires further and more sophisticated measurement techniques.
A second possible contribution to the decrease of the spin-valve signal at $T > 100\,\mathrm{K}$, on the contrary, can be sustained by experimental data obtained by I/V characterisation. I/V curves recorded at various temperatures are shown in Fig. 3.10b. This data reveal that with increasing temperature the non-linearity of the I/V response, which can be interpreted as measure for the tunneling contribution to the total device resistance, is significantly diminished. In particular, this reduction becomes evident regarding the temperature dependence of the differential resistance which is displayed in Fig. 3.10c. Assuming that the spin-valve signal is caused by a tunneling effect, a reduced tunneling resistance is therefore reflected in the measured MR ratio as well.

Although spin scattering may additionally contribute to the decrease of the MR effect's amplitude at elevated temperatures, another support for the scenario of a spin-valve signal caused by charge and spin transfer via tunneling is found by the magnetotransport studies within the temperature range between $4.2\,\mathrm{K}$ and $200\,\mathrm{K}$.

3.2.5   Thickness Dependence of the Spin-Valve Effect

In this chapter results from experiments investigating the influence of the PDI layer's thickness d_{PDI} on the (magneto)transport behaviour are summarised. Based on these results more reliable information can be gained concerning the question to which extent the charge transport in devices exhibiting a spin-valve effect can be regarded as diffusive or not. In this context diffusive transport is equivalent to charge transfer through a thick OSC layer by mechanisms like VRH and MTR (see chapter 2.2.1) and constitutes the opposite to the,

so far favourable, scenario involving (direct and/or multiple step) tunneling between the two electrodes.

Fig. 3.11 comprises MR traces recorded for ten different devices with varying d_{PDI} taken under same conditions, e.g. with the same applied U_{bias}, when possible. d_{PDI} is increasing from the top to the bottom of Fig. 3.11 and, except of row 4, each row displays results of structures with a nominally identical d_{PDI}. It becomes already evident at first sight that there is no clear, if any, relation between the device resistance R and d_{PDI}. Whereas in the case of diffusive charge transport an exponential dependence of R on d_{PDI} should be present, the data in Fig. 3.11 exhibit a rather random distribution of R.
Moreover, a large variation of R can even be discerned for devices with the same d_{PDI} (e.g. in Figs. 3.11**c/d** and **e/f**). Such statistical variations, typically in the range of one order of magnitude, are observed even for structures on the same sample as illustrated in Fig. 3.12**a** which shows the resistance distribution of 20 devices on a sample with $d_{\mathrm{PDI}} = 150\,\mathrm{nm}$. Similarly, a definite relation between the MR effect's magnitude, measured by either MR_{total}, MR_{rem} or $MR_{\mathrm{rem}}/MR_{\mathrm{total}}$, and d_{PDI} cannot be discerned. This becomes obvious regarding the results in Figs. 3.11**d** and **h** which exhibit nearly the same effect ratio and same R but are obtained from structures which employ PDI layer thicknesses differing by a factor of > 2. These data could therefore suggest that the MR ratio is depending on R rather than on d_{PDI}. However, considering the entirety of all MR traces in Fig. 3.11 the correlation $MR(R)$ turns out to be as unclear as $MR(d_{\mathrm{PDI}})$.

In addition to the observations with respect to the MR ratio, a large variation concerning the shape of the spin-valve traces also becomes obvious from the results in Fig. 3.11. In some devices the signal is very pronounced and comprises distinct switching events, e.g. in Figs. 3.11**a**, **c** and **e**, whereas in other structures it is, in fact, resembling either a rotation of the electrodes' magnetisation or OMAR contributions caused by fringe fields as almost no sharp resistance steps are visible (Figs. 3.11**b**, **f** and **g**). Such dissimilarities even occur in devices with the same d_{PDI} (e.g. Figs. 3.11**a/b** and **e/f**). Similar results have been demonstrated by Vinzelberg *et al.* [Vinzelberg08] who found, amongst other things, large variations in the shape, size and sign of the spin-valve effect in a large number of AlQ$_3$-based OSVs with the same nominal OSC layer thickness.
Special attention should also be paid to the two MR curves for $d_{\mathrm{PDI}} = 600\,\mathrm{nm}$ in Figs. 3.11**i** and **j**. In contrast to the data in Fig. 3.11**i**, which are very similar to all other results, a very peculiar behaviour can be identified in Fig. 3.11**j**. This trace also comprises two components one of which is the well-known non-linear negative background signal. The other one is a spin-valve-like behaviour with a positive effect (switching from low resistance to high resistance and back). As will be discussed later (see chapter 3.4), the latter very likely has to be interpreted in terms of a significant TAMR contribution to the MR effect.

Despite the obvious lack of a clear correlation between d_{PDI} and the MR performance of the OSVs under discussion one general observation tantamount to a systematic behaviour has to be noted. For intermediate d_{PDI} ($100 - 250\,\mathrm{nm}$) most of the devices exhibit the typical MR effect consisting of a background and the actual spin-valve signal. However, when the
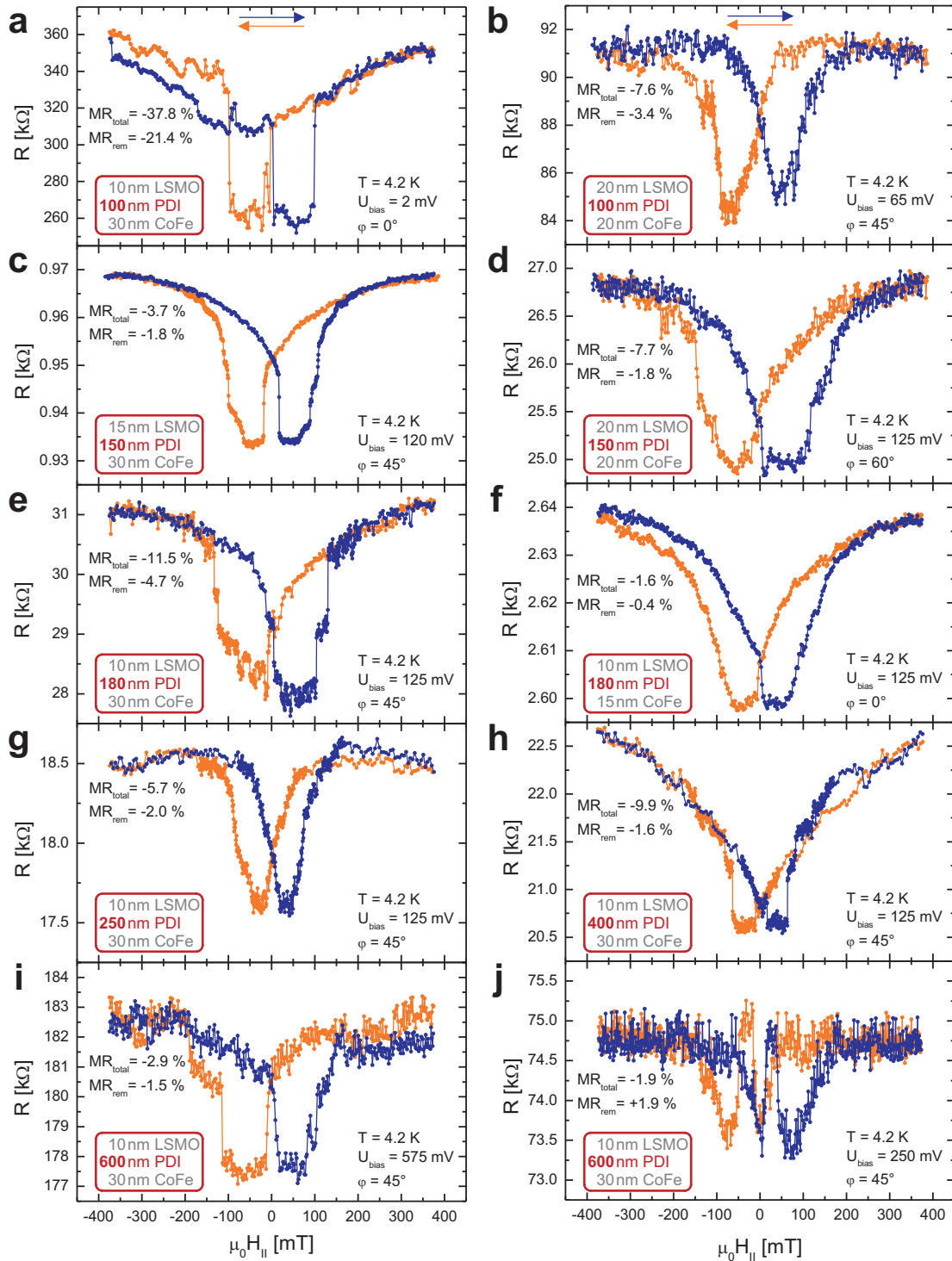
Figure 3.11: MR traces of ten different PDI-based OSV devices with varying PDI layer thickness ($d_{PDI} = 100 - 600\,\text{nm}$) illustrating the lack of any consistent correlation between d_{PDI} and several devices' and effects' features, such as the device resistance and the shape/size of the MR signal.

thickness of the PDI layer is increased beyond 250 nm equally the number of devices with a strong temperature dependence of R significantly increases (see also Figs. 3.5**c-e**), i.e. the yield of structures exhibiting any MR effect is reduced. In the $d_{\mathrm{PDI}} < 100$ nm regime, on the contrary, all devices are short-circuited and therefore no magnetotransport data are available.
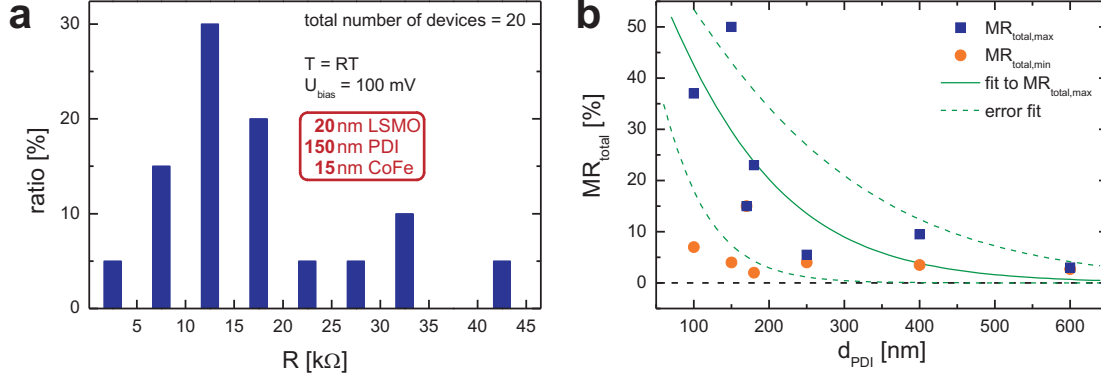
Figure 3.12: **a**: Resistance distribution for 20 devices on the same sample showing a variation of approximately one order of magnitude. **b**: Dependence of the MR ratio MR_{total} on the PDI layer thickness d_{PDI}. For each d_{PDI} the maximum and minimum (non-zero) observed MR_{total} is shown. The fit and its error bar (green lines) according to [Xiong04] shows that an evaluation of the displayed data based on the assumption of diffusive spin transport is possible, however, neither reliable nor meaningful.

A summary of the results obtained in all PDI-based OSVs can be found in Fig. 3.12**b** containing the minimum and maximum MR_{total} measured for each $d_{\mathrm{PDI}} \geq 100$ nm under investigation. The corresponding data for MR_{rem} look similar and, for the sake of clarity, are not displayed here. Especially for $d_{\mathrm{PDI}} \leq 200$ nm, there is a large deviation between $MR_{\mathrm{total,max}}$ and $MR_{\mathrm{total,min}}$. Nevertheless, a trend of diminishing MR amplitude with increasing d_{PDI} can be discerned in this representation, which can be considered a common observation in OSV devices [Xiong04, Shim08, Dediu08]. Although an interpretation of these findings in terms of diffusive charge and spin transport, e.g. in order to determine the spin diffusion length in PDI, is obvious and tempting, such an analysis should not be undertaken blindly for several reasons.

First, it would contradict the clear indications for the opposite scenario given by the extensive amount of results presented in the previous chapters, which is spin and charge transfer by tunneling at pinhole sites. Moreover, the tunneling scenario can likewise be complemented with a thickness dependence by taking into account that the pinhole statistics, i.e. the number and depth of single pinholes, may depend on the OSC layer thickness [Rabson01], effectively leading to results as they are observed here. Hence, the data in Fig. 3.12**b** can also be understood without the need of spin-polarised transport and therefore be integrated into the favourable model employing an MR effect originating from tunneling.
Second, despite the apparently clear trend exhibited by the data in Fig. 3.12**b** they are only insufficiently suited for an evaluation with respect to diffusive spin transport. This is illustrated by an exemplary fit using the equation proposed by Xiong *et al.* in [Xiong04], which

is based on the Jullière model [Jullière75] and can be used to determine the spin-diffusion length l_{sf} in PDI:

$$MR(d_{PDI}) = \frac{2P_1 P_2 e^{-(d_{PDI}-d_{red})/l_{sf}}}{1 + P_1 P_2 e^{-(d_{PDI}-d_{red})/l_{sf}}} \qquad (3.3)$$

In Equ. 3.3 d_{red} denotes the reduction of the nominal OSC layer thickness due to the ill-defined interface between the OSC layer and the top electrode, and P_1 and P_2 are the electrodes' spin polarisations ($P_1 = 100\%$ for LSMO and $P_2 = 32\%$ for CoFe). The solid green line in Fig. 3.12**b** shows the result of this fitting procedure applied to $MR_{total,max}$ which, in principle, is obviously feasible. Nevertheless, the significantly large error bar, which is represented by the dashed green lines, suggests that any further interpretation of this evaluation will not yield reliable information. Thus, it is clear, even without elaborating on the exact figures for l_{sf} or d_{red}, that these results rather should be interpreted as indication for an injection and hereby tunneling dominated MR effect as also proposed by Dediu *et al.* [Dediu09].

3.2.6   Summary

The magnetoresistive behaviour in the PDI-based OSVs with two ferromagnetic electrodes is extensively studied with respect to a broad set of parameters. As a core conclusion of these studies it can be stated that nearly all results strongly indicate that the spin-valve functionality is stemming from tunneling-based effects. This applies to the class of devices for which a weak temperature dependence of R is observed. For the second class, structures that do not show any MR effect, R is increasing by several orders of magnitude at low temperatures which can be traced back to a diffusive charge transport mechanism (bulk limited charge transfer).

Although the indications given for the above mentioned scenario are strong and likewise consistent, they must not be regarded as robust experimental evidence. However, this evidence can be provided by Hanle measurements as the corresponding results presented in the next chapter reveal.

3.3 Measurements in Perpendicular Magnetic Fields - The Hanle Effect

In chapter 2.1.4 it has been outlined that the presence of spin injection, subsequent diffusive spin transport and electrical spin detection can unambiguously be identified by the investigation of spin precession in perpendicular magnetic fields. Evidently and with the same impact, such experiments can also prove the absence of one of these mechanisms. Up to now, spin precession and the so-called Hanle effect, respectively, have mainly been studied in the field of inorganic spintronics (lateral spin-valve devices) [Lou07, Huang07, Tombros07]. The feasibility and meaningfulness of this measurement technique in vertical OSVs are discussed in chapter 3.3.1 before the corresponding results are presented in chapter 3.3.2. An interpretation of the results can be found in chapter 3.3.3.

3.3.1 Hanle Effect in Vertical Organic Structures

Although a rather extensive amount of results has already been presented in chapters 3.2.1-3.2.5, it is not possible yet to draw an unambiguous conclusion concerning the origin of the MR observed in vertical PDI-based OSVs. Therefore, experiments in the perpendicular geometry are employed to get more and a reliable insight into the mechanisms behind the spin-valve effect [Grünewald13b]. As outlined in chapter 2.1.4, the application of a perpendicular magnetic field $H_\perp$ leads to a precession of the charge carriers' spins in the non-magnetic spacer layer of a spin-valve device, which is reflected in the respective magnetoresistance trace $R(H_\perp)$ as either so-called Hanle oscillations or as quench of the spin-valve signal depending on the charge transport's coherency in the material under investigation (see Fig. 2.6 in chapter 2.1.4). The term quench describes the reduction (increase) of R_P (R_AP) in a negative spin-valve signal towards an intermediate resistance due to spin dephasing.

In the case of experiments in the perpendicular geometry performed in an OSV where actually spin precession is occurring in the OSC spacer layer, one can expect to observe a quench of the spin-valve signal only, whilst the occurrence of Hanle oscillations is rather unlikely. This assumption is based on two factors. First, the incoherent charge transport mechanisms usually prevailing in OSCs (chapter 2.2.1) should result in spin dephasing due to the spin precession. Moreover, the probability of observing spin dephasing in OSVs is enhanced by the fact that in these devices the transition time t_trans (the time a charge carrier - electron hereafter - or spin, respectively, needs to travel through the OSC layer) is very long compared to the typical spin precession time t_prec. This can be ascribed to the typically rather low mobilities in OSCs as can be shown by the following back-of-the-envelope calculation.

t_prec can be calculated from Equ. 2.6. The electron spin g-factor in an OSC material can be assumed to be nearly identical to that of a free electron ($g \approx 2.0023$) as proved for a number of OSCs, e.g. by means of pulsed electrically detected magnetic resonance [Boehme09]. This technique furthermore has also been applied to obtain a direct proof for the conduction electrons' spin precession in OSCs in perpendicular magnetic fields [Lupton10, Baker12], demonstrating that this basic phenomenon behind the Hanle effect is present in OSC mate-

rials as well. Using $g = 2$ for transposing Equ. 2.6 yields:

$$t_{\text{prec}} = \frac{2\pi m_{\text{e}}}{e\mu_0 H_\perp} \tag{3.4}$$

From this $t_{\text{prec},10\,\text{mT}} \approx 3.6\,\text{ns}$ is obtained for a rather small perpendicular field of $\mu_0 H_\perp = 10\,\text{mT}$.

The transition time t_{trans} can be estimated as follows:

$$t_{\text{trans}} = \frac{d_{\text{PDI}}}{v} = \frac{d_{\text{PDI}}}{\mu_{\text{PDI}}\,|\boldsymbol{\mathcal{E}}|} = \frac{d_{\text{PDI}}^2}{\mu_{\text{PDI}}U_{bias}} \tag{3.5}$$

v is the velocity of the electrons/spins, $|\boldsymbol{\mathcal{E}}| = U_{\text{bias}}/d_{\text{PDI}}$ the electric field strength and μ_{PDI} the electron mobility in PDI. Typical parameters for an OSV experiment are $d_{\text{PDI}} = 150\,\text{nm}$ and $U_{bias} = 100\,\text{mV}$. The maximum electron mobility reported for PDI is $\mu_{\text{PDI,max}} = 0.6\,\text{cm}^2/\text{Vs}$ [Oh07]. Evaluating Equ. 3.5 with these values $t_{\text{trans}} = 3.8\,\text{ns} \approx t_{\text{prec},10\,\text{mT}}$ is obtained. Already considering this ideal limiting case, which represents the minimum theoretical t_{trans}, it becomes obvious that relatively weak perpendicular fields in the range of $\mu_0 H_\perp \approx 10\,\text{mT}$ should be sufficiently strong to cause a measurable spin precession in the devices under discussion.

A more realistic estimation can be made when taking into account that the present vertical OSV structures are significantly different from the OFETs that have been investigated by Oh *et al.* in order to obtain $\mu_{\text{PDI}} = 0.6\,\text{cm}^2/\text{Vs}$, which is a value for the field-effect mobility [Oh07]. In vertical transport structures, on the contrary, typically the so-called drift mobility that can be determined by techniques like, for instance, TOF measurements is dominating the charge transport. Considering real devices, there can be large discrepancies between these two measures for the same material.

For PDI unfortunately no values for the drift mobility are available, neither from own experiments nor from the literature. Therefore, the electron drift mobilities $\mu_{\text{PTCDI-C7}} \approx 1 \cdot 10^{-2}\,\text{cm}^2/\text{Vs}$ [Kim04] and $\mu_{\text{PTCDI-C4Ph}} \approx 1 \cdot 10^{-4}\,\text{cm}^2/\text{Vs}$ [Kim05], which are obtained by TOF for two similar materials from the perylene diimide family, are used for a presumably more realistic estimate of $\mu_{\text{PDI}} = 1 \cdot 10^{-3}\,\text{cm}^2/\text{Vs}$. It should be emphasised here that, compared to μ in other OSCs frequently investigated in the field of organic spintronics (e.g. $\mu_{\text{AlQ}_3} \approx 1 \cdot 10^{-6}\,\text{cm}^2/\text{Vs}$ [Kepler95]), this is still a rather large value. With this value of μ_{PDI} Equ. 3.5 yields $t_{\text{trans}} = 2.25\,\mu s \approx 600 \cdot t_{\text{prec},10\,\text{mT}}$ explicitly sustaining the assumption that only spin dephasing is to be expected as result of experiments in the perpendicular geometry in the devices under discussion.

Eventually, this juxtaposition of transition and precession time shows that already a small perpendicular field of $\mu_0 H_\perp \approx 10\,\text{mT}$ should induce a spin precession that is fast enough to cause sizeable modifications of the spin-valve signal.

Thus, from these fundamental considerations it becomes clear that the investigation of spin precession is likewise sensible in the present vertical OSVs. Nevertheless, there are further potential obstacles to the successful realisation of these experiments which should be discussed now. First, the applied perpendicular field may be overcome by intrinsic magnetic fields such as the hyperfine field B_{hf}. However, it has been demonstrated by several theoretical and corresponding experimental studies (e.g. [Bobbert07] and [Schoonus09]) undertaken for various OSC materials that these intrinsic fields are typically smaller than a few mT. Consequently, they are easily surpassed by a perpendicular magnetic field in the range discussed above ($\mu_0 H_\perp \approx 10\,\text{mT}$).

Another obstacle may be stemming from the vertical layer arrangement in the devices under investigation. In this configuration the applied perpendicular field $\boldsymbol{H}_\perp$ might be shielded by the ferromagnetic electrodes leading to a suppression of the spin precession. However, a shielding of $\boldsymbol{H}_\perp$ can be excluded as long as the electrodes' in-plane magnetisation $\boldsymbol{M}_{electrode}$ determining the OSV's spin-valve state is not forced out of the sample plane.
The $H_\perp$ at which such a rotation of $\boldsymbol{M}_{electrode}$ sets in is determined by the respective electrode's shape anisotropy, which in turn is correlated to the material's saturation magnetisation M_{sat} in the case of thin ferromagnetic layers. The M_{sat} that can be found in the literature for the materials employed in the present devices ($M_{sat,LSMO} = 600\,\text{emu/cm}^3$ [Ziese10] and $M_{sat,CoFe} = 1500\,\text{emu/cm}^3$ [Burkert04]) suggest that a perpendicular magnetic field $\mu_0 H_\perp$ of several $100\,\text{mT}$ must be applied in order to destroy the in-plane magnetisation configuration. As the above estimate reveals, a sizeable spin dephasing effect should already be measurable at perpendicular magnetic fields well below $\mu_0 H_\perp \approx 100\,\text{mT}$. Thus both a shielding of $\boldsymbol{H}_\perp$ by the electrodes as well as a destruction of the in-plane magnetisation state by the application of $\boldsymbol{H}_\perp$ can be discarded as an obstacle to the investigation of spin precession. It is worth mentioning that, if the latter should occur anyway, this could be easily identified as sharp steps in the MR traces as, for instance, reported by Riminucci *et al.* [Riminucci13].

Finally, another issue with respect to the Hanle effect in vertical OSV devices recently has been brought up by Yu [Yu13]. In this theoretical work, which is sustained by experimental data of Riminucci *et al.* [Riminucci13] who did not find any evidence for spin precession in AlQ$_3$-based OSVs, it is discussed why the Hanle effect in OSV devices may only appear under very specific circumstances. The reasoning can be summarised as that, generally speaking, the spin precession in these devices is suppressed to such an extent that the Hanle effect can only be observed at unusually strong $H_\perp$ and unusually low bias voltages.
As stated by Yu, the origin of this suppression is a decoupling of charge carrier motion and spin transport. Whereas the former is occurring via conventional slow mechanisms (similar to VRH), the spin information can be independently transferred through an OSC layer by a rather strong exchange interaction originating from the single charge carriers' wave functions' overlap. In consequence, significantly stronger $H_\perp$ are necessary to cause a spin precession fast enough to be detected in the experiments with perpendicular fields. However, it can be shown by the estimate employed by Yu that the proposed exchange mechanisms can be neglected in the present devices.

Yu uses a diffusion equation to describe the spin-polarisation dynamics inside the OSC layer where, in the first instance, both mechanisms are included by the diffusion constants D_h (simultaneous spin and charge transport via hopping/VRH) and D_e (independent spin transport via the exchange mechanism). Obviously the wave functions' overlap and hereby the effectiveness of the exchange mechanism, indicated by the ratio D_e/D_h, strongly depends on the charge carriers' density n inside the OSC layer. Therefore, a first estimate of D_e/D_h can be done on the basis of n which can be roughly determined from the charge carrier mobility μ_{OSC}, the device dimensions (area A and OSC layer thickness d_{OSC}), and resistance R [Yu13]:

$$n = \frac{d_{OSC}}{e\mu_{OSC}RA} \tag{3.6}$$

Below a critical $n_{limit} \approx 10^{17} \text{cm}^{-3}$, according to the data presented in [Yu13], $D_e/D_h \approx 0$, i.e. spin and charge transport are not decoupled and consequently spin precession should occur when a perpendicular magnetic field is applied.
Using the aforementioned material parameters for PDI and typical values for the devices under investigation ($R = 100\,k\Omega$ and $A = 150 \times 500\,\mu m^2$), $n_{PDI} \approx 10^{15}\,\text{cm}^{-3}$ is obtained from Equ. 3.6.
Further comparisons between theory and experiment which are provided by Yu for AlQ$_3$-based OSVs cannot be undertaken here as for PDI most of the material parameters that are necessary for the calculations performed by Yu are not available in the literature. Nevertheless, $n_{PDI} \ll n_{limit}$ strongly suggests that the proposed exchange mechanism and a potential decoupling of charge and spin transfer very likely only plays a minor, if any, role in the PDI-based OSVs.

On the basis of the theoretical considerations and estimates outlined above any potential obstacle to the viability of the experiments in the perpendicular geometry can be excluded. Hence, they can be considered to be a powerful tool for the investigation of spin-valve signals in vertical OSVs. These experiments yield clear and robust experimental evidence concerning the nature of the spin-valve signal in the PDI-based OSVs, which is summarised in the upcoming chapter.

3.3.2   Results

The results presented in this chapter are obtained for a device with $d_{PDI} = 150\,\text{nm}$. The MR traces for $U_{bias} = 50\,\text{mV}$ and $\varphi = 0°$ are shown in Fig. 3.13c, again consisting of a non-linear background effect, which is rather small in the device under investigation, and the actual spin-valve signal. The MR amplitude is $MR_{total} \approx MR_{rem} \approx -6.0\%$. Although the device resistance can be considered rather high compared to this of the majority of working PDI-based OSVs, the basic features of the charge transfer determined by I/V characterisation, e.g. the I/V traces non-linearity as well as the weak temperature dependence of R, are identical (see Figs. 3.13a and b).
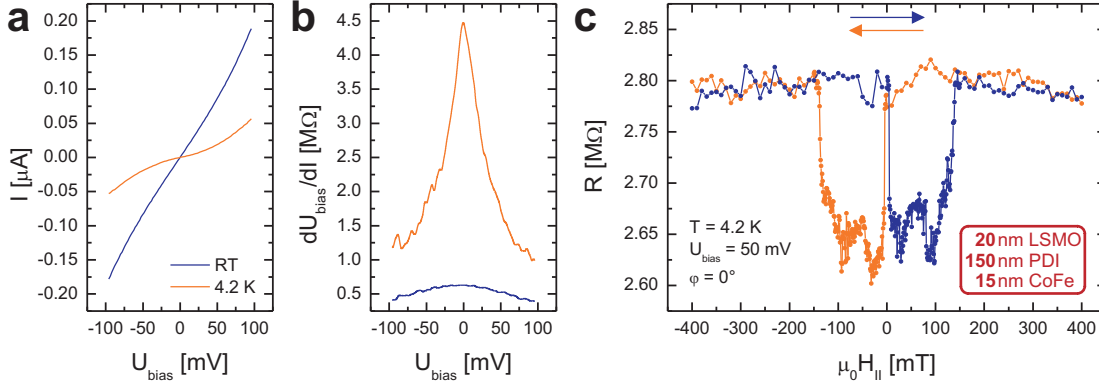
Figure 3.13: Basic transport properties of a PDI-based OSV studied in perpendicular magnetic fields. **a, b**: Non-linear I/V curves and corresponding differential resistance traces reveal typical features concerning the charge transfer mechanism. **c**: MR trace exhibiting a similar behaviour as it is obtained for nearly all PDI-based structures, whereas the background signal at elevated $H_{||}$ is less pronounced for this device. The data are recorded previously to the experiments in the perpendicular geometry.

As already explained in chapter 2.1.4, preceding to the experiments in the perpendicular geometry a remanent spin-valve state, either the parallel or the anti-parallel, has to be prepared by sweeping the in-plane magnetic field $\boldsymbol{H}_{||}$ in a suitable manner. Fig. 3.14a comprises the respective measurement for the preparation of the remanent anti-parallel state, a so-called minor-loop sweep. Starting at negative saturation $H_{||}$ is decreased towards small positive fields (passing $R_{\text{zero-field}} = 2.83\,\text{M}\Omega$ at $\mu_0 H_{||} = 0\,\text{mT}$) until the full reversal of the LSMO electrode's magnetisation is reached indicated by the minimum device resistance $R_{\text{AP}} = 2.68\,\text{M}\Omega$ (blue curve in Fig. 3.14a). Subsequently, $H_{||}$ is set to zero (orange curve in Fig. 3.14a). The blow up in Fig. 3.14a, which contains the corresponding area of interest, clarifies that after turning off any magnetic field the device is still in the R_{AP} state. Thus, the electrodes remain in the anti-parallel configuration, i.e. this magnetisation state actually is remanent. The respective MR ratio for this minor-loop measurement is $MR_{\text{rem}} = -5.7\,\%$.

Having prepared the anti-parallel state, the magnetic field is applied perpendicular to the sample plane. Fig. 3.14b displays the results of five measurements in the perpendicular geometry. In order to enhance the comparability of the data, the y-axes in Fig. 3.14 are scaled identically for all panels. Similarly as for the previous characterisation of the spin-valve signal, magnetotransport measurements with $\boldsymbol{H}_\perp$ sweeps from negative to positive maximum field amplitudes and vice versa are performed.
The displayed data are obtained in a series of experiments, in which the maximum applied perpendicular magnetic field progressively is increased from $\mu_0 H_{\perp,\text{max}} = \pm 2.5\,\text{mT}$ to $\mu_0 H_{\perp,\text{max}} = \pm 20\,\text{mT}$ and therefore the spin's minimum precession time, calculated using Equ. 3.4, is reduced from $t_{\text{prec,min}} = 14.3\,\text{ns}$ to $t_{\text{prec,min}} = 1.8\,\text{ns}$. Although apparently R is varying from measurement to measurement between $\sim 2.66\,\text{M}\Omega$ and $\sim 2.72\,\text{M}\Omega$ it can be considered constant for any single measurement apart from fluctuations in the range of maximum $\pm 25\,\text{k}\Omega \approx \pm 1\,\%$ and drifts. Thus, the spin-valve signal is obviously not influenced by the application of $\boldsymbol{H}_\perp$ and consequently these results do not contain any positive evidence

for spin precession.
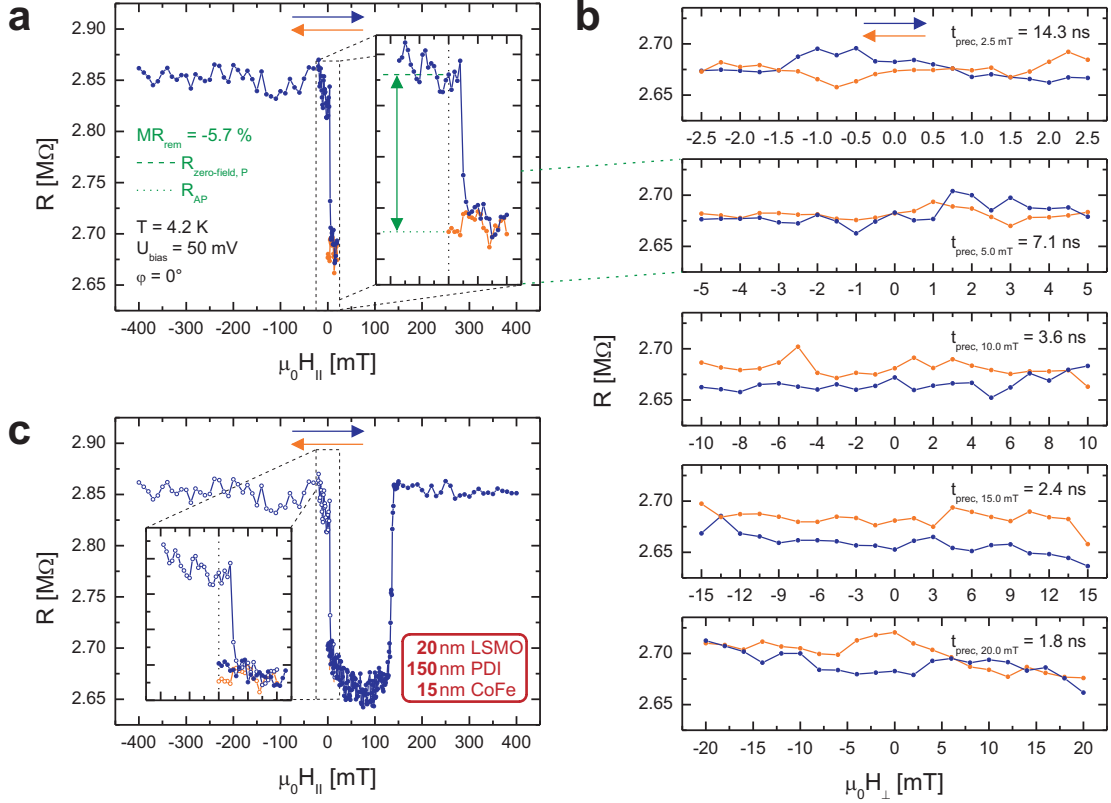
Figure 3.14: Complete sequence of measurements in the perpendicular geometry for the anti-parallel spin-valve state. **a**: The remanent spin-valve state is prepared by running a minor-loop sweep of $H_{||}$. **b**: No modification of the spin-valve signal is observed during a series of measurements in the perpendicular geometry. **c**: The initial minor loop is finally completed, yielding a good reproduction of the previously recorded MR trace.

The final measurement of any characterisation in perpendicular magnetic fields is an in-plane MR measurement completing the field sweep used for the preparation of the spin-valve state under investigation. In the present experiment this is equivalent to sweeping $H_{||}$ from zero field to positive saturation.

The respective result is shown in Fig. 3.14**c** (line with filled symbols) together with those of the minor-loop trace of Fig. 3.14**a** (lines with open symbols). The latter is obviously resumed nearly perfectly by the new data. The final MR signal in Fig. 3.14**c** is a good reproduction of the one recorded prior to the investigations in the perpendicular geometry (Fig. 3.13**c**). The concluding MR measurement is done in order to verify that the electrodes' magnetisation has not been (permanently) disturbed by the application of $H_\perp$. In consequence, its result strengthens the interpretation that the observed variations of R within a single measurement have a statistical origin and are not caused by any change of the spin-valve state. This observation additionally allows to exclude any other conceivable scenario where the Hanle effect is suppressed by artifacts or unforeseeable effects involving a modification of the electrodes'

magnetisation.

Similarly to the anti-parallel, the parallel spin-valve state is also investigated with respect to the presence of spin precession. For the preparation of the parallel remanent state $\boldsymbol{H}_\parallel$ is swept from negative saturation to zero field yielding a device resistance of $R_{\text{zero-field}} = 2.84\,\text{M}\Omega$ (Fig. 3.15a).
Fig. 3.15b again shows the results of a series of measurements in the perpendicular geometry conducted with the same parameters as for the anti-parallel spin-valve configuration (decrease of $t_{\text{prec,min}}$ from 14.3 ns to 1.8 ns). Again, only variations of R similar to those observed in the experiments for the anti-parallel state can be identified, whilst obviously no actual modification of the spin-valve signal resembling spin dephasing is present.
Also this characterisation sequence is finished by completing the preparation sweep (Fig. 3.15c). The corresponding result nicely reproduces the previously recorded MR trace suggesting the same conclusions as in the case of the anti-parallel configuration.
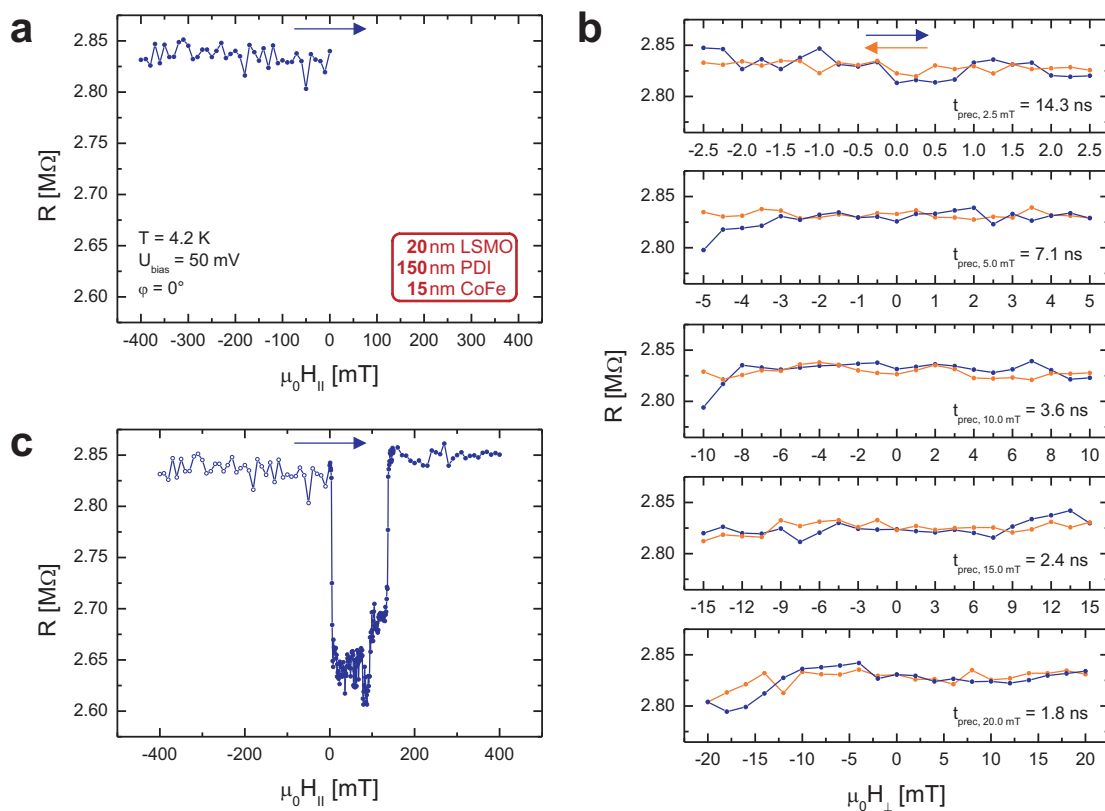
Figure 3.15: Complete sequence of measurements in the perpendicular geometry for the parallel spin-valve state.**a**: Preparation sweep from negative saturation to zero field. **b**: Measurements in the perpendicular geometry do not show any modification of the spin-valve signal. **c**: The experiment is finished completing the initial sweep from zero field to positive saturation reproducing the MR trace recorded prior to the experiments in the perpendicular geometry.

Hence, in this device likewise as in other PDI-based OSVs (see [Grünewald13b]) no in-

dication for the presence of spin precession and electrical spin detection is found for both remanent spin-valve states. In this context, it should be mentioned that identical investigations have also been undertaken for AlQ$_3$-based OSVs exhibiting comparable characteristics with respect to spin-valve functionality, magnitude of the MR effect and temperature dependence of R [Grünewald13b]. Neither do the results of measurements in the perpendicular geometry obtained for these structures show any indication of spin precession and the Hanle effect. In the following chapter this key finding is discussed based on a summary of all possible explanations for the absence of the Hanle effect. This discussion includes general aspects as well as particular ones that specifically apply for the present PDI-based vertical devices.

3.3.3   Discussion and Summary

The observation of a mostly negative spin-valve signal in OSV devices already suggests that a straightforward interpretation of the MR effect according to the fundamentals presented in chapter 2.1 may probably not be reasonable. Thus, it is also not very likely to observe a textbook-like behaviour comparable to the traces in Fig. 2.6, which are exhibiting an equally strong modification of the spin-valve signal for the parallel and anti-parallel magnetisation state, during measurements in the perpendicular geometry. Nevertheless, irrespectively of these considerations, if spin injection, diffusive spin transport and electrical spin detection, i.e. GMR, is causing the observed spin-valve signal, the application of a perpendicular magnetic field must lead to any modification of the spin-valve signal due to the spin dephasing. As already stated in the introduction to this section (chapter 3.3.1), the approach to explain the absence of spin precession with a strong spin exchange mechanism [Yu13] seems to be negligible for the interpretation of the present results. There are, however, two further hypothetical scenarios that explain the absence of the Hanle effect in devices in which the observed MR effect can be attributed to GMR.

   The first of these scenarios is that $\boldsymbol{H}_\perp$ cannot influence the spin-valve signal because spin precession does not occur despite diffusive spin transport. However, this was equivalent to $t_{prec} \to \infty$ and therefore to $g \to 0$ which has already been excluded in chapter 3.3.1 on the basis of experimental evidence.

Furthermore, as discussed above, spin dephasing may not be observed when $t_{\text{trans}} < t_{\text{prec}}$, which is the second possible scenario. The minimum t_{prec} in the present experiments is $t_{\text{prec,min}} = 1.8\,\text{ns}$ and is determined by the maximum applied $H_\perp$ only. A transition time as low as this can be explained by either an enhanced μ_{PDI} or a decreased d_{PDI}.

Using the actual parameters of the experiment ($t_{\text{trans}} = t_{\text{prec,min}} = 1.8\,\text{ns}$, $d_{\text{PDI}} = 150\,\text{nm}$ and $U_{\text{bias}} = 100\,\text{mV}$) Equ. 3.5 yields a hypothetical mobility of $\mu_{\text{PDI, hypo}} = 1.25\,\text{cm}^2/\text{Vs}$. This is approximately more than two times $\mu_{\text{PDI,max}} = 0.6\,\text{cm}^2/\text{Vs}$. $\mu_{\text{PDI,max}}$ itself, however, represents a presumably unrealistic limiting case considering the charge transport in vertical devices. Consequently, $\mu_{\text{PDI, hypo}}$ should rather be compared to the more realistic value of $\mu_{\text{PDI}} = 1 \cdot 10^{-3}\,\text{cm}^2/\text{Vs}$ from which it differs by approximately four orders of magnitude. Therefore, it is reasonable to disregard this attempt of an explanation.

A reduced d_{PDI}, on the contrary, seems more likely regarding the results presented in chapter 3.2. Evaluating Equ. 3.5 with a constant mobility (and $t_{\text{trans}} = t_{\text{prec,min}} = 1.8\,\text{ns}$, $U_{\text{bias}} = $

$100\,\mathrm{mV}$) $d_{\mathrm{PDI,red}} \approx 4.2\,\mathrm{nm}$ is obtained for $\mu_{\mathrm{PDI}} = 1 \cdot 10^{-3}\,\mathrm{cm^2/Vs}$ and $d_{\mathrm{PDI,red}} \approx 100\,\mathrm{nm}$ for $\mu_{\mathrm{PDI,max}} = 0.6\,\mathrm{cm^2/Vs}$. Although apparently these values represent a substantial deviation from the nominal $d_{\mathrm{PDI}} = 150\,\mathrm{nm}$, it is, in fact, well known that the effective thickness of an OSC layer can be significantly lower than the nominal. Xiong *et al.* [Xiong04] report a deviation of $\sim 90\,\mathrm{nm}$, other studies comprise similar results [Xu07, Vinzelberg08]. Furthermore, it is worth noting that a reduced effective layer thickness can also be interpreted in terms of a finite density of pinholes instead of a precise and rigid figure for $d_{\mathrm{PDI,red}}$ as already insinuated in chapter 3.2.5 [Rabson01]).

It should also be emphasised that experiments comparable to those presented above can be considered unique in the field of organic spintronics.
Riminucci *et al.* likewise report the absence of the Hanle effect in AlQ$_3$-based OSVs, however, use a different measurement technique [Riminucci13]. Regarding their data, apparently only magnetic field sweeps in one distinct direction with respect to the sample plane can be performed. The desired sequence of the initial preparation of a remanent in-plane spin-valve state and the subsequent application of the perpendicular magnetic field at zero in-plane field thus cannot be realised. Consequently, and strictly speaking, the investigation of the original Hanle effect is not possible and moreover the results' interpretation is complicated significantly.
More recently, Watanabe *et al.* [Watanabe14] have demonstrated that Hanle precession can actually occur in an OSC layer that is part of a vertical structure. In their work, the inverse spin Hall effect in the device's non-magnetic bottom electrode is employed to detect a pure spin current which is injected from the ferromagnetic top electrode into the OSC film by spin pumping. The inverse spin Hall effect's dependence on the angle between the applied magnetic field and the sample surface can be considered to be a strong proof of spin precession in the OSC layer. Nevertheless, it should also be stressed that this experiment, similarly as others already mentioned in chapter 2.1.4 [Drew09, Cinchetti09, Nguyen10, Nguyen12], does not derive the electrical signal from spin accumulation at a ferromagnetic contact. As a result, it cannot provide any decisive information about the potential electrical spin detection in an actual OSV device comprising two ferromagnetic electrodes.

In summary, the experiments in the perpendicular geometry give an irrefutable proof that the MR in the devices under investigation is not originating from GMR, i.e. from spin injection, subsequent diffusive spin transport and electrical spin detection. Together with the results presented in chapters 3.2.1-3.2.5 these findings can be consequently regarded as robust evidence that the observed spin-valve signal is actually caused by a tunneling-based MR effect.

3.4   Tunneling Anisotropic Magnetoresistance

Most of the findings presented in the previous chapters, especially the exclusion of GMR as underlying effect based on the results of Hanle measurements, reveal that the observed spin-valve signal in the PDI-based OSVs must be originating from a tunneling effect.

However, considering the charge transport and injection mechanisms discussed in chapter 2.2.1 and the fact that the devices very likely suffer from an ill-defined interface between the OSC layer and the top electrode, another issue remains open. It is not clear whether tunneling injection from the electrodes into the PDI or direct tunneling from one electrode to the other at pinhole-sites is causing the spin-valve effect. In this context, the investigation of TAMR (chapter 2.1.3) in OSV-like structures comprising an LSMO bottom contact, the OSC AlQ$_3$ or PDI, and a non-magnetic counterelectrode, can provide further information whether and to which extent the injection process is influencing the devices' MR behaviour. The use of AlQ$_3$ (chapter 3.4.1, [Grünewald14]) is motivated by the fact that, despite this material is apparently most widely investigated in the field of organic spintronics, dedicated TAMR devices have not yet been subject of any published study so far. Consequently, TAMR itself is very rarely addressed when results of conventional OSVs are interpreted. PDI-based structures (chapter 3.4.2, [Grünewald11]) are studied in order to obtain the aforementioned additional information concerning the different tunneling contributions to the observed MR, eventually allowing for a complete understanding of the spin-valve effect.

3.4.1   AlQ$_3$-based Devices

As stated in chapter 2.1.3, TAMR can mimic spin-valve functionality in devices in which tunneling processes are governing the charge transfer/injection and which comprise an electrode with a biaxial magnetocrystalline anisotropy, e.g. LSMO grown on STO(001) [Steenbeck99]. Additionally, the occurrence of this behaviour requires a symmetry breaking between the two magnetic easy axes, eventually resulting in an anisotropic DOS, which then can be reflected in the tunneling resistance. In the case of the present LSMO films this symmetry breaking very likely is originating from the layers' morphology as equally outlined in chapter 2.1.3.

Similarly to other magnetotransport studies, most of TAMR characterisation is performed at $T = 4.2\,\mathrm{K}$ as well. Figs. 3.16**a** and **b** contain the results of the standard preliminary characterisation at room temperature and $4.2\,\mathrm{K}$ for a device with an AlQ$_3$-layer thickness of $d_{\mathrm{AlQ}} = 100\,\mathrm{nm}$ and a Cu counterelectrode. This representative device, from which most of the results presented in the following are acquired, is labeled 'AlQ$_3$ TAMR'. As the I/V and differential resistance traces clearly show, the device resistance R has a weak temperature dependence and even is reduced by a factor of $2-3$ within the U_{bias} range under investigation when the sample is cooled. Furthermore, the non-linearity of the I/V response is significantly enhanced at low temperatures, which again is indicative of a large tunneling contribution to R.

The MR trace shown in Fig. 3.16**c** is resembling a negative spin-valve effect with two distinct resistance states named R_{L} and R_{H} hereafter. However, when compared to the behaviour of conventional PDI-based devices this single trace exhibits a striking difference
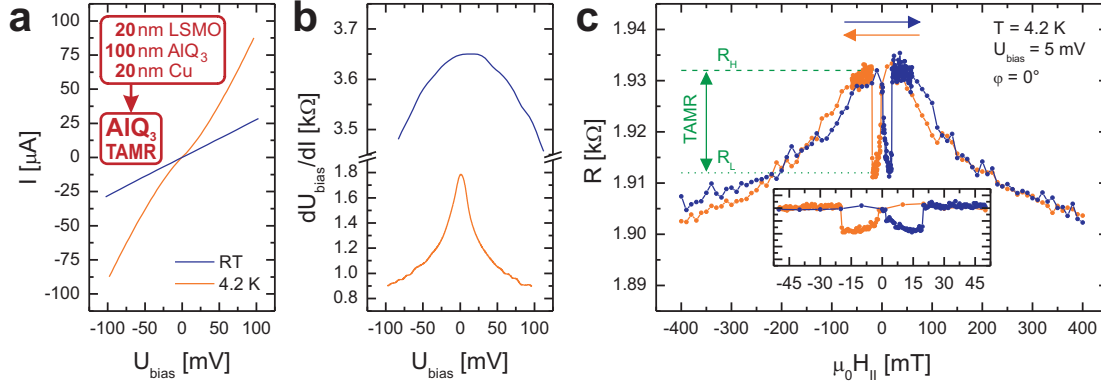
Figure 3.16: Basic transport properties of an AlQ_3-based TAMR device at room temperature and 4.2 K. **a,b**: I/V characterisation reveals a weak temperature dependence of the device resistance. An increase of the I/V curve's non-linearity at low temperatures can be identified regarding the differential resistance traces in **b**. **c**: In magnetotransport measurements a distinct spin-valve-like signal caused by TAMR and two-step magnetisation reversal is observed.

concerning the switching back from R_L to R_H. Whereas for the conventional PDI-based OSVs this switching usually is occurring via multiple steps at in-plane magnetic fields in the range of $\mu_0 H_{||} \approx 100 - 150$ mT, here a sharp switching at relatively low fields of $\mu_0 H_{||} \approx 20$ mT can be identified. Considering that in TAMR devices the second switching is caused by a change of the crystalline LSMO electrode's magnetisation as well and not from a magnetisation reversal of a rather rough ferromagnetic electrode on top of an OSC layer, this difference can be readily understood.

A common feature of the MR traces of TAMR and OSV structures is the non-linear background. In the former this signal, a decrease in resistance with increasing $H_{||}$, can very likely be ascribed to either to the Stoner-Wohlfarth rotation of the LSMO electrode's magnetisation towards (away from) the easy axes with decreasing (increasing) $H_{||}$ [Stoner48] or an intrinsic effect like HFMR or CMR (see chapter 2.4.4).

As mentioned before, such a spin-valve-like behaviour in devices with only one ferromagnetic electrode can be explained by the presence of TAMR and a two-step magnetisation reversal in the electrode from which TAMR is originating. The tunneling processes involved either may be injection processes from the LSMO into the OSC layer [Parker94, Baldo01] or occur as direct tunneling between the LSMO and the Cu counterelectrode at pinhole-sites. Regarding the physics behind the phenomenon of two-step magnetisation reversal, it becomes clear that TAMR can be identified in a very straightforward manner by the investigation of the MR signal's dependence on the orientation of $\boldsymbol{H}_{||}$ (described by the in-plane angle φ, see chapter 2.1.3). The typical φ dependence of TAMR comprises several characteristics, of which the most striking are, on one side, the effect's sign change and, on the other side, the quench of the signal when $\boldsymbol{H}_{||}$ is swept along one of the electrode's easy axes. These features are also observed in the present structure as can be seen in Fig. 3.17 which contains results of measurements recorded for three different φ. For $\varphi = 15°$ the spin-valve-like signal is positive, i.e. the resistance switches from R_L to R_H and back, whilst a virtually constant

resistance, except of the background signal, is obtained when the magnetic field is applied in the 90° direction. When φ is further increased, a negative effect similar to the one shown in Fig. 3.16c is obtained.

Especially from the blowup for $\mu_0 H_{||} = \pm 25\,\text{mT}$ in Fig. 3.17b two further characteristics of TAMR become obvious. First, the loci of the switching events are changing with φ. The second switching event, for instance, is observed at $\mu_0 H_{||} = 17.0\,\text{mT}$ for $\varphi = 15°$ and is shifted to $\mu_0 H_{||} = 5.5\,\text{mT}$ when $\boldsymbol{H}_{||}$ is applied in the 150° direction. Second, the distinct resistance states between which the switching occurs do not depend on φ. In the present measurements these states are $R_L \approx 1915\,\Omega$ and $R_H \approx 1930\,\Omega$ yielding a TAMR ratio (Equ. 2.5) of $\sim 0.8\,\%$.
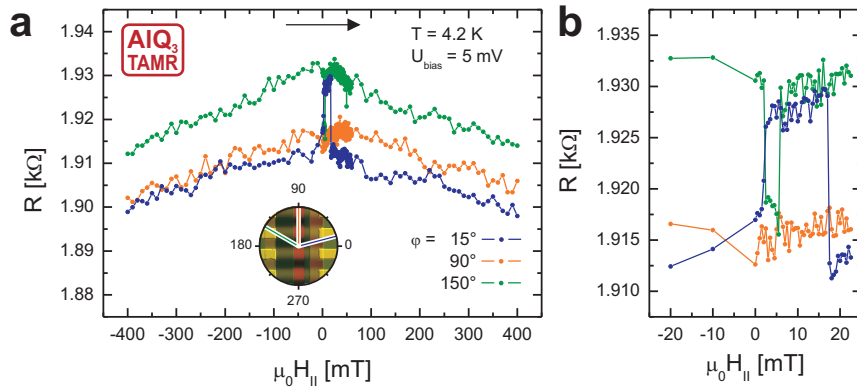
Figure 3.17: MR traces of a TAMR device recorded for three different orientations φ of $\boldsymbol{H}_{||}$. **b** is a blowup of the $\pm 25\,\text{mT}$ region of **a**. Typical features of TAMR like the change of the effect's sign and the shift of the switching fields for different φ become clear.

Employing SQUID measurements the two-step magnetisation reversal of the LSMO electrode can be experimentally proved. In the top panels of Fig. 3.18 the magnetisation hysteresis loops taken for two orientations of $\boldsymbol{H}_{||}$ which are not along one of the magnetic easy axes of single LSMO layers (45°/225° and 135°/315°, $\langle 110 \rangle$ crystalline orientations [Steenbeck99]), respectively, are displayed. It can clearly be discerned that the magnetisation is not completely reversed in a single step for $\varphi = 30°$. The first partial reversal is observed at $\pm \mu_0 H_{c,1} \approx 1.5 - 3.5\,\text{mT}$ and is followed by a plateau, which is not not very pronounced but unambiguously present, and a second step at $\pm \mu_0 H_{c,2} \approx 5.5 - 6.5\,\text{mT}$. The data recorded for $\varphi = 15°$ reveals that a further rotation of the magnetic field away from the easy axis leads, as expected, to a shift of the second reversal towards higher $H_{||}$.

In the next step, a very good agreement between SQUID and magnetotransport results is found. The latter are displayed in the bottom panels of Fig. 3.18. This consistency strongly indicates that the observed spin-valve-like signal is actually correlated to the magnetisation dynamics of the LSMO layer. The MR traces for the same orientations of $\boldsymbol{H}_{||}$ as in the SQUID measurements evidently exhibit switching events at in-plane fields comparable to the $H_{c,i}$ read from the magnetisation hysteresis loops. The deviations of less than a few mT are more than acceptable regarding the fact that for both measurement techniques uncertainties
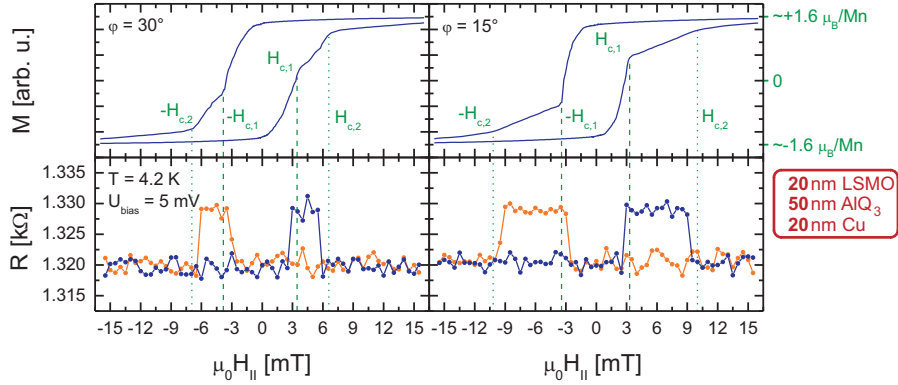
Figure 3.18: Juxtaposition of SQUID (top panels) and magnetotransport (bottom panels) results of an AlQ$_3$-based TAMR sample/structure for two orientations of $\boldsymbol{H}_{||}$. For both measurement techniques $\boldsymbol{H}_{||}$ is applied in directions off the easy axes of the LSMO electrode which are along $45\,°/225\,°$ and $135\,°/315\,°$. The saturation magnetisation measured by SQUID is only originating from the LSMO layer and is significantly lower than for pristine, single LSMO films.

for φ cannot be avoided during sample mounting.

The aforementioned anisotropy of the spin-valve-like signal originating from TAMR can also be illustrated in a waterfall-plot in which the single curves for $\varphi = 0 - 180\,°$ are displayed with an offset ($27\,\Omega$ in Fig. 3.19**a**). In this representation the regular pattern concerning the shift of the switching fields, on the one hand, and the sign of the effect, on the other hand, becomes perfectly clear. The measurement series starts with a negative MR at $\varphi = 0\,°$, whilst for $\varphi = 15\,°$ the effect is positive. When φ is further increased, the width of the R_{H} plateau becomes smaller indicating that the tilt of $\boldsymbol{H}_{||}$ with respect to the magnetic easy axis corresponding to R_{L} is reduced. The next sign change is observed between the $90\,°$- and $105\,°$- direction, for both of which no spin-valve-like switching is discernable, followed by an increase of the R_{L} plateau's width.

Another way to represent these data is a so-called fingerprint (Fig. 3.19**b**), in which the switching fields $H_{\mathrm{c},i}$ read from the signals in Fig. 3.19**a** for each φ are plotted in a polar graph for $\varphi = 0 - 360\,°$. A color code for the resistance additionally is applied in Fig. 3.19**b** indicating regions where the device is in the R_{H} (R_{L}) state by shaded grey (white) areas. This data reveals that the systematic behaviour shown in the $0 - 180\,°$-waterfall-plot is symmetrically continued for $\varphi = 180 - 360\,°$.
As the magnetotransport behaviour in these devices is governed by a two-step magnetisation reversal in the LSMO electrode, these results reflect the magnetic anisotropy of this electrode. Hence, the biaxial symmetry of the displayed data implies a biaxial magnetic anisotropy in the present LSMO layer. However, the magnetic properties of the LSMO layer constituting the electrode of the device under investigation are obviously significantly different from those of a single, pristine LSMO layer. For the latter, the magnetic easy axes are along the $\langle 110 \rangle$ crystalline axes [Steenbeck99] corresponding to $\varphi = 45/225\,°$ and $135/315\,°$, respectively. The results summarised in 3.19**a** and **b**, on the contrary, strongly suggest that both of these
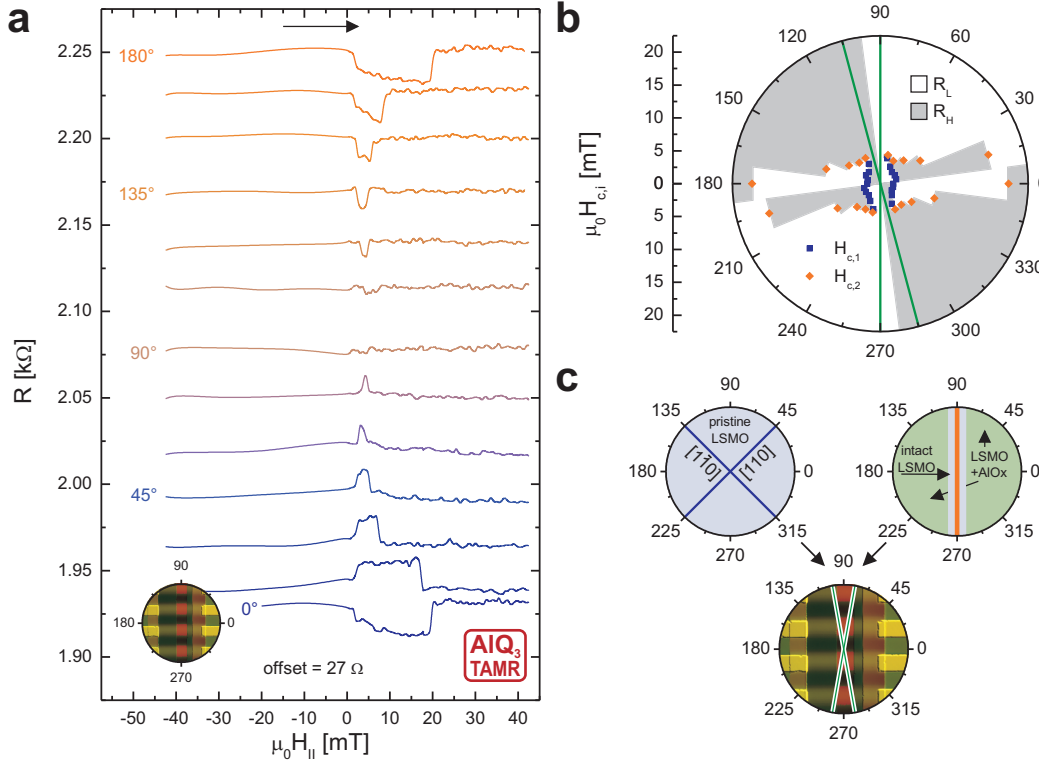
Figure 3.19: Angular dependence of the MR effect obtained for an AlQ$_3$-based TAMR device. **a**: Waterfall-plot for $\varphi = 0 - 180\,^\circ$ exhibiting a regular pattern concerning the sign and width of the spin-valve-like signal. **b**: Fingerprint of the TAMR effect reflecting the magnetic anisotropy of the LSMO electrode. **c**: Schematic representation of the superposition of the biaxial crystalline (blue lines, top left) and the uniaxial shape anisotropy (orange line, top right) in the LSMO electrode yielding a biaxial anisotropy with tilted axes (green lines, bottom).

axes are tilted towards the $\varphi = 90\,^\circ/270\,^\circ$ direction in the present device. This becomes evident when regarding the MR traces for $\varphi = 90\,^\circ$ and $\varphi = 105\,^\circ$ (green lines in Fig. 3.19**b**). The absence of a spin-valve-like effect for these orientations of $\boldsymbol{H}_{||}$ implies a strong magnetic anisotropy in these directions. Additionally, the device is in the low resistance state for $\varphi = 90\,^\circ$, whilst the resistance is at the R_H level for $\varphi = 105\,^\circ$, which can only be explained by the presence of two different easy axes.

A very probable explanation for this observation can be given by taking the influence of an uniaxial anisotropy in the $90\,^\circ/270\,^\circ$ direction into account which is superimposed to the aforementioned biaxial anisotropy with the easy axes along the $45/225\,^\circ$- and $135/315\,^\circ$-directions. This uniaxial component may be originating from shape anisotropy of a rectangularly patterned magnetic layer as schematically shown in Fig. 3.19**c**.
It is known that non-noble metals deposited on top of LSMO layer can cause a substantial change of the oxygen stoichiometry and, as a result, a significant modification of the layer's crystal structure as well as an equally significant decrease of its magnetisation [Homonnay]. One can imagine that a similar effect is initiated by the deposition of alumina (AlOx),

which is used for the indirect patterning of the LSMO electrode. In consequence, a stripe
($200\,\mu$m $\times$ 5 mm, aspect ratio $1 : 25$) of magnetically intact LSMO which is aligned along
the $90\,°/270\,°$ direction and exhibits both, uniaxial and biaxial anisotropy, is constituting the
bottom electrode. In this case the foregoing seeming discrepancies can easily be understood.
Actually, considering the saturation magnetisation $M_{\mathrm{sat,LSMO}}$ of a TAMR sample's electrode
determined by SQUID this scenario is sustained. In the TAMR sample $M_{\mathrm{sat,LSMO}}$ is found to
be significantly lower ($\sim 1.6\,\mu_{\mathrm{B}}$/Mn, Fig. 3.18) than the values obtained for single, pristine
LSMO layers ($\sim 2.0 - 3.0\,\mu_{\mathrm{B}}$/Mn [Homonnay], theoretically $3.7\,\mu_{\mathrm{B}}$/Mn [Millis95]).

In addition to conventional MR characterisation, so-called phiscan measurements can be
applied to identify TAMR unambiguously. In a phiscan measurement the amplitude of $\boldsymbol{H}_{\parallel}$
is kept constant at a value large enough to ensure magnetic saturation of the electrode which
is causing the TAMR and φ is swept from $0\,°$ to $360\,°$. If TAMR is present, an anisotropic
resistance trace is obtained reflecting the dependence of R on the electrode's relative magneti-
sation with respect to its crystalline axes. Hence, in contrast to the TAMR effect's angular
dependence displayed in Fig. 3.19a, a phiscan signal does not reflect the magnetic anisotropy
of the electrode but is providing information about the anisotropy of the DOS which is cou-
pled to the magnetisation as discussed in chapter 2.1.3.
With regard to the TAMR results of PDI-based dedicated TAMR devices and conventional
OSV structures (see chapter 3.4.2), it is also worth noting here that this measurement tech-
nique can be employed in conventional OSVs, too. When an OSV's spin-valve functionality
is exclusively caused by an effect originating from the relative magnetisation of the two ferro-
magnetic electrodes, e.g. by TMR or GMR, a phiscan measurement performed as described
above must yield a constant R corresponding to a circular trace in a polar-plot representation.
Evidently, this is because both electrodes always are in magnetic saturation and thus the de-
vice permanently is in the parallel spin-valve state. Conversely, if an anisotropic resistance
trace is observed in this measurement, TAMR must also be contributing to the MR effect.
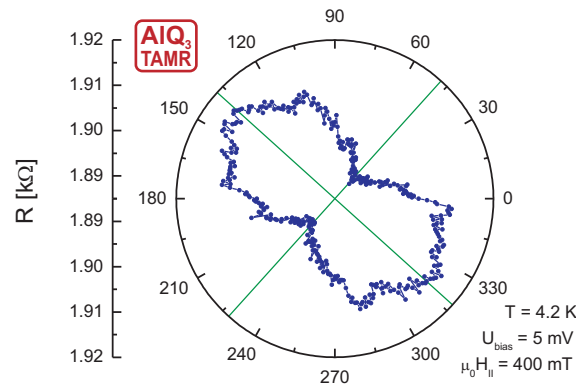
Figure 3.20: Phiscan MR trace of an AlQ$_3$-based TAMR device. The green lines are the mirror axes
of the signal and represent the [110]- and [1$\bar{1}$0]-direction of the LSMO layer.

A typical phiscan result for an AlQ$_3$-based TAMR device is shown in Fig. 3.20. Again,
a clear biaxial symmetry is discernable with a minimum R when the LSMO electrode is

magnetised along the $45°/225°$ direction and a maximum R for the $135°/315°$ direction. As indicated by the green lines, which represent the mirror axes of the MR trace, there is a small deviation of $\sim 3°$ from the mentioned orientations. Once more, this can be explained by uncertainties in φ due to the sample mounting.

Furthermore, this data reveals that, despite the probable superposition of a uniaxial magnetic shape anisotropy along the $90°/270°$ direction, the $45°/225°$- and the $135°/315°$-directions are still distinguished axes, namely concerning the DOS anisotropy. Since the latter is originating from the LSMO electrode's crystalline structure only, the phiscan result can be regarded as evidence for the layer's structural integrity. Moreover, it should be emphasised that this result is not in contradiction to the the scenario that has been proposed above to explain the LSMO layer's magnetisation dynamics. This readily becomes clear considering the fundamentally different origins of the DOS anisotropy and the magnetic shape anisotropy.

To conclude this chapter, the dependence of the observed TAMR effect on U_{bias}, the temperature and d_{AlQ} will be discussed now. Fig. 3.21**a** comprises the data acquired in a series of single MR measurements conducted with different U_{bias}. The obtained behaviour is similar to this of the spin-valve signal in PDI-based OSV devices (see chapter 3.2.3) and, again, as to be expected for an MR effect caused by tunneling processes. The TAMR magnitude is maximum at zero voltage, diminished significantly with increasing U_{bias} and asymmetric with respect to $0\,$V. At $U_{bias} = \pm 40\,$mV (higher voltages are not applied at this stage of the experiments) the size of the effect has dropped to $\sim 38\,\%$ and $\sim 25\,\%$, respectively, of its original value at $U_{bias} = 0\,$V.
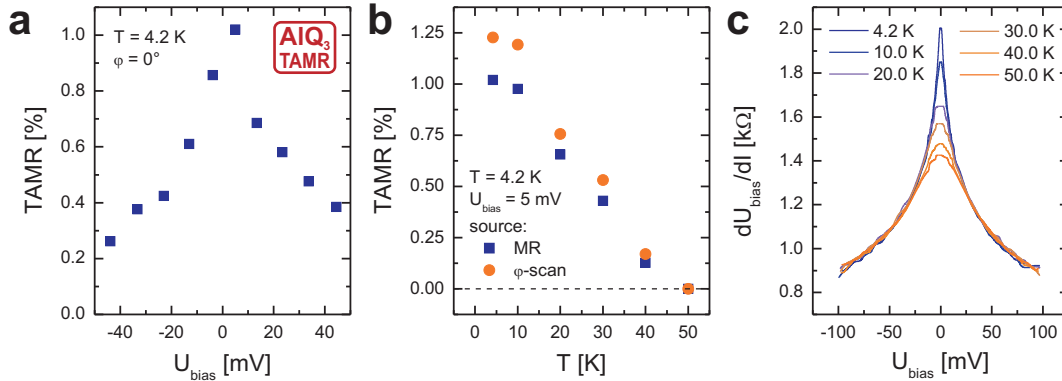
Figure 3.21: Bias- and temperature-dependence of the TAMR effect in an AlQ$_3$-based device. **a**: The observed MR significantly is reduced with increasing U_{bias}. **b,c**: At elevated temperatures the TAMR effect is diminished reaching $0\,\%$ at $T = 50\,$K. As can be seen from the differential resistance traces, this is very likely caused by, amongst other things, a decrease of the tunneling contribution to the total device resistance.

A substantial decrease of the TAMR amplitude is likewise observed at elevated temperatures ($T > 10\,$K, Fig. 3.21**b**). Fig. 3.21**b** shows the temperature dependence of the TAMR amplitude determined by applying Equ. 2.5 to results from single MR and phiscan measurements taken at different temperatures (the minimum/maximum R observed is used instead

of $R_{\text{H/L}}$ in order to evaluate the phiscan results). In general, the effect's size calculated from phiscan results is slightly larger than the one extracted from MR sweeps. Nevertheless, both measures exhibit a well comparable temperature dependence. Whereas for $T = 10\,\text{K}$ only small changes compared to $T = 4.2\,\text{K}$ can be identified, at $T = 40\,\text{K}$ the TAMR is reduced to $\sim 10\,\%$ of its respective initial value. When the temperature is further raised to $50\,\text{K}$ it is impossible to clearly discern any MR effect in the measurements. In consequence, TAMR has to be regarded as completely quenched for $T = 50\,\text{K}$.

The decrease of the TAMR effect is occurring at relatively low temperatures compared to the corresponding behaviour of the spin-valve signal in conventional PDI-based OSV devices (see chapter 3.2.4). When interpreting this result, two aspects have to be taken into account. First, a decrease of the tunneling contribution to the total device resistance with increasing temperature is found employing I/V characterisation as shown by the differential resistance traces displayed in Fig. 3.21c. As a direct consequence thereof, obviously the magnitude of an MR effect stemming from tunneling processes is diminished as well.
The second factor that can lead to the observed temperature dependence of the TAMR signal is a decrease of the LSMO layer's bulk magnetisation $M_{\text{LSMO,B}}$ (see also Fig. 3.10a) resulting in a reduced spin dependence of the DOS [Gould04]. As a result, the coupling between the LSMO layer's magnetisation and the DOS by spin-orbit interaction, in other words the mechanism actually leading to the DOS anisotropy from which TAMR is originating, is likewise diminished. Thus, eventually the TAMR magnitude itself is reduced when $M_{\text{LSMO,B}}$ is decreased at elevated temperatures.
It is very likely that the TAMR ratio's decrease with increasing temperature depicted in Fig. 3.21b is caused by both mechanisms outlined above. Based on the experimental results a clear quantitative analysis of the respective mechanism's contribution cannot be given here. However, it seems justifiable to assume that a smaller tunneling resistance at elevated temperatures is the dominating effect which becomes evident regarding the significant differences in the differential resistance traces shown in Fig. 3.21c. On the contrary, the typical temperature dependence of $M_{\text{LSMO,B}}$ (see Fig. 3.10a) exhibits a relatively small reduction of only $\sim 20\,\%$ within the temperature range under investigation suggesting a minor contribution of the second effect.

Additionally, also the dependence of TAMR on d_{AlQ} is studied investigating samples with three different d_{AlQ} ranging from $50\,\text{nm}$ to $150\,\text{nm}$. All in all, similarly as for the MR magnitude in PDI-based OSV structures, no clear correlation between d_{AlQ} and the TAMR ratio can be determined, but rather statistical variations of the latter are observed from device to device. Hence, this observation indicates again that either direct or multiple step tunneling is dominating the charge transfer in the devices under investigation.
Despite the aforementioned lack of a clear correlation $TAMR(d_{\text{AlQ}})$ a reduced yield of structures exhibiting a sizeable TAMR effect is obtained when d_{AlQ} is increased, which can be readily explained assuming that multiple step tunneling is prevailing in devices comprising thick AlQ_3 layers. This is because in this scenario the injection process' resistance contribution, which is actually modulated by TAMR, is presumably relatively small compared to the total device resistance. Eventually, this is obviously equivalent to a diminished measurable

MR ratio.

In summary, additionally to the weak temperature dependence of R, the clear and unambiguous identification of TAMR shows that in the AlQ_3 TAMR devices the charge transfer is dominated by tunneling processes, which most likely occur during charge injection at the LSMO-AlQ_3 interface.

3.4.2 PDI-based Devices

In order to determine whether TAMR is contributing to the spin-valve signal observed in PDI-based conventional OSV devices (see chapter 3.2), a full magnetotransport characterisation is performed for a sample with seven LSMO-PDI-Al devices, i.e. dedicated TAMR devices. The yield of structures actually exhibiting an MR effect is very poor for this sample (2/7), and exemplary results are shown for only one device ('PDI TAMR').

Compared to the previously presented results for AlQ_3-based devices the temperature dependence of the resistance is, with an increase by almost two orders of magnitude for $|U_{bias}| \lesssim 100\,mV$ when cooling from room temperature to $4.2\,K$, more pronounced for the PDI-based devices as shown in Figs. 3.22a and b. Associated therewith the I/V traces' non-linearity is significantly raised at low temperatures again.
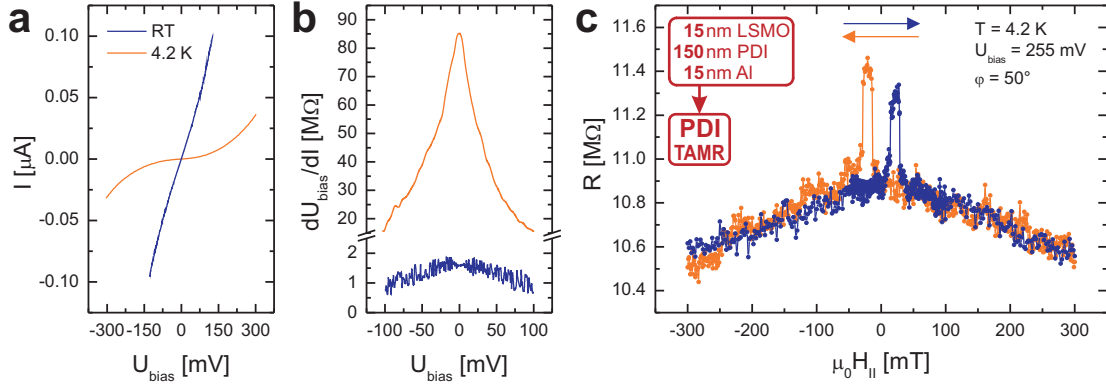
Figure 3.22: Basic transport properties of a PDI-based TAMR device at room temperature and $4.2\,K$. **a,b**: The I/V curve is substantially more non-linear at low temperatures (see differential resistance in **b**). Consequently, a relatively strong temperature dependence of the device's resistance is observed at low U_{bias} ($\lesssim \pm 100\,mV$), whilst at elevated U_{bias} the resistance is less increased when the sample is cooled. **c**: In magnetotransport measurements a very distinct spin-valve-like signal caused by TAMR and two-step magnetisation reversal is obtained.

The devices under discussion exhibit a spin-valve-like effect (Fig. 3.22c) that can be declared similar to the one observed in AlQ_3-based TAMR structures with respect to the signal's shape. The signal consists of a rather linear and negative (decreasing resistance with increasing $H_{||}$) background and the actual spin-valve-like component. For $\varphi = 50\,°$ and $U_{bias} = 255\,mV$ a positive effect is observed, i.e. the device is in the R_L state in saturation before a switching to R_H is observed at $\mu_0 H_{||} \approx \pm 15\,mT$ and the R_L state is reached again

at $\mu_0 H_{||} \approx \pm 30\,\mathrm{mT}$.

TAMR as underlying mechanism of the MR can again be identified on the basis of single MR sweeps taken at different φ and phiscan measurements. The angular dependence of the effect is summarised in Fig. 3.23 which contains a plot with results of two measurements with the magnetic field applied in a direction near the [110]- and [1$\bar{1}$0]-orientation, respectively, in Fig. 3.23**a** and a waterfall-plot for those of a complete $0 - 360\,°$-series in Fig. 3.23**c**.
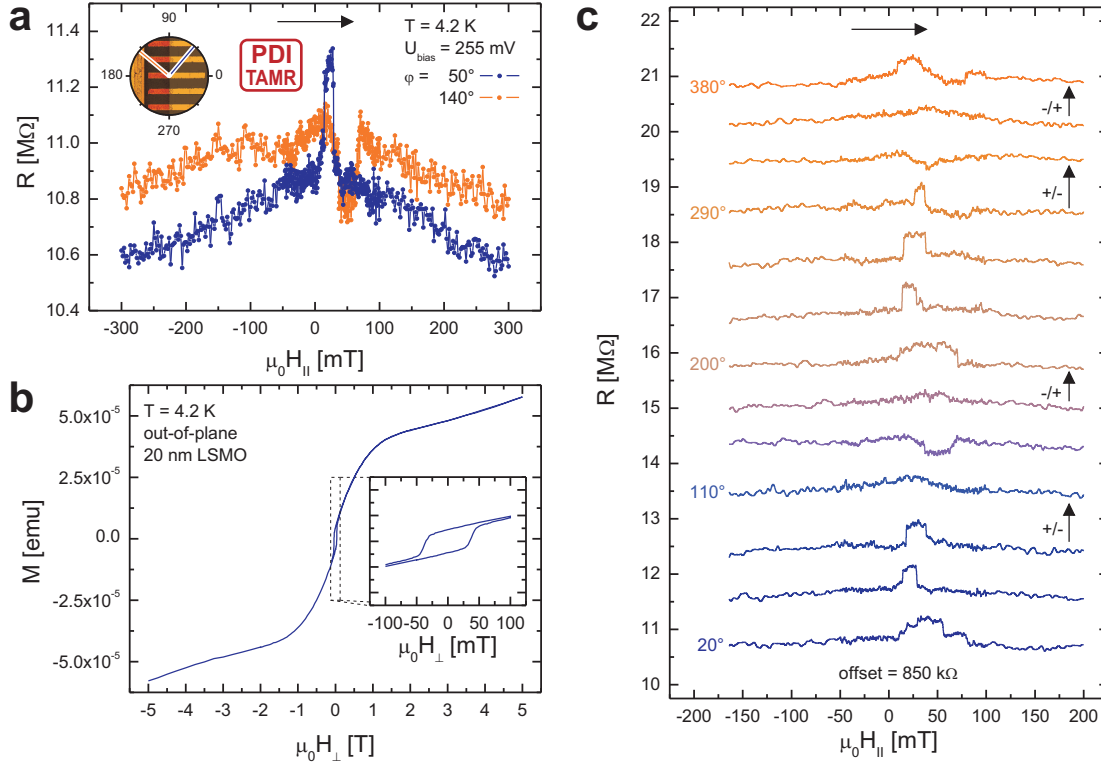
Figure 3.23: Angular dependence of the MR effect obtained for a PDI-based TAMR device. **a**: Results of two measurements with the magnetic field applied in different directions φ displayed without any offset clearly exhibit typical TAMR features. **b**: Deviations from the ideal behaviour can be explained by an out-of-plane magnetisation of single domains in the LSMO layer. **c**: The waterfall-plot for $\varphi = 0 - 360\,°$ shows a regular pattern concerning the shape and sign of the spin-valve-like signal. The sign changes of the effect, which in this device can be most reliably identified regarding the device resistance at high $H_{||}$, are indicated by the vertical arrows on the right hand side.

The typical features of TAMR with respect to the change of the effect's sign and the switching plateau's width can be discerned in both representations. The data Fig. 3.23**a** show, on the one hand, that a switching between two distinct resistive states, $R_{\mathrm{H}} \approx 11.0\,\mathrm{M\Omega}$ and $R_{\mathrm{L}} \approx 10.7\,\mathrm{M\Omega}$ in the 140° measurement, is obtained yielding a TAMR amplitude of $\sim 2.8\,\%$. On the other hand, the switching plateau is shifted and the effect's sign is reversed when φ is changed. Thus, a good agreement with the behaviour of the AlQ$_3$-based devices is found.

In contrast to the latter, however, the present structure seems to exhibit different R_H states in the MR signals shown in Fig. 3.23**a**. Such an apparent discrepancy can be explained by multidomain switching and an out-of-plane contribution to the LSMO layer's magnetisation, which indeed is found by SQUID measurements (Fig. 3.23**b**). This can be ascribed to the presumably relatively low crystalline quality of the LSMO layer under investigation which is grown by CSA [Dediu95, Bergenti04].

Additionally, it becomes obvious from the data in Figs. 3.23**a** and **c** that a significantly higher noise is present in these measurements when compared to the results obtained for the AlQ$_3$ devices. As a consequence of both, the high noise level and the multidomain behaviour, an extensive evaluation of these results with respect to the orientation of the two magnetic easy axes of the LSMO layer is hampered. Nevertheless, a systematic and nearly symmetric pattern is discernable reflecting the LSMO electrode's biaxial magnetocrystalline anisotropy with the easy axes along the [110]- and [1$\bar{1}$0]-direction, respectively. This pattern becomes obvious regarding the vertical arrows in Fig. 3.23**c** marking the MR effect's sign changes, which obviously occur approximately every 90°. Thus, the aforementioned restrictions do not affect the interpretation of the observed MR signal as originating from TAMR and two-step magnetisation reversal in the LSMO bottom contact.

Also for the PDI-based devices phiscan measurements are employed in order to unambiguously identify TAMR and to gain information concerning the DOS anisotropy in the LSMO electrode. A good agreement with the results obtained for AlQ$_3$ structures is found as shown in Fig. 3.24**a** (the maximum field available in the used setup is only 300 mT, which, however, is large enough to ensure nearly full saturation). Again, a resistance trace with a biaxial symmetry is observed exhibiting minimum (maximum) resistance when $\boldsymbol{H}_{||}$ is applied along the 45°/225°- (135°/315°-) direction.

When compared to the result of the AlQ$_3$-based device (Fig. 3.20) the signal in Fig. 3.24**a** only differs concerning the relative width of the low and high resistance state. Whereas the device's resistance is high within a small angular interval around the 135°/315° direction only, the low resistance state is more extended around the 45°/225° axis here. In the case of AlQ$_3$-based TAMR structures, on the contrary, the angular distribution of the two resistive states is nearly even. This behaviour may either be observed as the LSMO electrode cannot be fully saturated with the used magnet or be stemming from the aforementioned lower crystalline quality.

The investigation of the bias dependence of the TAMR effect in PDI-based devices is not feasible to such an extent as it is the case for the AlQ$_3$-structures. As mentioned before, the signal-to-noise ratio in the measurements for the present devices is rather low, which in consequence means that reliable results cannot be obtained for $|U_{\text{bias}}| < 200$ mV. Although at elevated U_{bias} the noise is lowered, eventually the reduction of the effect ratio with increasing bias does not allow for a full characterisation in the range of $|U_{\text{bias}}| > 300$ mV as well. Hence, the amount of exploitable results that can be collected with respect to the bias dependence is not sufficient for a more detailed analysis.

However, concerning the MR effect at elevated temperatures a full data set can be recorded
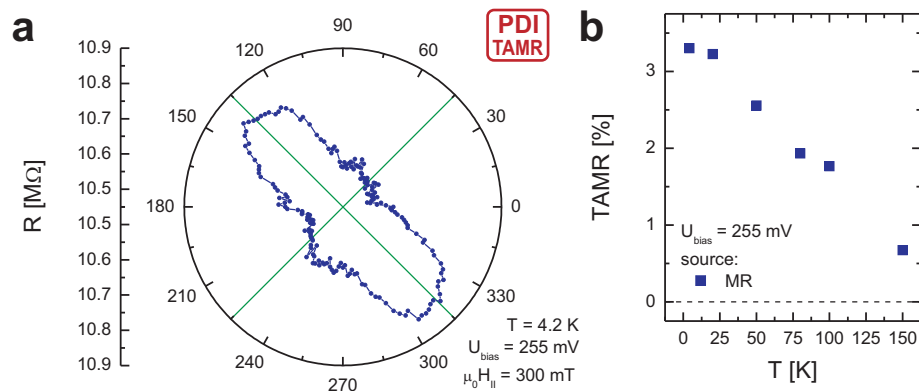
Figure 3.24: a: Phiscan MR trace of a PDI-based TAMR device. The green lines are the mirror axes of the signal and again represent the [110]- and [1$\bar{1}$0]-direction of the LSMO layer. **b**: Temperature dependence of the TAMR effect which is persistent up to $T = 150$ K in this device.

yielding the behaviour summarised in Fig. 3.24**b**. Again, a decrease of the TAMR ratio with increasing temperature is obtained. Here, the MR is persistent up to $T = 150$ K, where it is diminished to $\sim 20\%$ of its original value recorded at $T = 4.2$ K. As already stated in chapter 3.4.1, there are two mechanisms causing a reduction of the TAMR magnitude with increasing temperature, namely a decrease of the tunneling contribution to the total device resistance and the influence of a reduced magnetisation in the LSMO electrode.

Whereas for the AlQ$_3$-based devices the former is assumed to be dominating the temperature dependence of the TAMR, here both effects are presumably more evenly influencing the behaviour depicted in Fig. 3.24**b**. First, this becomes clear regarding the fact that the TAMR is persistent up to 150 K, whilst it is already completely quenched at 50 K in the AlQ$_3$-structures. Furthermore, the non-linearity of I/V curves recorded within the temperature range under consideration (not shown here) is not changing with T to such an extent as it is the case for the AlQ$_3$-based devices. Thus, although the aforementioned relatively strong temperature dependence of R suggests, in the first instance, that the charge transfer through the PDI-layer is dominating R, the TAMR results presented above clearly reveal that for $T \leq 150$ K a substantial contribution to R is rather originating from tunneling injection processes at the interface LSMO-PDI.

From the physics behind TAMR presented in chapter 2.1.3 it becomes clear that this effect can also occur in devices comprising two ferromagnetic electrodes, as long as at least one of them is fulfilling the prerequisites for TAMR. Hence, also in conventional PDI-based OSVs with an LSMO bottom electrode, TAMR may contribute to the observed MR and, in particular, to the spin-valve effect. As insinuated before, standard MR investigation may already be indicative of a TAMR contribution, as is the case for the (rare) observation of a positive MR effect (Fig. 3.11**j**) or a φ-dependent R in the saturation regime of $H_{\parallel}$ (Fig. 3.8**a**).

Therefore, phiscan measurements are likewise performed for a number of conventional OSVs in order to gain reliable information about a potential TAMR contribution to the MR effect in these structures. Fig. 3.25 contains a typical result of such a measurement in a device
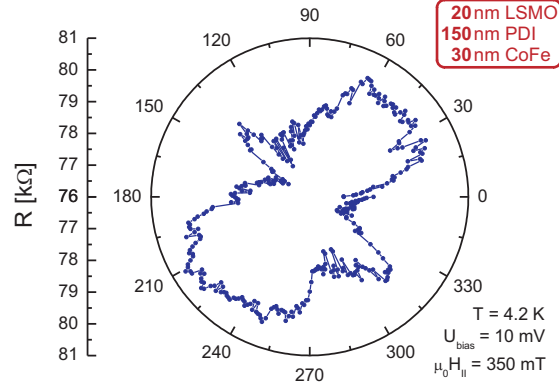
Figure 3.25: Phiscan MR trace of a PDI-based conventional OSV device. Based on this measurement a contribution of TAMR to the spin-valve signal can be unambiguously identified.

exhibiting a spin-valve signal with $MR_{total} \approx -18.5\,\%$ and $MR_{rem} \approx -3.8\,\%$. As can be seen from the trace in Fig. 3.25, a strongly anisotropic resistance distribution, which exhibits more features than the corresponding signal in a dedicated TAMR structure, is observed. Unfortunately, due to the presence of two ferromagnetic electrodes in this device a detailed interpretation of the phiscan trace is not feasible in a straightforward manner despite the clear biaxial symmetry [Rüster05b]. Nevertheless, an anisotropic phiscan result cannot be attributed to MR effects originating from the electrodes' relative magnetisation only. Instead, this is a clear proof for a TAMR contribution to the MR effect, which therefore effectively is very likely caused by the superposition of a TMR and a TAMR signal.

3.4.3 Summary

TAMR is observed in three types of samples, two of them comprising dedicated TAMR devices (non-magnetic counterelectrodes) based on AlQ_3 and PDI. Herewith, for the first time a general proof is provided that TAMR can be observed in organic structures with an LSMO electrode. The main conclusion that can be drawn from the observation of TAMR is that tunneling processes during charge injection obviously provide a substantial contribution to the measured device resistance in these structures.

In the case of the AlQ_3-based devices TAMR later will be used to probe interface modifications induced by voltage pulses (see chapter 3.7). The results obtained for PDI-based TAMR devices and conventional PDI-based OSVs, which are the third type of devices under investigation, mainly constitute additional and supporting information about the physics behind the spin-valve signal yielding the device model presented in the following chapter.

3.5 Device Model for PDI-based Vertical Organic Spin Valves

3.5.1 Estimate of Pinhole Concentration

All experimental evidence discussed in chapters 3.2 and 3.4 suggests that the spin-valve signal observed in the conventional PDI-based OSVs is caused by tunneling-based MR effects. It should be noted here that these results are in good agreement with many others in the literature, which are obtained for OSV devices comprising various OSC materials [Xu07, Vinzelberg08, Shim08, Yoo09, Lin10]. The strongest evidence for this scenario comes from the experiments in perpendicular magnetic fields (chapter 3.3) as they provide an irrefutable proof for the absence of spin precession and electrical spin detection and therefore allow to exclude GMR as underlying mechanism. As a consequence thereof, the charge transport in all devices under investigation which exhibit a sizeable MR signal must be dominated by tunneling processes.

Regarding the nominal PDI-layer thickness d_{PDI} in these structures, it is thus very likely that they suffer from an ill-defined interface between the OSC and the top electrode resulting in pinholes, i.e. sites at which d_{PDI} is reduced to such an extent that direct or multiple step tunneling between the electrodes becomes the favourable charge transfer mechanism. In order to sustain this scenario, it is desirable to employ imaging techniques demonstrating the existence of pinholes. AFM studies alone, as they have been conducted for PDI layers similar to those in the PDI-based OSVs [Grünewald07, Wahler09], are not sufficient for this purpose, even though they already reveal a rather rough surface. This is because the surface morphology and especially the interface between top electrode and OSC layer may be further modified during the deposition of the former [Dürr03]. This eventually hampers the acquisition of reliable information concerning complete OSV layer-stacks by AFM and brings forth the need for other techniques like transmission electron microscopy (TEM). Although TEM preparation is feasible for samples comprising soft OSC layers, the following estimate shows that such an analysis is not very promising.

A good prospect of successfully spotting pinholes by techniques like TEM obviously requires a sufficiently high density of these defects. Based on the findings presented in the previous chapters and those of Barraud *et al.* [Barraud10] the pinhole density can be roughly evaluated. Barraud *et al.* have investigated the spin-valve signal of pinholes that were artificially created in AlQ$_3$-based vertical structures by nanoindentation. In these nm-sized OSVs with $d_{\mathrm{AlQ}} \lesssim 5\,\mathrm{nm}$ a large TMR/TAMR effect of $MR_{\mathrm{total}} \approx 100 - 300\,\%$ is observed at a device resistance of $R \approx 1\,\mathrm{M\Omega} - 100\,\mathrm{G\Omega}$. These results can be integrated into the basic concept of a vertical OSV device comprising pinholes which is illustrated by an equivalent circuit diagram in Fig. 3.26. In this simplified picture the total device resistance R_{device} is a parallel connection of a resistance R_{PDI} caused by diffusive transport through a rather undisturbed PDI-layer (orange box in Fig. 3.26) and another parallel circuit of N_{pinholes} equivalent pinholes, each of them providing R_{pinhole} (blue box in Fig. 3.26). Concerning the spin-valve operation of this model device it is now assumed that only R_{pinhole} depends on the relative magnetisation of the electrodes, whilst R_{PDI} is constant. This yields the following equation for R_{device} in the parallel and anti-parallel spin-valve state, respectively:
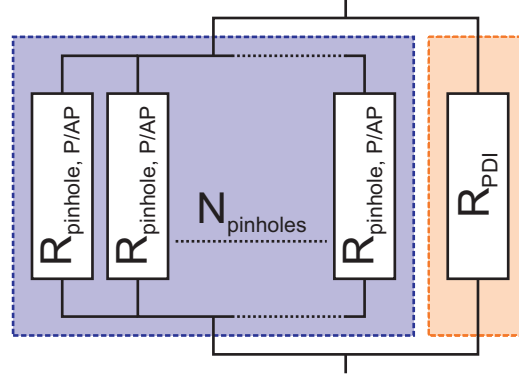
Figure 3.26: Equivalent circuit diagram of a vertical OSV structure comprising pinholes employed for the back-of-the-envelope calculation of the pinhole density. The total device resistance is represented as parallel circuit of a pinhole (blue) and diffusive transport contribution (orange). The former itself is a parallel circuit of N_{pinholes} pinholes.

$$\frac{1}{R_{\text{device,P/AP}}} = \frac{1}{R_{\text{PDI}}} + \frac{N_{\text{pinholes}}}{R_{\text{pinhole,P/AP}}} \tag{3.7}$$

By transposing Equ. 3.7 and using the the formula for MR_{total} from Equ. 3.1 eventually an expression for the number of pinholes N_{pinholes} can be found:

$$N_{\text{pinholes}} = \frac{MR_{\text{total,device}}}{MR_{\text{total,pinhole}}} \frac{R_{\text{pinhole,P}}}{R_{\text{device,P}}} \tag{3.8}$$

Useful values for an estimate of N_{pinholes} can be extracted from the previously presented results and those of Barraud *et al.*: MR ratio for PDI-based OSVs $MR_{\text{total,device}} = 10\,\%$, MR ratio for pinholes $MR_{\text{total,pinhole}} = 100\,\%$, resistance of a PDI-based device $R_{\text{device,P}} = 10\,\text{k}\Omega$ and resistance of a pinhole $R_{\text{pinhole,P}} = 1\,\text{G}\Omega$. With these values $N_{\text{pinholes}} = 10,000$ is obtained from Equ. 3.8 which is equivalent to a density of one pinhole per $6.0 - 22.5\,\mu\text{m}^2$ depending on the active area of a device, which is in the range of $150 \times 400 - 1500\,\mu\text{m}^2$. Regarding these figures it becomes clear that, on the one hand, looking for rather small (nanoscale) pinholes by TEM is neither very promising nor sensible and, on the other hand, a relatively small amount of pinholes is already sufficient to cause a sizeable MR effect.

3.5.2 Proposed Device Model

A suitable device model comprising the possible charge transfer mechanisms that are suggested by experimental results is summarised in Fig. 3.27. This sketch also contains information about possible MR effects observable for the corresponding transport mechanism. On the left hand side of Fig. 3.27 a vertical OSV device is sketched in which the thickness of the PDI layer is reduced at single spots to a varying extent; potential charge (electron) transfer paths are indicated by arrows (for the sake of clarity, only one direction is depicted). On the right hand side an equivalent circuit diagram corresponding to this model is shown, in which
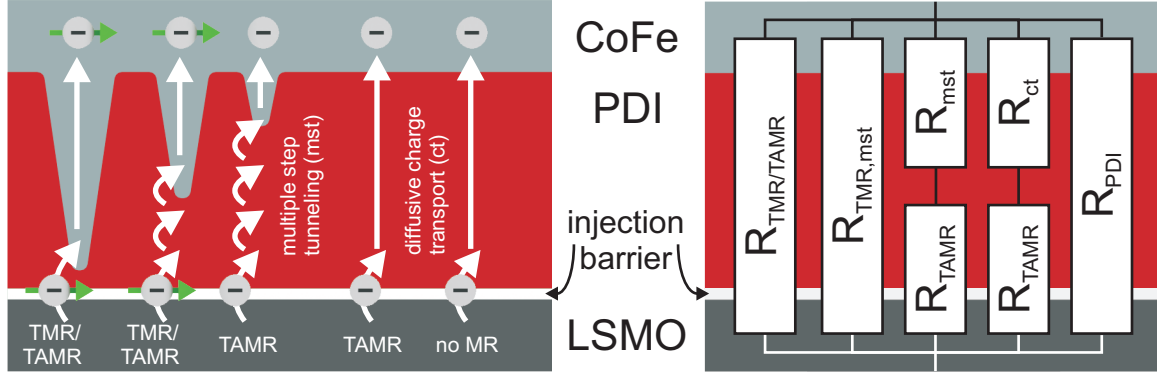
Figure 3.27: Schematic representation of the proposed device model for the PDI-based transport structures. On the left hand side potential charge transfer paths from the bottom to the top electrode are depicted (the opposite direction is omitted for the sake of clarity). Depending on the reduction of the PDI layer's thickness (equivalent to the pinhole depth) the charge transfer may take place via either direct tunneling or tunneling injection from the LSMO electrode into the PDI layer and subsequent charge transport (multistep tunneling or conventional mechanisms). In the bottom part on the left hand side the MR effects which can occur in the respective configuration are listed. The right hand side shows the corresponding equivalent circuit diagram.

the single current paths are connected in parallel again.

The first path is via direct tunneling of spin-polarised charge carriers between the bottom and the top electrode (left hand side, the spin polarisation is indicated by the green arrow), which becomes probable when the effective d_{PDI} is a few nm only. Although in this case ideally only TMR is observed, TAMR can likewise contribute to the spin-valve signal as the charge transfer includes a tunneling step starting in the LSMO electrode where all prerequisites for TAMR are met.

Three further paths are shown in the center of Fig. 3.27 on which, subsequent to the charge injection by tunneling, the charge transport is taking place via either multiple step tunneling at sites of a moderately reduced d_{PDI} or conventional mechanisms like VRH or MTR at sites where the OSC layer can be considered undisturbed. Evidently, in the case of multiple step tunneling TMR may occur when the number of tunneling steps is rather small as schematically sketched in the second path from the left. [Schoonus09]. Additionally, these three paths comprise a tunneling step starting in the LSMO electrode, thus allowing for the occurrence of TAMR. It is important to note that a potential TAMR contribution is only measurable when the device is operated in the injection limited regime, i.e. when the tunneling injection processes are dominating the total device resistance. Furthermore, it should be borne in mind that the injection process by tunneling alone is sufficient to cause TAMR, as this effect requires neither spin-injection nor spin-polarised transport nor electrical spin-detection.

The last conduction path that has to be considered is illustrated on the right hand side and comprises charge injection into the OSC without the occurrence of TAMR, and subsequent charge transfer by VRH or MTR. This path obviously cannot provide any contribution to the MR effect.

Regarding the equivalent circuit diagram on the right hand side of Fig. 3.27 it becomes clear

that this picture is consistent with the one employed for the estimate of the pinhole density
in the previous chapter (see Fig. 3.26).

Furthermore, using this model nearly all experimental results collected for PDI-based
OSVs and TAMR structures can be readily explained. Any MR in a device similar to the
one sketched in Fig. 3.27 is originating from tunneling processes, whereas the underlying
mechanisms of GMR (spin injection, diffusive spin transport and electrical spin detection)
do not have to be taken into account. This is justified by the results of the experiments
in the perpendicular geometry. Hence, the proposed model includes the physics behind the
spin-valve signal, the weak temperature dependence of R and the findings concerning the MR
effect's dependence on d_{PDI}. Therefore, it can be considered conclusive and complete.

3.6   Summary

In chapters 3.2-3.4 the results of investigations in vertical organic spintronics devices have
been summarised. They comprise standard magnetotransport studies addressing nearly all
parameters that may influence the spin-valve functionality observed in conventional PDI-
based OSVs. Additional information is gained by measurements in the perpendicular geom-
etry, an experiment that so far has only rarely been conducted in organic structures, and the
first-time demonstration of TAMR in OSC-based structures.

Thus, based on the results presented in the previous chapters both questions raised in the
introduction to this section can be clearly answered. First, obviously PDI can be employed
in organic spintronic devices as non-magnetic spacer material. A sizeable MR effect of up to
$\sim 50\,\%$ at low temperatures is observed in conventional OSV structures with two ferromag-
netic electrodes. Likewise, a spin-valve-like signal is found in OSC-based single-sided spin
valves. In these devices with only one ferromagnetic electrode the MR is caused by TAMR,
which is underlining the governing role of tunneling injection from the LSMO electrode into
the OSC layer with respect to the charge transfer and hereby to the total device resistance.
The second question addresses the underlying mechanisms of the conventional OSVs' spin-
valve functionality, which can be regarded as an issue still under debate for many reports
in the literature. Here, it can be reliably answered considering the results of extensive in-
vestigations including the spin-valve effect's dependence on the applied bias voltage, the
temperature, and the thickness of the PDI layer. As outlined in the previous chapters, all
observations made in these experiments are suggesting that the MR is caused by tunneling
processes, i.e. by TAMR and TMR, in the first instance. GMR, on the contrary, can be ex-
cluded as the MR effect's origin on the basis of the very robust experimental proof obtained
by investigations in the perpendicular geometry, namely the absence of spin precession and
of the Hanle effect, respectively.

All results can be condensed into a model consistently describing the origin of the spin-
valve signal (chapter 3.5). The basis for the proposed phenomenological approach is the
assumption that the PDI layer in the devices exhibiting spin-valve functionality is very likely
disturbed by pinholes and/or metal inclusions. Consequently, the effective thickness of this

layer is significantly reduced allowing for a substantial contribution of direct or multiple step tunneling to the charge and spin transfer, which is a prerequisite for TMR. Furthermore, obviously also the injection from the LSMO electrode into the OSC layer is occurring via tunneling which is, as already mentioned, unambiguously revealed by the TAMR results for both dedicated TAMR devices and conventional OSVs.

Evidently, this model and these conclusions are valid for the present structures only and must not be applied to other experiments in a straightforward manner. Nevertheless, these findings show that on the basis of transport measurements a lot of information can be acquired with respect to the physics in organic spintronics devices, which, however, requires a careful and coherent analysis of all available results.

3.7 Resistive Switching in AlQ$_3$-based TAMR-Devices

As stated in chapter 2.3, the investigation of resistive switching (RS) effects recently has become a research field of increasing interest. The term RS comprises any kind of remanent change of a device's resistance induced by a driven current or an applied voltage (pulse). In the field of organic spintronics, RS as well as an interplay of RS and MR has been demonstrated in AlQ$_3$-based OSV devices with LSMO electrodes [Hueso07, Prezioso11, Prezioso12]. However, neither the microscopic origin of the RS is completely understood for these structures nor any attempt of an explanation is substantially underpinned by experimental evidence (see chapter 2.3.2). In the following chapter results of RS investigations in AlQ$_3$-based TAMR structures likewise including evidence for a clear correlation between both effects, TAMR and RS, are presented [Grünewald14]. A phenomenological model is outlined in chapter 3.7.2, which can be used to explain this interaction and the RS effect and, moreover, might also be transferable to the aforementioned results reported for conventional OSVs.

3.7.1 Experimental Analysis of the Resistive Switching Effect

All results presented in this chapter are obtained for a number of different devices with a nominal $d_{\mathrm{AlQ}} = 50\,\mathrm{nm}$. The RS measurements are performed as outlined in appendix D. Voltage pulses U_{pulse} with the length t_{pulse} are applied to the top contact and the pulse height is stepwise increased/decreased (referred to as RS- or U_{pulse}-sweep hereafter). R is measured at a constant $U_{\mathrm{bias}} = 1\,\mathrm{mV}$ in between the steps. A typical RS hysteresis trace, R plotted against U_{pulse}, of a TAMR device recorded with $t_{\mathrm{pulse}} = 50\,\mathrm{ms}$ is displayed in Fig. 3.28a.
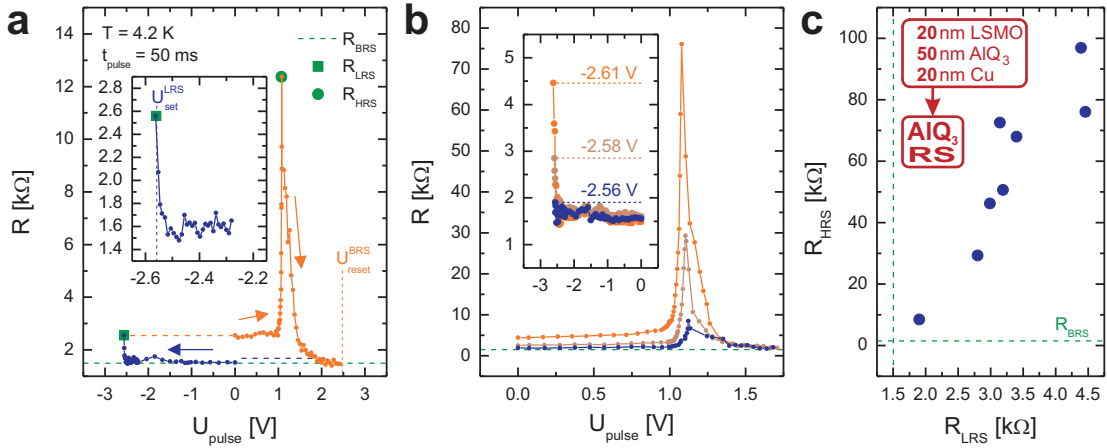
Figure 3.28: **a**: Typical full RS trace of an AlQ$_3$-based TAMR device comprising three different characteristic resistive states. **b**: Three different RS hysteresis loops reveal that R_{HRS} (high resistance state HRS) strongly depends on the previously prepared low resistance state LRS (inset). **c**: Summary of this correlation extracted from eight RS traces with a maximum ON/OFF ratio of ~ 75.

At the beginning of the measurement shown in Fig. 3.28a the device is in the base resistance state BRS (minimum R). If U_{pulse} is applied with positive polarity R does not change as indicated by the dashed blue line. Likewise, neither negative pulses with a rather small

magnitude ($U_{\mathrm{pulse}} \gtrsim -2.0\,\mathrm{V}$) do have any influence on R. However, if $|U_{\mathrm{pulse}}|$ is further enhanced in the negative range a slight decrease of R can be discerned followed by a sharp increase starting at $U_{\mathrm{pulse}} \approx -2.5\,\mathrm{V}$ (blue curve and blow-up in Fig. 3.28a). The resistance at the end of this rising edge (U_{set}^{LRS}) is referred to as low resistance R_{LRS} hereafter, the corresponding state as low resistance state LRS.

When the height of U_{pulse} is decreased to $0\,\mathrm{V}$ again, R is not significantly modified (dashed orange line). Subsequently, the voltage pulses are applied with opposite polarity and their magnitude is swept from $0\,\mathrm{V}$ to $+2.5\,\mathrm{V}$ (orange curve in Fig. 3.28a). For this sweep one would expect a constant R and a switching back to R_{BRS} at $U_{\mathrm{pulse}} = U_{\mathrm{reset}}^{\mathrm{BRS}} \approx -U_{\mathrm{set}}^{\mathrm{LRS}}$ in the case of typical bipolar switching as discussed in chapter 2.3. Actually, at $U_{\mathrm{reset}}^{\mathrm{BRS}}$ the BRS is restored. However, the RS trace in Fig. 3.28a exhibits a sharp maximum at an intermediate positive $U_{\mathrm{pulse}} \approx +1.1\,\mathrm{V}$ before the transition back to the BRS sets in. Hence, a fundamental deviation from typical bipolar and bistable RS is obtained and therefore a third resistive state labeled high resistance state HRS is introduced. It is important to note that the HRS seemingly does not appear when the transition BRS→LRS is omitted, i.e. when, starting from the BRS, positive voltage pulses are immediately applied.

Another feature of the RS effect is illustrated in Figs. 3.28b and c. These data reveal a clear correlation between R_{HRS} and the resistance R_{LRS} of the previously prepared LRS. Evidently, the maximum resistance at positive U_{pulse} depends on the maximum applied negative U_{pulse}. As a result, depending on the sweep parameters or limits, respectively, it is possible to adjust R in the interval between $R_{\mathrm{BRS}} \approx 1.6\,\mathrm{k\Omega}$ and $R_{\mathrm{HRS}} \approx 120\,\mathrm{k\Omega}$ corresponding to a maximum ON/OFF ratio of ~ 75 in this device.

As the devices under investigation do not only exhibit the described RS behaviour but also a clear spin-valve-like signal that must be originating from TAMR (see chapter 3.4), the next intuitive step is to check whether there is any interaction between these two effects. TAMR is unambiguously caused at the interface between the LSMO bottom-electrode and the AlQ$_3$ layer, where charge carriers are injected by tunneling, i.e. through any kind of tunnel barrier. Consequently, TAMR analysis can be employed to probe this interface and to check whether the change of R induced by the voltage pulses is originating from any modification of the interfacial barrier.

For this purpose a series of TAMR investigations is performed for a set of different HRSs with $R_{\mathrm{HRS}} = 5 - 120\,\mathrm{k\Omega}$. The results thereof are summarised in Fig. 3.29a as absolute ($R_H - R_L$) and relative (Equ. 2.5) TAMR amplitude plotted against R_{HRS}. The data points as well as the error bars are calculated by averaging the results of several single MR measurements recorded for each HRS. Exemplary traces for four HRSs are shown in Figs. 3.29b-e, where the averaging performed for R_H and R_L of a single measurement is also illustrated by the dashed and dotted green lines.

It becomes clear from the data in Fig. 3.28a that the magnitude of the observed spin-valve-like signal depends on R_{HRS}. For $R_{\mathrm{HRS}} \lesssim 85\,\mathrm{k\Omega}$ a rather linear relation between both, $TAMR_{\mathrm{abs}}$ and $TAMR_{\mathrm{rel}}$, and R_{HRS} can be discerned starting with a effect ratio of $TAMR_{\mathrm{rel}} \approx 2\,\%$ ($TAMR_{\mathrm{abs}} \approx 90\,\Omega$) at low resistance and ending at $TAMR_{\mathrm{rel}} \approx 20\,\%$ ($TAMR_{\mathrm{abs}} \approx 13\,\mathrm{k\Omega}$) at $R_{\mathrm{HRS}} \approx 85\,\mathrm{k\Omega}$. For higher R_{HRS} a saturation or even decrease of the MR effect appears.

A pure scaling effect, i.e. an increased TAMR amplitude due to the increased device resis-

tance alone, can be excluded here which becomes evident considering the two aforementioned data points. For these R_{HRS} differs by a factor of only ~ 21, whilst $TAMR_{\mathrm{abs}}$ is raised by a factor of ~ 140. In other words, the enhancement of the absolute MR effect is significantly higher than the increase of R_{HRS}, which is equivalent to the observed change of $TAMR_{\mathrm{rel}}$ with changing R_{HRS}. Hence, this result is strongly indicative of a modification of the interface where the MR effect is caused, namely the LSMO-AlQ₃ interface and the tunnel barrier included therein.
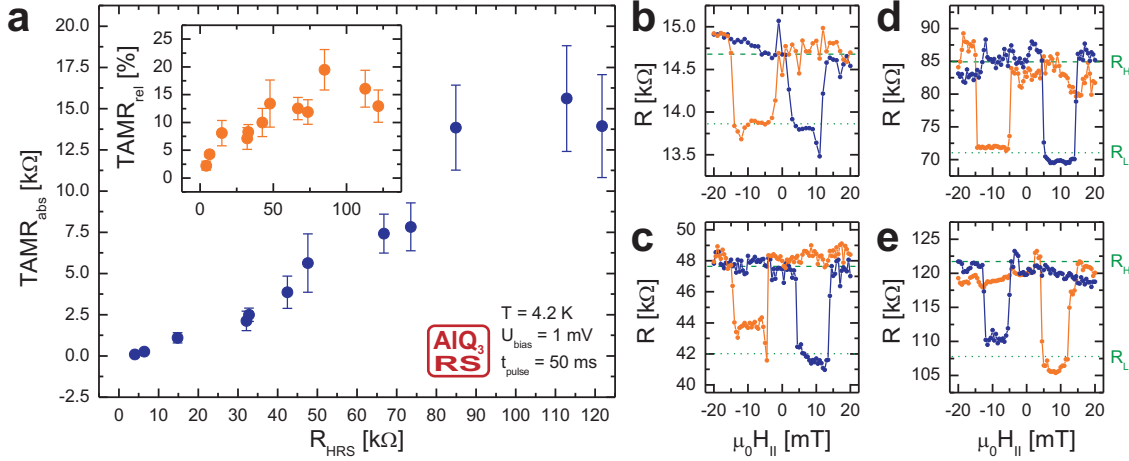
Figure 3.29: Interplay of resistive switching and TAMR. **a**: The absolute and relative TAMR amplitude scales with the device resistance (denominated by R_{HRS}). **b-e**: Single MR traces for different HRSs show the reproducibility of the spin-valve-like signal caused by TAMR. The dashed and dotted lines indicate the average high and low resistance used for the calculation of the error in a single measurement. The error bars in **a** are derived from averaging results of several single MR measurements for each R_{HRS}.

This assumption is sustained by magnetotransport and RS measurements undertaken for several reference samples of various compositions listed in appendix E, amongst them also devices where the AlQ₃ layer is omitted. These investigations are performed in order to ensure that, on one side, potential short circuits through the insulating alumina film (see Fig. 3.3) can be excluded and, on the other side, the observed RS effect is not originating from the LSMO, AlQ₃ or alumina layer alone. Eventually, none of the reference devices does exhibit any kind of RS which thus is underlining the governing role of the LSMO-AlQ₃ interface.

It also seems worth interjecting that the maximum TAMR observed in this experiment ($\sim 20\,\%$, see Fig. 3.29**d**) is significantly exceeding any reported value for TAMR, which is, irrespective of the material under investigation, only a few % [Gould04, Bolotin06, Moser07, Park08, Wang14]. According to the theoretical approach proposed for (Ga,Mn)As [Gould04] TAMR ratios as high as they are observed here can be explained, for instance, by a cleaner and more crystalline interface/barrier and consequently an increased relative contribution of charge carriers with large k_z to the tunneling current (see chapter 2.1.3). Such substantial modifications of an interface buried inside a device, initiated after device fabrication and by the application of voltage pulses alone, seem rather unlikely. As a result, obviously a direct

transfer of this scenario to the present devices and the tunnel barrier at the LSMO-AlQ$_3$ interface is questionable.

Turning back to the RS under investigation, obviously further analysis is required in order to understand the physics behind the effect and its apparent interplay with TAMR. Therefore, in the first instance, the tunnel barrier parameters thickness d_barrier and energetic height Φ_0 are investigated in the low bias regime ($|U_\mathrm{bias}| \lesssim 5\,\mathrm{mV}$). For this purpose the I/V curves that are recorded for each HRS investigated by MR measurements are fitted employing a suitable methodology derived from the Simmons model ([Simmons63], see appendix F). Exemplary data of a typical I/V response and the corresponding nearly perfect parabolic fit to the differential conductance dj/dU_bias are displayed in Fig. 3.30a. As outlined in appendix F, the two barrier features d_barrier and Φ_0 can be calculated from the fit parameters. The general prerequisites that have to be met in order to ensure the meaningfulness of the Simmons analysis are given in appendix F, too. These include, for instance, that the applied U_bias has to be small compared to Φ_0, which can be easily maintained by using the right measurement parameters for the acquisition of the I/V curves.
In order to derive d_barrier and Φ_0 from I/V curves, it is furthermore mandatory that the current flow is homogeneous over the whole barrier. This is only the case if the resistance of the materials on both sides of the barrier is small enough compared to the barrier resistance, which can be deemed justified for the devices under discussion considering, for instance, typical values of the in plane resistance of LSMO given in chapter 3.2.1 (see also [Grünewald14]). It is therefore allowed to treat the devices as one-dimensional and to calculate the current density j necessary for the determination of dj/dU_bias by dividing the current by the active device area.

Another assumption made for the sake of simplification is sketched in Fig. 3.30d. In the following, the total device resistance R is considered as serial connection of two components which are the variable non-linear contribution of the tunnel barrier (R_TB) and the constant ohmic resistance caused by the rest of the structure (R_rest). Thus, it is assumed that the non-linearity of the I/V curve is originating from the injection barrier at the LSMO-AlQ$_3$ interface only and, as a consequence thereof, that R is dominated by R_TB for small U_bias. This can be regarded justified by the observed rise in TAMR with increasing R_HRS (Fig. 3.29a) and the nearly perfect match of the Simmons fit to the experimental data shown in Fig. 3.30a.

Hereafter, the following representation is chosen for the results of the I/V evaluation undertaken for different HRSs: the barrier parameters are plotted as differences $\Delta d_\mathrm{barrier}$ and $\Delta\Phi_0$ of the the respective values in the HRS and the reference values obtained for the BRS ($d_\mathrm{barrier}^\mathrm{BRS}$ and Φ_0^BRS). $\Delta d_\mathrm{barrier}$ and $\Delta\Phi_0$ are summarised in Figs. 3.30b and c, respectively, for the whole R_HRS interval under investigation. The error bars are calculated from the errors given for the fit parameters. The reference values $d_\mathrm{barrier}^\mathrm{BRS}$ and Φ_0^BRS (dashed lines in Figs. 3.30b and c) indicate that initially a thin and rather high tunnel barrier is present. When the HRS is set, apparently both barrier features are modified sizeably. For the HRS with the highest resistance ($R_\mathrm{HRS} \approx 120\,\mathrm{k\Omega}$) d_barrier is raised modestly by a factor of only ~ 3, whereas Φ_0 is diminished in a more pronounced manner to $\sim 15\,\%$ of its original value.
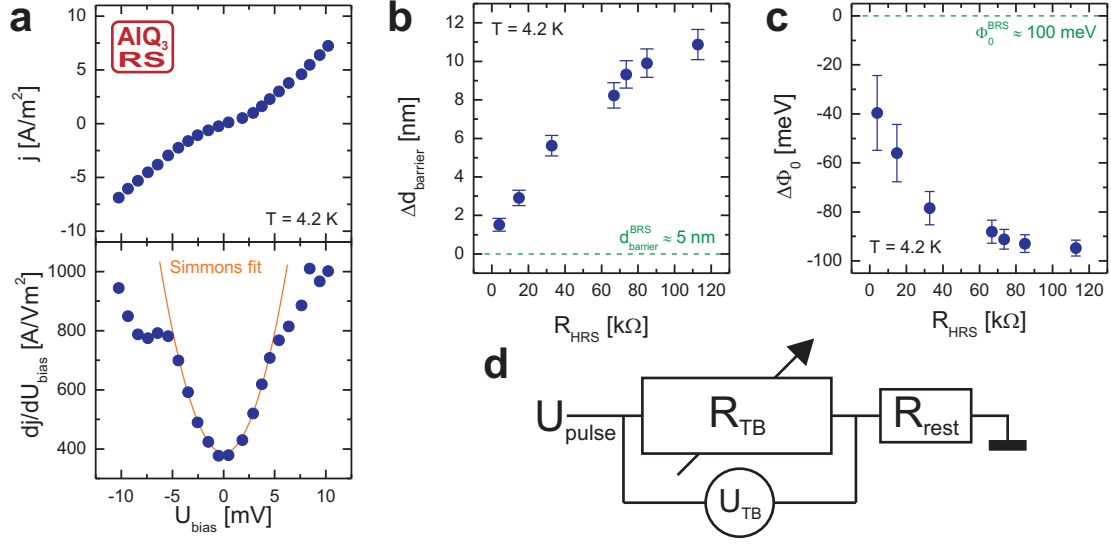
Figure 3.30: Analysis of the tunnel barrier employing the Simmons fit. **a**: Exemplary I/V data and corresponding Simmons fit to the differential conductance for $R_{HRS} \approx 85\,k\Omega$. **b, c**: Barrier thickness $d_{barrier}$ and height Φ_0 extracted from fits to I/V curves recorded for several HRSs. These differential data are related to the value obtained for the BRS. **d**: Equivalent circuit diagram of the device based on the assumption that R consists of two components. These are a variable and bias-dependent (non-linear) contribution R_{TB} of the tunnel barrier and a constant, rather small ohmic part R_{rest} caused by the rest of the device.

Hence, these results constitute an unambiguous proof for the scenario proposed above, namely that the enhanced TAMR ratio at high R_{HRS} can be ascribed to a change of the tunnel barrier and consequently an increase of the relative contribution of the tunnel barrier's resistance to the total device resistance.

The data in Figs. 3.30**b** and **c** only show a snapshot of the RS cycle in Fig. 3.28**a**, namely the situation in the HRS. Next, a similar analysis of the barrier parameters' dynamics is performed for a complete RS cycle in another device. In this experiment the RS measurement yielding the trace shown in Fig. 3.31**a** is periodically interrupted for the acquisition of I/V curves which then are evaluated as described above. The RS signal in this device is qualitatively well comparable to the one displayed in Fig. 3.28**a** although, amongst other differences to the RS traces shown so far, the maximum for the HRS is less pronounced. Concerning the behaviour of $d_{barrier}$ and Φ_0 phenomenologically similar observations as those presented above can be made here. As depicted in Figs. 3.31**b** and **c** which contain the respective differential data, an increase (decrease) of R always is equivalent to an increase (decrease) of $d_{barrier}$ and a decrease (increase) of Φ_0. Additionally, the reversibility of the RS effect concerning both the resistive state of the device and the barrier modifications actually causing the change of R becomes evident from these results.

As a first interpretation of the information gained by the I/V curve analysis, the dynamics of the barrier parameters during an RS cycle can be considered resembling the description of the space-charge region in a p/n-junction according to the Schottky model although an
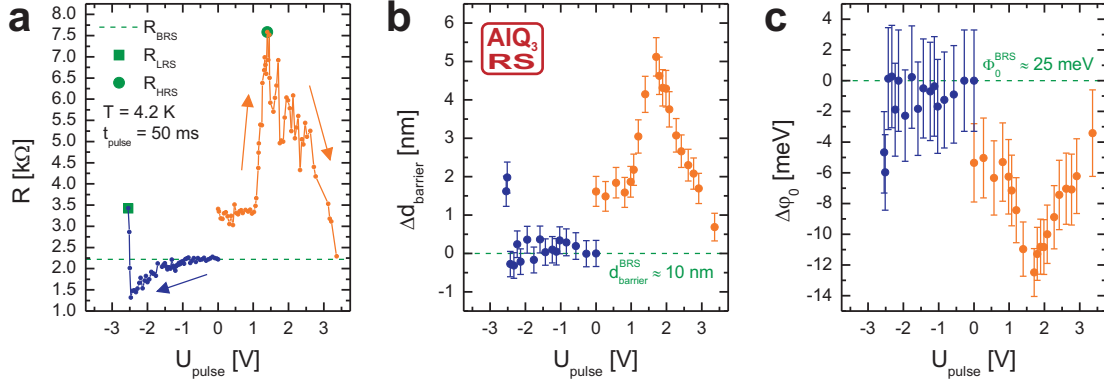
Figure 3.31: Barrier parameters' dynamics during a complete RS cycle recorded in another TAMR device. **a**: The RS trace of this device exhibits the same characteristic features as the one shown before. **b,c**: A clear correlation between the barrier parameters' behaviour and R is observed which is in agreement with the findings for different HRSs presented in Fig. 3.30.

explicit analogy must not be applied here. In the Schottky model the built-in potential V_{bi} of a p/n-junction (equivalent to Φ_0 in this comparison) depends on the charge densities on both sides of the junction. Let it now be assumed that a certain amount of charge carriers is concentrated near the interface of a p/n-junction (equivalent to a thin barrier). In this case, V_{bi} (Φ_0) is relatively high, whilst the charge density and hereby V_{bi} (Φ_0) is decreased when the same amount of charge carriers spatially is distributed more widely around the interface (equivalent to a thick barrier).

Evidently, any decisive hints towards the microscopic origin of the RS effect cannot be extracted from this comparison. Nevertheless, the basic idea of any kind of charged species and their spatial distribution as origin of the tunnel barrier should be borne in mind as basis for an explanatory model (see chapter 3.7.2), on one side, and as motivation for further experiments, on the other side.

Before the results of the latter will be presented, the reproducibility of the RS traces obtained for different structures as well as by subsequent measurements in the same device should be shortly addressed. First, a comparison of RS traces acquired from different structures (see, Figs. 3.28**a**, 3.31**a** and 3.32**a**) reveals significant variations concerning characteristic features of the effect. It can be observed that the height of the voltage pulses required for the RS transitions differs from device to device and that likewise the maximum in the HRS is differently pronounced.

This can be readily understood when taking into account the aforementioned very simple though rather realistic scenario that the device resistance consists of two parts connected in series, namely R_{TB} and R_{rest} (see Fig. 3.30**d**). Since U_{pulse} is applied to this resistance series, the ratio R_{TB}/R_{rest}, which is presumably varying for different structures, is decisive for the magnitude of the voltage drop U_{TB} over the tunnel barrier. As the previously presented observations strongly suggest that this barrier is modified, U_{TB} and hereby R_{TB}/R_{rest} should be governing the RS behaviour. Thus, in a device with a relatively high R_{TB}/R_{rest} a large U_{TB} is present at a certain U_{pulse}, whereas U_{TB} is lower in another device with a lower R_{TB}/R_{rest}

for the same U_{pulse}. This is equivalent to a higher total U_{pulse} necessary to achieve the same U_{TB}, e.g. to initiate the BRS→LRS switching, in the second case, exactly as it is observed experimentally (see, for instance, Fig. 3.32**a**).

Actually, such variations in the $R_{\text{TB}}/R_{\text{rest}}$ ratio are indicated by results of transport characterisation undertaken directly after sample fabrication. The device resistances that are measured for different structures on the same sample are distributed within an interval of approximately one order of magnitude, suggesting that different interfacial tunnel barriers may be present in the first place. As a consequence thereof, a quantitative comparison of the RS results obtained for different devices is hardly feasible.

Furthermore, even for the same device some sort of lacking reproducibility concerning the transitions BRS→LRS and HRS→BRS has to be acknowledged. Although these switchings are occurring at nearly identical U_{pulse} for consecutive RS measurements, small variations of the respective pulse heights $U_{\text{set}}^{\text{LRS}}$ and $U_{\text{reset}}^{\text{BRS}}$ are present and complicating a deeper analysis of the RS effect, for example with respect to the pulse length's influence.

In response to this issue, another measurement procedure, which is referred to as RS minor loop (RS-ML) hereafter, is established. RS-MLs turn out to yield perfectly reproducible results for the same experimental parameters and allow for more detailed investigations of, at least parts of, the RS cycle.

The U_{pulse} sequence necessary for an RS-ML is illustrated by the data recorded for another device in Fig. 3.32**a**. After the preparation of the LRS by applying negative voltage pulses (blue curve), the sweep direction for U_{pulse} is reversed similarly as for a standard RS characterisation (green curve). In contrast to the latter, however, the sweep direction is reversed once more at a positive $U_{\text{pulse}} = U_{\text{stop}}$ before the HRS is reached. During the subsequent sweep towards negative values R is switched back from R_{IRS} (intermediate resistance state, IRS) to R_{LRS} at $U_{\text{pulse}} = U_{\text{reset}}^{\text{LRS}}$.

As can be seen in Fig. 3.32**a**, the resulting trace is closed and nearly symmetric with respect to $U_{\text{pulse}} = 0\,\text{V}$ with a higher slope for the transition LRS→IRS than for reverse operation IRS→LRS. Similarly as for the complete RS hysteresis, also for an RS-ML loop an analysis of the tunnel barrier employing Simmons fits is undertaken yielding identical results concerning the barrier parameters' dynamics (Figs. 3.32**c**-**e**). Furthermore, the data clearly unveil that the initial barrier parameters are restored after a full RS-ML.

On the basis of these findings RS-MLs can be assessed as useful tool for further and more detailed investigations. The first one comprises sequences of minor-loop measurements with different U_{stop}. Fig. 3.32**b** displays five exemplary traces obtained during one of these series. In each measurement the transition LRS→IRS seemingly sets in at the same threshold voltage U_{th} in the positive U_{pulse} range. Additionally, these data reveal that the height of an RS-ML signal, measured by $\Delta R_{\text{ML}} = R_{\text{IRS}} - R_{\text{LRS}}$, obviously depends on U_{stop}, whereby R_{IRS} is modified and R_{LRS} is constant and stable in a certain sense. This stability can be identified best from the ML-traces with low U_{stop} where R does not further change significantly when U_{pulse} has surpassed $U_{\text{reset}}^{\text{LRS}}$ during the reset sweep.

Furthermore, the minor loops become likewise wider with increasing U_{stop}. For instance,
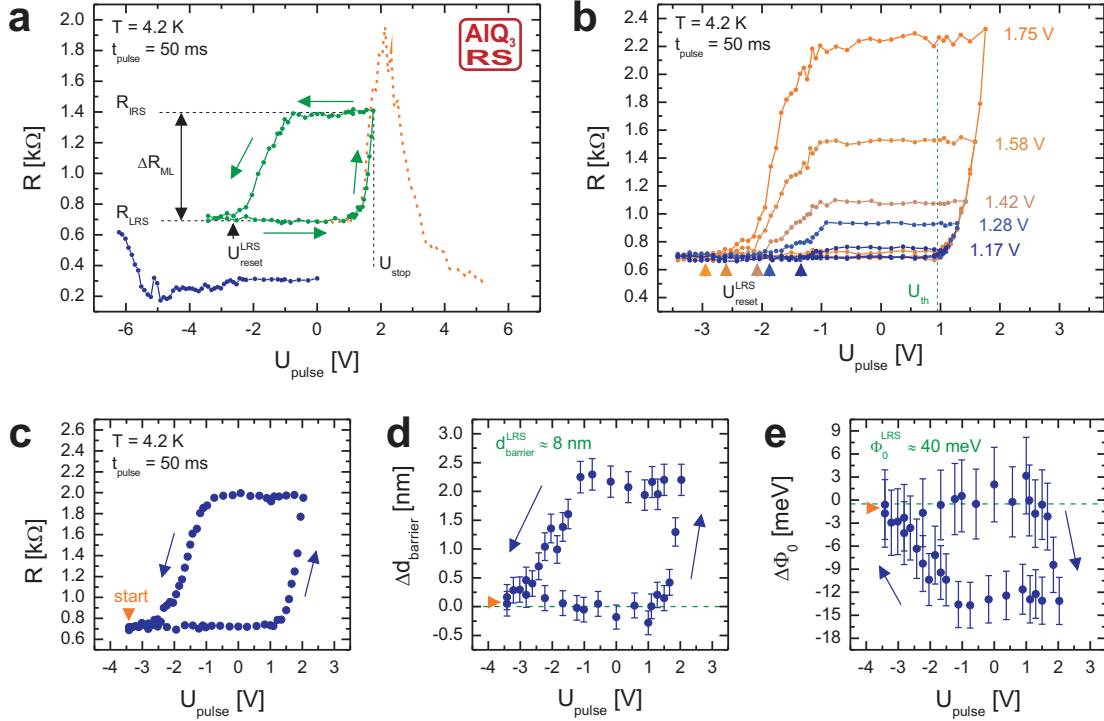
Figure 3.32: Results of RS minor-loop measurements. **a**: Illustration of the U_{pulse} sequence for an RS-ML yielding a closed, nearly symmetric resistance trace (green line). Prerequisite for this measurement is the preparation of the LRS (blue line). The dashed orange line represents the full RS cycle in the positive U_{pulse} range recorded after all RS-ML measurements. **b**: Five RS-MLs with different U_{stop} show that with increasing U_{stop} the loop gets wider and higher. The LRS is obviously stable. **c-e**: The tunnel barrier parameters, plotted in relation to the respective value for the LRS, are determined by employing Simmons fits for I/V curves recorded during the RS-ML shown in **c**. $d_{barrier}$ and Φ_0 obviously are re-established after a complete minor loop.

when the sweep is stopped at $U_{stop} = 1.75\,\text{V}$ in the positive range, a negative pulse with $U_{pulse} = U_{reset}^{LRS} \approx -3\,\text{V}$ has to be applied in order to completely restore the LRS, whilst for a relatively low U_{stop} of $1.28\,\text{V}$ the LRS is reached again already at $U_{reset}^{LRS} \approx -1.9\,\text{V}$. Thus, seemingly the RS-MLs are less symmetric at higher U_{stop}, i.e. the difference between $\left|U_{reset}^{LRS}\right|$ and U_{stop} is raised. This is also indicated by the arrows in the bottom left of Fig. 3.32**b** which represent the U_{reset}^{LRS} for the five different loops. A possible explanation for the different trends of U_{reset}^{LRS} and U_{stop} can be given assuming that the strength of the electric field applied to the barrier, i.e. $\mathcal{E} = \left|U_{pulse}\right|/d_{barrier}$, is governing the RS. Since $d_{barrier}$ is larger in the IRS compared to the LRS, the negative U_{pulse} that has to be applied to the IRS must be higher than the positive U_{pulse} applied to the LRS in order to obtain the same strength of $\mathcal{E}$. Effectively, this leads to the mentioned increase of the RS-MLs' asymmetry. Having outlined a theoretical description of the RS effect in chapter 3.7.2, this issue is addressed again in chapter 3.7.3.

In order to investigate the influence of the pulse length t_{pulse} on the RS behaviour, another series of RS-MLs is recorded for another device. A subset of the results, five RS-MLs with $U_{stop} = 1.95\,\text{V}$ which in this structure corresponds to a reversal of the sweep direction
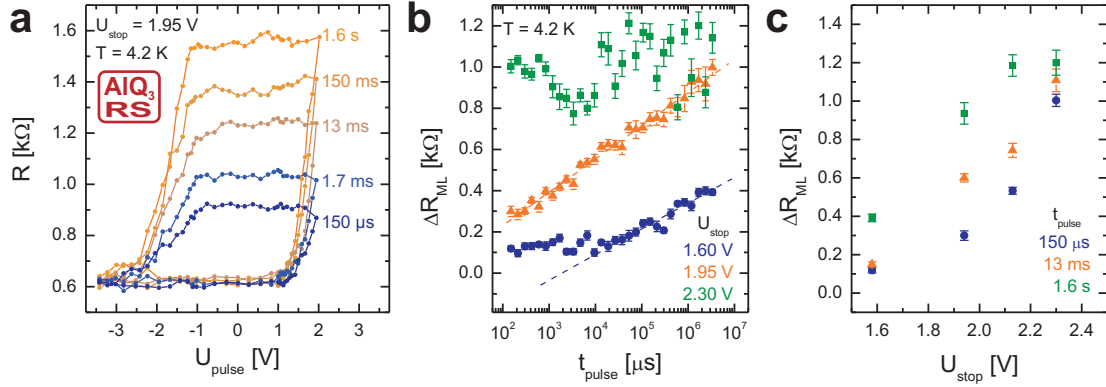
Figure 3.33: Influence of the pulse length on the RS behaviour. **a**: A clear relation between t_{pulse} and the resistance change ΔR_{ML} is found in RS-ML measurements where the sweep towards positive U_{pulse} is stopped at the center of the rising edge between the LRS and the HRS. **b**: The influence of t_{pulse} on the RS behaviour obviously also depends on U_{stop} of the respective RS-ML measurement employed for the investigation. **c**: Dependence of ΔR_{ML} on U_{stop} for three characteristic pulse lengths (equivalent to vertical intersections in **b**).

approximately at the center of the rising edge between the LRS and the HRS, is summarised in Fig. 3.33**a**. In each of the measurements t_{pulse} is increased by a factor of ~ 10 leading to an enhancement of ΔR_{ML}. In contrast to the previous experiment with different U_{stop}, the width of the loops does not change with t_{pulse}.

For a more detailed analysis four series with different U_{stop}, each of them comprising 40 RS-MLs with $t_{\text{pulse}} = 150\,\mu\text{s} - 3.3\,\text{s}$, are evaluated. For the representation of this experiment's results in Fig. 3.33**b** (only data of three RS-ML series are displayed) the ΔR_{ML} are computed from the mean values of R_{LRS} and R_{IRS}. The standard deviation of this averaging procedure is used for the error calculus. A semi-logarithmic representation [ΔR_{ML} plotted over $\log\,(t_{\text{pulse}})$] is chosen in order to enhance clarity.

The data sets in Fig. 3.33**b** reveal different relations between ΔR_{ML} and t_{pulse} depending on U_{stop}. When looking at low minor loops, i.e. those with a relatively low U_{stop}, a nearly constant ΔR_{ML} is obtained for $t_{\text{pulse}} \lesssim 10\,\text{ms}$, which is followed by a linear increase for longer pulses (blue circles). For intermediate U_{stop}, equivalent to RS-MLs ending at the center of the rising edge between the LRS and the HRS, the dependence of ΔR_{ML} on $\log\,(t_{\text{pulse}})$ can be considered linear for the whole t_{pulse} interval under investigation (orange triangles). Finally, when the RS-MLs are stopped near the HRS (green squares), a clear relation between ΔR_{ML} and t_{pulse} can hardly be discerned. On one side, apparently, the data points are statistically varying around $\Delta R_{\text{ML}} \approx 1\,\text{k}\Omega$ and, on the other side, a decisive interpretation is hampered by the increased noise in the single measurements which is reflected by the significantly larger error bars.

One can conclude here that the height of a minor-loop trace as well as the dynamics of the microscopic processes causing the RS do not only depend on U_{stop} but also on t_{pulse}. This twofold relation can also be demonstrated by another representation of a subset of the complete series' results. In Fig. 3.33**c** the height of the RS-ML is plotted against U_{stop} for three characteristic t_{pulse} (equivalent to vertical intersections in Fig. 3.33**b**). For relatively

short pulses ($t_{\text{pulse}} \lesssim 1.5\,\text{ms}$ for this device, blue circles) a non-linear, seemingly parabolic, dependence $\Delta R_{\text{ML}}(U_{\text{stop}})$ is obtained, similar to the one that can be extracted from the aforementioned results with different U_{stop} (see Fig. 3.32b). In an intermediate t_{pulse} interval ($\sim 1.5 - 150\,\text{ms}$, orange triangles) a rather linear increase of ΔR_{ML} is observed which starts from the same point as the data for short pulses. The same linear dependence can be discerned for $t_{\text{pulse}} \gtrsim 150\,\text{ms}$ (green squares). In this case, however, the data points are shifted towards lower U_{pulse}, i.e. for long low pulses a significantly larger ΔR_{ML} is measured than for shorter low pulses. Furthermore, ΔR_{ML} is obviously saturating for $U_{\text{pulse}} \gtrsim 2.1\,\text{V}$ here. Evidently, this interplay of U_{pulse} and t_{pulse} has to be considered when trying to draw conclusions with respect to the the processes that are causing the RS during the minor loops. For the following reasoning a very simplified scenario is employed in which again charged particles are the species governing the RS. Let it be assumed that these particles are constituting the tunnel barrier that consequently may be modified by a motion of them in the electric field $\mathcal{E}$ caused by the voltage pulses. In this case, ΔR_{ML} is very likely proportional to the distance traveled by these particles. The data acquired for low U_{stop} reveal that obviously for weak $\mathcal{E}$ a certain threshold time has to be surpassed in order to increase ΔR_{ML}. In the present scenario this observation may be indicative of some sort of inertia which has to be overcome. Since for intermediate U_{stop} an immediate response of ΔR_{ML} on t_{pulse} is obtained, $\mathcal{E}$ can be regarded as sufficiently strong in this case to allow for a rather free motion of the particles. The last case where the RS-MLs are swept almost up to the HRS and for which a decisive influence of t_{pulse} on ΔR_{ML} cannot be discerned would be equivalent to an equilibrium state in this picture. Such a behaviour may be explained by an opposing field which impedes a further motion of the particles, either generally or when a critical spatial distribution is reached.

Thus, the RS-ML investigations with different U_{stop} and t_{pulse} strongly suggest that the RS effect and the modifications of the tunnel barrier associated therewith may be described by the motion of charged particles at the interface between the LSMO electrode and the AlQ$_3$ layer. Unfortunately, this scenario does not comprise the changes of R outside the minor loops. Hence, presumably there are additional or other mechanisms equally contributing to the RS effect as it is likewise suggested by the results presented in the following.

The next experiment addresses the investigation of a temperature change's influence on a previously prepared resistive state and is performed according to the following protocol. Having prepared a resistive state at $T = 4.2\,\text{K}$ and recorded an I/V response, the sample is heated to a certain temperature setpoint T_{heat} in the range of $20 - 290\,\text{K}$. Subsequently, the system is left at T_{heat} for 10 minutes and cooled to $4.2\,\text{K}$ again where finally the I/V characterisation is repeated. From a comparison of the two I/V curves it can be concluded whether the resistive state under investigation has been modified by the described heating-cooling cycle or not.
The course and the results of the complete experiment conducted with $T_{\text{heat}} = 290\,\text{K}$ for the BRS, LRS and an IRS are summarised in Fig. 3.34. The top panels of Fig. 3.34 contain the pairs of I/V curves for each state. Having finished a single state's investigation the next state is prepared by the RS sweep that is shown in the bottom panels of Fig. 3.34. The I/V curves are compared on the basis of the average difference in device resistance ΔR_{T} before
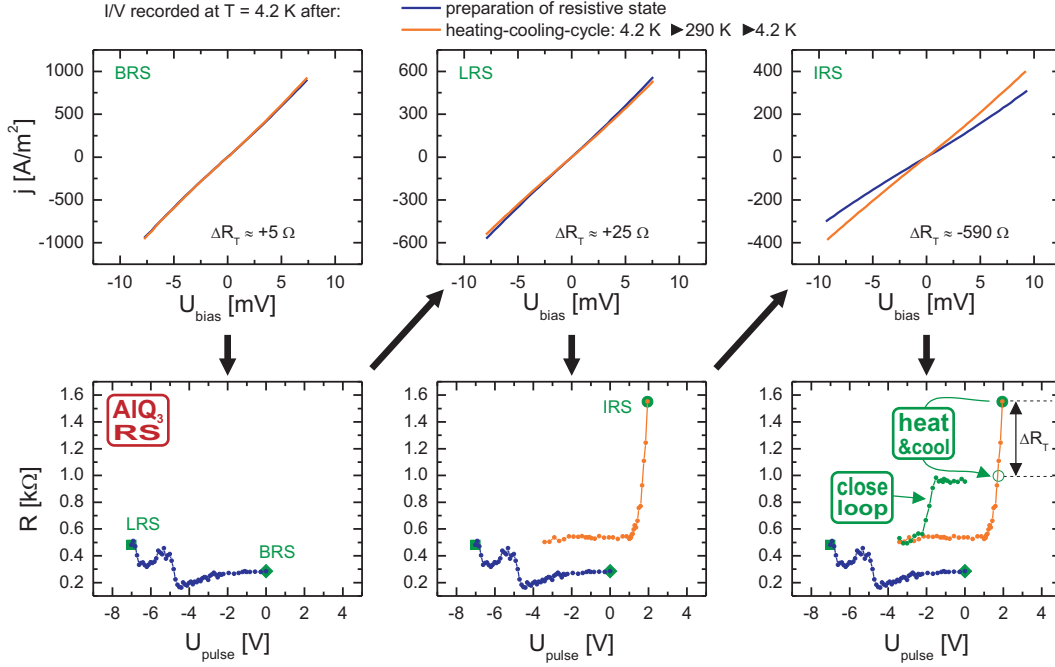
Figure 3.34: Influence of heating on resistive states investigated by heating-cooling cycles and I/V characterisation and analysis. The top panels display the two I/V curves for each state under investigation, recorded at 4.2 K before (blue line) and after (orange line) the heating cooling cycle with $T_{heat} = 290$ K. The RS trace swept for the preparation of the single states at 4.2 K is shown in the bottom panels. A comparison of the I/V traces allows for a conclusion whether the respective state has been modified or not. A change is only observed for the IRS, namely a reduction of R_{IRS} towards R_{LRS}, as illustrated in the bottom panel on the right hand side. Starting from the reduced IRS the RS-ML can be closed by applying negative voltage pulses.

and after the heating procedure. For the BRS (left hand side, top row) and LRS (center, top row) only a slight and negligible increase of R is observed. As a consequence thereof, no further evaluation is undertaken and these states are considered stable in the temperature interval between 4.2 K and 290 K. For the IRS (right hand side, top row), on the contrary, a significant change can already be discerned at first sight. The initial difference between the IRS and LRS of $\Delta R_{ML} \approx 1.1$ kΩ is reduced by $\sim 55\,\%$ as indicated in bottom right panel of Fig. 3.34. This strongly suggests that the LRS is energetically more favourable than the IRS.

As demonstrated, the supply of thermal energy leads to a decrease of R (measured by ΔR_T) when the device is in the IRS, i.e. the IRS can be considered reduced. The re-application of the same U_{pulse} that is used to prepare the IRS before the heating-cooling cycle can compensate this reduction and restore the initial IRS. Otherwise, starting from the reduced IRS the RS-ML can also be closed by sweeping U_{pulse} back into the negative range. The device is hereby set back to the same R_{LRS} that has served as starting point for the IRS's preparation (see bottom right panel of Fig. 3.34), as suggested by the LRS's stability demonstrated before.

Motivated by these findings a series of heating-cooling experiments is undertaken for different T_{heat} but the same RS-ML, i.e. the same LRS and IRS following the procedure described above. Starting from the LRS with $R_{\text{LRS}} \approx 0.5\,\text{k}\Omega$ a minor loop is partially swept until the IRS with $R_{\text{IRS}} \approx 1.6\,\text{k}\Omega$ is reached. Subsequently, a heating-cooling cycle including the aforementioned I/V characterisation is performed. Finally, the RS-ML is closed by sweeping U_{pulse} back into the negative range, i.e. the LRS is restored and serves as starting point of the next cycle with a different T_{heat}. The same RS-ML parameters are used for all $T_{\text{heat}} = 20 - 290\,\text{K}$. Fig. 3.35a comprises the result of this series of heating-cooling cycles represented as ΔR_{T} plotted against T_{heat}.

In the first instance, this data reveals that for $T_{\text{heat}} = 290\,\text{K}$ a quantitatively similar behaviour is observed as in the previously discussed preliminary experiment. The initially prepared difference between R_{LRS} and R_{IRS} of $\sim 1.05\,\text{k}\Omega$ is diminished by $\sim 55\,\%$. Moreover, ΔR_{T} is constantly decreasing for $100\,\text{K} < T_{\text{heat}} < 290\,\text{K}$, whilst for $T_{\text{heat}} < 100\,\text{K}$ it is not possible to clearly identify any difference between the I/V curves recorded before and after the heating-cooling-cycle.

The barrier parameters' modification induced by the heating-cooling procedure can be determined by the already known evaluation of the I/V curves. Similarly as ΔR_{T}, the results for d_{barrier} and Φ_0 are summarised as difference of the respective value before and after the heating-cooling cycle in Figs. 3.35b and c (error bars calculated from fit parameters). Considering the data in Figs. 3.35a-c it becomes obvious that ΔR_{T} has the same phenomenological origin as any ΔR initiated by a voltage pulse. Evidently, d_{barrier} is reduced and Φ_0 is enhanced during the heating-cooling cycle. This strongly suggests that the actual microscopic processes that cause the thermally induced ΔR_{T} are identical or at least very similar to those involved in the RS dynamics investigated in other experiments.
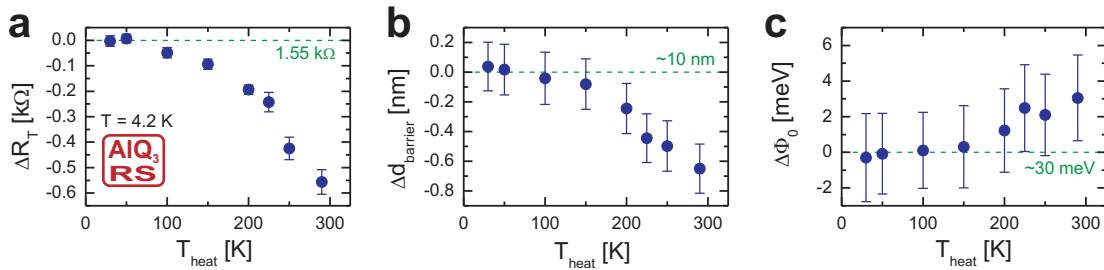
Figure 3.35: Summary of the results of a series of heating-cooling cycles. From the I/V analysis the influence of heating on the same IRS, which is freshly prepared for each data point, can be observed. **a-c**: Change of R and the barrier parameters plotted against T_{heat}. For $T_{\text{heat}} \geq 100\,\text{K}$ a significant modification of the resistive state can be discerned. The reference in each plot (dashed green line) is the respective value determined directly after the IRS's preparation, i.e.before the heating procedure.

To conclude this chapter it can be stated that on the basis of transport measurements a lot of characteristic features of the RS effect presented at the beginning of this chapter can be unveiled. These findings can be condensed into a model that phenomenologically explains the microscopic mechanisms causing this effect and is outlined in the next chapter.

3.7.2 Theoretical Description of the Resistive Switching Effect

It has already been insinuated before that, so far, only a few results with respect to RS effects in devices comprising an LSMO electrode and an AlQ$_3$ layer have been reported [Hueso07,Prezioso11,Prezioso12]. Likewise, the two approaches brought up by Prezioso *et al.* to explain the bipolar RS in their spin-valve devices and its interplay with the MR effect are presented in chapter 2.3.2. These scenarios, involving trapping domains [Prezioso11], on one side, and highly conducting filaments [Prezioso12], on the other side, cannot be taken into account as explanation of an RS behaviour that goes beyond bipolar RS as it is observed in the present TAMR devices. Furthermore, they do not comprise any modification of the interface LSMO-AlQ$_3$ which, however, necessarily has to be involved in any theoretical description. The latter requisite is stemming from the clear correlation between the TAMR amplitude and the resistive state which is found in the TAMR devices. Neither can the existing models for dedicated RS devices comprising an AlQ$_3$ layer and non-magnetic electrodes, which are outlined in chapter 2.3.2, be deemed applicable here for similar reasons. Therefore, an alternative explanation of the observed RS effect addressing all characteristic results presented in the previous chapter will be outlined hereafter.

As a first step towards a phenomenological model, the RS trace is now regarded as consisting of two components. The distinction between these two components is based on the observation presented at the end of the previous chapter, namely that for different resistive states different responses upon an interim temperature change are found. This can be considered as strong indication that the respective changes in R are originating from, in a certain sense fundamentally, different mechanisms leading to the following split-up of the RS. On one side, R is evidently in a temperature-stable state after the transitions BRS→LRS and HRS→BRS. These switchings are the first component of the RS trace and referred to as major loop hereafter. The second one is the already known minor loop that, on the other side, comprises resistive states (IRS and HRS) and changes in R ($R_{\text{LRS}} \to R_{\text{IRS/HRS}}$ and vice versa) which are substantially modified at elevated temperatures.

As aforementioned, the HRS does not appear as a sizeable change of R when, starting from the BRS, voltage pulses with positive polarity are immediately applied. Therefore, the transition BRS→LRS can be regarded as enabling procedure that sets the device to a state in which the HRS can be observed and RS-MLs can be swept. Analogously, the back-switching to the BRS is the reverse, disabling process. Thus, although the different temperature stabilities suggest different microscopic mechanisms involved in the two components of the RS trace, there must be an interlink between them resulting in the described enable/disable-functionality. In the proposed theoretical description this interlink is taken into account by the second key assumption that only one unique species of defects is involved in the RS effect. Hence, there are two key assumptions based on which a model of the RS readily explaining all experimental observations can be elaborated. A short summary thereof should be anticipated here: during the major loop transitions at high voltage pulses, defects constituting the tunnel barrier are added to the interface LSMO-AlQ$_3$ and removed from it, respectively, whereas the minor loop behaviour can be ascribed to these defects' motion in the electric field caused by U_{pulse}.

The main question that should be addressed next is what kind of defects may be considered governing the RS. A first hint towards an answer comes from a contemplation of the materials at the interface where the RS is unambiguously caused, namely LSMO and AlQ$_3$. As mentioned in the introductory paragraph of this chapter and in chapter 2.3.2, any existing model for the description of RS effects in devices comprising either an LSMO-AlQ$_3$-interface or an AlQ$_3$ layer only is not capable to explain an effect which goes beyond bipolar switching. Together with the negative results obtained in a reference device in which the LSMO contact is replaced by a Pt electrode (see appendix E) this suggests the exclusion of any intrinsic effect in the OSC layer causing the RS.
Furthermore, as discussed above, it seems rather implausible that the two parts of the RS trace, major and minor loop, can be treated completely independently. Hence, a scenario where the major loop transitions are caused in the LSMO electrode and those of the minor loop in the AlQ$_3$ layer or vice versa can likewise be discarded. Consequently, it is very likely that the microscopic origin of the RS effect has to be located in the LSMO electrode, which, however, must not be understood in the sense that an eminent role of the specific interface LSMO-AlQ$_3$ can be excluded.

In contrast to MIM devices employing OSC layers, for oxide-based devices quite a lot experimental and theoretical work has been published (see chapter 2.3.1). Many results indicate that processes changing the oxide's stoichiometry with respect to the oxygen content are causing the RS effect in the respective structures [Baikalov03, Sawa04, Waser07]. Additionally, the effect of oxygen deficiency on the physical properties of perovskite manganites is extensively investigated and well understood. In chapter 2.4.4 it has already been insinuated that, especially for LSMO, such investigations have brought forth a lot of insight into this correlation, which can be briefly summarised as follows. An increased concentration of oxygen vacancies (V_Os) in a thin LSMO layer changes the structure of this layer due to an increase of the lattice strain. Hence, a decreased oxygen content has a deteriorating influence on the layer's structural, magnetic, and electronic properties which can be regarded as related to each other [Goyal97, Rajeswari98, Tsui00, Dho03, Li05, deJong05].
Very often the stoichiometry of LSMO is modified during (PLD) layer growth by changing the oxygen partial pressure [Goyal97, Rajeswari98, Dho03] or afterwards by performing suitable annealing procedures [Li05, deJong05]. As already stated in chapter 2.3.1, V_Os in oxides can also be generated or removed, for instance, by electrochemical redox reactions. Recently it has been shown by Jeong *et al.* that such reactions can be initiated in vanadium dioxide by a (locally) strong electric field $\mathcal{E}$ [Jeong13]. Another way to create V_Os in LSMO has been demonstrated by Homonnay *et al.* [Homonnay] for thin LSMO layers fabricated with the same equipment as those used for the present devices. The deposition of non-noble metals on top of an LSMO layer can induce a partial loss of its magnetisation and a change of its crystal structure, both unambiguously originating from the extraction of oxygen.
Considering these widely recognised findings, it therefore seems reasonable to assume that the tunnel barrier between the LSMO electrode and the AlQ$_3$ layer is partially formed by an oxygen deficient sublayer in the former. This component of the barrier is seemingly modified due to the applied voltage pulses in an RS experiment. A rather small and constant additional contribution to the tunnel barrier is provided by the actual injection barrier (contact

barrier) at the LSMO-AlQ$_3$ interface (see chapter 2.2.1).

In summary, these considerations result in the following third basic assumption for the proposed model. The defect species involved in the microscopic mechanisms behind the RS effect are Frenkel pairs of one V$_O$ and one interstitial oxygen ion (O$_{is}^{2-}$, [Dong07]). They can be formed inside the LSMO electrode near its surface by removal of lattice oxygen ions onto interstitial sites in a strong electric field. As discussed in chapter 2.3.1, the retention of the removed oxygen ions near the V$_O$s is mandatory for a reversible RS.

The particular microscopic processes causing the transitions during an RS cycle will now be outlined in detail for six distinguished points of the typical RS trace depicted in Fig. 3.36**a**. For each of these points the barrier is displayed together with a schematic drawing of the LSMO layer's composition (further information can be found in the figure legend). Furthermore, the strength and direction of $\mathcal{E}$, which is causing any modification, is indicated by the blue arrow in the top of each panel.

For the sake of clarity, again the simplified picture of a rectangular barrier is used for the graphical representation. This is consistent with the analytical treatment of the I/V curves using the Simmons model in the previous chapter and sufficient for the understanding of the model and basic quantitative considerations. Moreover, the detailed shape of the barrier, on the contrary, could only be obtained by determining the exact distribution of V$_O$s in the LSMO layer for each of the resistive states. This distribution, however, is not accessible in the experiments undertaken for the devices under discussion.

Fig. 3.36**b** shows the initial situation in the BRS with a relatively thin and high barrier which is originating from the injection barrier and a thin oxygen deficient layer at the LSMO electrode's surface [deJong05]. The presence of a tunnel barrier in the BRS is experimentally proved by positive TAMR results (see chapter 3.4.1 where only results of experiments with a device in the BRS are presented).

For the major loop switching BRS→LRS an increase of d_{barrier} is revealed by the I/V analysis. In the proposed scenario, this transition is therefore equivalent to the creation of V$_O$s at the interface LSMO-AlQ$_3$ via the aforementioned mechanism (Fig. 3.36**c**). As a consequence of the particles' charge (V$_O$s in perovskites carry a relative positive charge, [Waser90]), $\mathcal{E}$ additionally results in a separation of the defects. V$_O$s are collected at the surface of the LSMO layer enhancing d_{barrier}, whilst the negatively charged O$_{is}^{2-}$ ion are pushed away from it into the bulk. Furthermore, also the barrier height Φ_0 is changed at this point of the RS trace. This can be integrated into this model by the assumption that Φ_0 depends on the charge density at the interface which itself is evidently related to the concentration of vacancies c_{V_O}. This is equivalent to the resemblance to the situation in a p/n-junction which already has been outlined in the previous chapter.

V$_O$s can be regarded as relatively mobile defects in perovskite oxides [Waser90] which readily explains the minor-loop trace (orange line in Fig. 3.36**a**). At intermediate positive U_{pulse}, where $\mathcal{E}$ is still too weak to significantly move the rather immobile O$_{is}^{2-}$ ions, V$_O$s are pushed away from the interface and R increases (LRS→IRS/HRS, Figs. 3.36**d** and **e**). Likewise, they are attracted to it during the minor-loop transition IRS→LRS (not included
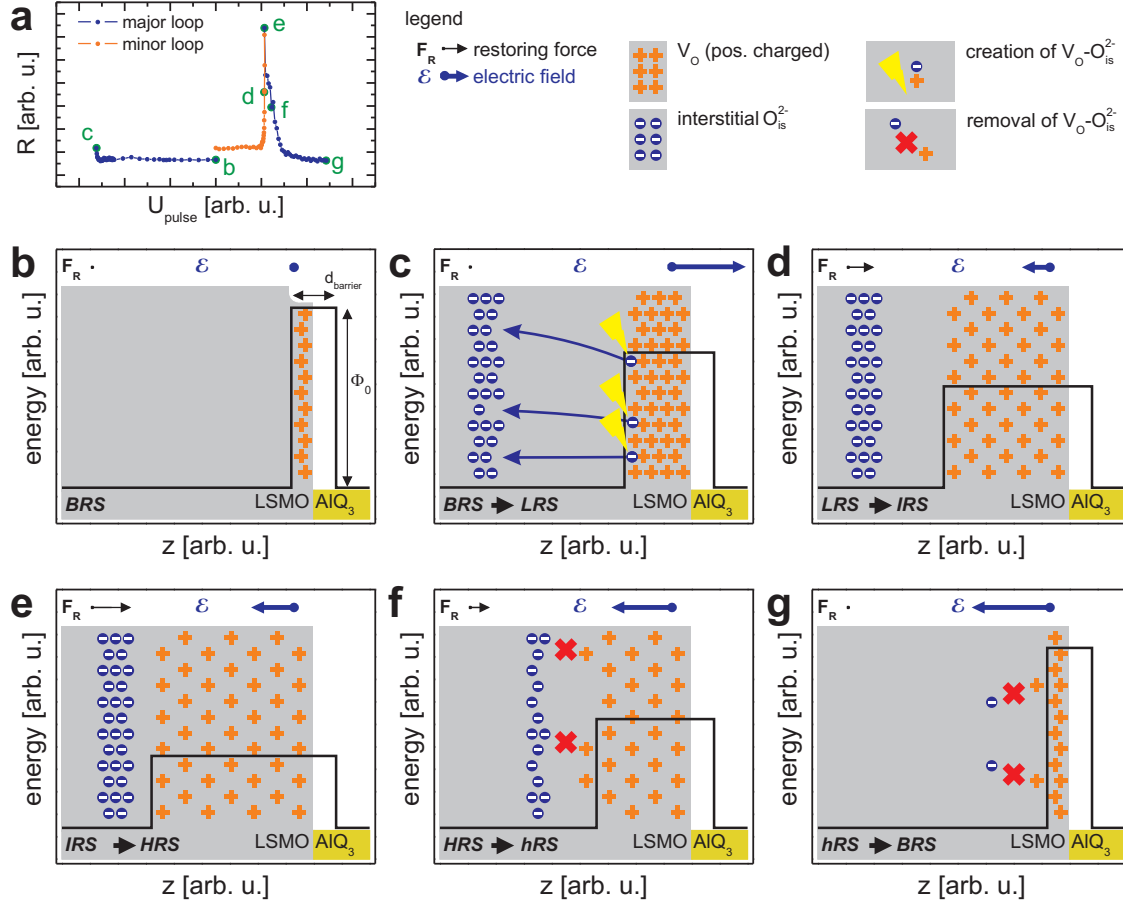
Figure 3.36: Schematic qualitative representation of the model explaining the RS in AlQ$_3$-based TAMR devices. The model includes the separation of the RS trace into the major and the minor loop (**a**). Distinct points are marked for which the interface LSMO-AlQ$_3$ is sketched in panels **b-g**. Arrows in the top of each panel illustrate the strength and direction of the electric field $\mathcal{E}$ and the restoring force $\boldsymbol{F}_R$ originating from the lattice distortion that is caused by the change of stoichiometry. Starting from the BRS with a high and thin barrier (**b**) the initial negative voltage pulse moves oxygen ions from their lattice site into the LSMO as interstitials (O$_{is}^{2-}$ ions), leaving V$_O$s at the surface (**c**). An increasing reverse voltage creates a broadening of the V$_O$s' distribution while keeping their number constant, causing an increase of the barrier thickness and a decrease of the barrier height (**d** and **e**). When the field is strong enough, V$_O$s and O$_{is}^{2-}$ ions recombine (**f**) and the initial state is restored (**g**). The intermediate state during the transition HRS→BRS is labeled hRS here.

in Fig. 3.36). Hereby both their spatial distribution and c_{V_O} are changed leading to a modification of both barrier parameters and finally a change in R. The influence of the increasing barrier thickness is stronger than that of the decreasing barrier height (see appendix F), i.e. a broader distribution yields a higher R.

At this point of the discussion, the restoring force $\boldsymbol{F}_R$ should be introduced. $\boldsymbol{F}_R$ is originating from the lattice distortion which, itself, is caused by the introduction of additional V$_O$s [Li05]. Since the distortion has a lower energy at the LSMO layer's surface, a wider distribution of the V$_O$s as present in the IRS and HRS is equivalent to a higher energy state. Thus, $\boldsymbol{F}_R$

is the force restoring the configuration with minimal distortion energy. The strength and direction of $\boldsymbol{F}_\mathrm{R}$ is indicated by the black arrows in the top of each panel. It is also worth noting that, regarding the IRS's and HRS's stability at 4.2 K, obviously at low temperatures $\boldsymbol{F}_\mathrm{R}$ is too weak (and the V$_\mathrm{O}$s' mobility too low) to move the V$_\mathrm{O}$s.

Turning back to the RS trace, at sufficiently high U_pulse (strong $\boldsymbol{\mathcal{E}}$) in the positive range the V$_\mathrm{O}$- and O$_\mathrm{is}^{2-}$ - distribution are approaching each other (Figs. 3.36e and f). This is because, on the one hand, the O$_\mathrm{is}^{2-}$ ions start to move and, on the other hand, d_barrier is sufficiently increased. At this point, the aforementioned creation mechanism can take place reversely, i.e. effectively V$_\mathrm{O}$s are removed and a decrease of R is observed in the RS trace (HRS→BRS, Figs. 3.36f and g).

In the next chapter it will be demonstrated that this approach does not only phenomenologically explain the typical RS loop but also allows, to a certain extent, for a quantitative analysis of minor-loop results and explicitly includes particular features of the effect, namely those revealed by the heating-cooling experiments.

3.7.3 Application of the Model to Experimental Results

First, the results of RS-MLs acquired with increasing U_stop should be considered now. It becomes clear from the respective data (see Fig. 3.32b) that the minor loops' height ΔR_ML is related to U_stop non-linearly. On the basis of the proposed model and a further simplifying assumption this relation can be analysed. In the scenario outlined above the increase of R during the minor-loop switching LRS→IRS is due to a motion of V$_\mathrm{O}$s in the applied $\boldsymbol{\mathcal{E}}$, which changes the V$_\mathrm{O}$ distribution and hereby, in the first instance, d_barrier. It is now assumed that the V$_\mathrm{O}$s' motion is only influenced by $\boldsymbol{\mathcal{E}}$ and can be described as a uniformly accelerated motion with the velocity $v_\mathrm{V_O}$ and acceleration $a_\mathrm{V_O}$:

$$d_\mathrm{barrier} = d_\mathrm{barrier,0} + v_\mathrm{V_O} t_\mathrm{pulse} = d_\mathrm{barrier,0} + a_\mathrm{V_O} t_\mathrm{pulse}^2 \tag{3.9}$$

$d_{barrier,0}$ is the initial barrier thickness (barrier thickness in the LRS). With a V$_\mathrm{O}$'s charge q and its mass m the acceleration can be transformed using

$$a_\mathrm{V_O} = \frac{F}{m} = \frac{q\mathcal{E}}{m} \tag{3.10}$$

and eventually, Equ. 3.9 can be written as:

$$d_\mathrm{barrier}(U_\mathrm{single}) = d_\mathrm{barrier,0} + \frac{q}{m} \frac{U_\mathrm{single}}{d_\mathrm{barrier}(U_\mathrm{single})} t_\mathrm{pulse}^2 \tag{3.11}$$

Equ. 3.11 describes the influence of a single voltage pulse U_{single} on d_barrier and can be further simplified by combining all constants to $\alpha = q t_\mathrm{pulse}^2 / m$. With this, the following solution is obtained for $\Delta d_\mathrm{barrier} = d_\mathrm{barrier}(U_\mathrm{single}) - d_\mathrm{barrier,0}$:

$$\Delta d_\mathrm{barrier}(U_\mathrm{single}) = \frac{-d_\mathrm{barrier,0}(\overset{+}{-}) \sqrt{d_\mathrm{barrier,0}^2 + 4\alpha U_\mathrm{single}}}{2} \tag{3.12}$$

During a measurement a number of pulses between $0\,\mathrm{V}$ and U_pulse is applied to the barrier which leads to a total $\Delta d_\mathrm{barrier}(U_\mathrm{pulse})$ that can be calculated by integrating $\Delta d_\mathrm{barrier}(U_\mathrm{single})$. This integration yields:

$$
\begin{aligned}
\Delta d_\mathrm{barrier}(U_\mathrm{pulse}) &= \int_0^{U_\mathrm{pulse}} \Delta d_\mathrm{barrier}(U_\mathrm{single})\,dU_\mathrm{single} \\
&= \frac{1}{2}\left(-d_\mathrm{barrier,0}U_\mathrm{pulse} + \frac{\left(d_\mathrm{barrier,0}^2 + 4\alpha U_\mathrm{pulse}\right)^{3/2}}{6\alpha} - \frac{d_\mathrm{barrier,0}^3}{6\alpha}\right)
\end{aligned}
\tag{3.13}
$$

Before the formula displayed in Equ. 3.13 is used to fit the experimental results, another simplifying assumption has to be made. As mentioned earlier, U_pulse seemingly needs to overcome a certain threshold U_th until a significant change of R appears in an RS-ML measurement. Therefore, it appears justified to replace U_pulse by $U_\mathrm{pulse} - U_\mathrm{th}$ in Equ. 3.13 hereafter:

$$
\begin{aligned}
d_\mathrm{barrier}(U_\mathrm{pulse}) &= d_\mathrm{barrier,0} + \Delta d_\mathrm{barrier}(U_\mathrm{pulse} - U_\mathrm{th}) \\
&= \frac{1}{2}\left(-d_\mathrm{barrier,0}\left(U_\mathrm{pulse} - U_\mathrm{th}\right) + \frac{\left[d_\mathrm{barrier,0}^2 + 4\alpha\left(U_\mathrm{pulse} - U_\mathrm{th}\right)\right]^{3/2}}{6\alpha}\right. \\
&\qquad\qquad\qquad\qquad\qquad\left. - \frac{d_\mathrm{barrier,0}^3}{6\alpha}\right) + d_\mathrm{barrier,0}
\end{aligned}
\tag{3.14}
$$

To a certain extent, this simplification also takes into account that the voltage drop on the barrier is only a fraction of the total applied voltage (see also Fig. 3.30d). The expression in Equ. 3.14 is now employed to fit the results that are gained by I/V characterisation and Simmons analysis for d_barrier during an RS-ML loop (data points in Fig. 3.37a). $d_\mathrm{barrier,0}$, U_th and α are the fit parameters, whereby $d_\mathrm{barrier,0}$ and U_th are limited to a certain interval that is determined by the experimentally obtained values.

The best reproductions of the experimental $d_\mathrm{barrier}(U_\mathrm{pulse})$ which can be calculated using Equ. 3.14 are shown in Fig. 3.37a (orange lines) for both minor-loop transitions. For the opposite switching IRS→LRS, obviously, the fit function has to be modified slightly in order to obtain a negative $\Delta d_\mathrm{barrier}(U_\mathrm{pulse})$. It can be seen that a rather good description of the results is provided by the fit for LRS→IRS, whilst a larger aberration is present for the back-switching process. A possible explanation for these differently pronounced discrepancies between fit and experimental data lies in the simplifications made above. It is assumed that the V_Os' motion is only influenced by the electric field, and any other force or field, be it enhancing or hampering the motion, is excluded.
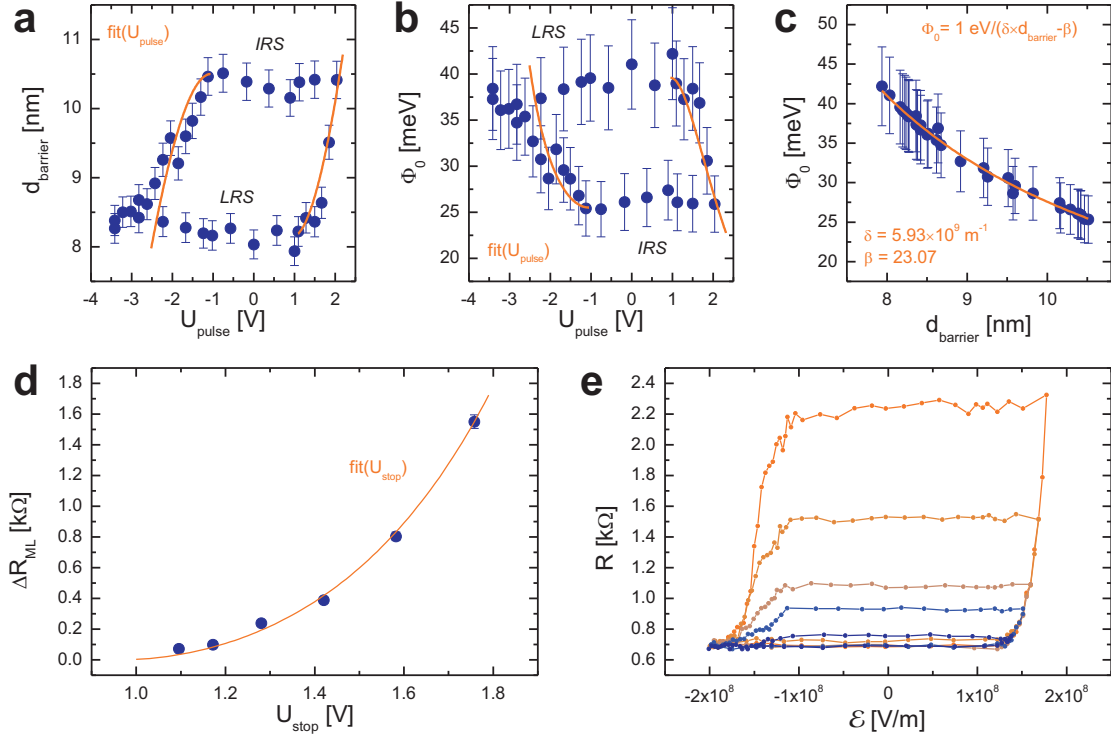
Figure 3.37: Analysis of RS-ML traces of different height and width using fitting procedures derived from the proposed model. **a**: Change of d_{barrier} during a minor loop determined by Simmons fits (see also Fig. 3.32**d**). The orange curves are the results of fits calculated using Equ. 3.14. **b**: Change of Φ_0 during the same RS-ML experiment. Here, the orange curves are calculated from the fit data for d_{barrier} (see **c**). **c**: Plotting Φ_0 against d_{barrier} taken from **a** and **b**, respectively, reveals a clear correlation between the barrier parameters which is employed to calculate the Φ_0 traces in **b** from the d_{barrier} fit in **a**. **d**: From both computed barrier parameters the dependence of the minor loops' height ΔR_{ML} on U_{stop} can be reproduced on the basis of the Simmons model (Equ. F.5). The data points are taken from Fig. 3.32**d**. **e**: Knowing the relation between d_{barrier} and U_{pulse} the RS-ML traces with different U_{stop} (see also Fig. 3.32**b**) can likewise be plotted against the electric field strength $\mathcal{E}$ resulting in nearly perfectly symmetric hysteresis loops.

One of these additional forces, the restoring force $\boldsymbol{F}_{\text{R}}$ originating from the lattice distortion when the V$_{\text{O}}$s are widely distributed in the LSMO layer, has already been introduced in chapter 3.7.2. Likewise, it has been insinuated and argued there that $\boldsymbol{F}_{\text{R}}$, which is forcing the system back into the LRS and consequently retarding the transition LRS→IRS, can very likely be neglected at low temperatures. Therefore, the simplified expression for $d_{\text{barrier}}(U_{\text{pulse}})$ yields a rather good description in this case.

During IRS→LRS, on the contrary, another force has to be taken into account. Here, the V$_{\text{O}}$ distribution has to be compressed by $\boldsymbol{\mathcal{E}}$ at the surface which, of course, is a process limited by a certain maximum V$_{\text{O}}$ concentration that must not be overcome. Consequently, also during the back-switching the V$_{\text{O}}$s' motion is hampered by an opposing force $\boldsymbol{F}_{\text{O}}$. Simplistically, it is plausible to expect that the influence of $\boldsymbol{F}_{\text{O}}$ can be regarded as not depending on the temperature due to its origin. Thus, the larger deviations between fit and experimental data for the transition back to the LRS might be originating from the missing integration of $\boldsymbol{F}_{\text{O}}$

into the calculus.

The data describing $d_{\mathrm{barrier}}(U_{\mathrm{pulse}})$ can be further used to find a fit to Φ_0 as well (Fig. 3.37**b**). The Φ_0 trace is calculated exploiting the fact that there is a clear correlation between d_{barrier} and Φ_0 which is illustrated in Fig. 3.37**c**. It should be mentioned here that this relation agrees pretty well with the assumption made above concerning the dependence of Φ_0 on the V_O concentration, which suggests in the first instance $\Phi_0 \propto 1/d_{\mathrm{barrier}}$. Evidently, the experimental and calculated values of $\Phi_0(U_{\mathrm{pulse}})$ in Fig. 3.37**b** exhibit a congruence that is comparable to this of the respective $d_{\mathrm{barrier}}(U_{\mathrm{pulse}})$ data in Fig. 3.37**a**.
In appendix F, furthermore, an equation is given that allows to calculate ΔR_{ML} from the barrier parameters (Equ. F.5). Based on this equation and the fit results for d_{barrier} and Φ_0, the RS-ML height as a function of the maximum positive pulse voltage U_{stop}, i.e. $\Delta R_{\mathrm{ML}}(U_{\mathrm{stop}})$, can be computed as shown in Fig. 3.37**d**. Again, the calculated curve (orange line) nicely reproduces the experimental results that are taken from Fig. 3.32**d**.

Moreover, the expression for $d_{\mathrm{barrier}}(U_{\mathrm{pulse}})$ can be exploited to present the minor-loop traces from Fig. 3.32**d** in another, and in certain aspects more conclusive manner, namely as plots of R against the electric field $\mathcal{E}$. In this representation, which can be found in Fig. 3.37**e**, the hysteresis loops are almost perfectly symmetric, i.e. the transitions LRS→IRS and back again occur at the same $|\mathcal{E}|$ in the positive and negative range. Hence, the apparent increase of the RS-MLs' asymmetry with increasing U_{stop}, which has already been discussed in chapter 3.7.1, is very likely stemming from the chosen representation only as presumed before.

The next logical step is a similar analysis of the pulse length's influence on the RS dynamics. Therefore, t_{pulse} has to be extracted from $\alpha = q/m \cdot t_{\mathrm{pulse}}^2 = \alpha^{\star} \cdot t_{\mathrm{pulse}}^2$ in Equ. 3.12:

$$\Delta d_{\mathrm{barrier}}(U_{\mathrm{single}}, t_{\mathrm{pulse}}) = \frac{-d_{\mathrm{barrier},0}(\pm) \sqrt{d_{\mathrm{barrier},0}^2 + 4\alpha^{\star} U_{\mathrm{single}} t_{\mathrm{pulse}}^2}}{2} \tag{3.15}$$

Subsequently, two integrations of Equ. 3.15, one over U_{single} and one over t_{pulse}, are performed yielding a rather spacious expression for $d_{\mathrm{barrier}}(U_{\mathrm{pulse}}, t_{\mathrm{pulse}})$ which then can be employed to find a fit for the data already evaluated above (see Equ. G.1). Again, the fit parameters are limited to a certain interval determined by the experimental results and measurement parameters. Figs. 3.38**a** and **b** show the best fits for d_{barrier} and Φ_0 which can be obtained with $t_{\mathrm{pulse}} = 50\,\mathrm{ms}$ (actual pulse length employed in the experiments). The quality of these reproductions is comparable to this of the ones presented above where only U_{pulse} is taken into account (Figs. 3.37**a** and **b**). A similar conclusion can be drawn with respect to the RS-ML height's dependence on U_{stop} calculated from the fit parameters (Fig. 3.38**c**).

However, when these fit parameters are used to describe the interaction between U_{stop} and t_{pulse} which is found experimentally (see Fig. 3.33), the limits of this theoretical framework are clearly unveiled. This becomes obvious when comparing computed and experimental data for the minor-loop height ΔR_{ML} as a function of t_{pulse} which is summarised in Fig. 3.38**d**. The experimentally determined $\Delta R_{\mathrm{ML}}(t_{\mathrm{pulse}})$ is plotted for three different fixed U_{stop} in the
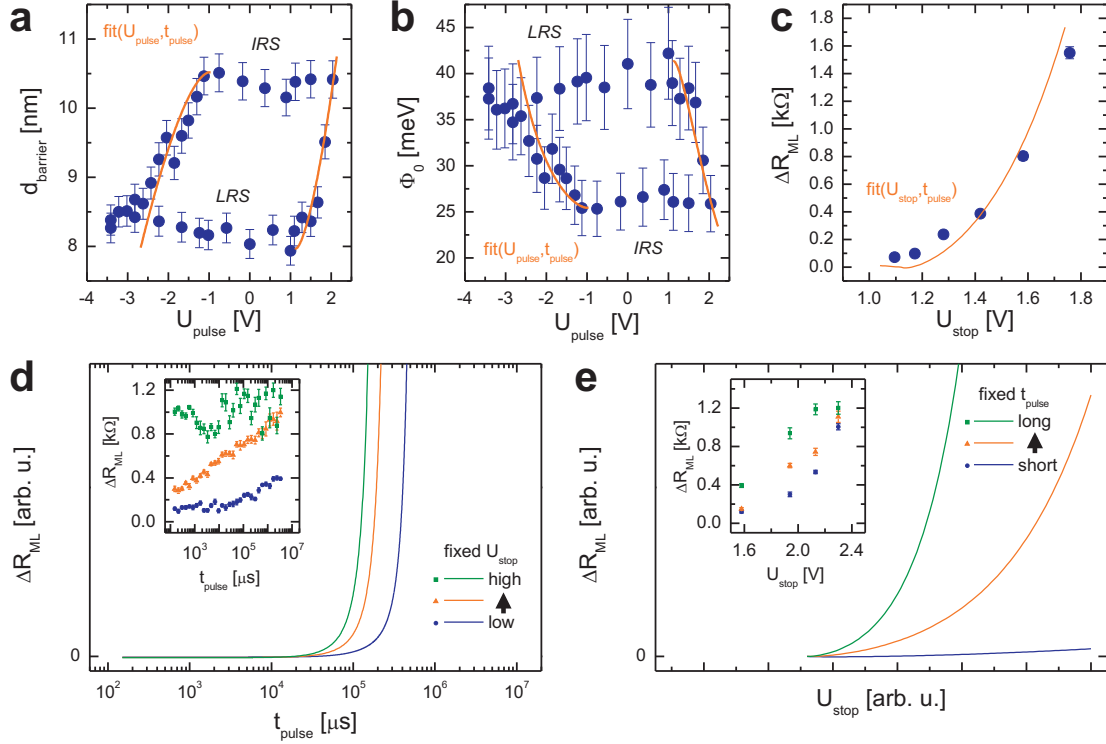
Figure 3.38: Application of the theoretical approach to minor-loop measurements recorded with different t_{pulse}. **a**: Dynamics of $d_{barrier}$ determined during a minor loop and the respective fit calculated using a function of U_{stop} and t_{pulse}. Again the fit variables are limited to an interval specified by experimental results and measurement parameters. **b**: A similarly good agreement between theory and experiment is found for Φ_0. **c**: From both computed barrier parameters the dependence of the minor loops' height on U_{stop} can be reproduced. t_{pulse} is set to the value used in the experiments ($t_{pulse} = 50\,\text{ms}$) for the calculated traces in **a-c**. **d** and **e**: Two representations of the interaction between U_{stop} and t_{pulse} with respect to the RS-ML dynamics. The insets contain the experimental results from Fig. 3.33. The data in the main panels are calculated using the parameters describing the barrier dynamics determined by the fits in **a** and **b**. The lack of congruence between calculus and experiment demonstrates the limits of the theoretical framework.

inset (taken from Fig. 3.33**b**), whilst the main panel contains the corresponding calculated curves for the same t_{pulse} range. Although the calculation yields different traces for different U_{stop}, these cannot be considered even rudimentarily matching the experimental data. The same conclusion has to be drawn for the alternative representation of ΔR_{ML} as a function of U_{stop} for different fixed t_{pulse} (Fig. 3.38**e**).

Consequently, at this point it has to be stated that obviously a more extensive approach is necessary to fully describe the V$_O$s' motion. As discussed above, such a theoretical description would also take influences beyond the applied electric field into account. In addition to the already mentioned retarding forces $\boldsymbol{F}_O$ and $\boldsymbol{F}_R$, the fact that for high RS-MLs (equivalent to high U_{stop}) hardly any influence of t_{pulse} on ΔR_{ML} is measurable should be borne in mind in this context. Considered cumulatively, these demands very likely result in a quite high complexity of a potential theoretical framework, which therefore goes beyond the scope of the present work.

A similar reasoning has to be brought up with respect to a further analytical interpretation of the major-loop transitions. For this purpose a deeper insight into the interface LSMO-AlQ$_3$ of a specific device, e.g. with respect to the energetic landscape and the exact defect distribution, is mandatory, however, cannot be provided here. Furthermore, it was equally helpful to know more about the exact reactions taking place during the RS major loop or, in other words, the microscopic mechanisms leading to the creation and annihilation, respectively, of pairs of V$_O$s and O$_{is}^{2-}$ ions.

Another obstacle to a precise and complete theoretical framework has already been stated in chapter 3.7.1. The loci of major-loop switching events on the U_{pulse} scale are varying significantly from device to device suggesting that local characteristics of the interface LSMO-AlQ$_3$ are governing the RS effect here. Thus, the proposed model unfortunately cannot be translated into and sustained by concrete calculations. However, a short comparison with results from the literature for RS in other materials can be undertaken yielding a good agreement with respect to the strength of the electric field that has to be applied in order to initiate the processes of V$_O$ creation and removal [Baikalov03, Dong07, Nian07, Sawa08, Yang09]. Usually, values in the range of $\sim 10^7 - 10^9$ V/m are reported for $\mathcal{E}$ which is well comparable to the situation in the present experiments (see Fig. 3.37e).

Turning back to the application of the proposed scenario, now the results of heating-cooling experiments should be addressed. These experiments reveal that, on the one hand, the BRS and LRS are obviously stable upon an interim temperature enhancement, whereas, on the other hand, the IRS/HRS is substantially modified. The IRS's/HRS's modification is observed as a decrease of R and $d_{barrier}$ and an increase of Φ_0.

This can be readily understood when taking the influence of $\boldsymbol{F}_R$ into account. $\boldsymbol{F}_R$ is the restoring force that originates from the lattice distortion present in states with a spatially extended V$_O$ distribution. At low temperatures, the V$_O$s' mobility is too low to allow for any significant influence of the relatively weak $\boldsymbol{F}_R$. At elevated temperatures, however, $\boldsymbol{F}_R$ can drag the V$_O$s back to the surface due to their enhanced mobility. Obviously, and as observed experimentally, this only applies for states that depend on the V$_O$ distribution's width, i.e. the IRS and HRS. The LRS and BRS, on the contrary, already represent states with a minimised distortion energy. This reasoning is similar to the one proposed by Nian *et al.* [Nian07] who have also observed a temperature dependent relaxation of resistive states which can be attributed to a strain enhanced diffusion of defects (V$_O$s and oxygen ions in Pr$_{0.7}$Ca$_{0.7}$MnO$_3$).

This relaxation process can now be treated as a thermally activated diffusion process of which the direction is determined by $\boldsymbol{F}_R$. The temperature dependence of the diffusion constant D is given by:

$$D(T) = D_0 \cdot \exp\left[-\frac{E_a}{k_B T}\right] \tag{3.16}$$

E_a is the diffusion process' activation energy. For a further, simplified interpretation the thermally induced change of the barrier width $\Delta d_{barrier}(T_{heat})$ is assumed to be proportional to $D(T_{heat})$ (analogously to the Fick's first law):

$$\Delta d_{\text{barrier}}(T_{\text{heat}}) \propto \exp\left[-\frac{E_{\text{a}}}{k_{\text{B}}T_{\text{heat}}}\right] \tag{3.17}$$

The relation described by Equ. 3.17 can now be used to fit the experimental results (see Fig. 3.35) in order to determine E_{a}. A convenient data representation for this procedure is the so-called Arrhenius-plot, i.e. a logarithmic plot over $1/k_{\text{B}}T$. Fig. 3.37**a** contains the Arrhenius-plot for $\Delta d_{\text{barrier}}(T_{\text{heat}})$. E_{a} can be readily extracted from this representation as the slope of a linear fit to the data points. It can be seen from Fig. 3.37**a** that a good fit (orange line) is only obtained when the data for $T_{\text{heat}} < 100\,\text{K}$ are not taken into account. The activation energy that can be derived from the fit is $E_{\text{a}} = (47 \pm 5)\,\text{m}e\text{V}$.

Knowing an expression describing $\Delta d_{\text{barrier}}(T_{\text{heat}})$ further data can be calculated following the protocol introduced before for the RS-MLs. First, the T_{heat} dependent values of d_{barrier} (Fig. 3.37**b**) are obtained by subtracting the fit function from the value for d_{barrier} determined at 4.2 K before the heating-cooling cycles. Subsequently, again the correlation between d_{barrier} and Φ_0 can be exploited to compute $\Phi_0(T_{\text{heat}})$ (not shown here). Eventually, hereby the dependence of the thermally induced resistance change ΔR_{T} on T_{heat} can be reproduced using Equ. F.5 as shown in Fig. 3.37**c**. Similarly as for the RS-ML results, the calculated data are matching the experimental results quite well.
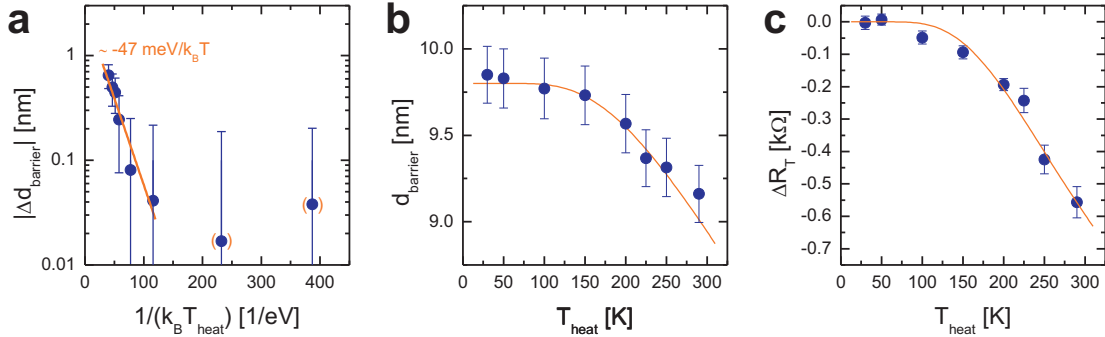

Figure 3.39: Analysis of heating-cooling cycle experiments using the proposed model. **a**: Arrhenius plot of the thermally induced change of d_{barrier}. For $T_{\text{heat}} > 100\,\text{K}$ a linear fit can be applied to the data (orange line). The slope of this fit corresponds to the activation energy of the diffusion process that is used to describe the relaxation of the V_{O} distribution leading to a reduction of d_{barrier}. The error bars for small $|\Delta d_{\text{barrier}}|$ are partially hidden as they extend to the negative range which is not available in this logarithmic representation. **b**: The calculated and experimentally determined values of $d_{\text{barrier}}(T_{\text{heat}})$ are matching well. **c**: Reproduction of $\Delta R_{\text{T}}(T_{\text{heat}})$ based on the Simmons model which can be computed exploiting Equ. F.5 and the correlation between Φ_0 and d_{barrier} shown in Fig. 3.37**c**.

Thus, the model proposed in the previous chapter does not only provide a phenomenological and qualitative description of the RS but also allows, to a certain extent, for a quantitative analysis of specific features of the effect. To conclude this chapter, it should be emphasised that this scenario can likewise be employed to explain the observations made in conventional OSVs comprising an AlQ$_3$ layer and an LSMO electrode [Prezioso11, Prezioso12]. As demonstrated by Prezioso *et al.*, the spin-valve signal in their devices is quenched when they are set

to a highly resistive state. The results in [Prezioso11, Prezioso12] are interpreted as an MR caused by GMR, i.e. by spin injection, diffusive spin transport and electrical spin detection. TAMR contributions are not considered, which seems rather justifiable as Prezioso *et al.* have performed their experiments at $T = 100\,\mathrm{K}$, i.e. in a temperature regime where TAMR can very likely be neglected (see chapter 3.4.1). The relation between a thicker charge injection barrier as it is proposed by the model under discussion for high R and a loss of spin-valve functionality can be explained recalling the TMR in MTJs (chapter 2.1.2). In MTJs usually an exponential decay of the spin-valve signal is observed with increasing barrier thickness due to a loss of spin polarisation during the tunneling process [Moodera99]. Taking a tunnel barrier of variable thickness at the spin injecting interface of a conventional GMR-OSV into account, the aforementioned suppression of the MR at elevated R becomes immediately evident. This is because the spin polarisation of charge carriers that are injected through a thick injection barrier is presumably rather low, even directly after the injection process, and, as a result, cannot be detected at the counterelectrode after being further reduced during the charge carriers' transition through the OSC layer. In TAMR devices, by contrast, spin injection is not necessary and consequently the inverse behaviour, an enhanced MR amplitude with increasing R, must not be regarded as contradiction to the work of Prezioso *et al.*.

3.7.4   Summary

Summing up, the results presented above include several novel findings that might be further exploited in organic spintronics devices. The voltage-pulse induced RS effect that is observed in AlQ$_3$-based TAMR structures is, generally speaking, more complex than the commonly known bipolar RS and allows for changes of a device's resistance in a range of approximately two orders of magnitude.

Due to the device composition, TAMR can be used as a powerful tool to probe the injection interface between the LSMO electrode and the AlQ$_3$ layer, eventually yielding irrefutable evidence for the presence of a tunnel barrier at this interface. Furthermore, TAMR analysis as well as the analysis of I/V curves reveal that this barrier is modified by the applied voltage pulses. As a consequence of this modification, an enhancement of the TAMR amplitude to up to $\sim 20\,\%$ at $4.2\,\mathrm{K}$ can be achieved, which is a massive improvement regarding the typical TAMR ratios reported so far in any other material system.

Based on the results of extensive investigations it is possible to draw a complete and conclusive phenomenological picture of the microscopic processes involved in the effect. In the proposed model it is suggested that the RS is stemming from mechanisms taking place at the surface of and inside the LSMO electrode, i.e. the effect is apparently related to the electrode material. This is contrary to many other results where the origin of the RS is usually located inside the insulating layer between the two electrodes. Since in the proposed scenario defects, pairs of V_Os and O_{is}^{2-} ions, are the species governing the RS behaviour, it can be regarded in agreement with many other models introduced for various oxide materials. Besides the qualitative description, the presented approach also provides, to a certain extent, a basis for a quantitative analysis of experimental results.

Nevertheless, an unambiguous experimental proof of parts of the model, namely the creation and removal of pairs of V_Os and O_{is}^{2-} ions, cannot be provided here. A very promising ap-

proach to gain this proof is a combination of transport and magnetometry (SQUID) measurements in suitable devices with a larger active area. Assuming that the RS effect is distributed and not localised (see chapter 2.3.1), this experiment can reveal whether the LSMO layer's magnetisation is changing with R in the course of an RS loop. The observation of such a correlation could be considered explicitly supporting the proposed scenario.

Chapter 4

Lateral Spin-Valve Structures

4.1 Motivation

As discussed in chapters 2.2.2 and 3.5, the performance of vertical OSVs may be strongly influenced by an ill-defined interface between the OSC layer and the top electrode. Moreover, it is indeed very likely that a spin-valve signal in these devices is only observable when pinholes, i.e. sites where the OSC layer thickness is dramatically reduced, are present. A straightforward interpretation of the respective results is therefore hampered by these side effects that are mainly resulting from the vertical structure and thus should be suppressed in the lateral device configuration. Besides the circumvention of these unwanted side effects there is also a more general motivation for the development and investigation of lateral OSVs [Grünewald13a]. The realisation of working lateral OSVs would allow for the implementation of non-volatile switching elements into OFET-based electronic circuits and thus give the possibility to enhance their functionality.

So far, there is a rather common lack of suitable fabrication methods for lateral OSVs for reasons that will be discussed below. Hence, one can only find very few reports on such devices in the literature although in one of the first publications in the field of organic spintronics Dediu *et al.* have reported on MR in a lateral structure [Dediu02]. A major drawback of this study, however, is the fact that the devices investigated therein are not actual spin valves in which a distinct parallel/anti-parallel magnetisation state can be prepared.

A simplified scheme of a lateral spin-valve device is shown in Fig. 4.1. The two ferromagnetic electrodes FM1/2 are arranged in the sample plane separated by a short gap or channel, respectively, (length l_{channel}, width w_{channel}) which is filled with an OSC material as non-magnetic spacer (NM). Similarly as for the vertical OSVs, certain prerequisites have to be met in order to obtain devices exhibiting spin-valve functionality. These are the need of different coercive fields H_{c} for the two electrodes, clean interfaces and the demand concerning l_{channel} that must not exceed the spin-diffusion length l_{sf} of the OSC under investigation. Based on the reported values for l_{sf} in typical OSC materials the latter requisite is equivalent to $l_{\mathrm{channel}} \leq 100\,\mathrm{nm}$. Eventually, the aforementioned prerequisites are rather challenging with respect to the sample preparation as they, amongst other things, strongly limit the applicable fabrication methods and technologies as will be outlined in the following.
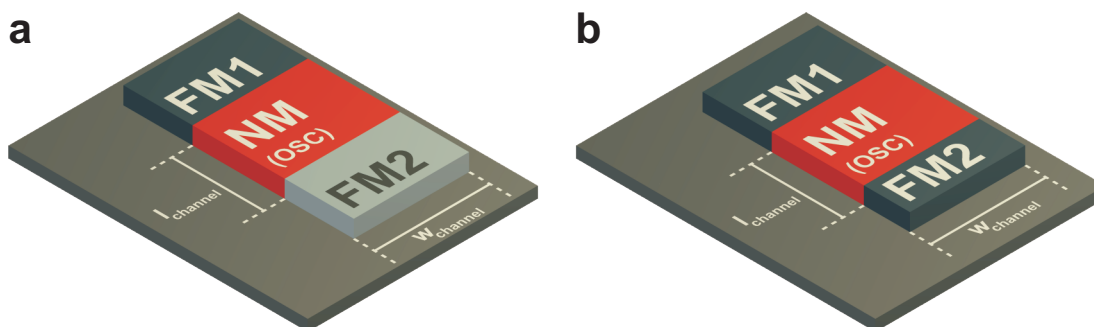
Figure 4.1: Schematic representation of two realisations of a lateral (organic) spin valve. **a:** Different materials are employed in order to obtain different coercive fields H_c for both electrodes. **b:** Exploiting shape anisotropy different aspect ratios of the electrodes can yield different H_c as well.

Lateral spin-valve devices are very often employed to investigate the spin transport performance of inorganic semiconductors or non-magnetic metals [Jedema01, Lou07, Tombros07]. In this case, the sample fabrication is rather straightforward. Usually, electron beam lithography (EBL) and suitable deposition and patterning techniques like lift-off and/or etching are used to realise the arrangement of the electrodes and the channel in between on the required scale. Electrodes with different coercive fields are obtained by either using different materials (see Fig. 4.1**a**) or by patterning stripe-shaped electrodes of different aspect ratios (see Fig. 4.1**b**). With the latter approach, the shape anisotropy is exploited as stripes of the same material with different aspect ratios exhibit different coercive fields [Aharoni98, Jedema01]. This procedure has already been applied for the patterning of drain and source electrodes of spin-valve-OFETs [Michelfeit08], however, not yielding promising results with respect to possible spin-valve functionality.

It turns out that the main drawback of using any kind of lithography for the fabrication of lateral OSVs is the massive contamination and possible oxidation of the electrode material during sample fabrication [Michelfeit08, Golmar12]. An alternative approach based on solid shadow masks as they typically are used for the fabrication of vertical OSVs is not feasible. This is because these masks are not available on the required scale.

4.2 Development of Fabrication Process

As stated above, there is a need for a fabrication process that allows to pattern the required electrodes in a suitable distance to each other and that equally provides clean and reproducible interfaces between the electrodes and the OSC material. Since in-situ deposition is the optimum way to obtain clean interfaces, the fabrication method presented in the present chapter will involve as much in-situ steps as possible.

Fig. 4.2 shows the flow chart of the latest, so far final, version of the preparation process and a schematic representation of a sample. Intermediate stages of the process development will be shortly addressed in chapter 4.3.1. All samples are based on silicon substrates covered with $1\,\mu$m silicon dioxide (SiO_2).

For the patterning of the two electrodes two steps are necessary. The first step (Fig. 4.2**a**) is the deposition of a thick rectangularly shaped Ni or Co contact (lateral dimension 0.75 mm × 4.00 mm, thickness $d_{Ni/Co} = 40 - 80$ nm) by optical or electron beam lithography, electron beam evaporation and lift-off. For the lithography a bilayer resist is used in order to obtain vertical contact sides and to avoid the formation of sidewalls which later would impede the process' functionality.

Subsequently, the sample is inserted into one of the UHV chambers where CoFe and the OSC layer can be deposited in-situ. The next step (Fig. 4.2**b**) is the deposition of a thin CoFe layer. During this step the sample is tilted by an angle Θ_{evap} so that in the shadow of the thick Ni/Co contact no CoFe is deposited. Hence, two separate metal layers, i.e. electrodes, which are separated by a short channel are fabricated. One electrode consists of the thin CoFe layer only (single layer contact, SLC), the second one is a bilayer contact (BLC) comprising the thick Ni/Co layer and the thin CoFe layer. Evidently, the length of the channel is determined by Θ_{evap} and $d_{Ni/Co}$:

$$l_{channel} = d_{Ni/Co} \cdot tan(\Theta_{evap}) \tag{4.1}$$

The final step (Fig. 4.2**c**) is the deposition of the OSC layer (thickness $d_{OSC} \approx 100$ nm). Again, the sample is tilted but in the opposite direction in order to ensure a homogenous filling of the channel.

During these in-situ steps the sample is covered by a solid shadow mask with rectangular windows (150 μm × 3.0 mm) in order to obtain separate and uniform devices with a well-defined $w_{channel}$ as shown in Fig. 4.2**d**. Furthermore, Ti/Au contact pads for all electrodes are patterned either prior to device fabrication by optical lithography and lift-off or afterwards by the use of solid shadow masks. An optical micrograph of a sample showing all relevant device components is displayed in Fig. 4.2**f**.

4.3   Results

In general, two types of devices are fabricated and investigated which are different concerning the OSC material under investigation and the BLC's composition and patterning. Lateral OSVs comprising PDI have a Ni/CoFe BLC which is patterned by optical lithography, whilst for devices with other OSC materials EBL is used for the fabrication of the Co/CoFe BLC. These differences are mainly due to material and technology availability as well as to further improvements of the fabrication process.

4.3.1   Preliminary Investigations

The first PDI-based samples (see Fig. 4.2**e**) are fabricated with a preliminary process not including Ti/Au contact pads that would allow to contact single devices via ultrasonic bonding. Additionally, instead of using a solid shadow mask, device separation is achieved by cleaving the sample, which consists of extended areas of the SLC and BLC, into small stripes after the actual preparation process. As the samples have to be mounted to a chip carrier for measurements in setup #1, the contacting to the chip carrier is done using a gold bond-wire
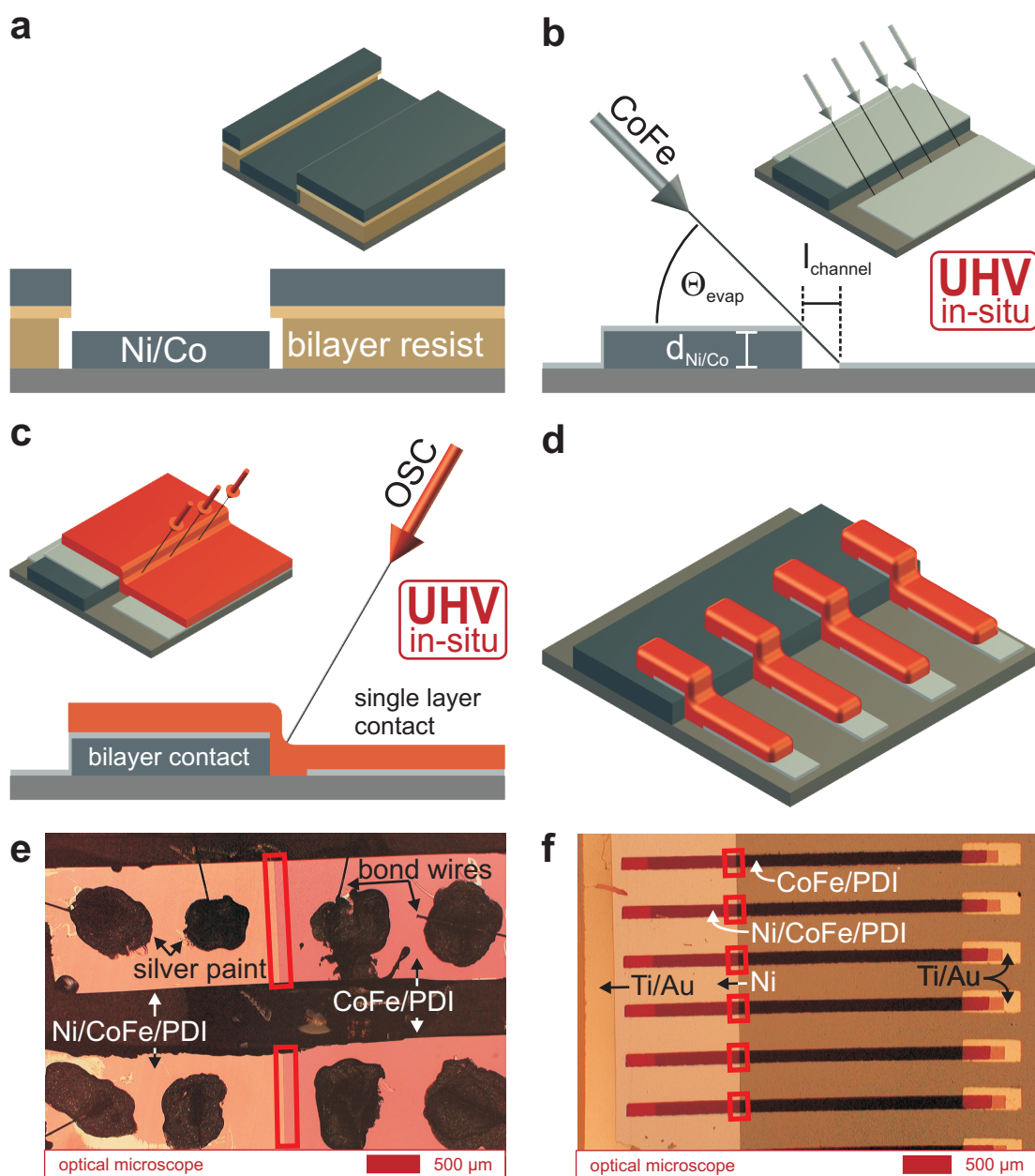
Figure 4.2: Fabrication process for lateral OSV devices employing shadow evaporation technique. **a**: Patterning of a large-area thick Ni/Co layer by optical or electron beam lithography and lift-off using a bilayer resist system. **b**: With the sample tilted a thin CoFe layer is evaporated. The shadow of the thick Ni/Co layer provides an insulating gap between the bilayer and single layer contact. **c**: The gap is filled with an OSC without breaking the UHV. **d**: The schematic representation of a sample shows four uniform devices obtained by using a shadow mask during the two preceding steps. **e,f**: In the optical micrographs of devices fabricated at two different stages of the process development the gap is marked by red rectangles.

and conductive silver-paint (see Fig. 4.2e).

Obviously, these simple solutions for device separation and contacting have crucial draw-backs. For instance, it is not possible to reproducibly achieve uniform, or at least within certain limits similar, device dimensions considering w_{channel}. Additionally, the silver-paint contacts turn out to be not sufficiently reliable with respect to their mechanical and electrical stability. Eventually, these drawbacks have motivated the modifications of the fabrication method leading to the process presented above.

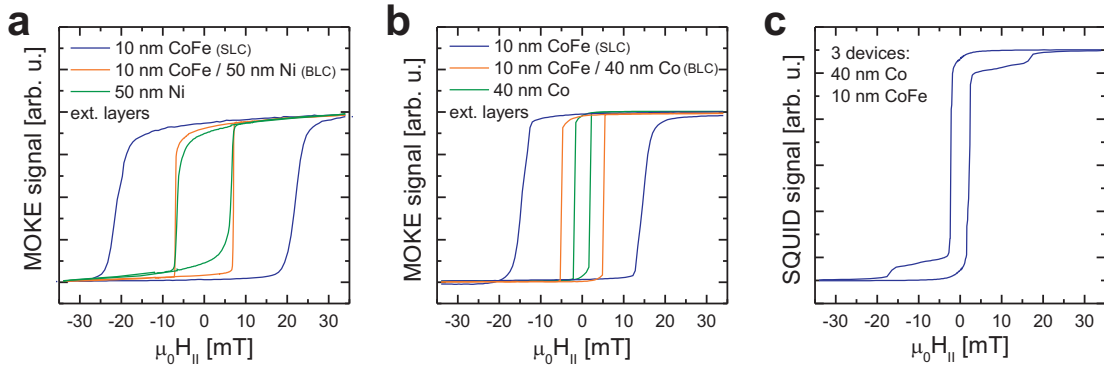**Figure 4.3:** Magnetometry data for extended layers of the lateral OSVs' electrode materials and for a fully processed sample. **a,b**: MOKE traces for extended layers of the SLC, BLC and the thick ferromagnetic contact as they are used in lateral OSVs based on PDI (**a**) and other OSC materials (**b**). **c**: Hysteresis loop of three lateral OSVs exhibiting a very pronounced double switching behaviour as expected for a spin-valve device.

However, despite these drawbacks the samples with extended contact layers can be and actually are used to check the suitability of the process for spin-valve fabrication employing magnetometry measurements (magneto-optical Kerr effect, MOKE). Figs. 4.3a and **b** show results from MOKE measurements (taken at room temperature) for all ferromagnetic layers present in lateral OSVs fabricated with the shadow evaporation process. Fig. 4.3a includes MOKE traces for a single 50 nm thick Ni layer, a single 10 nm thick CoFe layer and a bilayer consisting of 50 nm Ni and 10 nm CoFe. The data in Fig. 4.3b are recorded for a sample where Ni is replaced by Co ($d_{\text{Co}} = 40$ nm).

Both sets of results reveal that H_{c} of the BLC is closer to that of the thick single layer made of the magnetically softer material, Ni or Co, than to that of the hard material, CoFe. Hence, one can conclude that the magnetisation M_{CoFe} of the thin CoFe layer's fraction that is part of the BLC is pinned to the magnetisation $M_{\text{Ni/Co}}$ of the thick Ni/Co layer. This pinning is achieved by choosing the layers' thickness such that $M_{\text{Ni/Co}} \gg M_{\text{CoFe}}$. Thus, the coercive fields of the BLC and SLC, respectively, which are relevant for the OSVs' functionality, actually are discernably different from each other as the summary in Tab. 4.1 shows.

This is sustained by SQUID measurements undertaken at $300\,K$ for a fully processed sample, i.e. a sample fabricated using the solid shadow mask for single devices. Fig. 4.3c contains a full hysteresis of three OSV structures (40 nm Co + 10 nm CoFe and 10 nm CoFe, respectively, for the electrodes) with a sharp two step magnetisation reversal which is, in-

material	thickness [nm]	$\mu_0 H_{c,\text{MOKE}}$ [mT]	$\mu_0 H_{c,\text{SQUID}}$[mT]
CoFe	10 nm	15 − 20	15 − 18
CoFe + Co	10 nm + 40 nm	5.0	2.5
CoFe + Ni	10 nm + 50 nm	7.5	n.a.

Table 4.1: Coercive fields of electrode materials and combinations thereof employed in lateral OSV devices. The data are collected by MOKE and SQUID measurements.

cidentally, more pronounced than for the vertical OSVs. Furthermore, a comparison of the SQUID and MOKE results for the sample containing the Co/CoFe BLC yields a good agreement concerning the H_c of both electrodes.

The next prerequisite to be checked with respect to spin-valve functionality is the electrodes' separation. For the PDI-based samples imaging methods like electron microscopy are not available or feasible, respectively. Therefore, the separation of the electrodes is checked indirectly by means of preliminary transport measurements. Two methods are deployed for this purpose: OFET measurements and I/V characterisation in combination with additional processing. All measurements are carried out at room temperature.
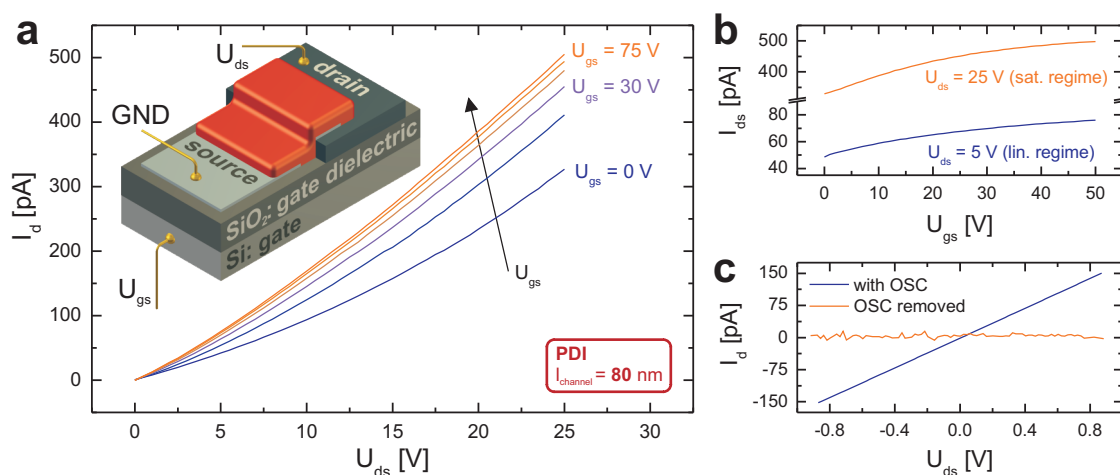
Figure 4.4: Preliminary transport measurements in lateral OSV devices. **a,b**: Output (**a**) and transfer (**b**) characteristics of a lateral OSV device operated as OFET as schematically shown in the insert. Although short channel effects unambiguously can be identified, these data can be regarded as proof for the electrodes' separation. **c**: I/V response of a lateral device taken before (blue curve) and after (orange curve) removing the PDI layer.

For the OFET characterisation the two electrodes, SLC and BLC, are used as drain and source of the transistor. The gate-source voltage U_{gs} is applied between the substrate and the respective electrode, i.e. the SiO$_2$ layer is used as gate dielectric. The corresponding circuit is shown in the inset of Fig. 4.4**a** in which the data for the output characteristics of a lateral OSV device are plotted. Output characteristics are taken at constant U_{gs} while the drain-

source voltage U_{ds} is swept and the drain current I_{d} is measured. The obtained characteristics clearly exhibit deviations from the ideal OFET behaviour (see, for instance, [Horowitz98]), so-called short channel effects [Tsividis99, Sze06, Pierret96, Haddock06]. For elevated U_{ds}, i.e. in the saturation regime, neither saturation of I_{d} nor the typical quadratic dependence of I_{d} on U_{gs} is observed. Short channel effects are also reflected in the transfer characteristics $I_{\mathrm{d}}(U_{\mathrm{gs}})$ in Fig. 4.4b recorded at constant U_{ds}.

Regarding the applied voltages and the dimensions of the devices under investigation these deviations are to be expected. As l_{channel} (nominally $\sim 80\,\mathrm{nm}$ for this device) is much smaller than the thickness of the gate dielectric ($1\,\mu\mathrm{m}$), the strength of the electric field between drain and source becomes comparable to that of the field between gate and source or even larger. In consequence, the gradual channel approximation is violated and short channel effects emerge.

As shown by Golmar *et al.* [Golmar12], another important factor influencing the OFET performance of any lateral device is the combination of electrode and OSC material. This combination may not be optimum in the present devices but cannot deliberately be modified for reasons of material availability, prerequisites concerning material properties and technological limitations. Nevertheless, the results of OFET characterisation for the lateral OSVs can be regarded as evidence that the charge transfer is through the OSC layer and the electrodes are electrically separated from each other.

These findings are sustained by another experiment that is summarised in Fig. 4.4c. After I/V characterisation (blue curve) the OSC layer is removed from the device using a suitable solvent. Subsequently, another I/V curve is recorded yielding the orange trace in Fig. 4.4c. Obviously, the latter shows that there is no current between the two electrodes. Hence, the only current path in the present device before the OSC removal must be through the OSC layer, and consequently, weak metallic links or even short circuits can be excluded.

As interim conclusion it can be stated that the separation of the electrodes can be proved indirectly by means of transport measurements. At this point it should be additionally noted that the devices' resistance at room temperature is rather high, namely in the range of several $\mathrm{G\Omega}$ to several hundreds of $\mathrm{G\Omega}$s. These values seem to be in contradiction to a device consisting of a high-mobility OSC like PDI. However, the measured I_{d} in the lateral OSVs is in good agreement with data obtained in standard OFET structures, which have been fabricated by optical lithography in order to preliminarily investigate this material [Steinbacher07]. Moreover, it is also important to keep in mind that the contact resistance at the interface between the electrodes and the PDI layer is more prevailing in devices with short channels ($l_{\mathrm{channel}} < 1\,\mu\mathrm{m}$) and small-area contacts, i.e. with a rather small w_{channel}.

For samples based on other OSC materials than PDI (Co/CoFe BLC), additionally environmental scanning electron microscopy (ESEM) is available for checking the electrodes' separation. However, due to the similar atomic mass of Co and CoFe, the contrast for this material combination is very likely rather poor. A sample structure for ESEM investigations therefore is fabricated where Co is replaced by Au and CoFe by Ti. The thickness of the Au layer is $d_{\mathrm{Au}} = 80\,\mathrm{nm}$. During the deposition of the thin Ti layer the sample is tilted by

$\Theta_{\text{evap}} = 45°$ leading to a nominal $l_{\text{channel}} = 80\,\text{nm}$ according to Equ. 4.1.

ESEM results for this sample are shown in Fig. 4.5 for two different magnifications. The ESEM micrographs reveal that the two metal layers corresponding to the SLC and BLC of the lateral OSV are actually separated. Fig. 4.5a furthermore shows that the separation is not only achieved locally but is also present along the complete edge of the thick contact. Additionally, two more features visible in the ESEM micrographs have to be emphasised as they are crucial for the understanding of the devices' behaviour observed in MR measurements. On the one hand, despite the use of a bilayer resist system, the sides of the thick contact apparently are not perfectly vertical (not explicitly shown here). As a result, the actual l_{channel} is substantially smaller than the nominal l_{channel} calculated from Equ. 4.1 (a deviation by a factor of ~ 0.5 can be extracted from Fig. 4.5b). This reduction of l_{channel} may be additionally enhanced by material diffusion on the sample surface during the deposition of the thin Ti layer. On the other hand, it can be seen in Fig. 4.5b that irregularities of the Au layer are present although EBL is employed for the patterning. Even more importantly, these alleged defects are transferred to the thin Ti layer due to the shadow evaporation leading to local variations and hereby to a further reduction of l_{channel} at single spots of the gap.
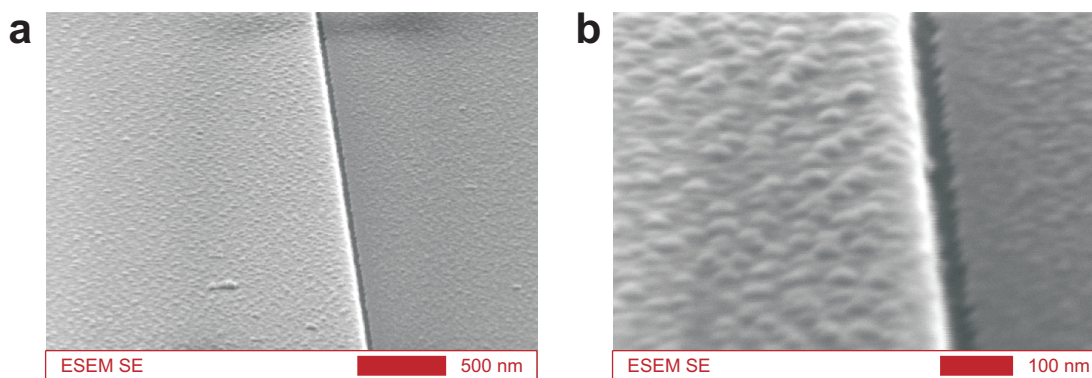
Figure 4.5: ESEM secondary electron micrographs (SE) showing the fabrication process' functionality. In this reference sample, the BLC on the left hand side consists of Au and Ti, the SLC on the right hand side of Ti only. For both magnifications the long ranging separation of the electrodes is visible. In **b** the effect of irregularities in the thick contact layer on the shape of the gap can be discerned as small, randomly sized protrusions.

4.3.2 Magnetotransport Measurements

All devices for which the electrodes' separation has been proved experimentally exhibit a resistance in the GΩ regime. Therefore, and since R is expected to be further increased when cooling the sample to cryogenic temperatures (see also chapter 2.2.1), all magnetotransport measurements are conducted at room temperature only (setups #2 and #5).

Moreover, in this high-resistance regime a relatively high noise-level and fluctuations of R have to be dealt with bringing forth the need for a more elaborate experimental approach with respect to the measurement technique. This also gets evident considering the results of first magnetotransport investigations undertaken for the PDI-based structures. Whereas in MR measurements in vertical OSVs a sufficiently high signal-to-noise-ratio (SNR) of ~ 100

can be achieved by recording one data point per field step, the same procedure yields a SNR of only 10 or less in the lateral devices. Such data obviously can hardly be interpreted with respect to the presence of any MR effect with a magnitude of several % as it can be optimistically expected on the basis of results available in the literature. However, it turns out that in the case of PDI-based lateral OSVs this impediment can be circumvented by averaging several (usually 50 or more) single resistance measurements per magnetic field step in an MR measurement, eventually leading to the results presented in the following.

Fig. 4.6**a** shows the MR trace of a device fabricated at an intermediate stage of the preparation process' development (no solid shadow mask). A clearly hysteretic effect with a total MR ratio $(R_{\mathrm{max}} - R_{\mathrm{min}})/R_{\mathrm{min}}$ of $\sim +2\,\%$ which is symmetric with respect to zero field can be discerned for both sweep directions. However, as the signal does not exhibit sharp switching features between two distinct resistance states and looks rather blurry, it is not possible to refer to an anti-parallel/parallel spin-valve state here.

For rather new structures fabricated with a later version of the process (using a solid shadow mask), on the contrary, a clear spin-valve behaviour can be identified in the respective MR results displayed in Figs. 4.6**b-d** for two selected devices. Both of them exhibit a large MR at room temperature.
The MR trace of the first device (Fig. 4.6**b**) includes very pronounced switching events between the two resistive states of $R_{\mathrm{AP}} \approx 6.3\,\mathrm{G\Omega}$ and $R_{\mathrm{P}} \approx 6.7\,\mathrm{G\Omega}$ corresponding to an MR amplitude of $\sim -8\,\%$ $(\Delta R/R_{\mathrm{AP}})$. It is noteworthy that these results comprise significant deviations from the conventional spin-valve behaviour as is presented in chapter 2.1 and observed in the vertical OSVs.
On one side, the switching from R_{P} to R_{AP} occurs at negative fields ($\mu_0 H_{||} \approx -25\,\mathrm{mT}$) when sweeping from negative to positive magnetic fields and similarly at positive fields ($\mu_0 H_{||} \approx +50\,\mathrm{mT}$) for the opposite sweep direction. On the other side, the loci of this first switching event obviously depend on the sweep direction, i.e. the MR signal is not symmetric with respect to zero magnetic field. As the change of R between R_{P} and R_{AP} has to be ascribed to a magnetisation reversal of one of the electrodes, these observations are counterintuitive at first sight and will be discussed in detail in chapter 4.4. The second switching event, by contrast, observed at $\mu_0 H_{||} \approx \pm 100\,\mathrm{mT}$ is symmetric in the mentioned sense.
In the second device R is significantly higher compared to the previously presented data although both structures have the same nominal l_{channel} and the same actual w_{channel}. The magnetotransport behaviour is represented in Figs. 4.6**c** and **d** on the basis of results collected for two different orientations φ of the in-plane magnetic field $\boldsymbol{H}_{||}$. Again, a hysteretic and negative MR effect of at least 50 % (up to 100 % when also taking into account the sharp features) is observed with the corresponding resistance states of $R_{\mathrm{AP}} \approx 400 - 500\,\mathrm{G\Omega}$ and $R_{\mathrm{P}} \approx 600 - 700\,\mathrm{G\Omega}$.

Contrary to the MR signal in Fig. 4.6**b**, the traces in Figs. 4.6**c** and **d** do not exhibit pronounced switching events that can be assigned to a sharp reversal of the electrodes' magnetisation but rather are suggesting a rotation thereof. Furthermore, when the traces of
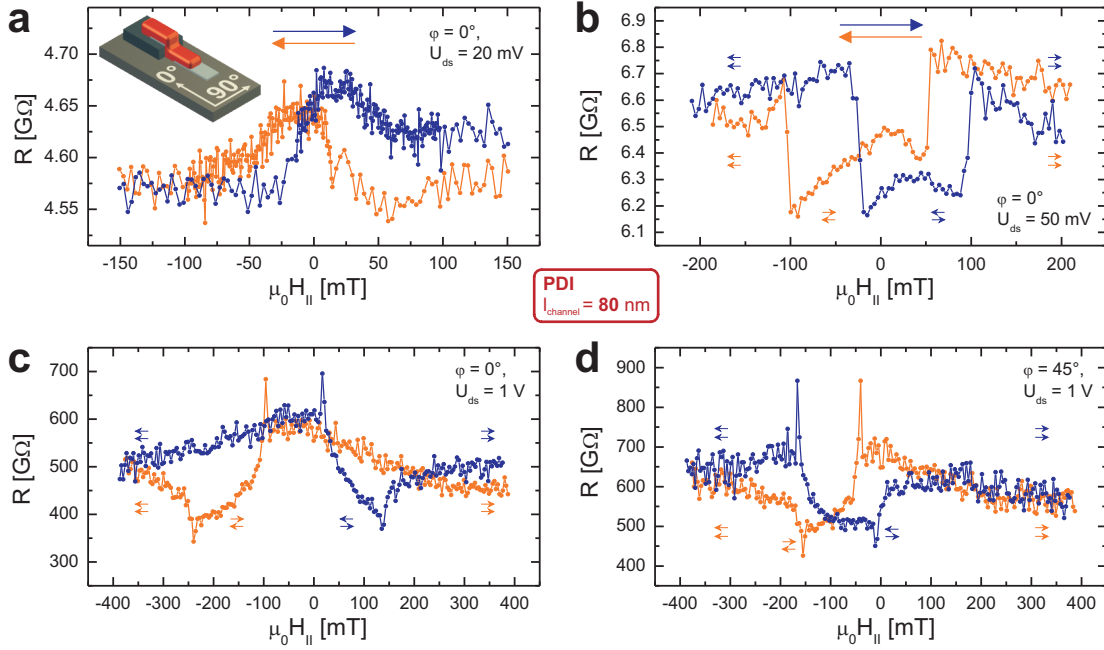
Figure 4.6: Large room-temperature MR in three lateral OSV devices employing PDI. **a**: Preliminary results for a structure fabricated at an early stage of the experiments already exhibit a hysteretic MR effect. **b**: Spin-valve signal with sharp switching events recorded in another OSV. **c,d**: The MR trace of the device showing the largest MR ratio of $\sim -50\%$ is reminiscent of a magnetisation rotation rather than of a distinct magnetisation reversal. In all measurements significant deviations from the ideal spin-valve behaviour become evident.

both sweep directions for a specific φ are considered together, a symmetric behaviour can be discerned in this device. However, the symmetry is not with respect to $\mu_0 H_{||} = 0\,\text{mT}$, but rather a lateral shift of all switching/rotation events towards negative values of $H_{||}$ is present. Similarly to the discrepancies observed in the previously discussed device, neither can this behaviour be understood in a straightforward manner. It will be addressed in the following chapter as well as another issue that becomes evident from a juxtaposition of transport and magnetometry data for both devices. According to spin-valve theory the H_c of both electrodes specify the loci of the switching events observable in a magnetotransport measurement. Obviously, this does not apply here considering the values for H_c given in Tab. 4.1 and the MR signals in Fig. 4.6.

As already outlined above, lateral OSV structures employing other OSC and electrode materials have likewise been fabricated and investigated. Fig. 4.7 shows the results of MR measurements performed at $U_{\text{ds}} = 1\,\text{V}$ for devices on two samples comprising the quite established OSC H_2Pc (Figs. 4.7**a** and **b**) and the rather new material NDI, respectively (Figs. 4.7**c** and **d**). For each structure results of two subsequent measurements with different φ are displayed. Similarly as in the MR traces of the PDI-based OSVs in Fig. 4.6, here every data point is computed by averaging several single resistance measurements per field step. As can be discerned from all plots of Fig. 4.7 (20 measurements per data point), in these devices apparently this measurement technique does not lead to a sufficiently high SNR.
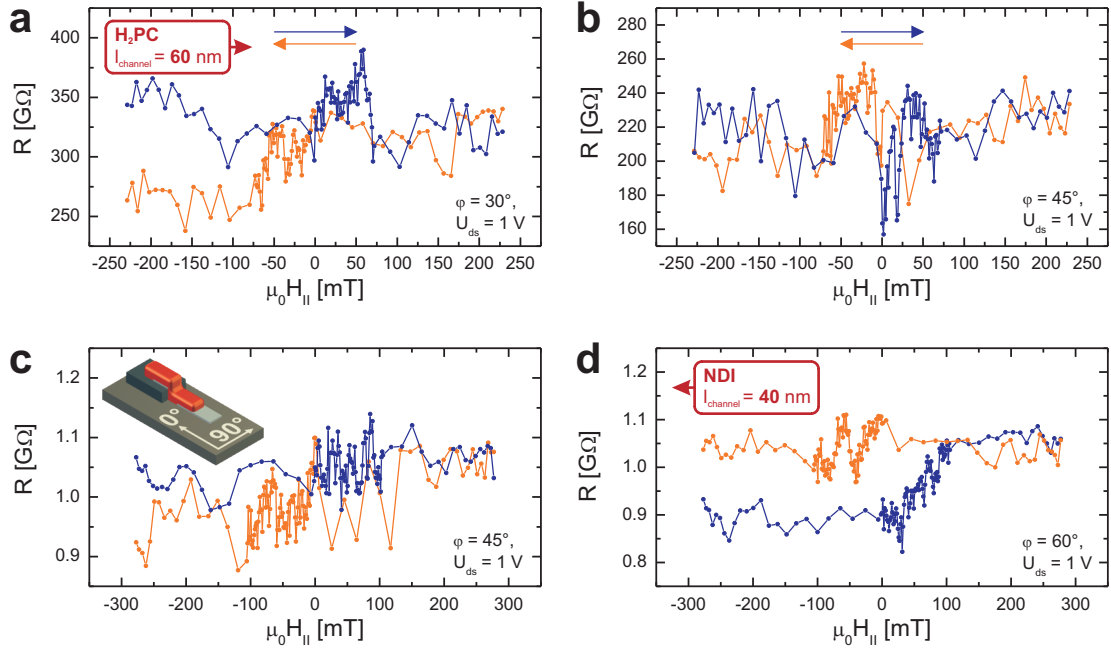
Figure 4.7: Results of MR measurements for lateral OSV structures based on H_2Pc (**a** and **b**) and NDI (**c** and **d**). All data suffer from a rather high noise-level. Furthermore, the resistance is not stable but drifting, even within the course of one measurement. Both observations are decisively hampering the analysis of these results with respect to the existence of any MR effect.

In addition to the rather high noise-level, another obstacle to a reliable interpretation of these results can be identified from the MR traces in Fig. 4.7. R is obviously not stable but drifting towards higher or lower values in the course of the measurements. This drift behaviour is most likely originating from side effects like, for instance, degradation caused by a long-term voltage stress of the OSC layer [Libsch93, Salleo04, Steinbacher07]. The high noise-level can be understood when the common charge transport mechanisms present in amorphous or polycrystalline OSC layers are taken into account (see chapter 2.2.1). As for the charge transfer via MTR or VRH trap states play an important role, slight changes of the ambient conditions (temperature, lightness) may have considerable impact on the OSC layer's transport properties and thus on R.
Any attempts to avoid the observed resistance drift and to improve the SNR, e.g. by increasing the number of measurements per magnetic field step, do not yield a significant enhancement for the devices under discussion, virtually rendering impossible any conclusion whether the data in Fig. 4.7 comprise an MR effect in the range of several % to tens of % or not.

As a preliminary summary it can be stated that in the PDI-based devices a large MR effect is measured which even exceeds all room-temperature MR values reported for vertical OSV so far. A more extensive experimental analysis of the spin-valve behaviour is desirable as it would be substantially easing the interpretation of the presented results. Unfortunately,

due to the poor stability of the structures and the fact that the magnetotransport studies have been very time- and herewith device-consuming, investigations comparable to those presented for the vertical PDI-based OSVs have not been feasible. However, the available data are sufficient to draw conclusion with respect to the MR effect's underlying mechanisms, which is the content of the following chapter.

4.4   Discussion of the Magnetoresistance Effect

Before presenting a device model that can explain the MR effect in lateral PDI-based OSVs and its deviations from the normal spin-valve signal, the latter are summarised again.

- A switching between R_P and R_{AP} is observed at negative $H_\parallel$ when sweeping from negative to positive fields and vice versa in one of the devices.

- The MR traces are equally shifted with respect to zero magnetic field for both sweep directions of the magnetic field in another device.

- Magnetometry and transport data significantly differ with respect to coercive and switching fields for all devices.

- There are large variations of R in nominally identically scaled structures.

Two ingredients are necessary to understand this rather unconventional MR behaviour. The first is the existence of an exchange bias caused by antiferromagnetic coupling in the BLC [Meiklejohn56]. Although the fabrication process involves as many in-situ steps as possible, one part of the BLC, namely the thick Ni/Co layer, has to be structured in ambient conditions and therefore may undergo oxidation. As a result, it is very likely that a NiO sublayer is present in the BLC. Since NiO is an antiferromagnet with a Néel temperature well above room temperature [CRC96], this may lead to exchange bias and consequently to the φ-dependent shift of the hysteresis observed in the spin-valve signal (see Figs. 4.6**c** and **d**). However, exchange bias alone cannot explain the other aspects mentioned above.

For a further discussion the lateral OSV structures will be compared to the vertical artificial-pinhole-OSVs presented by Barraud *et al.* [Barraud10]. As already mentioned in chapter 3.5.1, these nm-scaled devices exhibit a large TMR/TAMR effect and a resistances in the range of $R \approx 1\,\mathrm{M\Omega} - 100\,\mathrm{G\Omega}$. Drawing analogies between these structures and the lateral OSVs under discussion is suggested by two aspects. On the one hand, the resistance of both kinds of devices is of the same order of magnitude, and, on the other hand, in both cases rather complex MR traces seemingly inconsistent with the electrodes' magnetisation dynamics are observed.

Thus, if the charge transport mechanism in the present structures is reconsidered on the basis of the findings of Barraud *et al.*, the shape of the MR traces as well as other observations can be readily understood. As can be seen in Fig. 4.5, l_{channel} of the lateral OSVs must not be considered constant but may be varying rather strongly due to protrusions. Similarly to the scenario of a reduced layer thickness in vertical OSVs, it is therefore appropriate to assume that a lateral device exhibits spots where l_{channel} is decreased to such an extent that lateral

tunneling becomes probable. Fig. 4.8**a** schematically shows a possible configuration in which a protrusion dramatically decreases $l_{channel}$ as indicated by the red arrows (potential tunneling paths) in the top view in Fig. 4.8**b**. As already stated before, these protrusions very likely are stemming from irregularities in the thick Ni/Co contact and cannot be completely avoided during sample fabrication. Based on the assumption that the conducting channel in the lateral OSVs is a very small lateral tunnel junction, further answers to the issues raised at the beginning of this chapter can be given.

The formation, shape and number of protrusions cannot be controlled during the fabrication process. Instead, there are statistical variations from device to device which, for instance, can be reflected in variations of R if the charge transfer is dominated by tunneling at these sites. For non-shorted, nominally identical structures these variations apparently are in the range of two orders of magnitude (see Fig. 4.6). If, on the contrary, the charge transfer was taking place through a wide channel via mechanisms like VRH or MTR, one would expect similar values of R for identically scaled devices.
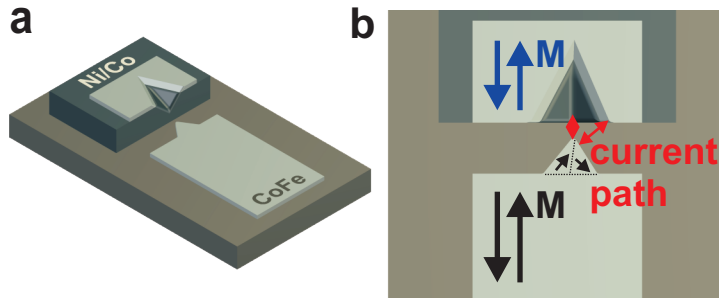

Figure 4.8: Schematic, exaggerated representation of a protrusion's influence on the channel length in a lateral OSV device. Irregularities in the BLC (**a**) can lead to a dramatically reduced channel length as well as to a different magnetic behaviour of the electrodes when lateral tunneling at sites with nm-scaled tips is dominating the charge transfer as indicated in **b**.

Furthermore, the concept of lateral tunneling can also explain discrepancies between MR measurements and the magnetisation dynamics, such as the deviation of the switching loci from the H_c determined by MOKE. This is because in the small lateral tunnel junction under consideration the magnetotransport behaviour is not necessarily determined by the whole contact but only by the small fraction thereof which is forming the protrusion, e.g. a nanoscale tip on one side of the channel. The response of a small structure's magnetisation to an external magnetic field can significantly differ from that of extended layers [L-Pelecky96] for mainly two reasons.

On one side, the magnetisation of such a tip very likely is governed by the local domain structure within the protrusion as exemplary indicated by the small black arrows and dashed lines in Fig.4.8**b** [Kittel46]. Therefore, it must be treated as independent from the magnetisation of the bulk part of the electrodes (large black and blue arrows in Fig.4.8**b**). On the other side, likewise the influence of fringe fields originating from the macroscopic ferromagnetic layers, which are in direct vicinity of the tip, has to be considered.

In summary, it is possible to understand the anomalies observed in the spin-valve signal in lateral OSVs by taking the probability of lateral tunneling at nanoscale protrusions and this assumption's consequences into account. At this point it is also worth to get back to the null results obtained in magnetotransport studies for H_2Pc- and NDI-based devices. These structures are fabricated using EBL for the patterning of the thick Co layer, whilst the Ni contact of all devices exhibiting an MR effect is fabricated by optical lithography. EBL can be assumed to yield more precise and reproducible results concerning the sharpness of the crucial layer edge compared to patterning by optical lithography. Hence, one would expect less and smaller protrusions for these devices, i.e. a more homogeneous $l_{channel}$ and therefore a charge transfer dominated by mechanisms like VRH or MTR instead of lateral tunneling. The experimental results, e.g. the more pronounced occurrence of resistance drifting, the relatively high noise-level and smaller variations of R indeed can be interpreted as sustaining this assumption. In this sense these allegedly negative findings can sustain the model for the charge transport in lateral OSVs that exhibit spin-valve functionality.

4.5   Summary

Lateral organic spintronic devices are very seldom reported due to the difficulties with respect to the sample preparation already mentioned in the introduction to this section. Here, lateral organic transport structures that clearly exhibit a typical hysteretic spin-valve signal have been demonstrated for the first time. The most important key to their realisation is the novel fabrication method that is based on an alternative technique, namely the presented shadow evaporation process. As virtually no results of actual lateral OSVs are available in the literature, the presented findings cannot be directly compared to other data. The observed MR therefore is interpreted by employing suitable analogies to results and models existing for particular vertical structures (artificial-pinhole-OSVs).

The main conclusion that has to be drawn with respect to the spin-valve behaviour in lateral OSV devices is similar to the one found for the PDI-based vertical structures. Again, experimental results suggest that the observed spin-valve signal is very likely originating from an MR effect based on tunneling. Lateral tunneling may become probable when the channel length of a device is reduced at single spots due to the fabrication process. Such a spot can be regarded as analogue to a pinhole in vertical OSVs. Consequently, one of the main motivations for the characterisation of lateral devices, which is the prevention of detrimental side effects, cannot yet be considered fulfilled here.

Looking ahead the observation of a spin-valve signal that is apparently caused by tunneling clearly unveils distinguished features of the devices that can be further improved. Results obtained from the first steps of improvement are likewise presented in the previous chapter. For instance, structures in which the crucial lithographic patterning is done by electron beam lithography apparently do not suffer from irregularities in the channel length, thus minimizing the tunneling contribution to the charge transfer. Starting from this, additional promising steps are a further reduction of $l_{channel}$ and variations of the electrode/OSC-material combination under investigation.

Chapter 5

Summary and Outlook

At the beginning of the work for this thesis two main objectives have been specified. On the one hand, experiments with vertical transport structures based on a new OSC material, namely PDI, should be conducted in order to obtain, in the first instance, basic information about this material's suitability for organic spintronics applications. Furthermore, it has been expected to gain an optimum understanding of the physics behind the spin-valve signal that is observed in these devices by different transport characterisation techniques and the modification of device and measurement parameters. On the other hand, the lack of a suitable fabrication process for lateral organic spin valves has been addressed as these structures are a promising approach towards the acquisition of additional insight into the physics behind spintronics-related effects in OSCs.

In the first part of chapter 3 it has been demonstrated that PDI indeed can successfully be implemented into vertical OSV devices. A clear spin-valve signal is obtained reaching MR ratios of up to 50 % at low temperatures and low bias, a value that can be considered as state of the art. A large series of structures has been studied by, in the first instance, mainly standard magnetotransport measurements. These experiments aimed the investigation of the spin-valve signal's dependence on the thickness of the OSC layer, the applied bias voltage, the temperature and the orientation of the applied in-plane magnetic field, thus covering the variation of four device and measurement parameters. An overall examination of these results in comparison to data from the literature [Xu07, Vinzelberg08, Shim08, Yoo09, Lin10] is strongly suggesting that the observed spin-valve signal is originating from tunneling processes.

In order to sustain this scenario, which in principle can be applied to many results in the literature, further and more robust experimental insight was deemed mandatory. Therefore, the feasibility and meaningfulness of measurements in the perpendicular geometry, i.e. the investigation of spin precession and the so-called Hanle effect, was checked and subsequently the corresponding experiments have been performed for selected devices. The results thereof, which are summarised in chapter 3.3, do not show any sign of spin precession. Hence, they clearly reveal that a GMR-like effect, i.e. a spin-valve signal due to spin injection, subsequent diffusive spin transport and electrical spin detection, must be excluded in the present structures. As shown in the discussion associated with these findings, the only conclusion that is not in contradiction to other results in the literature is that actually tunneling is governing

the MR in the devices under investigation.

Starting from this and in order to fully exploit the whole range of data accessible by transport measurements, in a last step alternative devices have been studied. These are dedicated TAMR devices or so-called single-sided spin valves, i.e. devices with only one ferromagnetic electrode. TAMR is an MR effect that can mimic spin-valve behaviour under certain circumstances [Gould04] and, so far, virtually never has been taken into account for the interpretation of MR results in the field of organic spintronics. This also is because apparently there has been no particular interest in investigating this effect. In this work for both types of structures, single-sided and conventional OSVs, a clear proof of TAMR and for a TAMR contribution to the spin-valve signal, respectively, is provided. Moreover, the demonstration of TAMR shows that a substantial part of the devices' resistance is originating from an injection tunnel barrier at the interface between the LSMO electrode and the OSC layer.

All results obtained for the PDI-based vertical transport structures finally can be condensed into a model explaining the charge transfer and the origin of the spin-valve signal. The latter is very likely a combination of TMR and TAMR. TMR is occurring at pinhole sites, where the OSC layer thickness is significantly reduced, and, as already mentioned, TAMR can be considered as interfacial effect.

In summary, on the one hand, the experiments with vertical transport structures employing a PDI layer clearly reveal that transport measurements can yield a remarkable amount of evidence which is sufficient to draw reliable and concise conclusions with respect to the physics behind the spin-valve functionality of a specific device. On the other hand, they underline the importance of a careful interpretation taking into account the entirety of all results. In this context especially the novelties presented in the scope of this work should be emphasised.

On one side, experiments in the perpendicular geometry investigating the Hanle effect for the remanent spin-valve states are mandatory in order to gain irrefutable and direct information whether an MR effect is actually caused by diffusive spin-polarised transport and electrical spin detection. Such measurements could also further enhance the validity of results strongly suggesting a GMR-like behaviour which have been found, for instance, by Nguyen *et al.* (isotope effect on the MR in OSVs [Nguyen10] and spin-polarised light emitting diodes [Nguyen12]). Here, likewise, an analogy to the field of inorganic spintronics should be drawn where the observation of the Hanle effect has been established and acknowledged as the most robust proof for the GMR effect's underlying mechanisms [Johnson85, Johnson88, Lou07, Huang07, Tombros07].

On the other side, the demonstration of pure TAMR and a TAMR contribution to the spin-valve signal is informative of the mechanisms involved in the charge transfer and particularly of the role of tunneling processes. Even in conventional OSVs TAMR can be easily proved by measurements at various in-plane orientations of the magnetic field, especially by so-called phiscan measurements.

Furthermore, TAMR can likewise be employed as a tool to analyse the interface where it is originating from, which necessarily is between the LSMO electrode and the OSC layer in all devices under investigation. As a result, it has been possible to deeply investigate an-

other effect which is not related to spintronics, the so-called resistive switching in AlQ_3-based TAMR structures presented in chapter 3.7.

Here, the resistive switching effect is observed as a reversible change of the devices' resistance R which is induced by the application of voltage pulses. It is found that not only R is modified but also the TAMR amplitude is modulated, namely enhanced with increasing R. These experiments have been motivated by similar, and yet substantially different, studies by the group of Alek Dediu, who demonstrated a similar interaction of RS and the spin-valve functionality in conventional OSVs [Hueso07, Prezioso11, Prezioso12].

It should be noted here that, in contrast to a common spin-valve signal, TAMR also yields reliable and decisive information about the prevailing charge transfer mechanism. The interpretation of the results concerning the interplay between RS and TAMR consequently is significantly simplified and a robust basis for conclusions with respect to the origin of the RS effect is ensured.

The results outlined in chapter 3.7 reveal that a tunnel barrier exists at the aforementioned interface and that this barrier is modified during the RS cycle. Sustained by quantitative analysis using I/V characterisation and appropriate fitting procedures and models, it has been possible to develop a phenomenological model to describe the RS. At the interface between the LSMO and the AlQ_3 layer the strong electric field caused by the applied voltage pulses can initiate a substantial change of the LSMO electrode's composition, namely the creation, motion or removal of pairs of oxygen vacancies and interstitial oxygen ions. Eventually, this leads to a change of the material's properties and hereby of the injection tunnel barrier at the interface LSMO-AlQ_3. In addition to the complete qualitative description, the proposed theoretical approach allows, to a certain extent, for a quantitative analysis of experimental results as well.

Hence, these experiments give an example how TAMR can be exploited as a powerful tool of investigation. Moreover, the results comprise the demonstration of a novel RS effect which goes beyond the typical bipolar/bistable behaviour usually reported in the literature. It has been shown conclusively that the RS observed in the present structures is clearly related to the specific interface LSMO-AlQ_3, one of the archetypical material combinations in the field of organic spintronics. Starting from the findings presented here, further and deeper investigations of the RS and its interplay with any MR originating from tunneling processes thus seems a very promising way towards multifunctional devices.

In the last part of this thesis the second main objective is addressed, namely the fabrication and characterisation of lateral OSV structures. A fabrication process based on the principle of shadow evaporation has been developed and improved which allows for the preparation of lateral devices that fulfill all prerequisites for spin-valve functionality (chapter 4). Up to now, experiments with this device geometry have mainly been hampered by deteriorating contaminations associated with other patterning techniques [Michelfeit08, Golmar12]. As the positive magnetotransport results indicate, obviously such side effects can be excluded for the structures fabricated with the shadow evaporation process. Although the amount of experimental data is not as extensive as for the vertical OSVs due to the still rather unsatisfying device stability, an interpretation of the results has been feasible yielding a scenario explaining the observed spin-valve signal. This scenario is based on the assumption that also

in the lateral OSVs showing MR the charge transfer is dominated by tunneling, which is quite non-obvious at first sight considering the nominal device dimensions. Nevertheless, on one side, it is possible to explain all particular features of the MR traces with this model and, on the other side, a good agreement with results obtained in vertical structures of allegedly similar dimensions is found [Barraud10].

Considering these first positive results it can be expected that this fabrication technique can be further improved, which may open the path to lateral structures where a potential spin-valve signal is originating from true diffusive spin transport and to the actual integration of magnetoresistive switching into OFET circuits. Moreover, such devices would then allow to deeply investigate an OSC material's spintronics related properties, e.g. by performing spin precession experiments as likewise done in lateral structures employing inorganic semiconductors or consisting of metals only.

Appendices

Appendix A

Organic Molecular Beam Deposition - OMBD

For the preparation of thin (monolayers to a few hundreds of nm) OSC films several technologies have been established. Whereas polymers are usually applied to substrates by solution-based processes (spin-coating, drop-casting, spraying), small molecules like those investigated in the scope of this work are mostly sublimed under HV or UHV conditions. This technology is named organic molecular beam deposition (OMBD) and is comparable to the well-known molecular beam epitaxy for inorganic semiconductors.

For this work, two types of self-built effusion cells are used for OMBD, which are different concerning their design and crucible capacity. The small cells, which are installed in the stand-alone OMBD chamber where the PDI is deposited, consist of a quartz crucible (volume $\sim 0.5\,\mathrm{cm}^3$) containing the source material, which usually is available as a powder. The crucible is mounted to a body made of tantalum which is heated by a tungsten wire. The temperature is measured by a type-K thermocouple.

The OMBD chamber which is part of the UHV cluster and in which the $\mathrm{AlQ_3}$-based devices are fabricated is equipped with a newly developed type of effusion cell shown in Fig. A.1. This cell basically consists of a quartz crucible (volume $\sim 5\,\mathrm{cm}^3$) as well, which is surrounded by a copper corpus heated by a dedicated heating wire. The temperature is measured by a resistive thermometer (Pt100). Further components of this cell are a shutter, a stainless steel shield and a water cooling unit that allows for counter cooling. The cell is capped with a heated nozzle that is attached to the copper body.

All cells are designed for operation temperatures between $\sim 50\,^\circ\mathrm{C}$ and $\sim 350\,^\circ\mathrm{C}$ ($\sim 500\,^\circ\mathrm{C}$ for the new ones), which is sufficient for the sublimation of the majority of small molecule materials. Stable temperatures are achieved by the use of PID control units. In both OMBD chambers the film thickness is monitored during deposition using a quartz crystal microbalance.

Additionally, the substrate holders can be heated up to $\sim 450\,^\circ\mathrm{C}$. The possibility to heat the substrate before and/or during the OMBD process is used for two purposes. On the one hand, it allows for in-situ annealing steps before OMBD. On the other hand, the morphology

of an OSC layer significantly depends on the substrate temperature during deposition and can therefore be tuned by varying this parameter if wanted. Thus, for instance, the charge transport performance can already be influenced during layer deposition.
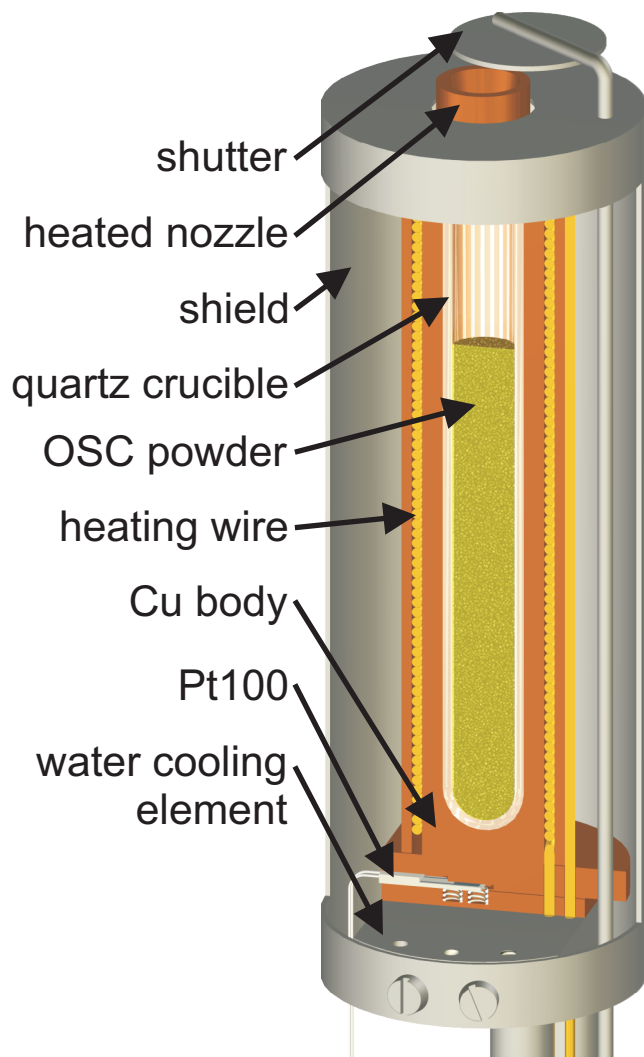

Figure A.1: Schematic representation of the newly developed effusion cell's design.

Appendix B

Setups for Transport Measurements

For (magneto)transport characterisation several measurement setups equipped with different instrumentation (see appendix C) are used. Most of the characterisation is performed in cryostats (listed in Tab. B.1) in which the magnetic field is generated by either an internal superconducting magnet (SCM) or an external electromagnet (EM). Furthermore, these setups differ concerning the maximum magnetic field H_{max}, the feasibility of changing the orientation of $\boldsymbol{H}$ with respect to the sample and the temperature range, within which a sufficient temperature stability can be achieved.

	type	magnet	$\mu_0 H_{\mathrm{max}}$	rotation of $\boldsymbol{H}$	T range	location
#1	^{4}He flow cryostat	EM	$\sim \pm 600\,\mathrm{mT}$	in plane	$4.2\,\mathrm{K}$ and RT	WÜ
#2	^{4}He bath cryostat	SCM	$\pm 300\,\mathrm{mT}$	3D	$1.8 - 200\,\mathrm{K}$	WÜ
#3	^{4}He bath cryostat	SCM	$\pm 400\,\mathrm{mT}$	3D	$1.8 - 300\,\mathrm{K}$	HAL
#4	probe station	EM	$\sim \pm 50\,\mathrm{mT}$	in plane	room temp.	WÜ
#5	probe station	EM	$\sim \pm 380\,\mathrm{mT}$	in plane	room temp.	HAL

Table B.1: List of all setups (cryostats and probe stations) for transport characterisation used in the scope of this work. Characteristic features of each setup are the maximum magnetic field H_{max}, the possibility to change the orientation of $\boldsymbol{H}$ (rotation of $\boldsymbol{H}$) and the temperature range (T range) in which a stable operation is feasible.

Setup #2 and #3 are equipped with a so-called vector-magnet that consists of three pairs of Helmholtz-coils arranged along the three axes of a cartesian coordinate system. The magnetic field generated by each coil can be independently controlled. As the total magnetic field is the superposition of three components, with such a magnet a magnetic field pointing in any direction in space (3d) can be applied to the sample. The PDI-based samples are mainly investigated in setup #1 and #2, only few of them in the (newer) setup #3.

For measurements in cryostats the samples have to be mounted to so-called chip-carriers which also requires electrical connection via ultrasonic bonding. If samples are too large for chip-carrier-mounting and/or too sensitive for bonding they are usually characterised in a probe station. These setups are also used for preliminary measurements (e.g. I/V characterisation, OFET characterisation) at room temperature. In the scope of this work

two probe stations are used, both equipped with four probes attached to micromanipulators and with an electromagnet. Setup #4 is available for the characterisation of PDI-based samples (no MR measurements due to the weak magnetic field), whereas the (newer) AlQ$_3$-based devices and other lateral spin valves are investigated in a setup with a stronger magnet also allowing for MR measurements (setup #5).

Appendix C

Transport Measurement Schematics

Fig. C.1 shows the schematic measurement circuit diagram using the example of an MR measurement. The scheme also includes peripheral components like the computer from which all measurement procedures are controlled by suitable programs (Labview virtual instruments). The output of measurement parameters (e.g. the bias voltage and the magnetic field) is indicated by blue connections in Fig. C.1 and are provided by digital-analog-converters (DAC, self-built external equipment or input/output-controllers installed to the computer) that can be addressed by the programm. The analog voltage then is either used as regulating variable for a magnet's power supply or applied to the actual measurement circuit, which is depicted on the right hand side of the two panels in Fig. C.1.

The fundamental component of (magneto)transport studies is the determination of the device's resistance, i.e. of the voltage drop U_{device} on the device and of the current I through the device. There are two possibilities how these values can be acquired. On one side (Fig. C.1**a**), a reference resistor R_{ref} (with a known resistance) can be placed in series to the device and the circuit is closed by a grounding contact. Using differential amplifiers (diff. amp.) both voltage drops, on the device and on R_{ref}, can be extracted and measured. The voltage drop on R_{ref} is then used to calculate I using Ohm's law.

On the other side (Fig. C.1**b**), likewise, a current amplifier (c. amp.) can be placed in series to the device. The output of the current amplifier is an analog voltage which is proportional to the current driven through the device. U_{device}, i.e. the voltage drop on the device, can be measured directly as the input connection of a current amplifier represents (virtual) electric ground.

In both cases, two voltages have to be measured. The standard equipment for this measurement is a highly sensitive and precise two-channel-voltmeter (Agilent 34420A) with which voltages in the nV-range can be recorded. The output channel of the voltmeter is connected to the measurement programm as well as indicated by the orange lines in Fig. C.1.

The diagram displayed in Fig. C.1 and the aforementioned equipment can only be used for measurements with bias voltages in range of $\pm 10\,\mathrm{V}$ due to the limits of the DACs ($\pm 2.5\,\mathrm{V}$ when differential amplifiers are used). Whereas magnetotransport studies usually are carried out in the low bias regime ($|U_{\mathrm{bias}}| \ll 1\,\mathrm{V}$), OFET characterisation, on the contrary, often requires the application and measurement of high voltages (up to $\pm 100\,\mathrm{V}$). Therefore, for the latter so-called semiconductor parameter analysers (Hewlett Packard HP4140b and HP4145b)
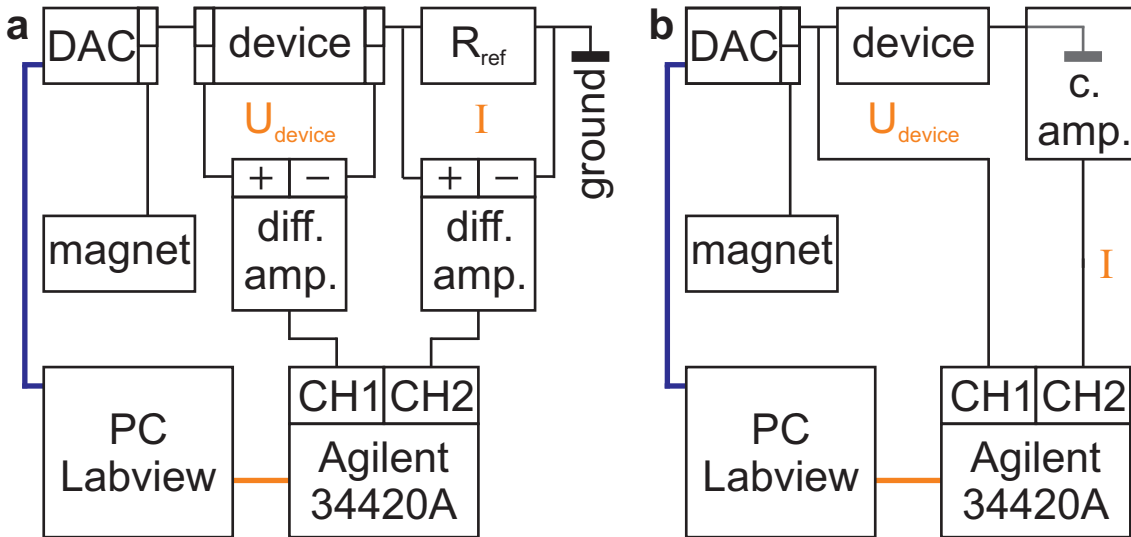
Figure C.1: Schematic representation of the measurement circuit diagram including peripheral components (PC, magnet, digital-analog-converters, Agilent voltmeter, differential amplifiers). The two possible configurations with which the fundamental measurements, the determination of the device's resistance, can be realised are sketched. These are the serial connection of either a reference resistor R_{ref} (**a**) or a current amplifier (**b**).

are used which can provide and measure the necessary voltages and the resulting currents. However, as a consequence of their relatively low precision, they are not well suited for sensitive analysis like MR studies.

Appendix D

Resistive Switching Measurements with Pulsed Bias Voltage

Rather frequently, the phenomenon of resistive switching in organic transport structures is characterised by recording I/V curves, i.e. by the subsequent increase (decrease) of U_{bias} and the simultaneous measurement of the current I [Mahapatro04, Hueso07, Prezioso11, Prezioso12]. In the scope of this work another characterisation technique is used. The basic element of this procedure is the application of a single voltage pulse (amplitude U_{pulse}, length t_{pulse}) and the subsequent resistance measurement at another bias voltage U_{meas}. For an RS experiment this elementary measurement sequentially is performed with increasing or decreasing U_{pulse} yielding the bias-voltage profile depicted in Fig. D.1.
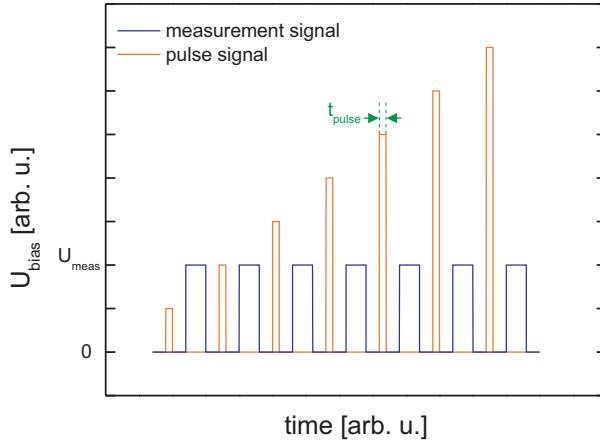
Figure D.1: Bias voltage profile of a resistive switching experiment with increasing U_{pulse}.

The choice of this technique is motivated by two considerations. On one side, it obviously provides a straightforward and simply feasible possibility to investigate the RS dynamics more extensively than it can be done using conventional I/V sweeps, e.g. with respect to the influence of t_{pulse}. On the other side, the interpretation of the results is substantially simplified. As R is measured at a fixed $U_{\mathrm{bias}} = U_{\mathrm{meas}}$, an eventual non-linearity of the

I/V characteristics does not appear in the RS trace and any change of R is reflected in the measured data immediately and unambiguously. Thus, the investigation of the RS effect by applying voltage pulses yields more information, clearer results and, last but not least, an enhanced controllability of the measurement.

Appendix E

Reference Samples Analysed in the Context of Resistive Switching

The origin of the RS effect in AlQ_3-based TAMR devices (layer sequence LSMO-AlQ_3-Cu) presented in chapter 3.7 is ascribed to processes occurring at the interface LSMO-AlQ_3. In order to exclude any misinterpretation of the obtained results, suitable control experiments are carried out. These experiments comprise investigations in several reference samples of the compositions listed below. The sample fabrication is realised by accordingly modifying the process presented in chapter 3.1. None of the reference devices does exhibit any kind of RS, which thus is underlining the governing role of the LSMO-AlQ_3 interface.

- LSMO-AlOx-Cu: In the present sample layout pinholes through the AlQ_3 film may end at the thin insulating alumina layer eventually yielding this device composition (see Fig. 3.3). This experiment is performed in order to exclude any RS effect caused in the alumina layer.

- Pt-AlQ_3-Cu: The importance of LSMO, the first component of the aforementioned interface, is verified by replacing LSMO by the noble metal Platinum. Platinum is chosen as it is available in the sputtering chamber.

- LSMO-Cu: Based on measurements in these devices the eminent role of the AlQ_3 layer and the interface LSMO-AlQ_3, respectively, can be confirmed.

Appendix F

The Simmons Model - Analysing I/V Curves of Tunnel Junctions

Several models have been established for the analysis of tunnel barriers based on suitable fitting procedures applied to I/V curves. The model proposed by Simmons [Simmons63] provides a good theoretical description for the rather simple case of a symmetric rectangular tunnel barrier (thickness d_{barrier}, height Φ_0). It can be applied when U_{bias} is small compared to Φ_0, which is obviously the case in the present experiments (for larger bias other models like Fowler Nordheim tunneling [Fowler1928] represent a better theoretical approach). Furthermore, a low U_{bias} allows to average Φ_0, i.e. to treat the barrier as basically rectangular [Simmons63], and to assume that any tilt of the barrier due to the bias is small compared to Φ_0, both other important prerequisites for the Simmons fit's evaluation.

For this evaluation, first the tunnel current density j as a function of U_{bias} is described as follows:

$$j = \frac{e}{4\pi^2 \hbar d_{\text{barrier}}^2} \left\{ \left(\Phi_0 - \frac{eU_{\text{bias}}}{2} \right) \exp\left[-\frac{\sqrt{8m_{\text{e}}}}{\hbar} \left(\Phi_0 - \frac{eU_{\text{bias}}}{2} \right)^{1/2} d_{\text{barrier}} \right] \right.$$

$$\left. - \left(\Phi_0 + \frac{eU_{\text{bias}}}{2} \right) \exp\left[-\frac{\sqrt{8m_{\text{e}}}}{\hbar} \left(\Phi_0 + \frac{eU_{\text{bias}}}{2} \right)^{1/2} d_{\text{barrier}} \right] \right\} \tag{F.1}$$

j in Equ. F.1 is derived from more general formulas assuming $eU_{\text{bias}} < \Phi_0$. The differential tunnel conductance $G = dj/dU_{\text{bias}}$ can be calculated from Equ. F.1:

$$G(U_{\text{bias}}) = G(0) + G(0) \left(\frac{e^2 m_{\text{e}}}{4\hbar^2} \frac{d_{\text{barrier}}^2}{\Phi_0} \right) U_{\text{bias}}^2 \tag{F.2}$$

with

$$G(0) = \frac{e^2}{4\pi^2 \hbar^2 d_{\text{barrier}}} \sqrt{2m_{\text{e}} \Phi_0} \exp\left(-\frac{\sqrt{8m_{\text{e}}}}{\hbar} \sqrt{\Phi_0} d_{\text{barrier}} \right) \tag{F.3}$$

Thus, from a quadratic fit to $G(U_{\mathrm{bias}})$ the barrier parameters Φ_0 and d_{barrier} can be determined. Fig. F.1 shows the exemplary I/V curve (Fig. F.1a, j plotted against U_{bias}) which has already been presented in chapter 3.7 together with the calculated corresponding differential conductance and the parabolic Simmons fit (Fig. F.1b). The data in Fig. F.1b reveal a significant deviation from the quadratic behaviour for $|U_{\mathrm{bias}}| \gtrsim 5\,\mathrm{mV}$. Therefore, the data input for all I/V analysis performed in the scope of this work is limited to $|U_{\mathrm{bias}}| < 5\,\mathrm{mV}$, where the fit yields a nearly perfect reproduction of the experimental data. The barrier parameters that can be calculated from the exemplary fit in Fig. F.1b are $\Phi_0 = (17.2 \pm 2.4)\,\mathrm{meV}$ and $d_{\mathrm{barrier}} = (15.2 \pm 0.5)\,\mathrm{nm}$.

Finally, it can be seen from Equs. F.2 and F.3 that G and hereby equally a device's resistance is mainly governed by d_{barrier}.
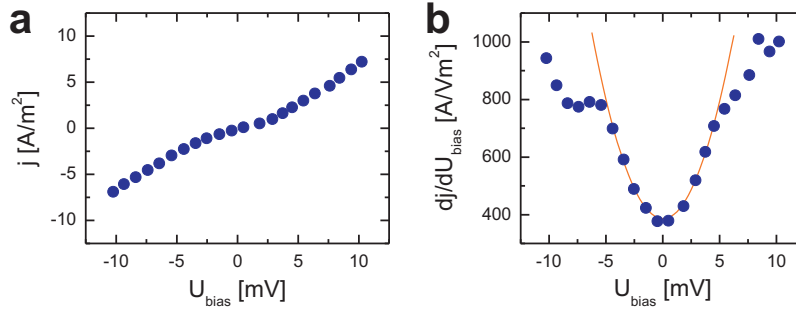

Figure F.1: Example of an I/V curve's analysis employing the Simmons fit. **a**: The result of the I/V characterisation is represented as current density j. **b**: In the low bias regime ($|U_{\mathrm{bias}}| < 5\,\mathrm{mV}$) the differential conductance calculated from the data in **a** can be fitted using a parabola (orange line).

In order to be able to reproduce resistive switching results by fitting procedures (see chapter 3.7.3), an expression for the device resistance R can be derived from the Simmons model as well. As in all RS measurements the bias voltage for the measurement of R is $U_{\mathrm{bias}} = 1\,\mathrm{mV}$ only, Equ. F.3 alone represents a sufficiently good basis here, whilst for higher U_{bias} Equ. F.2 has to be taken into account, too. First, the differential resistance R_{diff} can be easily derived from Equ. F.3:

$$R_{\mathrm{diff}} = \frac{1}{GA} = \frac{4\pi^2 \hbar^2}{\sqrt{2m_{\mathrm{e}}}Ae^2} \cdot \exp\left[\frac{\sqrt{8m_{\mathrm{e}}}}{\hbar}\sqrt{\Phi_0} \cdot d_{\mathrm{barrier}}\right] \cdot \frac{d_{\mathrm{barrier}}}{\sqrt{\Phi_0}} \tag{F.4}$$

A is the device active area. Using Equ. F.4 any ΔR_{diff} can be calculated for given pairs of d_{barrier} and Φ_0.

However, when comparing a computed R_{diff} with an actual experimental result R_{exp}, it must be borne in mind that these two values may differ by a certain factor c_{corr}. The origin of this difference is that R_{diff}, on the one hand, is a differential value calculated from the relation between U_{bias} and j (or the current, respectively), whereas R_{exp}, on the other hand,

is determined measuring U_{bias} and the current and employing Ohm's law. A demonstrative example is the simplified relation $j \propto U_{\text{bias}}^3$ which is often used for a very basic description of the tunnel current density. In this case $R_{\text{exp}} = 3 \cdot R_{\text{diff}}$, i.e. $c_{\text{corr}} = 3$, is obtained.

Finally, by introducing c_{corr} as a fitting parameter the following equation for the dependence of ΔR_{diff} on an arbitrary variable var, e.g. U_{pulse} or T_{heat}, is obtained:

$$\Delta R_{\text{diff}}\left(var\right) = c_{\text{corr}} \cdot \frac{4\pi^2\hbar^2}{\sqrt{2m_{\text{e}}}Ae^2} \cdot \left\{ \exp\left[\frac{\sqrt{8m_{\text{e}}}}{\hbar}\sqrt{\Phi_0\left(var\right)} \cdot d_{\text{barrier}}\left(var\right)\right] \cdot \frac{d_{\text{barrier}}\left(var\right)}{\sqrt{\Phi_0\left(var\right)}} \right.$$

$$\left. - \exp\left[\frac{\sqrt{8m_{\text{e}}}}{\hbar}\sqrt{\Phi_0^*} \cdot d_{\text{barrier}}^*\right] \cdot \frac{d_{\text{barrier}}^*}{\sqrt{\Phi_0^*}} \right\}$$

$$\text{(F.5)}$$

ΔR_{diff} is the difference between the resistances that can be calculated for two sets of barrier parameters. One of these sets is variable, whereas the other one represents the reference state and is denoted by a superscript $*$ in Equ. F.5.

Equ. F.5 is in agreement with the typical representation of $\Delta R_{\text{exp}}\left(var\right)$ and the barrier dynamics $d_{\text{barrier}}\left(var\right)$ and $\Phi_0\left(var\right)$, respectively, introduced in chapterf 3.7.1. Thus, Equ. F.5 can be used to fit an experimentally determined $\Delta R_{\text{exp}}\left(var\right)$ by only adjusting c_{corr} when $d_{\text{barrier}}\left(var\right)$ and $\Phi_0\left(var\right)$ are known.

Appendix G

Including the Pulse Length in Fit Procedure for Barrier Dynamics

The twofold integration of Equ. 3.15, which has been mentioned in chapter 3.7.3 in the context of a U_{pulse}- and t_{pulse}-dependent modeling of the barrier dynamics during RS-MLs, yields the following expression:

$$d_{\text{barrier}}(U_{\text{pulse}}, t_{\text{pulse}}) = d_{\text{barrier},0} + \int_0^{U_{\text{pulse}}} \int_0^{t_{\text{pulse}}} \Delta d_{\text{barrier}}(U_{\text{single}}, t_{\text{pulse}}^\star) dt_{\text{pulse}}^\star dU_{\text{single}}$$

$$\approx d_{\text{barrier},0} + \frac{1}{12\alpha^\star t_{\text{pulse}}} \left\{ d_{\text{barrier},0}^3 - d_{\text{barrier},0}^2 \sqrt{d_{\text{barrier},0}^2 + 4\alpha^\star t_{\text{pulse}}^2 \left(U_{\text{pulse}} - U_{\text{th}}\right)} \right.$$

$$- 2\alpha^\star t_{\text{pulse}}^2 \left(U_{\text{th}} - U_{\text{pulse}}\right) \left[\sqrt{d_{\text{barrier},0}^2 + 4\alpha^\star t_{\text{pulse}}^2 \left(U_{\text{pulse}} - U_{\text{th}}\right)} - 3d_{\text{barrier},0} \right]$$

$$- 3\imath \sqrt{\alpha^\star \left(U_{\text{th}} - U_{\text{pulse}}\right)} d_{\text{barrier},0}^2 t_{\text{pulse}}$$

$$\left. \times \log \left[2 \left(-2\imath \sqrt{\alpha^\star \left(U_{\text{th}} - U_{\text{pulse}}\right)} + \sqrt{d_{\text{barrier},0}^2 + 4\alpha^\star t_{\text{pulse}}^2 \left(U_{\text{pulse}} - U_{\text{th}}\right)} \right) \right] \right\}$$

$$(\text{G.1})$$

According to the reasoning outlined in chapter 3.7.3, U_{pulse} is replaced by $U_{\text{pulse}} - U_{\text{th}}$ after the integration in Equ. G.1 as well.

Bibliography

[Aharoni98]   A. Aharoni, *Demagnetizing Factors for Rectangular Ferromagnetic Prisms.* J. Appl. Phys., **83**, 3432 (1998).

[Alexandrov2012] A.S. Alexandrov, V.A. Dediu and V.V. Kabanov, *Hopping Magnetotransport via Nonzero Orbital Momentum States and Organic Magnetoresistance.* Phys. Rev. Lett., **108**, 186601 (2012).

[Bässler93]   H. Bässler, *Charge Transport in Disordered Organic Photoconductors, a Monte Carlo Simulation Study.* Phys. Status Solidi B, **175**, 15 (1993).

[Baibich88]   M.N. Baibich, J.M. Broto, A. Fert, F. Nguyen Van Dau, F. Petroff, P. Etienne, G. Creuzet, A. Friederich and J. Chazelas, *Giant Magnetoresistance of (001)Fe//(001)Cr Magnetic Superlattices.* Phys. Rev. Lett., **61**, 2472 (1988).

[Baikalov03]   A. Baikalov, Y.Q. Wang, B. Shen, B. Lorenz, S. Tsui, Y.Y. Sun, Y.Y. Xue and C.W. Chu, *Field-Driven Hysteretic and Reversible Resistive Switch at the Ag-$Pr_{0.7}Ca_{0.3}MnO_3$ Interface.* Appl. Phys. Lett., **83**, 957 (2003).

[Baker12]   W.J. Baker, K. Ambal, D.P. Waters, R. Baarda, H. Morishita, K. van Schooten, D.R., McCamey, J.M. Lupton and C. Boehme, *Robust Absolute Magnetometry with Organic Thin-Film Devices.* Nat. Commun., **3**, 898 (2012).

[Baldo01]   M.A. Baldo, and S.R. Forrest, *Interface-Limited Injection in Amorphous Organic Semiconductors.* Phys. Rev. B, **64**, 085201 (2001).

[Barraud10]   C. Barraud, P. Seneor, R. Mattana, S. Fusil, K. Bouzehouane, C. Deranlot, P. Graziosi, L. Hueso, I. Bergenti, V. Dediu, F. Petroff and A. Fert, *Unravelling the Role of the Interface for Spin Injection into Organic Semiconductors.* Nat. Phys., **6**, 615 (2010).

[Bergenti04]   I. Bergenti, V. Dediu, E. Arisi, T. Mertelj, M. Murgia, A. Riminucci, G. Ruani, M. Solzi and C. Taliani, *Spin Polarised Electrodes for Organic Light Emitting Diodes.* Org. Electron., **5**, 309 (2004).

[Bergenti07]   I. Bergenti, A. Riminucci, E. Arisi, M. Murgia, M. Cavallini, M. Solzi, F. Casoli and V. Dediu, *Magnetic Properties of Cobalt Thin Films Deposited on Soft Organic Layers.* J. Magn. Magn. Mater., **316**, 987 (2007).

[Bergeson08]   J.D. Bergeson, V.N. Prigodin, D.M. Lincoln, and A.J. Epstein , *Bipolaron Mechanism for Organic Magnetoresistance.* Phys. Rev. Lett., **100**, 067201 (2008).

[Berndt00]   L. M. Berndt, V. Balbarin and Y. Suzuki, *Magnetic anisotropy and strain states of (001) and (110) colossal magnetoresistance thin films.* Appl. Phys. Lett., **77**, 2903 (2000).

[Binasch89]   G. Binasch, P. Grünberg, F. Saurenbach and W. Zinn, *Enhanced Magnetoresistance in Layered Magnetic Structures with Antiferromagnetic Interlayer Exchange.* Phys. Rev. B, **39**, 4828 (1989).

[Bloom07]   F.L. Bloom, W. Wagemans, M. Kemerink and B. Koopmans, *Separating Positive and Negative Magnetoresistance in Organic Semiconductor Devices.* Phys. Rev. Lett., **99**, 257201 (2007).

[Bobbert07]   P.A. Bobbert, T.D. Nguyen, F.W.A. van Oost, B. Koopmans and M. Wohlgenannt, *Bipolaron Mechanism for Organic Magnetoresistance.* Phys. Rev. Lett., **99**, 216801 (2007).

[Boehme09]   C. Boehme, D.R. McCamey, K.J. van Schooten, W.J. Baker, S.-Y. Lee, S.-Y. Paik and J.M. Lupton, *Pulsed Electrically Detected Magnetic Resonance in Organic Semiconductors.* Phys. Status Solidi B, **246**, 2750 (2009).

[Bolotin06]   K.I. Bolotin, F. Kuemmeth and D.C. Ralph, *Anisotropic Magnetoresistance and Anisotropic Tunneling Magnetoresistance Due to Quantum Interference in Ferromagnetic Metal Break Junctions.* Phys. Rev. Lett., **97**, 127202 (2006).

[Boschker09]   H. Boschker, M. Mathews, E.P. Houwman, H. Nishikawa, A. Vailionis, G. Koster, G. Rijnders and D.H.A. Blank, *Strong Uniaxial In-plane Magnetic Anisotropy of (001)- and (011)-Oriented $La_{0.67}Sr_{0.33}MnO_3$ Thin Films on $NdGaO_3$ Substrates.* Phys. Rev. B, **79**, 214425 (2009).

[Bowen03]   M. Bowen, M. Bibes, A. Barthelemy, J.-P. Contour, A. Anane, Y. Lemaitre and A. Fert, *Nearly Total Spin Polarization in $La_{2/3}Sr_{1/3}MnO_3$ from Tunneling Experiments.* Appl. Phys. Lett., **82**, 233 (2003).

[Bozano04]   L.D. Bozano, B.W. Kean, V.R. Deline, J.R. Salem and J.C. Scott, *Mechanism for Bistability in Organic Memory Elements.* Appl. Phys. Lett., **84**, 607 (2004).

[Brown94]   A.R. Brown, D.M. de Leeuw, E.E. Havinga and A. Pomp, *A Universal Relation Between Conductivity and Field-Effect Mobility in Doped Amorphous Organic Semiconductors.* Synth. Met., **68**, 65 (1994).

[Bruchhaus10]   R. Bruchhaus and R. Waser, *Bipolar Resistive Switching in Oxides for Memory Applications.* in *Thin Film Metal-Oxides*, 131-167, Springer New York (2010).

[Burkert04]   T. Burkert, L. Nordström, O. Eriksson and O. Heinonen, *Giant Magnetic Anisotropy in Tetragonal FeCo Alloys.* Phys. Rev. Lett., **93**, 027203 (2004).

[Chang10]   T.Y Chand, Y.-W. Cheng and P.T. Lee, *Electrical characteristics of an organic bistable device using an $Al/Alq_3/nanostructured$ $MoO_3/Alq_3/p^+$-Si structure.* Appl. Phys. Lett., **96**, 043309 (2010).

[Cho11]   B. Cho, S. Song, Y. Ji, T.-W. Kim and T. Lee, *Organic Resistive Memory Devices: Performance Enhancement, Integration, and Advanced Architectures.* Adv. Funct. Mater., **21**, 2806 (2011).

[Cinchetti09]   M. Cinchetti, K. Heimer, J.-P. Wüstenberg, O. Andreyev, M. Bauer, S. Lach, C. Ziegler, Y. Gao and M. Aeschlimann, *Determination of Spin Injection and Transport in a Ferromagnet/Organic Semiconductor Heterojunction by Two-Photon Photoemission.* Nat. Mater., **8**, 115 (2009).

[Cox13]   M. Cox, P. Janssen, S.H.W. Wouters, E.H.M. van der Heijden, M. Kemerink and B. Koopmans, *The Influence of Device Physics on Organic Magnetoresistance.* Synth. Met., **173**, 10 (2013).

[Cowburn95]   R.P. Cowburn, S.J. Gray, J. Ferré, J.A.C. Bland and J. Miltat, *Magnetic Switching and In-Plane Uniaxial Anisotropy in Ultrathin Ag/Fe/Ag(100) Epitaxial Films.* J. Appl. Phys., **78**, 7210 (1995).

[CRC96]   D.R. Lide (Editor-in-Chief), *CRC Handbook of Chemistry and Physics, 77th Edition,* CRC Press (1996).

[Dagotto01]   E. Dagotto, T. Hotta and A. Moreo, *Colossal Magnetoresistant Materials: The Key Role of Phase Separation.* Phys. Rep., **344**, 1 (2001).

[Davids97]   P.S. Davids, I.H. Campbell and D.L. Smith, *Device Model for Single Carrier Organic Diodes.* J. Appl. Phys., **82**, 6319 (1997).

[DeTeresa99]   J.M. De Teresa, A. Barthélémy, A. Fert, J.P. Contour, R. Lyonnet, F. Montaigne, P. Seneor and A. Vaurès, *Inverse Tunnel Magnetoresistance in Co-$SrTiO_3$-$La_{0.7}Sr_{0.3}MnO_3$: New Ideas on Spin-Polarized Tunneling.* Phys. Rev. Lett., **82**, 4288 (1999).

[Dediu95]   V. Dediu, Q.D. Jian, F.C. Matacotta, P. Scardi, M. Lazzarino, G. Nieva and L. Civale, *Deposition of $MBa_2Cu_3O_{7-x}$ thin Films by Channel-Spark Method.* Supercond. Sci. Technol., **8**, 160 (1995).

[Dediu02]   V. Dediu, M. Murgia, F. Matacotta, C. Taliani and S. Barbanera, *Room Temperature Spin Polarized Injection in Organic Semiconductor.* Solid State Commun., **122**, 181 (2002).

[Dediu08]   V. Dediu, L.E. Hueso, I. Bergenti, A. Riminucci, F. Borgatti, P. Graziosi, C. Newby, F. Casoli, M.P. de Jong, C. Taliani and Y. Zhan, *Room-Temperature Spintronic Effects in Alq_3-Based Hybrid Devices.* Phys. Rev. B, **78**, 115203 (2008).

[Dediu09]   V.A. Dediu, L.E. Hueso, I. Bergenti and C. Taliani, *Spin Routes in Organic Semiconductors.* Nat. Mater., **8**, 850 (2009).

[Desai07]   P. Desai, P. Shakya, T. Kreouzis, W. P. Gillin, N. A. Morley, and M. R. J. Gibbs, *Magnetoresistance and efficiency measurements of Alq$_3$-based OLEDs* . Phys. Rev. B, **78**, 094423(2007).

[Dho03]   J. Dho, N.H. Hur, I.S. Kim and Y.K. Park, *Oxygen Pressure and Thickness Dependent Lattice Strain in La$_{0.7}$Sr$_{0.3}$MnO$_3$ Films.* J. Appl. Phys., **94**, 7670 (2003).

[Dong07]   R. Dong, W.F. Xiang, D.S. Lee, S.J. Oh, D.J. Seong, S.H. Heo, H.J. Choi, M.J. Kwon, M. Chang, M. Jo, M. Hasan and H. Hwang, *Improvement of Reproducible Hysteresis and Resistive Switching in Metal-La$_{0.7}$Ca$_{0.3}$MnO$_3$-Metal Heterostructures by Oxygen Annealing.* Appl. Phys. Lett., **90**, 182118 (2007).

[Drew09]   A.J. Drew, J. Hoppler, L. Schulz, F.L. Pratt, P. Desai, P. Shakya, T. Kreouzis, W.P. Gillin, A. Suter, N.A. Morley, V.K. Malik, A. Dubroka, K.W. Kim, H. Bouyanfif, F. Bourqui, C. Bernhard, R. Scheuermann, G.J. Nieuwenhuys, T. Prokscha and E. Morenzoni, *Direct Measurement of the Electronic Spin Diffusion Length in a Fully Functional Organic Spin Valve by Low-Energy Muon Spin Rotation.* Nat. Mater., **8**, 109 (2009).

[Dürr03]   A.C. Dürr, F. Schreiber, M. Kelsch, H.D. Carstanjen, H. Dosch and O.H. Seeck, *Morphology and Interdiffusion Behavior of Evaporated Metal Films on Crystalline Diindenoperylene Thin Films.* J. Appl. Phys., **93**, 5201 (2003).

[Eley53]   D.D. Eley, G.D. Parfitt, M.J. Perry and D.H. Taysum, *The Semiconductivity of Organic Substances, Part 1.* Trans. Faraday Soc., **49**, 79 (1953).

[Fert68]   A. Fert and I.A. Campbell, *Two-Current Conduction in Nickel.* Phys. Rev. Lett., **21**, 1190 (1968).

[Fert01]   A. Fert and H. Jaffrès, *Conditions for Efficient Spin Injection from a Ferromagnetic Metal into a Semiconductor.* Phys. Rev. B, **64**, 184420 (2001.

[Francis04]   T.L. Francis, Ö. Mermer, G. Veeraraghavan and M. Wohlgenannt, *Large Mgnetoresistance at Room Temperature in Semiconducting Polymer Sandwich Devices.* New J. Phys., **6**, 185 (2004).

[Fowler1928]   R.H. Fowler and L. Nordheim, *Electron Emission in Intense Electric Fields.* Proc. R. Soc. A, **119**, 173 (1928).

[Fujishiro98] H. Fujishiro, T. Fukase and M. Ikebe, *Charge Ordering and Sound Velocity Anomaly in La$_{1-x}$Sr$_x$MnO$_3$ (x $\geq$ 0.5).* J. Phys. Soc. Jpn., **67**, 2582, 1998).

[Golmar12]   F. Golmar, M. Gobbi, R. Llopis, P. Stoliar, F. Casanova and L.E. Hueso, *Non-Conventional Metallic Electrodes for Organic Field-Effect Transistors.* Org. Electron., **13**, 2301 (2012).

[Gould04] C. Gould, C. Rüster, T. Jungwirth, E. Girgis, G. Schott, R. Giraud, K. Brunner, G. Schmidt and L.W. Molenkamp, *Tunneling Anisotropic Magnetoresistance: A Spin-Valve-Like Tunnel Magnetoresistance Using a Single Magnetic Layer.* Phys. Rev. Lett., **93**, 117203 (2004).

[Goyal97] A. Goyal, M. Rajeswari, R. Shreekala, S.E. Lofland, S.M. Bhagat, T. Boettcher, C. Kwon, R. Ramesh and T. Venkatesan, *Material Characteristics of Perovskite Manganese Oxide Thin Films for Bolometric Applications.* Appl. Phys. Lett., **71**, 2535 (1997).

[Grünewald07] M. Grünewald, *Magnetowiderstandseffekte in Organischen Halbleitern.* Master's thesis, Physikalisches Institut der Julius-Maximilians-Universität Würzburg (2007).

[Grünewald11] M. Grünewald, M. Wahler, F. Schumann, M. Michelfeit, C. Gould, R. Schmidt, F. Würthner, G. Schmidt and L.W. Molenkamp, *Tunneling Anisotropic Magnetoresistance in Organic Spin Valves.* Phys. Rev. B, **84**, 125208 (2011).

[Grünewald13a] M. Grünewald, J. Kleinlein, F. Syrowatka, F. Würthner, L.W. Molenkamp and G. Schmidt, *Large Room-Temperature Magnetoresistance in Lateral Organic Spin Valves Fabricated by In Situ Shadow Evaporation.* Org. Electron., **14**, 2082 (2013).

[Grünewald13b] M. Grünewald, R. Göckeritz, N. Homonnay, F. Würthner, L.W. Molenkamp and G. Schmidt, *Vertical Organic Spin Valves in Perpendicular Magnetic Fields.* Phys. Rev. B, **88**, 085319 (2013).

[Grünewald14] M. Grünewald, N. Homonnay, J. Kleinlein and G. Schmidt, *Voltage Controlled Oxide Barriers in Organic/Hybrid Spin Valves Based on Tunneling Anisotropic Magnetoresistance.* Phys. Rev. B, **90**, 205208 (2014).

[Haddock06] J.N. Haddock, X. Zhang, S. Zheng, Q. Zhang, S.R. Marder and B. Kippelen, *A Comprehensive Study of Short Channel Effects in Organic Field-Effect Transistors.* Org. Electron., **7**, 45 (2006).

[Harmon2012] N. Harmon and M. Flatté, *Spin-Flip Induced Magnetoresistance in Positionally Disordered Organic Solids.* Phys. Rev. Lett., **108**, 186602 (2012).

[Harmon2013] N. Harmon and M. Flatté, *Distinguishing Spin Relaxation Mechanisms in Organic Semiconductors.* Phys. Rev. Lett., **110**, 176602 (2013).

[Hasan08] M. Hasan, R. Dong, H.J. Choi, D.S. Lee, D.-J. Seong, M.B. Pyun and H. Hwang, *Uniform Resistive Switching with a Thin Reactive Metal Interface Layer in Metal-$La_{0.7}Ca_{0.3}MnO_3$-Metal Heterostructures.* Appl. Phys. Lett., **92**, 202102 (2008).

[Hickmott62] T.W. Hickmott, *Low-Frequency Negative Resistance in Thin Anodic Oxide Films.* J. Appl. Phys., **33**, 2669 (1962).

[Homonnay]   N. Homonnay, C. Eisenschmidt, M. Wahler, J. Verbeeck, K. O'Shea and
                G. Schmidt, G.,   *Interface Reaction in LSMO-Metal Hybrid Structures.*
                manuscript in preparation.

[Horowitz98]   G. Horowitz, *Organic Field-Effect Transistors.* Adv. Mater., **10**, 365 (1998).

[Horowitz00]   G. Horowitz, M.E. Hajlaoui and R. Hajlaoui, *Temperature and Gate Volt-
                age Dependence of Hole Mobility in Polycrystalline Oligothiophene Thin Film
                Transistors.* J. Appl. Phys., **87**, 4456 (2000).

[Huang07]   B. Huang, D.J. Monsma and I. Appelbaum, *Coherent Spin Transport Through
                a 350 Micron Thick Silicon Wafer.* Phys. Rev. Lett., **99**, 177209 (2007).

[Hueso07]   L.E. Hueso, I. Bergenti, A. Riminucci, Y. Zhan and V. Dediu, *Multipurpose
                Magnetic Organic Hybrid Devices.* Adv. Mater., **19**, 26392642 (2007).

[Jedema01]   F.J. Jedema, A.T. Filip and B.J. van Wees, *Electrical Spin Injection and
                Accumulation at Room Temperature in an All-Metal Mesoscopic Spin Valve.*
                Nature, **410**, 345 (2001).

[Jeong13]   J. Jeong, N. Aetukuri, T. Graf, T.D. Schladt, M.G. Samant and S.S.P. Parkin,
                *Suppression of Metal-Insulator Transition in VO_2 by Electric Field-Induced
                Oxygen Vacancy Formation.* Science, **339**, 1402 (2013).

[Jin94]   S. Jin, T.H. Tiefel, M. McCormack, R.A. Fastnacht, R. Ramesh and L.H.
                Chen *Thousandfold Change in Resistivity in Mgnetoresistive La-Ca-Mn-O
                Films.* Science, **264**, 413 (1994).

[J-Åkerman00]   B.J. Jönsson-Åkerman, R. Escudero, C. Leighton, S. Kim, I.K. Schuller and
                D.A. Rabson, *Reliability of Normal-State CurrentVoltage Characteristics as
                an Indicator of Tunnel-Junction Barrier Quality.* Appl. Phys. Lett., **77**, 1870
                (2000).

[Johnson85]   M. Johnson and R.H. Silsbee, *Interfacial Charge-Spin Coupling: Injection
                and Detection of Spin Magnetization in Metals.* Phys. Rev. Lett., **55**, 1790
                (1985).

[Johnson88]   M. Johnson and R.H. Silsbee, *Spin-injection Experiment.* Phys. Rev. B, **37**,
                5326 (1988).

[Jones04]   B.A. Jones, M.J. Ahrens, M.-H. Yoon, A. Facchetti, T.J. Marks and M.R.
                Wasielewski, *High-Mobility Air-Stable n-type Semiconductors with Processing
                Versatility: Dicyanoperylene-3,4:9,10-bis(dicarboximides).* Angew. Chem.,
                Int. Ed. Engl., **43**, 6363, 2004).

[deJong03]   M.P. de Jong, V.A. Dediu, C. Taliani and W.R. Salaneck, *Electronic Struc-
                ture of $La_{0.7}Sr_{0.3}MnO_3$ Thin Films for Hybrid Organic/Inorganic Spintronics
                Applications.* J. Appl. Phys., **94**, 7292 (2003).

[deJong05]   M.P. de Jong, I. Bergenti, V.A. Dediu, M. Fahlman, M. Marsi and C. Taliani, *Evidence for Mn^{2+} Ions at Surfaces of $La_{0.7}Sr_{0.3}MnO_3$ Thin Films.* Phys. Rev. B, **71**, 014434 (2005).

[Jonker50]   G.H. Jonker and J.V. Santen, *Ferromagnetic Compounds of Manganese with Perovskite Structure.* Physica, **16**, 337 (1950).

[Jullière75]   M. Jullière, *Tunneling Between Ferromagnetic Films.* Phys. Lett. A, **54**, 225 (1975).

[Kepler95]   R.G. Kepler, P.M. Beeson, S.J. Jacobs, R.A. Anderson, M.B. Sinclair, V.S. Valencia and P.A. Cahill, *Electron and Hole Mobility in Tris(8-hydroxyquinolinolato-N1,O8) Aluminum.* Appl. Phys. Lett., **66**, 3618 (1995).

[Kim04]   J.Y. Kim, I.J. Chung, Y.C. Kim and J.-W. Yu, *Mobility of Electrons and Holes in a Liquid Crystalline Perylene Diimide Thin Film with Time of Flight Technique.* Chem. Phys. Lett., **398**, 367 (2004).

[Kim05]   J.Y. Kim, I.J. Chung, C. Lee, Y.C. Kim, J.K. Kim and J.-W. Yu, *Mobility of Electrons and Holes in an n-Type Organic Semiconductor Perylene Diimide Thin Film.* Curr. Appl. Phys., **5**, 615 (2005).

[Kittel46]   C. Kittel, *Theory of the Structure of Ferromagnetic Domains in Films and Small Particles.* Phys. Rev., **70**, 965 (1946).

[Klauk06]   H. Klauk (Editor), *Organic Electronics: Materials, Manufacturing, and Applications.* Wiley-VCH Weinheim (2006).

[Lach12]   S. Lach, A. Altenhof, K. Tarafder, F. Schmitt, M.E. Ali, M. Vogel, J. Sauther, P.M. Oppeneer and C. Ziegler, *MetalOrganic Hybrid Interface States of a Ferromagnet/Organic Semiconductor Hybrid Junction as Basis for Engineering Spin Injection in Organic Spintronics.* Adv. Funct. Mater., **22**, 989 (2012).

[Le Comber70]   P.G. Le Comber and W.E. Spear, *Electronic Transport in Amorphous Silicon Films.* Phys. Rev. Lett., **25**, 509 (1970).

[Lee98]   S.T. Lee, X.Y. Hou, M.G. Mason and C.W. Tang, *Energy Level Alignment at Alq/Metal Interfaces.* Appl. Phys. Lett., **72**, 1593 (1998).

[Lee08]   P.-T. Lee, T.-Y. Chang and S.-Y. Chen, *Tuning of the Electrical Characteristics of Organic Bistable Devices by Varying the Deposition Rate of Alq_3 Thin Film.* Org. Electron., **9**, 916 (2008).

[L-Pelecky96]   D.L. Leslie-Pelecky and R.D. Rieke, *Magnetic Properties of Nanostructured Materials.* Chem. Mater., **8**, 1770 (1996).

[Li05]   T. Li, B. Wang, H. Dai, Y. Du, H. Yan and Y. Liu, *Annealing Effect on the Structural and Magnetic Properties of $La_{0.7}Sr_{0.3}MnO_3$ Films.* J. Appl. Phys., **98**, 123505 (2005).

[Libsch93]   F.R. Libsch and J. Kanicki, *Bias-Stress-Induced Stretched-Exponential Time Dependence of Charge Injection and Trapping in Amorphous Thin-Film Transistors.* Appl. Phys. Lett., **62**, 1286 (1993).

[Lin10]   R. Lin, F. Wang, J. Rybicki, M. Wohlgenannt and K.A. Hutchinson, *Distinguishing Between Tunneling and Injection Regimes of Ferromagnet/Organic Semiconductor/Ferromagnet Junctions.* Phys. Rev. B, **81**, 195214 (2010).

[Lou07]   X. Lou, C. Adelmann, S.A. Crooker, E.S. Garlid, J. Zhang, K.S.M. Reddy, S.D. Flexner, C.J. Palmstrøm and P.A. Crowell, *Electrical Detection of Spin Transport in Lateral Ferromagnet-Semiconductor Devices.* Nat. Phys., **3**, 197 (2007).

[Lupton10]   J.M. Lupton, D.R. McCamey and C. Boehme, *Coherent Spin Manipulation in Molecular Semiconductors: Getting a Handle on Organic Spintronics.* ChemPhysChem, **11**, 3040 (2010).

[Mahapatro04] A.K. Mahapatro, R. Agrawal and S. Ghosh, *Electric-Field-Induced Conductance Transition in 8-Hydroxyquinoline Aluminum (Alq3).* J. Appl. Phys., **96**, 3583 (2004).

[Majumdar06a] S. Majumdar, R. Laiho, P. Laukkanen, I.J. Väyrynen, H.S. Majumdar and R. Österbacka, *Application of Regioregular Polythiophene in Spintronic Devices: Effect of Interface.* Appl. Phys. Lett., **89**, 122114 (2006).

[Majumdar06b] S. Majumdar, H.S. Majumdar, R. Laiho and R. Österbacka *Comparing Small Molecules and Polymer for Future Organic Spin-valves.* J. Alloys Compd., **423**, 169 (2006).

[Mathews05]   M. Mathews, F.M. Postma, J.C. Lodder, R. Jansen, G. Rijnders and D.H.A. Blank, *Step-Induced Uniaxial Magnetic Anisotropy of $La_{0.67}Sr_{0.33}MnO_3$ Thin Films.* Appl. Phys. Lett., **87**, 242507 (2005).

[Meiklejohn56] W.H. Meiklejohn and C.P. Bean, *New Magnetic Anisotropy.* Phys. Rev., **102**, 1413 (1956).

[Mermer05a]   Mermer, Ö., Veeraraghavan, G., Francis, T., Sheng, Y., Nguyen, D. T., Wohlgenannt, M., Köhler, A., Al-Suti, M. K. and Khan, M. S. Large magnetoresistance in nonmagnetic π-conjugated semiconductor thin film devices. *Phys. Rev. B*, **72**:205202 , 2005.

[Mermer05b]   Mermer, Ö., Veeraraghavan, G., Francis, T., and Wohlgenannt, M. Large magnetoresistance at room-temperature in small-molecular-weight organic semiconductor sandwich devices. *Solid State Commun.*, **134**(9):631 , 2005.

[Michelfeit08] M. Michelfeit, G. Schmidt, J. Geurts and L.W. Molenkamp, *Organic Field-Effect Transistors for Spin-Polarized Transport.* Phys. Status Solidi A, **205**, 656 (2008).

[Millis95]   A.J. Millis, P.B. Littlewood and B.I. Shraiman, *Double Exchange Alone does not Explain the Resistivity of $La_{1-x}Sr_xMnO_3$.* Phys. Rev. Lett., **74**, 5144 (1995).

[Miyazaki91]   T. Miyazaki, T. Yaoi, and S. Ishio *Large Magnetoresistance Effect in 82Ni-Fe/Al-Al_2O_3/Co Magnetic Tunneling Junction.* J. Magn. Magn. Mater., **98**, L7 (1991).

[Monzon99]   F.G. Monzon and M.L. Roukes, *Spin Injection and the Local Hall Effect in InAs Quantum Wells.* J. Magn. Magn. Mater., **198**, 632 (1999).

[Moodera99]   J.S. Moodera and G. Mathon, *Spin Polarized Tunneling in Ferromagnetic Junctions.* J. Magn. Magn. Mater., **200**, 248 (1999).

[Morley14]   N.A. Morley, A.J. Drew, H. Zhang, K. Scott, S. Hudziak and D.J. Morgan, *Study of the MagneticAlq_3 Interface in Organic Spin-valves.* Appl. Surf. Sci., **313**, 850 (2014).

[Moser07]   J. Moser, A. Matos-Abiague, D. Schuh, W. Wegscheider, J. Fabian and D. Weiss, *Tunneling Anisotropic Magnetoresistance and Spin-Orbit Coupling in Fe/GaAs/Au Tunnel Junctions.* Phys. Rev. Lett., **99**, 056601 (2007).

[Mott36]   N.F. Mott and H.H. Wills, *The Electrical Conductivity of Transition Metals.* Proc. R. Soc. A, **153**, 699 (1936).

[Mott69]   N.F. Mott, *Conduction in Non-Crystalline Materials.* Philos. Mag., **19**, 835 (1969).

[Nguyen10]   T.D. Nguyen, G. Hukic-Markosian, F. Wang, L. Wojcik, X.-G. Li, E. Ehrenfreund and Z.V. Vardeny, *Isotope Effect in Spin Response of π-Conjugated Polymer Films and Devices.* Nat. Mater., **9**, 345 (2010).

[Nguyen12]   T.D. Nguyen, E. Ehrenfreund and Z.V. Vardeny, *Spin-Polarized Light-Emitting Diode Based on an Organic Bipolar Spin Valve.* Science, **337**, 204 (2012).

[Nian07]   Y.B. Nian, J. Strozier, N.J. Wu, X. Chen and A. Ignatiev, *Evidence for an Oxygen Diffusion Model for the Electric Pulse Induced Resistance Change Effect in Transition-Metal Oxides.* Phys. Rev. Lett., **98**, 146403 (2007).

[Oh07]   J.H. Oh, S. Liu, Z. Bao, R. Schmidt and F. Würthner, *Air-Stable n-Channel Organic Thin-Film Transistors with High Field-Effect Mobility Based on N,N'-Bis(Heptafluorobutyl)3,4:9,10-Perylene Diimide.* Appl. Phys. Lett., **91**, 212107 (2007).

[Oh10]   J.H. Oh, S.-L. Suraru, W.-Y. Lee, M. Könemann, H.W. Höffken, C. Röger, R. Schmidt, Y. Chung, W.-C. Chen, F. Würthner, F. and Z. Bao, *High-Performance Air-Stable n-Type Organic Transistors Based on Core-Chlorinated Naphthalene Tetracarboxylic Diimides.* Adv. Funct. Mater., **20**, 2148 (2010).

[Park98a]   J.-H. Park, E. Vescovo, H.-J. Kim, C. Kwon, R. Ramesh and T. Venkatesan, *Direct Evidence for a Half-Metallic Ferromagnet.* Nature, **392**, 794 (1998).

[Park98b]   J.-H. Park, E. Vescovo, H.-J. Kim, C. Kwon, R. Ramesh and T. Venkatesan, *Magnetic Properties at Surface Boundary of a Half-Metallic Ferromagnet $La_{0.7}Sr_{0.3}MnO_3$.* Phys. Rev. Lett., **81**, 1953 (1998).

[Park08]   B.G. Park, J. Wunderlich, D.A. Williams, S.J. Joo, K.Y. Jung, K.H. Shin, K. Olejník, A.B. Shick and T. Jungwirth, *Tunneling Anisotropic Magnetoresistance in Multilayer-$(Co/Pt)/AlO_x/Pt$ Structures.* Phys. Rev. Lett., **100**, 087204 (2008).

[Parker94]   I.D. Parker, *Carrier Tunneling and Device Characteristics in Polymer Light-Emitting Diodes.* J. Appl. Phys., **75**, 1656 (1994).

[Pierret96]   R.F. Pierret, *Semiconductor Device Fundamentals, Second Edition.* Addison-Wesley (1996).

[Pratt91]   W.P. Pratt, S.-F. Lee, J.M. Slaughter, R. Loloee, P.A. Schroeder and J. Bass, *Perpendicular Giant Magnetoresistances of Ag/Co Multilayers.* Phys. Rev. Lett., **66**, 3060 (1991).

[Prezioso11]   M. Prezioso, A. Riminucci, I. Bergenti, P. Graziosi, D. Brunel and V.A. Dediu, *Electrically Programmable Magnetoresistance in Multifunctional Organic-Based Spin Valve Devices.* Adv. Mater., **23**(11), 1371 (2011).

[Prezioso12]   M. Prezioso, A. Riminucci, P. Graziosi, I. Bergenti, R. Rakshit, R. Cecchini, A. Vianelli, F. Borgatti, N. Haag, M. Willis, A.J. Drew, W.P. Gillin and V.A. Dediu, *A Single-Device Universal Logic Gate Based on a Magnetically Enhanced Memristor.* Adv. Mater., **25**, 534 (2012).

[Rabson01]   D.A. Rabson, B.J. Jönsson-Åkerman, A.H. Romero, R. Escudero, C. Leighton, S. Kim and I.K. Schuller, *Pinholes May Mimic Tunneling.* J. Appl. Phys., **89**, 2786 (2001).

[Rajeswari98] M. Rajeswari, R. Shreekala, A. Goyal, S.E. Lofland, S.M. Bhagat, K. Ghosh, R.P. Sharma, R.L. Greene, R. Ramesh, T. Venkatesan and T. Boettcher, *Correlation Between Magnetic Homogeneity, Oxygen Content, and Electrical and Magnetic Properties of Perovskite Manganite Thin Films.* Appl. Phys. Lett., **73**, 2672 (1998).

[Rashba00]   E.I. Rashba, *Theory of Electrical Spin Injection: Tunnel Contacts as a Solution of the Conductivity Mismatch Problem.* Phys. Rev. B, **62**, R16267 (2000).

[Riminucci13] A. Riminucci, M. Prezioso, C. Pernechele, P. Graziosi, I. Bergenti, R. Cecchini, M. Calbucci, M. Solzi, and V.A. Dediu, *Hanle Effect Missing in a Prototypical Organic Spintronic Device.* Appl. Phys. Lett., **102**, 092407 (2013).

[Rozenberg04]   M.J. Rozenberg, I.H. Inoue and M.J. Sánchez, *Nonvolatile Memory with Multilevel Switching: A Basic Model.* Phys. Rev. Lett., **92**, 178302 (2004).

[Rüster05a]   C. Rüster, *Magnetotransport Effects in Lateral and Vertical Ferromagnetic Semiconductor Junctions.* Ph.D. thesis, University of Würzburg (2005).

[Rüster05b]   C. Rüster, C. Gould, T. Jungwirth, J. Sinova, G.M. Schott, R. Giraud, K. Brunner, G. Schmidt and L.W. Molenkamp, *Very Large Tunneling Anisotropic Magnetoresistance of a (Ga,Mn) As/GaAs/(Ga,Mn)As Stack.* Phys. Rev. Lett., **94**, 027203 (2005).

[Rybicki12]   J. Rybicki, R. Lin, F. Wang, M. Wohlgenannt, C. He, T. Sanders and Y. Suzuki, *Tuning the Performance of Organic Spintronic Devices Using X-Ray Generated Traps.* Phys. Rev. Lett., **109**, 076603 (2012).

[Salleo04]   A. Salleo and R.A. Street, *Kinetics of Bias Stress and Bipolaron Formation in Polythiophene.* Phys. Rev. B, **70**, 235324 (2004).

[Santos07]   T.S. Santos, J.S. Lee, P. Migdal, I.C. Lekshmi, B. Satpati and J.S. Moodera, *Room-Temperature Tunnel Magnetoresistance and Spin-Polarized Tunneling Through an Organic Semiconductor Barrier.* Phys. Rev. Lett., **98**, 016601 (2007).

[Sanvito10]   S. Sanvito, *Molecular Spintronics the Rise of Spinterface Science.* Nat. Phys., **6**, 562 (2010).

[Saragi09]   T.P.I. Saragi, C. Schmidt, K. Schultz, T. Weis, J. Salbeck and A. Ehresmann, *Interface Morphologies and Magnetization Characteristics of $Co_{70}Fe_{30}$ Thin Films Deposited on Conjugated Polymer Thin Films.* J. Magn. Magn. Mater., **321**, 2204 (2009).

[Sawa04]   A. Sawa, T. Fujii, M. Kawasaki and Y. Tokura, *Hysteretic Current-Voltage Characteristics and Resistance Switching at a Rectifying $Ti/Pr_{0.7}Ca_{0.3}MnO_3$ Interface.* Appl. Phys. Lett., **85**, 4073 (2004).

[Sawa08]   A. Sawa, *Resistive Switching in Transition Metal Oxides.* Mater. Today, **11**, 28 (2008).

[Schmidt00]   G. Schmidt, D. Ferrand, L.W. Molenkamp, A.T. Filip and B.J. van Wees, *Fundamental Obstacle for Electrical Spin Injection From a Ferromagnetic Metal Into a Diffusive Semiconductor.* Phys. Rev. B, **62**, 4790 (2000).

[Schmidt09]   R. Schmidt, J.H. Oh, Y.-S. Sun, M. Deppisch, A.-M. Krause, K. Radacki, H. Braunschweig, M. Könemann, P. Erk, Z. Bao and F. Würthner, *High-Performance Air-Stable n-Channel Organic Thin Film Transistors Based on Halogenated Perylene Bisimide Semiconductors.* J. Am. Chem. Soc., **131**, 6215 (2009).

[Scholz09]   M. Scholz, R. Schmidt, S. Krause, A. Schöll, F. Reinert, and F. Würthner, *Electronic Structure of Epitaxial Thin Films of Bay-substituted Perylene Bisimide Dyes.* Appl. Phys. A, **95**, 285 (2009).

[Schoonus09]   J.J.H.M. Schoonus, P.G.E. Lumens, W. Wagemans, J.T. Kohlhepp, P.A. Bobbert, H.J.M. Swagten and B. Koopmans, *Magnetoresistance in Hybrid Organic Spin Valves at the Onset of Multiple-Step Tunneling.* Phys. Rev. Lett., **103**, 146601 (2009).

[Schulz11]   L. Schulz, L. Nuccio, M. Willis, P. Desai, P. Shakya, T. Kreouzis, V.K. Malik, C. Bernhard, F.L. Pratt, N.A. Morley, A. Suter, G.J. Nieuwenhuys, T. Prokscha, E. Morenzoni, W.P. Gillin, and A.J. Drew, *Engineering Spin Propagation Across a Hybrid Organic/Inorganic Interface Using a Polar Layer.* Nat. Mater., **10**, 39 (2011).

[Shim08]   J.H. Shim, K.V. Raman, Y.J. Park, T.S. Santos, G.X. Miao, B. Satpati and J.S. Moodera, *Large Spin Diffusion Length in an Amorphous Organic Semiconductor.* Phys. Rev. Lett., **100**, 226603 (2008).

[Simmons63]   J.G. Simmons, *Generalized Formula for the Electric Tunnel Effect Between Similar Electrodes Separated by a Thin Insulating Film.* J. Appl. Phys., **34**, 1793 (1963).

[Simmons67]   J.G. Simmons and R.R. Verderber, *New Conduction and Reversible Memory Phenomena in Thin Insulating Films.* Proc. R. Soc. London, Ser. A, **301**, 77 (1967).

[Spear57]   W.E. Spear, *Transit Time Masurements of Charge Carriers in Amorphous Selenium Films.* Proc. Phys. Soc., London, Sect. B, **70**, 669 (1957).

[Springer05]   W. Martienssen and H. Warlimont (Editors), *Springer Handbook of Condensed Matter and Materials Data.* Springer Berlin Heidelberg (2005).

[Steenbeck99]   K. Steenbeck and R. Hiergeist, *Magnetic Anisotropy of Ferromagnetic $La_{0.7}(Sr,Ca)_{0.3}MnO_3$ Epitaxial Films.* Appl. Phys. Lett., **75**, 1778 (1999).

[Steil13]   S. Steil, N. Grossmann, M. Laux, A. Ruffing, D. Steil, M. Wiesenmayer, S. Mathias, O.L.A. Monti, M. Cinchetti and M. Aeschlimann, *Spin-Dependent Trapping of Electrons at Spinterfaces.* Nat. Phys., **9**, 242 (2013).

[Steinbacher07] F. Steinbacher, *Organische Halbleiter mit ferromagnetischen Kontakten.* Master's thesis, Physikalisches Institut der Julius-Maximilians-Universität Würzburg (2007).

[Stoner48]   E.C. Stoner and E.P. Wohlfarth, *A Mechanism of Magnetic Hysteresis in Heterogeneous Alloys.* Philos. Trans. R. Soc., A, **240**, 599 (1948).

[Stratton62]   R. Stratton, *Volt-Current Characteristics for Tunneling Through Insulating Films.* J. Phys. Chem. Solids, **23**, 1177 (1962).

[Sze06]   S.M. Sze and K.K. Ng, *Physics of Semiconductor Devices, Third Edition.* Wiley & Sons (2006).

[Tang87]   C.W. Tang and S.A. VanSlyke, *Organic Electroluminescent Diodes.* Appl. Phys. Lett., **51**, 913 (1987).

[Tombros07]   N. Tombros, C. Jozsa, M. Popinciuc, H.T. Jonkman and B.J. van Wees, *Electronic Spin Transport and Spin Precession in Single Graphene Layers at Room Temperature.* Nature, **448**, 571 (2007).

[Tsividis99]   Y. Tsividis, *Operation and Modeling of the MOS Transistor, Second Edition.* Oxford University Press (1999).

[Tsui71]   D.C. Tsui, R.E. Dietz and L.R. Walker, *Multiple Magnon Excitation in NiO by Electron Tunneling.* Phys. Rev. Lett., **27**, 1729 (1971).

[Tsui00]   F. Tsui, M.C. Smoak, T.K. Nath and C.B. Eom, *Strain-Dependent Magnetic Phase Diagram of Epitaxial $La_{0.67}Sr_{0.33}MnO_3$ Thin Films.* Appl. Phys. Lett., **76**, 2421 (2000).

[Tsymbal99]   E.Y. Tsymbal and D.G. Pettifor, *The Influence of Impurities Within the Barrier on Tunneling Magnetoresistance.* J. Appl. Phys., **85**, 5801 (1999).

[Tsymbal03]   E.Y. Tsymbal, A. Sokolov, I.F. Sabirianov and B. Doudin, *Resonant Inversion of Tunneling Magnetoresistance.* Phys. Rev. Lett., **90**, 186602 (2003).

[Valet93]   T. Valet and A. Fert, *Theory of the Perpendicular Magnetoresistance in Magnetic Multilayers.* Phys. Rev. B, **48**, 7099 (1993).

[VanSanten50] J.H. Van Santen and G.H. Jonker, *Electrical Conductivity of Ferromagnetic Compounds of Manganese with Perovskite Structure.* Physica, **16**, 599 (1950).

[Vinzelberg08] H. Vinzelberg, J. Schumann, D. Elefant, R.B. Gangineni, J. Thomas and B. Büchner, *Low Temperature Tunneling Magnetoresistance on $(La,Sr)MnO_3/Co$ Junctions With Organic Spacer Layers.* J. Appl. Phys., **103**, 093720 (2008).

[Wagemans11]   W. Wagemans and B. Koopmans, *Spin Transport and Magnetoresistance in Organic Semiconductors.* Phys. Status Solidi B, **248**, 1029 (2011).

[Wahler09]   M. Wahler, *Spin-Ventile mit organischen Halbleitern.* Master's thesis, Physikalisches Institut der Julius-Maximilians-Universität Würzburg (2009).

[Wang05]   F.J. Wang, Z.H. Xiong, D. Wu, J. Shi and Z.V. Vardeny, *Organic Spintronics: The case of $Fe/Alq_3/Co$ Spin-Valve Devices.* Synth. Met., **155**, 172 (2005).

[Wang07]   F.J. Wang, C.G. Yang, Z.V. Vardeny and X.G. Li, *Spin Response in Organic Spin Valves Based on $La_{2/3}Sr_{1/3}MnO_3$ Electrodes.* Phys. Rev. B, **75**, 245324 (2007).

[Wang12]   F. Wang, F. Macià, M. Wohlgenannt, A.D. Kent and M.E. Flatté, *Magnetic Fringe-Field Control of Electronic Transport in an Organic Film.* Phys. Rev. X, **2**, 021013 (2012).

[Wang14]   K. Wang, J.G.M. Sanderink, T. Bolhuis, W.G. van der Wiel and M.P. de Jong, *Tunneling Anisotropic Magnetoresistance in C_{60}-based Organic Spintronic Systems.* Phys. Rev. B, **89**, 174419 (2014).

[Waser90]   R. Waser, T. Baiatu and K.-H. Härdtl, *dc Electrical Degradation of Perovskite-Type Titanates: II, Single Crystals.* J. Am. Ceram. Soc., **73**, 1654, 1990).

[Waser07]   R. Waser and M. Aono, *Nanoionics-Based Resistive Switching Memories.* Nat. Mater., **6**, 833 (2007).

[Watanabe14] S. Watanabe, K. Ando, K. Kang, S. Mooser, Y. Vaynzof, H. Kurebayashi, E. Saitho and H. Sirringhaus, *Polaron Spin Current Transport in Organic Semiconductors.* Nat. Phys., **10**, 308 (2014).

[Wu05]   D. Wu, Z.H. Xiong, X.G. Li, Z.V. Vardeny and J. Shi, *Magnetic-Field-Dependent Carrier Injection at $La_{2/3}Sr_{1/3}MnO_3$ and Organic Semiconductors Interfaces.* Phys. Rev. Lett., **95**, 016802 (2005).

[Xiong04]   Z.H. Xiong, D. Wu, Z.V. Vardeny and J. Shi, *Giant Magnetoresistance in Organic Spin-Valves.* Nature, **427**, 821 (2004).

[Xu07]   W. Xu, G.J. Szulczewski, P. LeClair, I. Navarrete, R. Schad, G. Miao, H. Guo and A. Gupta, *Tunneling Magnetoresistance Observed in $La_{0.67}Sr_{0.33}MnO_3$/Organic Molecule/Co Junctions.* Appl. Phys. Lett., **90**, 072506 (2007).

[Yang09]   M.K. Yang, J.-W. Park, T.K. Ko and J.-K. Lee, *Bipolar Resistive Switching Behavior in $Ti/MnO_2/Pt$ Structure for Nonvolatile Memory Devices.* Appl. Phys. Lett., **95**, 042105 (2009).

[Yoo09]   J.-W. Yoo, H.W. Jang, V.N. Prigodin, C. Kao, C.B. Eom and A.J. Epstein, *Giant Magnetoresistance in Ferromagnet/Organic Semiconductor/Ferromagnet Heterojunctions.* Phys. Rev. B, **80**, 205207 (2009).

[Yu13]   Z.G. Yu, *Suppression of the Hanle Effect in Organic Spintronic Devices.* Phys. Rev. Lett., **111**, 016601 (2013).

[Zener51]   C. Zener, *Interaction Between the d-Shells in the Transition Metals. II. Ferromagnetic Compounds of Manganese with Perovskite Structure.* Phys. Rev., **82**, 403 (1951).

[Zhan07]   Y.Q. Zhan, I. Bergenti, L.E. Hueso, V. Dediu, M.P. de Jong and Z.S. Li, *Alignment of Energy Levels at the $Alq_3/La_{0.7}Sr_{0.3}MnO_3$ Interface for Organic Spintronic Devices.* Phys. Rev. B, **76**, 045406 (2007).

[Zhan08]   Y.Q. Zhan, M.P. de Jong, F.H. Li, V. Dediu, M. Fahlman and W.R. Salaneck, *Energy Level Alignment and Chemical Interaction at Alq₃/Co Interfaces for Organic Spintronic Devices.* Phys. Rev. B, **78**, 045208 (2008).

[Zhan12]   Y. Zhan and M. Fahlman, *The Study of Organic Semiconductor/Ferromagnet Interfaces in Organic Spintronics: A Short Review of Recent Progress.* J. Polym. Sci., Part B: Polym. Phys., **50**, 1453 (2012).

[Ziese10]   M. Ziese, I. Vrejoiu and D. Hesse, *Inverted Hysteresis and Giant Exchange Bias in $La_{0.7}Sr_{0.3}MnO_3/SrRuO_3$ Superlattices.* Appl. Phys. Lett., **97**, 052504 (2010).

List of Publications

Journals (peer-reviewed)

- M. Grünewald, N. Homonnay, J. Kleinlein and G. Schmidt, *Voltage Controlled Oxide Barriers in Organic/Hybrid Spin Valves Based on Tunneling Anisotropic Magnetoresistance.* Phys. Rev. B, **90**, 205208 (2014).

- M. Grünewald, R. Göckeritz, N. Homonnay, F. Würthner, L.W. Molenkamp and G. Schmidt, *Vertical Organic Spin Valves in Perpendicular Magnetic Fields.* Phys. Rev. B, **88**, 085319 (2013).

- M. Grünewald, J. Kleinlein, F. Syrowatka, F. Würthner, L.W. Molenkamp and G. Schmidt, *Large Room-Temperature Magnetoresistance in Lateral Organic Spin Valves Fabricated by In Situ Shadow Evaporation.* Org. Electron., **14**, 2082 (2013).

- M. Grünewald, M. Wahler, F. Schumann, M. Michelfeit, C. Gould, R. Schmidt, F. Würthner, G. Schmidt and L.W. Molenkamp, *Tunneling Anisotropic Magnetoresistance in Organic Spin Valves.* Phys. Rev. B, **84**, 125208 (2011).

Conference Talks

- M. Grünewald, N. Homonnay, J. Kleinlein and G. Schmidt, *Resisitive Switching in Organic TAMR Devices.* In *DPG spring conference*, Dresden, Germany (2014)

- M. Grünewald, N. Homonnay, J. Kleinlein and G. Schmidt, *Resisitive Switching in AlQ3-based TAMR Devices.* In *European Workshop in Molecular Spintronics*, Puerto Santiago, Spain (2013)

- M. Grünewald, M. Wahler, F. Schumann, C. Gould, R. Schmidt, F. Würthner, L.W. Molenkamp and G. Schmidt, *Tunneling Anisotropic Magnetoresistance in Organic Spin Valves.* In *DPG spring conference*, Berlin, Germany (2012)

- M. Grünewald, F. Würthner, G. Schmidt, and L.W. Molenkamp *In-situ Fabrication of Lateral Organic Spin-valve Structures with sub 100-nm Channel Length.* In *DPG spring conference*, Regensburg, Germany (2010)

- M. Grünewald, M. Michelfeit, G. Schmidt, R. Schmidt, F. Würthner and L.W. Molenkamp, *Magnetoresistance Effects in a PTCDI-based Ferromagnetic/organic Semiconductor Hybrid Structure.* In *DPG spring conference*, Berlin, Germany (2008)

Conference Posters

- M. Grünewald, R. Göckeritz, N. Homonnay, C. Eisenschmidt and G. Schmidt, *Tunneling Anisotropic Magnetoresistance in H2-Phthalocyanine-based Organic Spin Valves.* In *Spins in Organic Semiconductors 2012*, London, United Kingdom (2012)

- M. Grünewald, M. Wahler, P. Graziosi, A. Dediu, F. Würthner, G. Schmidt and L.W. Molenkamp, *Investigation of Hanle-effect in Vertical Organic Spin Valves.* In *Spins in Organic Semiconductors 2010*, Amsterdam, The Netherlands (2010)

- M. Grünewald, P. Graziosi, A. Dediu, F. Würthner, G. Schmidt and L.W. Molenkamp, *In-situ Fabrication of Lateral Organic Spin-valve Structures with sub 100-nm Channel Length.* In *Spins in Organic Semiconductors 2009*, Salt Lake City, USA (2009)

Danksagung

Ich möchte mich bei all denen bedanken, die mich bei der Arbeit an der vorliegenden Dissertation im Laufe der letzten sieben Jahre unterstützt haben.

Zunächst einmal geht mein Dank an Herrn Prof. Dr. Laurens W. Molenkamp und Herrn Prof. Dr. Georg Schmidt, die es mir ermöglicht haben, meine Forschungsarbeiten im Bereich der organischen Spintronik am Lehrstuhl für Experimentelle Physik III der Julius-Maximilians-Universität Würzburg bzw. in der Fachgruppe Nanostrukturierte Materialien am Institut für Physik der Martin-Luther-Universität Halle-Wittenberg durchzuführen.

Herrn Prof. Dr. Georg Schmidt danke ich insbesondere für die stets wohlwollende Betreuung und engagierte Förderung in Form von Diskussionen, Anregungen und konstruktiver Kritik, sei es im Zusammenhang mit der vorliegenden Arbeit oder mit konkreten Experimenten und deren Resultaten. Desweiteren möchte ich ihm dafür danken, dass er es mir ermöglicht hat am Aufbau der Fachgruppe Nanostrukturierte Materialien mitzuwirken, was eine sehr interessante und lehrreiche Erfahrung war.
Weiterhin gilt mein Dank allen Mitarbeitern der Arbeits- und Fachgruppen, in denen ich an meiner Dissertation gearbeitet habe, für all die Unterstützung, die mir zugute gekommen ist. Von den ehemaligen Kollegen am Lehrstuhl für Experimentelle Physik III der Julius-Maximilians-Universität Würzburg möchte ich hier vor allem Herrn Volkmar Hock (Hilfe im Reinraum) und Herrn Roland Ebert (zuverlässige Versorgung mit flüssigem Helium) hervorheben. Von den Kollegen an der Martin-Luther-Universität Halle-Wittenberg danke ich in diesem Zusammenhang besonders Herrn Martin Wahler und Herrn Johannes Kleinlein, mit denen ich stets in einer entspannten Atmosphäre sowohl über physikalische Probleme als auch über anstehende Neuanschaffungen, Planungen und Konstruktionen diskutieren konnte. Herrn Robert Göckeritz danke ich für die kollegiale und inspirierende Zusammenarbeit in unserem Fachgebiet. Auch Herrn Christian Eisenschmidt möchte ich für seine Unterstützung bei der Inbetriebnahme diverser Anlagen und für die Organisation der Versorgung mit flüssigem Helium danken. Umfangreiche Hilfe im Reinraum und im Bereich Elektronenmikroskopie kam mir von Seiten der Herren Sven Schlenker, Dr. Bodo Fuhrmann, Frank Syrowatka und Dr. Frank Heyroth des Interdisziplinären Instituts für Materialwissenschaften zugute. Auch hierfür bin ich sehr dankbar.
Weiterhin danke ich den Herrn Martin Wahler und Herrn Florian Schumann, die ich im Rahmen ihrer Abschlussarbeiten betreuen durfte und die durch ihr Engagement ebenfalls maßgeblich zu dieser Arbeit beigetragen haben.

Lebenslauf

Persönliche Daten:

Name, Vorname:	Grünewald, Matthias
Adresse:	Große Märkerstr. 18, 06108 Halle
Geburtsdatum:	31. Oktober 1980
Geburtsort:	Erlenbach am Main
Staatsangeh.:	deutsch
Familienstand:	ledig

Schulische Ausbildung:

1991-2000:	Kronberg-Gymnasium Aschaffenburg
	Abschluss:
	Abitur

Studium:

2002-2007:	Hauptfach Physik,
	Julius-Maximilians-Universität Würzburg
	Diplomarbeitsthema:
	Magnetowiderstandseffekte in Organischen Halbleitern
	Abschluss:
	Diplom

Promotionsstudium:

2008-2009:	Hauptfach Physik,
	Julius-Maximilians-Universität Würzburg
2009-2013:	Hauptfach Physik,
	Martin-Luther-Universität Halle-Wittenberg

Halle (Saale), Dezember 2014

Matthias Grünewald

Eidesstattliche Erklärung

Ich erkläre an Eides statt, dass ich die Arbeit selbstständig und ohne fremde Hilfe verfasst, keine anderen als die von mir angegebenen Quellen und Hilfsmittel benutzt und die den benutzten Werken wörtlich oder inhaltlich entnommenen Stellen als solche kenntlich gemacht habe.

Weiterhin erkläre ich, dass ich bisher keine vergeblichen Promotionsversuche unternommen habe. Diese Dissertation hat in ihrer gegenwärtigen bzw. in einer anderen Fassung bisher keiner anderen Fakultät vorgelegen.

Halle (Saale), Dezember 2014

Matthias Grünewald